Electron spin transport in graphene-based devices

Maassen, Thomas

Publication date:
2013

Citation for published version (APA):
Maassen, T. (2013). Electron spin transport in graphene-based devices. Groningen: s.n.

Electron Spin Transport in Graphene–Based Devices

Thomas Maassen

FOM

university of groningen

faculty of mathematics and natural sciences

zernike institute for advanced materials

Zernike Institute PhD thesis series 2013-08
ISSN: 1570-1530
ISBN: 978-90-367-6181-9
ISBN: 978-90-367-6180-2 (electronic version)

The work described in this thesis was performed in the research group Physics of Nanodevices of the Zernike Institute for Advanced Materials at the University of Groningen, the Netherlands. This work is part of the research programme of the Foundation for Fundamental Research on Matter (FOM), which is part of the Netherlands Organisation for Scientific Research (NWO).

Cover: Artist's impression of a graphene spin transport device.
Printed by: GVO drukkers & vormgevers B.V., Ede

RIJKSUNIVERSITEIT GRONINGEN

ELECTRON SPIN TRANSPORT IN GRAPHENE–BASED DEVICES

Proefschrift

ter verkrijging van het doctoraat in de
Wiskunde en Natuurwetenschappen
aan de Rijksuniversiteit Groningen
op gezag van de
Rector Magnificus, dr. E. Sterken,
in het openbaar te verdedigen op
vrijdag 3 mei 2013
om 14:30 uur

door

Thomas Maassen

geboren op 12 februari 1984
te Viersen, Duitsland

Promotor: Prof. dr. ir. B.J. van Wees

Beoordelingscommissie: Prof. dr. Jaroslav Fabian
Prof. dr. Albert Fert
Prof. dr. Roland Kawakami

dedicated to my family

Contents

Chapter 1

Introduction

Abstract

The field of spintronics offers applications in nowadays and future technologies and a lot of interesting physics and surprising possibilities. Graphene is the thinnest possible material and brings many superlatives in different areas, including very high electronic quality. Both of these research fields were awarded the Nobel prize in physics in recent years. When combined they provide unique opportunities that shape the field of graphene spintronics which is the scope of this thesis.

In this book I discuss my research on spin transport in graphene–based devices that I performed in the last 4 years. Starting with general limitations of spin transport measurements due to the invasive effects of the contacts, I continue by showing that in the diffusive system of graphene charge and spin are transported by the same process. As transport in graphene is limited by the environment of the graphene channel, the next two chapters of this thesis represent two ways to examine the role of the graphene surroundings. First, using a stack of graphene layers in few-layer graphene to screen spurious electrical potentials of, e.g., impurities in the silicon oxide substrate or other contaminants in the environment of the graphene flake. And second, by using epitaxial graphene on silicon carbide, replacing the commonly used silicon oxide substrate with a highly pure semi-conductor. At the same time, as the graphene on silicon carbide is epitaxially grown, this system enables an upscaled production of graphene devices. Next, I discuss new physics with our model describing the influence of localized states on spin transport that we observed in the graphene/silicon carbide system. I conclude with a discussion of how the presented research fits into the bigger picture of spintronics in graphene and how the results relate to other research on spin transport in graphene performed recently.

1.1 Spintronics

Spintronics, short for spin-based electronics, relates to electron spin phenomena in solid state systems. The electron spin is the intrinsic, quantum mechanical property of electrons which make them behave as if spinning around an inner axis. The angular momentum of this "spinning" is associated with a magnetic moment, giving the spin a direction that can be used to store information.

The demonstration of the giant magnetoresistance (GMR) by the groups of Albert Fert and Peter Grünberg in the end of the 1980s [1, 2] was a first step to implement spin information into actual devices, where, until that time, only the electron charge was being exploited. The discovery of the GMR laid the foundation for the new field of spintronics [3] and for that Fert and Grünberg were awarded the Nobel prize in physics in 2007 [4]. In GMR devices the interaction of spins with magnetic materials is being used to store information. They consist of two or more ferromagnetic (FM) layers, each a few nanometers thick, that are separated by non-magnetic materials. When measured electrically, the devices show a lower resistance when the magnetizations of the FM layers are aligned compared to an antialigned orientation. This concept proved very successful, in particular in the read heads of nowadays standard computer hard disk drives [3]. At the same time it is also being used in the development of novel non-volatile magnetic random access memory elements (MRAM) for personal computers [3]. A promising discovery in this field was the prediction and observation of spin transfer torque effect (STT). Here it was shown that a spin polarized current can excite the magnetization of a ferromagnet and switch its direction even without an applied magnetic field [5–8], leading to the concept of STT-MRAM.

While there are many more interesting concepts for spintronic applications being developed like, e.g., spin light emitting diodes or using the spin state to obtain qubits for quantum computing, there is still a lot of fundamental research in the field [9]. Research focuses, e.g., on optical injection, manipulation and detection of spin ensembles with, e.g., pump-probe photoluminescence measurements, on the determination of spin properties in materials using electron spin resonance (ESR) or on the behavior of spins in quantum wells. At the same time, a lot of research is performed on electrical spin transport [9].

1.1.1 Spin transport

In spin transport devices the injected spins are transported over a certain distance while being manipulated before being detected. Though spin transport concepts like the spin field effect transistor where the conductance is switched by a magnetic field are already relatively old [10], one of the main ingredients is still missing: A good material for the channel. An important property the channel should provide is the possibility for the spins to maintain their spin information (direction) and not to lose it accidentally while being transported. On the other hand the channel also has to interact well with a spin injector and detector and research into suitable materials for these tasks has to be done as well.

To find an appropriate channel, materials are examined for their spin relaxation time and length, the time and length describing how long the spin information is maintained. To inspect the spin transport properties of a material it has clear advantages to use the so-called non-local technique [11–13]. With this technique one results in pure spin currents (see Chapter 2) being sent between injector and detector, avoiding spurious effects of charge currents that can be misinterpreted as spin signals [14]. While metallic systems started to be studied with the non-local technique about a decade ago [12, 13] promising results in recent time are obtained on semiconductors like silicon [15]. Graphene, a very novel material, also shows promising results on spin transport [16].

Before going into detail here, let us introduce this material in the following section.

1.2 Graphene

Graphene, the one atom thick honeycomb lattice of carbon atoms, is nowadays considered one of the most promising candidates in material science and condensed-matter physics as it combines many superlatives in one system [17–19]. Since graphene was isolated using the surprisingly easy and cheap method of mechanical cleaving of graphite [20, 21], its unusual properties have boosted research in many fields [17–19] and led to the Nobel prize in physics awarded to Andrei Geim and Konstantin Novoselov in 2010. Research first focused on electronic transport with its linear energy dispersion, the gate tunable charge carrier density and polarity [22] and the high electronic quality resulting in extremely high mobilities (up to 2.5×10^5 $\mathrm{cm}^2/\mathrm{Vs}$ with a mean free path of micrometers at room temperature [23]) and a measurable quantum Hall effect [24, 25] even at room temperature [26]. Graphene can carry current densities a million times higher than copper [27] and has an extraordinary high thermal conductivity [28]. At the same time, graphene is the strongest known material with a very high stiffness and elasticity (more than any other crystal) [18, 29, 30]. Next to superlatives graphene shows interesting features such as its light absorption of 2.3% that is directly linked to the fine structure constant [31] and it shrinks with increasing temperature [32]. Even though it is the thinnest possible material [18] it is impermeable to gases [33]. Being only one atom graphene is a material with only surface and no bulk properties. Accordingly, graphene is strongly influenced by the environment resulting in reduced electronic quality and electron-hole puddles, as the surroundings, e.g., the commonly used SiO_2 substrate

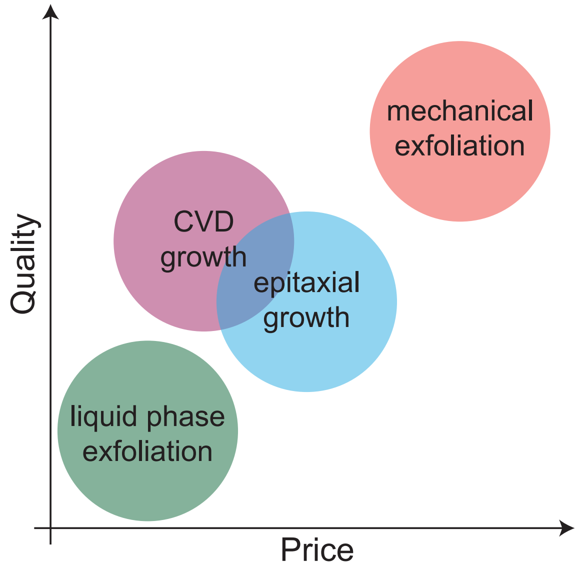

Figure 1.1: Different methods to produce graphene plotted as a function of graphene quality and price (adapted from Ref. [19]).

bear spurious electrical potentials [34, 35]. To avoid such influences and enhance the electrical quality one can suspend graphene by removing the substrate [36–38], screen spurious effects in a graphene stack [39, 40] or replace the commonly used silicon oxide (SiO_2) substrate by, e.g., hexagonal boron nitride [23, 41, 42]. At the same time, this strong effect of the environment can be used for sensor devices [19, 43].

1.2.1 Different graphene sources for different applications

The long-term goal is to move graphene from research in the lab to applications and real devices to innovate and improve existing technologies [19].

Mechanically exfoliated graphene

A lot of research is based on mechanically cleaved graphene, also called exfoliated graphene [21] which is of highest quality [19]. But as this type of graphene is produced by manual cleaving of graphite using scotch tape with a unique processing for every device [21], there is no possibility to upscale this production method at reasonable cost and it is therefore only suitable for use in research laboratories [19]. Hence, parallel to the research on the properties of (exfoliated) graphene there is a whole field of research on the production of graphene from different sources and its properties [18, 19, 44]. Those different production methods offer a wide range of quality and production costs [19]. The most widely used methods are displayed in Fig. 1.1. Depending on the application one can then choose the most appropriate material. In the moment the main graphene sources that are being used in research and first applications are mechanically exfoliated graphene, graphene obtained by liquid phase exfoliation and exfoliation by oxidation, chemical vapor deposition, and growth on silicon carbide (SiC). There are still further methods to obtain graphene that are being investigated [19].

Liquid phase exfoliation and exfoliation by oxidation

To produce big amounts of rather low quality and cheap graphene one can exfoliate graphene by liquid phase exfoliation. In this process graphite is put into a solvent which splits it into thin flakes with help of sonication. Under the right conditions one can get a considerable fraction of mono layers which then can be sorted and selected by centrifugation [45, 46]. A similar approach uses oxidized graphite that is then exfoliated in solution using, e.g., ultrasonication or heat and if needed the oxidized graphene can afterwards to some extent be reduced [47].

These types of low cost graphene are already being produced on industrial scale [48] and the idea is to produce, e.g., conductive inks or paints or composite materials with a considerable fraction of graphene inside. The idea is that these components inherit some of graphene's properties like strength, or electrical or thermal conductivity [19].

Chemical vapor deposition

High quality graphene on large scale can be produced using chemical vapor deposition (CVD) on transition metals with the most promising results on copper [49, 50]. Growing graphene on a metal implies that it has to be transfered to an insulating substrate to be able to do electronic measurements. This has been already achieved in a scalable approach for 30-inch graphene films [50]. Therefore to date, CVD grown graphene is the only production method that actually can produce graphene sheets of this size, even though the transfer still reduces the quality of the graphene sheet. CVD obtained graphene could already be used for touch screens in the near future as it combines transparency and conductivity [19, 50]. The flexibility of graphene lets us anticipate new kinds of flexible touch screen devices [19].

Though the growth on metals brings the challenge to find a non-damaging transfer technique for high quality applications, it also results in interesting possible uses of graphene as a contact barrier for, e.g., spin injection into the metal for current out-of-plane devices [51].

Next to developing a high quality transfer process and enhancing the graphene quality, the production costs have to be reduced to use CVD grown graphene on industrial scale for electronic applications. The cost reduction can be achieved by decreasing the energy consumption of the process and by optimizing the use and the properties of the metal substrates [19].

Epitaxial growth on silicon carbide

Already in 1962 Badami reported the growth of graphite on silicon carbide (SiC) when heating the substrate to more than two thousand degrees Celsius in vacuum [52]. Therefore the idea to grow graphene on SiC is not new and first tries were already conducted before mechanical exfoliation of graphene was invented [53]. (See a review on the early work on growth of thin graphite on SiC and by CVD in Ref. [54].) While the growth was in the beginning not well controlled [55], high quality graphene has been grown in recent years [56–61]. As SiC is an excellent semi-conductor [62] the combination of graphene and the substrate is already interesting itself [63] but measurements on this substrate can also give insights in the intrinsic graphene properties when comparing it to results obtained for graphene on SiO_2.

The main disadvantage of epitaxial graphene on SiC are the high wafer cost and the high temperatures needed to grow graphene [19]. The clear advantage though is that SiC has a wide band gap so that graphene grown on SiC does not have to be transfered to be used for electronic devices. Therefore there is no transfer related quality loss and this type of graphene could be used for high quality devices like high frequency transistors [19]. Also, epitaxial graphene on SiC has already proven its usability in resistance metrology, where it showed higher accuracy than commonly used GaAs resistance standards [61]. To accurately define the resistance is especially important as a well defined resistance leads to a metrology standard for the kilogram.

Further graphene applications

Due to its high mobilities graphene is in principle considered a good candidate for future logic devices, but the main challenge is here the missing band gap in the band structure of graphene, resulting in very low on/off ratios of graphene transistors [19]. To increase the on/off ratio nano ribbons [64, 65], functionalized graphene like graphane [66] and fluorographene [67], symmetry breaking in bilayer graphene [68] and other approaches have been tried, but until now none of the approaches lead to the needed effect.

Other applications include the use as transparent electrode material for solar cells [19], high surface electrodes in batteries [19], support materials in transmission electron microscopes [18] or the use in photonics due to the special optical properties of graphene [19].

1.3 Spin transport in graphene

The properties of graphene make it an interesting candidate for use in spintronic devices. The high mobilities combined with low spin-orbit coupling and weak hyperfine interaction with the nuclei of the carbon atoms [69, 70] promise long spin relaxation times and lengths [71]. High spin relaxation times in graphene were also expected due to ESR studies on graphite [72, 73] that result in spin relaxation times of ~ 10 ns at RT [73]. Around 2007 several groups presented first results on spin transport in mono- and few-layer graphene [16, 74–79]. While all studies reported spin injection and detection, only Tombros *et al.* [16] reported Hanle spin precession measurements (see Section 2.4) that provide a reliable proof for spin injection and transport in graphene [80] and can separately determine the spin relaxation time and the diffusion coefficient, and therefore the spin relaxation length of the system [11]. The reported spin relaxation time of about 100 ps and lengths of about $2\ \mu$m stayed far behind the expectations for graphene. As the order of magnitude of these values obtained by Hanle precession measurements in single layer graphene has been reproduced by most groups in the field [81–85], ongoing research is mainly aiming to understand the limitations for spin transport in graphene. One of the main goals is to understand the spin relaxation mechanisms of graphene [84, 86–94] (see also Chapter 6 and 10). Here the main focus lies on the challenge to determine if the Elliott-Yafet or D'yakonov-Perel' spin relaxation mechanism limits spin transport (see Section 2.5) as single layer graphene and bilayer graphene seemed to be dominated by different mechanisms [87, 90, 91] with bilayer graphene showing surprisingly high values for the spin relaxation time of up to several nanoseconds [90, 91]. Still the question is open if the spin relaxation is based on to date unknown principles. Other research examines the influence of different environments on spin transport in graphene like few-layer graphene [95] (see also Chapter 7), suspended graphene [96], different substrates [85, 97–99] (see also Chapter 8 and 9), contaminations, absorbents or chemical modifications [82, 100–102]. Comparing these results can help to understand the intrinsic spin properties of graphene but also the possible modification of these. Measurements on graphene from different sources (see Section 1.2.1) aims at upscaling of graphene spintronic devices. Correlating the results exposes the dependence of spin transport on the quality of the graphene channel but offers also the chance to find new physics [83, 85, 97, 99] (see also Chapter 8 and 9). At the same time research aims to understand spurious effects on graphene spin transport, like the role of the ferromagnetic contacts and the barrier between the contacts and the graphene channel [103–111] (see also Chapter 5). A new branch of the field focuses on the non-linear effects between charge and spin in graphene that could lead to spintronic devices without ferromagnetic elements [112–114].

For more background information, the early graphene spintronics research and its foundations are reviewed in [115]. Further publications summarize the work of two of the main groups in the field [104, 116] and present a point of view on non-local spin transport measurements in graphene [14]. A very recent work focuses on the report of surprisingly long spin relaxation lengths on multilayer epitaxial graphene on SiC extracted from low temperature local spin valve measurements [108] in the context of the well established results from non-local measurements [117].

1.4 Outline of this thesis

The first three chapters of this thesis discuss the physics and experimental techniques used to perform the research that is presented in Chapter 5–Chapter 9. These five chapters are presented as they were published in different journals with minor changes. Chapter 10 comments on new interpretations of the published results. See below a list with an overview of the content of each chapter.

- *Chapter 2* introduces the basic spin transport theory of a diffusive system like graphene under the conditions on hand in the samples discussed in this thesis. This information will help to understand the interpretations of the measurements we present and the spin transport concepts we introduce in the following chapters.

- *Chapter 3* discusses the band structure and density of states of single layer, bilayer and few-layer graphene.

- *Chapter 4* presents the experimental techniques used to do the research presented in this thesis. The chapter describes the methods to obtain the different types of graphene used, reports how the graphene spin transport samples are prepared and discusses the measurement techniques employed.

- *Chapter 5* focuses on the effect of the electrodes on spin relaxation in a transport channel by quantifying a model developed to describe the dependence of Hanle spin precession measurement on the resistance of the electrodes. Then the results are compared to graphene spin transport measurements from the literature. This chapter also explains general guidelines to perform a reliable analysis of Hanle precession data.

- *Chapter 6* compares charge and spin diffusion measurements for a wide range of charge carrier concentrations in a single-layer graphene channel and shows that both types of transport are conducted by the same carriers.

- *Chapter 7* characterizes charge and spin transport in few-layer graphene. By measuring the electrical gate dependence of the resistance the screening of electrical potentials in few-layer graphene flakes is observed. This screening is then used to explain the enhancement of the spin transport quality for increasing number of graphene layers.

- *Chapter 8* shows the first study of spin transport in epitaxially grown monolayer graphene on SiC(0001) which gives the perspective of upscalability. This study is at the same time the first one to perform spin transport in graphene on a different substrate than SiO_2. Surprisingly, a significant increase of the spin relaxation time and a strong decrease of the spin diffusion coefficient is measured. As the measured spin diffusion coefficient does not comply with the charge diffusion coefficient, a number of possible reasons for this difference is listed.

- *Chapter 9* develops a model describing the influence of localized states on spin transport. This model is then used to explain the surprising results on monolayer epitaxial graphene from Chapter 8. Using measurements on quasi-free-standing monolayer epitaxial graphene these localized states can be pinpointed to the so-called buffer layer between the graphene and the substrate of monolayer epitaxial graphene.

- *Chapter 10* summarizes the results of this thesis and discusses how the research presented in this thesis relates to the results of other research groups mentioned in Section 1.3. Here the focus lies on the ongoing discussion on the spin relaxation mechanism in graphene. The chapter also gives a brief outlook on interesting open questions of the field.

- *The Appendix* gives details on the lithography and lift-off processes described in Chapter 4.

References

[1] M. N. Baibich, J. M. Broto, A. Fert, F. N. Van Dau, F. Petroff, P. Eitenne, G. Creuzet, A. Friederich, and J. Chazelas, “Giant Magnetoresistance of (001)Fe/(001)Cr Magnetic Superlattices,” *Phys. Rev. Lett.* **61**(21), pp. 2472–2475, 1988.

[2] G. Binasch, P. Grünberg, F. Saurenbach, and W. Zinn, “Enhanced Magnetoresistance in Layered Magnetic Structures with Antiferromagnetic Interlayer Exchange,” *Phys. Rev. B* **39**(7), pp. 4828–4830, 1989.

[3] S. A. Wolf, D. D. Awschalom, R. A. Buhrman, J. M. Daughton, S. von Molnár, M. L. Roukes, A. Y. Chtchelkanova, and D. M. Treger, “Spintronics: A Spin-Based Electronics Vision for the Future,” *Science* **294**(5546), pp. 1488–1495, 2001.

[4] E. E. Fullerton and I. K. Schuller, “The 2007 Nobel Prize in Physics: Magnetism and Transport at the Nanoscale,” *ACS Nano* **1**(5), pp. 384–389, 2007.

[5] J. C. Slonczewski, “Current-Driven Excitation of Magnetic Multilayers,” *J. Magn. Magn. Mater.* **159**, pp. L1–L7, 1996.

[6] L. Berger, “Emission of Spin Waves by a Magnetic Multilayer Traversed by a Current,” *Phys. Rev. B* **54**(13), pp. 9353–9358, 1996.

[7] M. Tsoi, A. G. M. Jansen, J. Bass, W.-C. Chiang, M. Seck, V. Tsoi, and P. Wyder, “Excitation of a Magnetic Multilayer by an Electric Current,” *Phys. Rev. Lett.* **80**(19), pp. 4281–4284, 1998.

[8] J. A. Katine, F. J. Albert, R. A. Buhrman, E. B. Myers, and D. C. Ralph, “Current-Driven Magnetization Reversal and Spin-Wave Excitations in Co/Cu/Co Pillars,” *Phys. Rev. Lett.* **84**(14), pp. 3149–3152, 2000.

[9] I. Žutić, J. Fabian, and S. Das Sarma, “Spintronics: Fundamentals and Applications,” *Rev. Mod. Phys.* **76**(2), pp. 323–410, 2004.

[10] S. Datta and B. Das, “Electronic Analog of the Electro-optic Modulator,” *Appl. Phys. Lett.* **56**(7), pp. 665–667, 1990.

[11] M. Johnson and R. H. Silsbee, “Coupling of Electronic Charge and Spin at a Ferromagnetic-Paramagnetic Metal Interface,” *Phys. Rev. B* **37**(10), pp. 5312–5325, 1988.

[12] F. J. Jedema, A. T. Filip, and B. J. van Wees, “Electrical Spin Injection and Accumulation at Room Temperature in an All-Metal Mesoscopic Spin Valve,” *Nature (London)* **410**, pp. 345–348, 2001.

[13] F. J. Jedema, H. B. Heersche, A. T. Filip, J. J. A. Baselmans, and B. J. van Wees, “Electrical Detection of Spin Precession in a Metallic Mesoscopic Spin Valve,” *Nature (London)* **416**, pp. 713–716, 2002.

[14] M. Shiraishi, “Electrically-Generated Pure Spin Current in Graphene,” *Jpn. J. Appl. Phys.* **51**, p. 08KA01, 2012.

[15] S. P. Dash, S. Sharma, R. S. Patel, M. P. de Jong, and R. Jansen, “Electrical Creation of Spin Polarization in Silicon at Room Temperature,” *Nature (London)* **462**(7272), pp. 491–494, 2009.

[16] N. Tombros, C. Józsa, M. Popinciuc, H. T. Jonkman, and B. J. van Wees, “Electronic Spin Transport and Spin Precession in Single Graphene Layers at Room Temperature,” *Nature (London)* **448**, pp. 571–574, 2007.

[17] A. K. Geim and K. S. Novoselov, “The Rise of Graphene,” *Nat. Mater.* **6**, pp. 183–191, 2007.

[18] A. K. Geim, “Graphene: Status and Prospects,” *Science* **324**(5934), pp. 1530–1534, 2009.

[19] K. S. Novoselov, V. I. Fal´ko, L. Colombo, P. R. Gellert, M. G. Schwab, and K. Kim, “A Roadmap for Graphene,” *Nature (London)* **490**(7419), pp. 192–200, 2012.

[20] K. S. Novoselov, A. K. Geim, S. V. Morozov, D. Jiang, Y. Zhang, S. V. Dubonos, I. V. Grigorieva, and A. A. Firsov, “Electric Field Effect in Atomically Thin Carbon Films,” *Science* **306**(5696), pp. 666–669, 2004.

[21] K. S. Novoselov, D. Jiang, F. Schedin, T. J. Booth, V. V. Khotkevich, S. V. Morozov, and A. K. Geim, “Two-Dimensional Atomic Crystals,” *Proc. Natl. Acad. Sci. USA* **102**(30), pp. 10451–10453, 2005.

[22] A. H. Castro Neto, F. Guinea, N. M. R. Peres, K. S. Novoselov, and A. K. Geim, “The Electronic

Properties of Graphene," *Rev. Mod. Phys.* **81**(1), pp. 109–162, 2009.

[23] A. S. Mayorov, R. V. Gorbachev, S. V. Morozov, L. Britnell, R. Jalil, L. A. Ponomarenko, P. Blake, K. S. Novoselov, K. Watanabe, T. Taniguchi, and A. K. Geim, "Micrometer-Scale Ballistic Transport in Encapsulated Graphene at Room Temperature," *Nano Lett.* **11**(6), pp. 2396–2399, 2011.

[24] K. S. Novoselov, A. K. Geim, S. V. Morozov, D. Jiang, M. I. Katsnelson, I. V. Grigorieva, S. V. Dubonos, and A. A. Firsov, "Two-Dimensional Gas of Massless Dirac Fermions in Graphene," *Nature (London)* **438**, pp. 197–200, 2005.

[25] Y. Zhang, J. P. Small, W. V. Pontius, and P. Kim, "Fabrication and Electric-Field-Dependent Transport Measurements of Mesoscopic Graphite Devices," *Appl. Phys. Lett.* **86**(7), p. 073104, 2005.

[26] K. S. Novoselov, Z. Jiang, Y. Zhang, S. V. Morozov, H. L. Stormer, U. Zeitler, J. C. Maan, G. S. Boebinger, P. Kim, and A. K. Geim, "Room-Temperature Quantum Hall Effect in Graphene," *Science* **315**(5817), p. 1379, 2007.

[27] J. Moser, A. Barreiro, and A. Bachtold, "Current-induced Cleaning of Graphene," *Appl. Phys. Lett.* **91**(16), p. 163513, 2007.

[28] A. A. Balandin, S. Ghosh, W. Bao, I. Calizo, D. Teweldebrhan, F. Miao, and C. N. Lau, "Superior Thermal Conductivity of Single-Layer Graphene," *Nano Lett.* **8**(3), pp. 902–907, 2008.

[29] C. Lee, X. Wei, J. W. Kysar, and J. Hone, "Measurement of the Elastic Properties and Intrinsic Strength of Monolayer Graphene," *Science* **321**(5887), pp. 385–388, 2008.

[30] T. J. Booth, P. Blake, R. R. Nair, D. Jiang, E. W. Hill, U. Bangert, A. Bleloch, M. Gass, K. S. Novoselov, M. I. Katsnelson, and A. K. Geim, "Macroscopic Graphene Membranes and Their Extraordinary Stiffness," *Nano Lett.* **8**(8), pp. 2442–2446, 2008.

[31] R. R. Nair, P. Blake, A. N. Grigorenko, K. S. Novoselov, T. J. Booth, T. Stauber, N. M. R. Peres, and A. K. Geim, "Fine Structure Constant Defines Visual Transparency of Graphene," *Science* **320**(5881), p. 1308, 2008.

[32] W. Bao, F. Miao, Z. Chen, H. Zhang, W. Jang, C. Dames, and C. N. Lau, "Controlled Ripple Texturing of Suspended Graphene and Ultrathin Graphite Membranes," *Nat. Nanotechnol.* **4**, pp. 562–566, 2009.

[33] J. S. Bunch, S. S. Verbridge, J. S. Alden, A. M. van der Zande, J. M. Parpia, H. G. Craighead, and P. L. McEuen, "Impermeable Atomic Membranes from Graphene Sheets," *Nano Lett.* **8**(8), pp. 2458–2462, 2008.

[34] J. Martin, N. Akerman, G. Ulbricht, T. Lohmann, J. H. Smet, K. von Klitzing, and A. Yacoby, "Observation of Electron-Hole Puddles in Graphene Using a Scanning Single-Electron Transistor," *Nat. Phys.* **4**, pp. 144–148, 2008.

[35] Y. Zhang, V. W. Brar, C. Girit, A. Zettl, and M. F. Crommie, "Origin of Spatial Charge Inhomogeneity in Graphene," *Nat. Phys.* **5**(10), pp. 722–726, 2009.

[36] K. Bolotin, K. Sikes, Z. Jiang, M. Klima, G. Fudenberg, J. Hone, P. Kim, and H. Stormer, "Ultrahigh Electron Mobility in Suspended Graphene," *Solid State Commun.* **146**(9-10), pp. 351–355, 2008.

[37] X. Du, I. Skachko, A. Barker, and E. Y. Andrei, "Approaching Ballistic Transport in Suspended Graphene," *Nat. Nanotechnol.* **3**, pp. 491–495, 2008.

[38] N. Tombros, A. Veligura, J. Junesch, J. J. van den Berg, P. J. Zomer, M. Wojtaszek, I. J. Vera-Marun, H. T. Jonkman, and B. J. van Wees, "Large Yield Production of High Mobility Freely Suspended Graphene Electronic Devices on a Polydimethylglutarimide Based Organic Polymer," *J. Appl. Phys.* **109**(9), p. 093702, 2011.

[39] F. Guinea, "Charge Distribution and Screening in Layered Graphene Systems," *Phys. Rev. B* **75**(23), p. 235433, 2007.

[40] M. Koshino, "Interlayer Screening Effect in Graphene Multilayers with ABA and ABC Stacking," *Phys. Rev. B* **81**(12), p. 125304, 2010.

[41] C. Dean, A. Young, I. Meric, C. Lee, L. Wang, S. Sorgenfrei, K. Watanabe, T. Taniguchi, P. Kim, K. Shepard, and J. Hone, "Boron Nitride Substrates for High-Quality Graphene Electronics," *Nat.*

Nanotechnol. **5**(10), pp. 722–726, 2010.

[42] P. J. Zomer, S. P. Dash, N. Tombros, and B. J. van Wees, "A Transfer Technique for High Mobility Graphene Devices on Commercially Available Hexagonal Boron Nitride," *Appl. Phys. Lett.* **99**(23), p. 232104, 2011.

[43] A. Veligura, P. J. Zomer, I. J. Vera-Marun, C. Józsa, P. I. Gordiichuk, and B. J. van Wees, "Relating Hysteresis and Electrochemistry in Graphene Field Effect Transistors," *J. Appl. Phys.* **110**(11), p. 113708, 2011.

[44] P. N. First, W. A. de Heer, T. Seyller, C. Berger, J. A. Stroscio, and J.-S. Moon, "Epitaxial Graphenes on Silicon Carbide," *MRS Bull.* **35**, pp. 296–305, 2010.

[45] Y. Hernandez, V. Nicolosi, M. Lotya, F. M. Blighe, Z. Sun, S. De, M. T., B. Holland, M. Byrne, Y. K. Gun'Ko, J. J. Boland, P. Niraj, G. Duesberg, S. Krishnamurthy, R. Goodhue, J. Hutchison, V. Scardaci, A. C. Ferrari, and J. N. Coleman, "High-yield production of graphene by liquid-phase exfoliation of graphite," *Nat. Nanotechnol.* **3**(9), pp. 563–568, 2008.

[46] P. Blake, P. D. Brimicombe, R. R. Nair, T. J. Booth, D. Jiang, F. Schedin, L. A. Ponomarenko, S. V. Morozov, H. F. Gleeson, E. W. Hill, A. K. Geim, and K. S. Novoselov, "Graphene-Based Liquid Crystal Device," *Nano Lett.* **8**(6), pp. 1704–1708, 2008.

[47] D. R. Dreyer, R. S. Ruoff, and C. W. Bielawski, "From Conception to Realization: An Historial Account of Graphene and Some Perspectives for Its Future," *Angew. Chem. Int. Ed.* **49**(49), pp. 9336–9344, 2010.

[48] M. Segal, "Selling graphene by the ton," *Nat. Nanotechnol.* **4**(10), pp. 612–614, 2009.

[49] X. Li, W. Cai, J. An, S. Kim, J. Nah, D. Yang, R. Piner, A. Velamakanni, I. Jung, E. Tutuc, S. K. Banerjee, L. Colombo, and R. S. Ruoff, "Large-Area Synthesis of High-Quality and Uniform Graphene Films on Copper Foils," *Science* **324**(5932), pp. 1312–1314, 2009.

[50] S. Bae, H. Kim, Y. Lee, X. Xu, J.-S. Park, Y. Zheng, J. Balakrishnan, T. Lei, H. Ri Kim, Y. I. Song, Y.-J. Kim, K. S. Kim, B. Özyilmaz, J.-H. Ahn, B. H. Hong, and S. Iijima, "Roll-to-Roll Production of 30-Inch Graphene Films for Transparent Electrodes," *Nat. Nanotechnol.* **5**, p. 574, 2010.

[51] E. Cobas, A. L. Friedman, O. M. J. van´t Erve, J. T. Robinson, and B. T. Jonker, "Graphene As a Tunnel Barrier: Graphene-Based Magnetic Tunnel Junctions," *Nano Lett.* **12**(6), pp. 3000–3004, 2012.

[52] D. V. Badami, "Graphitization of [alpha]-Silicon Carbide," *Nature (London)* **193**(4815), pp. 569–570, 1962.

[53] I. Forbeaux, J.-M. Themlin, and J.-M. Debever, "Heteroepitaxial Graphite on 6H-SiC(0001): Interface Formation through Donduction-Band Electronic Structure," *Phys. Rev. B* **58**, pp. 16396–16406, 1998.

[54] C. Oshima and A. Nagashima, "Ultra-Thin Epitaxial Films of Graphite and Hexagonal Boron Nitride on Solid Surfaces," *J. Phys.: Condens. Matter* **9**(1), p. 1, 1997.

[55] C. Berger, Z. Song, T. Li, X. Li, A. Y. Ogbazghi, R. Feng, Z. Dai, A. N. Marchenkov, E. H. Conrad, P. N. First, and W. A. de Heer, "Ultrathin Epitaxial Graphite: 2D Electron Gas Properties and a Route toward Graphene-based Nanoelectronics," *J. Phys. Chem. B* **108**(52), pp. 19912–19916, 2004.

[56] C. Berger, Z. Song, X. Li, X. Wu, N. Brown, C. Naud, D. Mayou, T. Li, J. Hass, A. N. Marchenkov, E. H. Conrad, P. N. First, and W. A. de Heer, "Electronic Confinement and Coherence in Patterned Epitaxial Graphene," *Science* **312**(5777), pp. 1191–1196, 2006.

[57] T. Ohta, A. Bostwick, T. Seyller, K. Horn, and E. Rotenberg, "Controlling the Electronic Structure of Bilayer Graphene," *Science* **313**(5789), pp. 951–954, 2006.

[58] J. Hass, F. Varchon, J. E. Millán-Otoya, M. Sprinkle, N. Sharma, W. A. de Heer, C. Berger, P. N. First, L. Magaud, and E. H. Conrad, "Why Multilayer Graphene on 4H-SiC(000-1) Behaves Like a Single Sheet of Graphene," *Phys. Rev. Lett.* **100**(12), p. 125504, 2008.

[59] C. Virojanadara, M. Syväjarvi, R. Yakimova, L. I. Johansson, A. A. Zakharov, and T. Balasubramanian, "Homogeneous Large-Area Graphene Layer Growth on 6H-SiC(0001)," *Phys. Rev. B* **78**, p. 245403, 2008.

[60] K. V. Emtsev, A. Bostwick, K. Horn, J. Jobst, G. L. Kellogg, L. Ley, J. L. McChesney, T. Ohta, S. A.

Reshanov, J. Rohrl, E. Rotenberg, A. K. Schmid, D. Waldmann, H. B. Weber, and T. Seyller, “Towards Wafer-Size Graphene Layers by Atmospheric Pressure Graphitization of Silicon Carbide,” *Nat. Mater.* **8**(3), pp. 203–207, 2009.

[61] A. Tzalenchuk, S. Lara-Avila, A. Kalaboukhov, S. Paolillo, M. Syvajarvi, R. Yakimova, O. Kazakova, J. T. J. B. M., V. Fal´ko, and S. Kubatkin, “Towards a Quantum Resistance Standard Based on Epitaxial Graphene,” *Nat. Nanotechnol.* **5**, pp. 186–189, 2010.

[62] S. Dimitrijev, “Silicon Carbide as a Material for Mainstream Electronics,” *Microelectron. Eng.* **83**(1), pp. 123–125, 2006.

[63] F. Krach, S. Hertel, D. Waldmann, J. Jobst, M. Krieger, S. Reshanov, A. Schöner, and H. B. Weber, “A Switch for Epitaxial Graphene Electronics: Utilizing the Silicon Carbide Substrate as Transistor Channel,” *Appl. Phys. Lett.* **100**(12), p. 122102, 2012.

[64] M. Y. Han, B. Özyilmaz, Y. Zhang, and P. Kim, “Energy Band-Gap Engineering of Graphene Nanoribbons,” *Phys. Rev. Lett.* **98**, p. 206805, 2007.

[65] X. Li, X. Wang, L. Zhang, S. Lee, and H. Dai, “Chemically Derived, Ultrasmooth Graphene Nanoribbon Semiconductors,” *Science* **319**(5867), pp. 1229–1232, 2008.

[66] D. C. Elias, R. R. Nair, T. M. G. Mohiuddin, S. V. Morozov, P. Blake, M. P. Halsall, A. C. Ferrari, D. W. Boukhvalov, M. I. Katsnelson, A. K. Geim, and K. S. Novoselov, “Control of Graphene’s Properties by Reversible Hydrogenation: Evidence for Graphane,” *Science* **323**(5914), pp. 610–613, 2009.

[67] R. R. Nair, W. Ren, R. Jalil, I. Riaz, V. G. Kravets, L. Britnell, P. Blake, F. Schedin, A. S. Mayorov, S. Yuan, M. I. Katsnelson, H.-M. Cheng, W. Strupinski, L. G. Bulusheva, A. V. Okotrub, I. V. Grigorieva, A. N. Grigorenko, K. S. Novoselov, and A. K. Geim, “Fluorographene: A Two-Dimensional Counterpart of Teflon,” *Small* **6**(24), pp. 2877–2884, 2010.

[68] J. B. Oostinga, H. B. Heersche, X. Liu, A. F. Morpurgo, and L. M. K. Vandersypen, “Gate-Induced Insulating State in Bilayer Graphene Devices,” *Nat. Mater.* **7**, pp. 151–157, 2007.

[69] D. Huertas-Hernando, F. Guinea, and A. Brataas, “Spin-Orbit Coupling in Curved Graphene, Fullerenes, Nanotubes, and Nanotube Caps,” *Phys. Rev. B* **74**(15), p. 155426, 2006.

[70] B. Trauzettel, D. V. Bulaev, D. Loss, and G. Burkard, “Spin Qubits in Graphene Quantum Dots,” *Nat. Phys.* **3**, pp. 192–196, 2007.

[71] D. Huertas-Hernando, F. Guinea, and A. Brataas, “Spin Relaxation Times in Disordered Graphene,” *Eur. Phys. J-Spec. Top.* **148**(1), pp. 177–181, 2007.

[72] G. Wagoner, “Spin Resonance of Charge Carriers in Graphite,” *Phys. Rev.* **118**(3), pp. 647–653, 1960.

[73] K. Kawamura, S. Kaneko, and T. Tsuzuku, “Conduction Electron-Spin Resonance of Graphite,” *J. Phys. Soc. Jpn.* **52**(11), pp. 3936–3942, 1983.

[74] E. Hill, A. Geim, K. Novoselov, F. Schedin, and P. Blake, “Graphene Spin Valve Devices,” *IEEE T. Magn.* **42**(10), pp. 2694–2696, 2006.

[75] M. Nishioka and A. M. Goldman, “Spin Transport through Multilayer Graphene,” *Appl. Phys. Lett.* **90**(25), p. 252505, 2007.

[76] M. Ohishi, M. Shiraishi, R. Nouchi, T. Nozaki, T. Shinjo, and Y. Suzuki, “Spin Injection into a Graphene Thin Film at Room Temperature,” *Jpn. J. Appl. Phys.* **46**, pp. L605–L607, 2007.

[77] S. Cho, Y.-F. Chen, and M. S. Fuhrer, “Gate-Tunable Graphene Spin Valve,” *Appl. Phys. Lett.* **91**(12), p. 123105, 2007.

[78] W. H. Wang, K. Pi, Y. Li, Y. F. Chiang, P. Wei, J. Shi, and R. K. Kawakami, “Magnetotransport Properties of Mesoscopic Graphite Spin Valves,” *Phys. Rev. B* **77**(2), p. 020402, 2008.

[79] H. Goto, A. Kanda, T. Sato, S. Tanaka, Y. Ootuka, S. Odaka, H. Miyazaki, K. Tsukagoshi, and Y. Aoyagi, “Gate Control of Spin Transport in Multilayer Graphene,” *Appl. Phys. Lett.* **92**(21), p. 212110, 2008.

[80] X. Lou, C. Adelmann, S. A. Crooker, E. S. Garlid, J. Zhang, K. S. M. Reddy, S. D. Flexner, C. J. Palmstrom, and P. A. Crowell, “Electrical Detection of Spin Transport in Lateral Ferromagnet-Semiconductor Devices,” *Nat. Phys.* **3**(3), pp. 197–202, 2007.

[81] M. Shiraishi, M. Ohishi, R. Nouchi, N. Mitoma, T. Nozaki, T. Shinjo, and Y. Suzuki, “Robustness of Spin Polarization in Graphene-Based Spin Valves,” *Adv. Funct. Mater.* **19**, pp. 3711–3716, 2009.

[82] K. Pi, W. Han, K. M. McCreary, A. G. Swartz, Y. Li, and R. K. Kawakami, “Manipulation of Spin Transport in Graphene by Surface Chemical Doping,” *Phys. Rev. Lett.* **104**(18), p. 187201, 2010.

[83] A. Avsar, T.-Y. Yang, S. Bae, J. Balakrishnan, F. Volmer, M. Jaiswal, Z. Yi, S. R. Ali, G. Güntherodt, B. H. Hong, B. Beschoten, and B. Özyilmaz, “Toward Wafer Scale Fabrication of Graphene Based Spin Valve Devices,” *Nano Lett.* **11**(6), pp. 2363–2368, 2011.

[84] S. Jo, D.-K. Ki, D. Jeong, H.-J. Lee, and S. Kettemann, “Spin Relaxation Properties in Graphene Due to Its Linear Dispersion,” *Phys. Rev. B* **84**(7), p. 075453, 2011.

[85] B. Birkner, D. Pachniowski, A. Sandner, M. Ostler, T. Seyller, J. Fabian, M. Ciorga, D. Weiss, and J. Eroms, “Annealing-induced Magnetic Moments Detected by Spin Precession Measurements in Epitaxial Graphene on SiC,” *Phys. Rev. B* **87**, p. 081405, 2013.

[86] D. Huertas-Hernando, F. Guinea, and A. Brataas, “Spin-Orbit-Mediated Spin Relaxation in Graphene,” *Phys. Rev. Lett.* **103**(14), p. 146801, 2009.

[87] C. Józsa, T. Maassen, M. Popinciuc, P. J. Zomer, A. Veligura, H. T. Jonkman, and B. J. van Wees, “Linear Scaling between Momentum and Spin Scattering in Graphene,” *Phys. Rev. B* **80**(24), p. 241403(R), 2009.

[88] C. Ertler, S. Konschuh, M. Gmitra, and J. Fabian, “Electron Spin Relaxation in Graphene: The Role of the Substrate,” *Phys. Rev. B* **80**(4), p. 041405, 2009.

[89] A. H. Castro Neto and F. Guinea, “Impurity-Induced Spin-Orbit Coupling in Graphene,” *Phys. Rev. Lett.* **103**(2), p. 026804, 2009.

[90] T.-Y. Yang, J. Balakrishnan, F. Volmer, A. Avsar, M. Jaiswal, J. Samm, S. R. Ali, A. Pachoud, M. Zeng, M. Popinciuc, G. Güntherodt, B. Beschoten, and B. Özyilmaz, “Observation of Long Spin-Relaxation Times in Bilayer Graphene at Room Temperature,” *Phys. Rev. Lett.* **107**(4), p. 047206, 2011.

[91] W. Han and R. K. Kawakami, “Spin Relaxation in Single-Layer and Bilayer Graphene,” *Phys. Rev. Lett.* **107**(4), p. 047207, 2011.

[92] P. Zhang and M. W. Wu, “Electron Spin Relaxation in Graphene with Random Rashba Field: Comparison of the D’yakonov–Perel’ and Elliott–Yafet-like Mechanisms,” *New J. Phys.* **14**(3), p. 033015, 2012.

[93] M. Diez and G. Burkard, “Bias-Dependent D’yakonov-Perel’ Spin Relaxation in Bilayer Graphene,” *Phys. Rev. B* **85**, p. 195412, 2012.

[94] H. Ochoa, A. H. Castro Neto, and F. Guinea, “Elliot-Yafet Mechanism in Graphene,” *Phys. Rev. Lett.* **108**, p. 206808, 2012.

[95] T. Maassen, F. K. Dejene, M. H. D. Guimarães, C. Józsa, and B. J. van Wees, “Comparison between Charge and Spin Transport in Few-layer Graphene,” *Phys. Rev. B* **83**(11), p. 115410, 2011.

[96] M. H. D. Guimarães, A. Veligura, P. J. Zomer, T. Maassen, I. J. Vera-Marun, N. Tombros, and B. J. van Wees, “Spin Transport in High-Quality Suspended Graphene Devices,” *Nano Lett.* **12**(7), pp. 3512–3517, 2012.

[97] T. Maassen, J. J. van den Berg, N. IJbema, F. Fromm, T. Seyller, R. Yakimova, and B. J. van Wees, “Long Spin Relaxation Times in Wafer Scale Epitaxial Graphene on SiC(0001),” *Nano Lett.* **12**(3), pp. 1498–1502, 2012.

[98] P. J. Zomer, M. H. D. Guimarães, N. Tombros, and B. J. van Wees, “Long-Distance Spin Transport in High-mobility Graphene on Hexagonal Boron Nitride,” *Phys. Rev. B* **86**, p. 161416, 2012.

[99] T. Maassen, J. J. van den Berg, E. H. Huisman, H. Dijkstra, F. Fromm, T. Seyller, and B. J. van Wees, “Localized States Influence Spin Transport in Epitaxial Graphene,” *Phys. Rev. Lett.* **110**, p. 067209, 2013.

[100] K. M. McCreary, H. Wen, H. Yu, W. Ha, E. Johnston-Halperin, and R. K. Kawakami, “Enhancement of Spin Injection into Graphene by Water Dipping,” arXiv:1108.0380v1.

[101] K. M. McCreary, A. G. Swartz, W. Han, J. Fabian, and R. K. Kawakami, "Magnetic Moment Formation in Graphene Detected by Scattering of Pure Spin Currents," *Phys. Rev. Lett.* **109**, p. 186604, 2012.

[102] M. Wojtaszek, I. J. Vera-Marun, T. Maassen, and B. J. van Wees, "Enhancement of Spin Relaxation Time in Hydrogenated Graphene Spin Valve Devices," *Phys. Rev. B* **87**, p. 081402(R), 2013.

[103] C. Józsa, M. Popinciuc, N. Tombros, H. T. Jonkman, and B. J. van Wees, "Controlling the Efficiency of Spin Injection into Graphene by Carrier Drift," *Phys. Rev. B* **79**(8), p. 081402, 2009.

[104] M. Popinciuc, C. Józsa, P. J. Zomer, N. Tombros, A. Veligura, H. T. Jonkman, and B. J. van Wees, "Electronic Spin Transport in Graphene Field-Effect Transistors," *Phys. Rev. B* **80**(21), p. 214427, 2009.

[105] W. Han, K. Pi, K. M. McCreary, Y. Li, J. J. I. Wong, A. G. Swartz, and R. K. Kawakami, "Tunneling Spin Injection into Single Layer Graphene," *Phys. Rev. Lett.* **105**(16), p. 167202, 2010.

[106] B. Dlubak, P. Seneor, A. Anane, C. Barraud, C. Deranlot, D. Deneuve, B. Servet, R. Mattana, F. Petroff, and A. Fert, "Are Al2O3 and MgO Tunnel Barriers Suitable for Spin Injection in Graphene?," *Appl. Phys. Lett.* **97**(9), p. 092502, 2010.

[107] T. Yamaguchi, S. Masubuchi, K. Iguchi, R. Moriya, and T. Machida, "Tunnel Spin Injection into Graphene Using Al2O3 Barrier Grown by Atomic Layer Deposition on Functionalized Graphene Surface," *J. Magn. Magn. Mater.* **324**(5), pp. 849–852, 2012.

[108] B. Dlubak, M.-B. Martin, C. Deranlot, B. Servet, S. Xavier, R. Mattana, M. Sprinkle, C. Berger, W. A. De Heer, F. Petroff, A. Anane, P. Seneor, and A. Fert, "Highly Efficient Spin Transport in Epitaxial Graphene on SiC," *Nat. Phys.* **8**, pp. 557–561, 2012.

[109] J. Abel, A. Matsubayashi, T. Murray, C. Dimitrakopoulos, D. B. Farmer, A. Afzali, A. Grill, C. Y. Sung, and V. P. LaBella, "Fabrication of an Electrical Spin Transport Device Utilizing a Diazonium Salt/Hafnium Oxide Interface Layer on Epitaxial Graphene Grown on 6H-SiC(0001)," *J. Vac. Sci. Technol., B: Microelectron. Nanometer Struct.–Process., Meas., Phenom.* **30**(4), p. 04E109, 2012.

[110] T. Maassen, I. J. Vera-Marun, M. H. D. Guimarães, and B. J. van Wees, "Contact-Induced Spin Relaxation in Hanle Spin Precession Measurements," *Phys. Rev. B* **86**, p. 235408, 2012.

[111] J. Maassen, W. Ji, and H. Guo, "Graphene Spintronics: The Role of Ferromagnetic Electrodes," *Nano Lett.* **11**(1), pp. 151–155, 2011.

[112] D. A. Abanin, R. V. Gorbachev, K. S. Novoselov, A. K. Geim, and L. S. Levitov, "Giant Spin-Hall Effect Induced by the Zeeman Interaction in Graphene," *Phys. Rev. Lett.* **107**, p. 096601, 2011.

[113] I. J. Vera-Marun, V. Ranjan, and B. J. van Wees, "Nonlinear Interaction of Spin and Charge Currents in Graphene," *Phys. Rev. B* **84**, p. 241408, 2011.

[114] I. J. Vera-Marun, V. Ranjan, and B. J. van Wees, "Nonlinear Detection of Spin Currents in Graphene with Non-Magnetic Electrodes," *Nat. Phys.* **8**(4), pp. 313–316, 2012.

[115] C. Józsa and B.J. van Wees, "Graphene Spintronics," in *Handbook of Spin Transport and Magnetism*, E.Y. Tsymbal, I. Zutic, Eds. (CRC Press, Boca Raton, FL), pp. 579–598, 2011.

[116] W. Han, K. McCreary, K. Pi, W. Wang, Y. Li, H. Wen, J. Chen, and R. Kawakami, "Spin Transport and Relaxation in Graphene," *J. Magn. Magn. Mater.* **324**(4), pp. 369–381, 2012.

[117] P. Seneor, B. Dlubak, M.-B. Martin, A. Anane, H. Jaffrès, and A. Fert, "Spintronics with Graphene," *MRS Bull.* **37**, pp. 1245–1254, 2012.

Chapter 2

Spin transport in diffusive systems

Abstract

Spintronics is a large field with several different branches. In this chapter, we introduce the basic concepts that are needed to understand the physics behind the spin transport experiments and the new concepts presented in this thesis. After discussing the two current model for spin polarized currents and the spin-valve principle we will focus on spin injection from ferromagnetic into non-magnetic materials, on the non-local measurement geometry and Hanle precession measurements used throughout the thesis. In the end of the chapter we discuss the spin relaxation mechanisms that are expected to be present in graphene.

2.1 Two current model and local spin-valves

A descriptive approach to understand and explain spin transport effects, like the giant magnetoresistance (GMR) [1, 2], is the so-called two current model first presented by Valet and Fert in 1993 [3]. Following this model, electrons in ferromagnetic metals (FM) with spins aligned with the magnetization of the FM can be labeled "spin-up" and electrons pointing in the opposite direction "spin-down". Other spin directions are mapped on these two directions.

Spin-up and spin-down electrons have a different conductivity in the FM. In general, the conductivity of a material is described by the Einstein relation

$$\sigma = De^2\nu(E_F) \tag{2.1}$$

with the diffusion coefficient D, the electron charge e and the density of states (DOS) ν at the Fermi energy E_F. As the DOS at E_F in FM is different for the two spin directions, spin-up and spin-down experience a different conductivity of $\sigma_{\uparrow,\downarrow} = De^2\nu_{\uparrow,\downarrow}(E_F)$ and it is $\sigma = \sigma_\uparrow + \sigma_\downarrow$ and $\nu = \nu_\uparrow + \nu_\downarrow$. Here the indices $\uparrow$ and $\downarrow$ represent the spin directions, spin-up and spin-down.[1]

When connecting two FM in an electronic circuit in series, one can use this difference of conductivity to distinguish the relative orientation of their magnetization. When sending an electric current through these kind of devices one can sketch the representing two current model as depicted in Fig. 2.1 (a) and (b), neglecting the resistance of any material between the two FM. In case the magnetizations of both FM are oriented parallel one spin species experiences in both FM a low resistance while the other spin species experiences twice a high resistance (Fig. 2.1 (a)). For antiparallel orientation, both spin species experience in one of the FM a low and in the other a high resistance (Fig. 2.1 (b)). The antiparallel configuration results therefore in a higher resistance, R_{loc} than the parallel one. This is demonstrated in the measurement in Fig. 2.1 (c). The magnetizations of two ferromagnetic contacts connected to a single layer graphene channel are switched from parallel to antiparallel orientation and back, using a magnetic field [5]. The contacts switch independently as they have different coercive fields and the system shows an increase in the resistance when the contacts are antiparallel aligned.

This concept of a so-called local spin-valve, uses two FM that have to be separated by a non-magnetic material to enable the magnetizations to switch independently. The spins traveling between those FM have to be injected into and transported through the non-magnetic material without losing their spin orientation as the relative orientation of the magnetizations of the FM only influences the resistance of the device, when the spin orientation is maintained while the electrons travel between the FM. Therefore the next section discusses spin injection and relaxation in non-magnetic materials.

---

[1] The diffusion coefficient can in principle also be dependent on the spin direction [4].

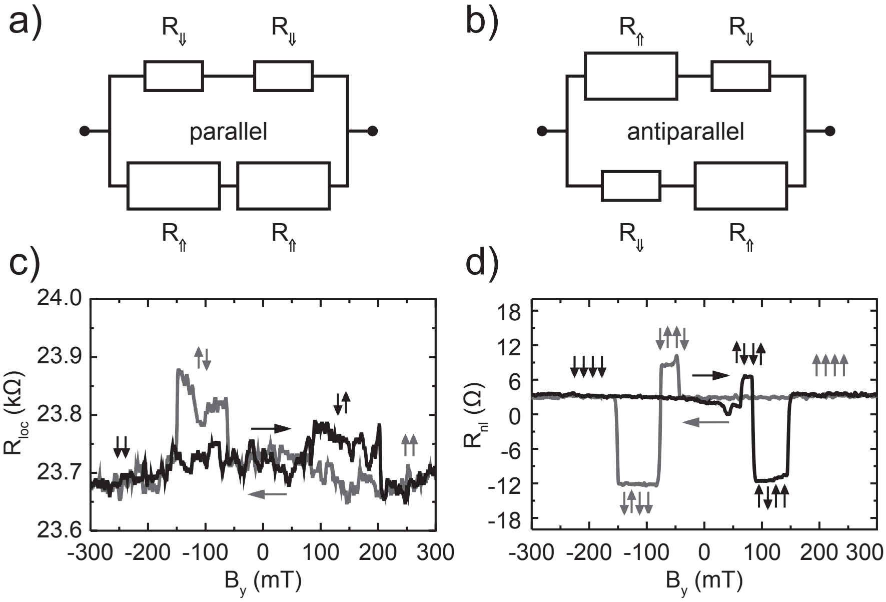

Figure 2.1: The two channel model for two FM connected in series. Spin-down electrons experience a low resistance $R_\Downarrow$ while spin-up electrons face a high resistance $R_\Uparrow$. The sketch for parallel (a) and antiparallel (b) orientation of the magnetizations demonstrates the different resulting resistances. Spin-valve measurements in local (c) and non-local (d) geometry performed on single layer graphene at $T = 4.2$ K, adapted from Ref. [5]. The horizontal arrows depict the magnetic field sweep direction and the vertical arrows the orientation of the magnetization of the two (c) and four (d) FM, respectively.

2.2 Spin injection and relaxation

The concept of spin injection is displayed in Fig. 2.2 (a). On the left side a sketch of the DOS of a FM in equilibrium is shown with a shifted DOS for spin-up and spin-down and an imbalance of the DOS at E_F, $\nu_\uparrow(E_F) > \nu_\downarrow(E_F)$. On the right side of Fig. 2.2 (a) a sketch of the DOS of a non-magnetic material (NM) in equilibrium is shown, with $\nu_\uparrow(E) = \nu_\downarrow(E)$. If electrons are being sent from the FM into the NM, the spin imbalance of the FM is transported into the NM, Fig. 2.2 (a), center, resulting in a spin accumulation close to the interface. As this is a non-equilibrium state for the NM and there is no spin accumulation in the bulk of the NM, the spin accumulation will diffuse from the interface into the bulk of the NM and at the same time the spins will relax.

This process and spin transport in general can be described by defining the spin

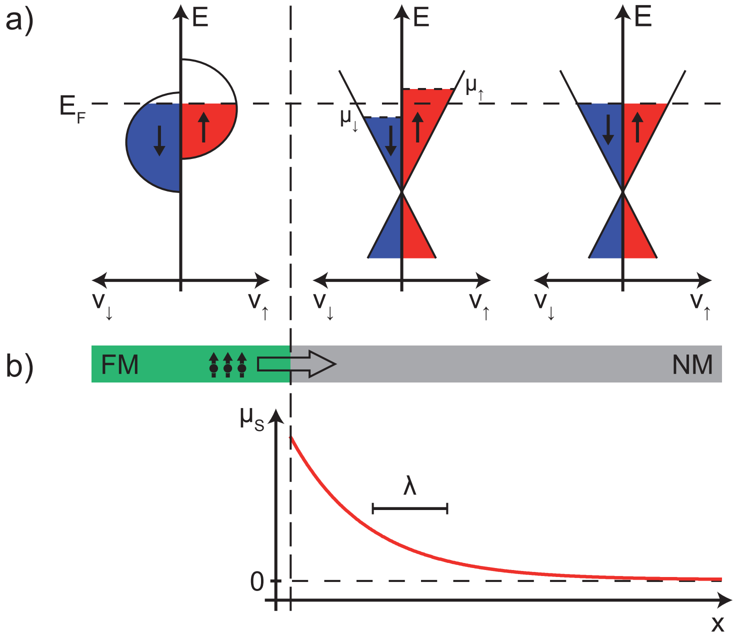

Figure 2.2: (a) Concept of spin injection by means of the spin-dependent DOS of a FM and a NM in equilibrium (left and right graph, respectively) and of the NM close to the interface when an electron current is flowing from the FM into the NM (center). (b) The spin electrochemical potential μ_S in the NM decays as a function of the position x with the spin relaxation length λ.

current density $J_S = J_\uparrow - J_\downarrow$ and the charge current density $J = J_\uparrow + J_\downarrow$ with

$$J_{\uparrow,\downarrow} = -\frac{\sigma_{\uparrow,\downarrow}}{e} \nabla \mu_{\uparrow,\downarrow}. \tag{2.2}$$

To define $J_{\uparrow,\downarrow}$ we use the spin-dependent electrochemical potentials of the electrons $\mu_{\uparrow,\downarrow}$ and can define the electrochemical potential $\mu_0 = 1/2\ (\mu_\uparrow + \mu_\downarrow)$ and the spin electrochemical potential $\mu_S = 1/2\ (\mu_\uparrow - \mu_\downarrow)$ that describes the spin accumulation [4].

As discussed in the last section, in the bulk of the FM we have $\sigma_\uparrow \neq \sigma_\downarrow$ and therefore $J_\uparrow \neq J_\downarrow$ while we have in the bulk of the NM $J_\uparrow = J_\downarrow$. Therefore a spin accumulation builds up at the interface. The dynamics of this accumulation defined by the spin electrochemical potential μ_S is described by the Bloch equation [4]

$$\frac{d\vec{\mu_S}}{dt} = D\nabla^2 \vec{\mu_S} - \frac{\vec{\mu_S}}{\tau} + \vec{\omega_L} \times \vec{\mu_S} \tag{2.3}$$

with the diffusion coefficient D, the spin relaxation time τ and the Larmor frequency

$\vec{\omega_L} = g\mu_B/\hbar\,\vec{B}$. Here $\vec{B}$ is the magnetic field with the gyromagnetic factor g (g-factor, $g = 2$ for free electrons) and the Bohr magneton μ_B. The spin chemical potential $\vec{\mu_S}$ in this equation is generalized as a vector, representing not only the projection of the spin chemical potential on the z-axis, $\mu_\uparrow$ and $\mu_\downarrow$, but the 3-dimensional spin accumulation that is, e.g., needed to described the spin dynamics of a Hanle precession measurement (see Section 2.4). For $\vec{B} = 0$ we get for the steady state of the system with $d\vec{\mu_S}/dt = 0$ and with $\mu_S(x \to \infty) = 0$ an exponential decay of the spin accumulation away from the interface with $\mu_S \propto \exp(-x/\lambda)$ where $\lambda = \sqrt{D\tau}$ is the spin relaxation length of the NM. The mechanisms causing spin relaxation in graphene will be discussed in Section 2.5.

2.2.1 Conductivity mismatch problem

Until now, we discussed spin injection but ignored the conductivity mismatch problem, that plays a significant role when trying to efficiently inject spins into a transport channel. Schmidt *et al.* [6] were the first to discuss this fundamental issue of spin injection from ferromagnetic metals into semi-conductors (SC). They explained that the difference in resistivity of the injector and the transport channel leads to a vanishing polarization of the injected spins [6]. Though it was shown that the mismatch can be circumvented when using ferromagnetic SC to inject spins [7, 8], this injection method is limited to low temperatures, due to the Curie temperatures of these materials.

Rashba [9], and Fert and Jaffrès [10] provided a solution to the challenge of combining FM with SC in spin transport devices by suggesting to implement a resistive barrier between the two materials. The effect of this barrier and its advantages for both spin injection and detection are well described in Ref. [10]. While the low polarization of the injected spins can be restored, also detection is optimized as spins escaping into the leads and contact induced relaxation is avoided when introducing the interface barrier resistance [10].

The spin polarization of the current is defined as $P_J = J_S/J$. For a system consisting of a FM, an interface barrier and a NM channel, the current polarization in the channel is [10]

$$P_J = \frac{P_F R_F + P_C R_C}{R_F + R_\lambda + R_C}. \tag{2.4}$$

Here P_F is the spin polarization of the current in the bulk of the ferromagnet, $P_C = (\nu_\uparrow - \nu_\downarrow)/\nu$ the spin polarization of the interface barrier at E_F and R_C the resistance of the barrier. R_F and R_λ are the spin resistances of the FM and the 2-dimensional channel with $R_F \approx \rho_F \lambda_F / A_F$ and $R_\lambda = R_{sq}\lambda/W$. Here we introduce the spin relaxation length (λ_F), the resistivity (ρ_F) and cross-sectional area (A_F) of the FM contact. To define the spin resistance R_λ we use the square resistance R_{sq} and the width of the channel W (Fig. 2.3 (a) and Fig. 2.4 (a)).[2] The spin resistance represents the resistance of a material over a spin relaxation length [4].

If we now assume no interface barrier ($R_C = 0$) we get for the spin polarization in the channel $P_J = R_F P_F/(R_\lambda + R_F)$. For matched resistances of the contact and the channel ($R_\lambda \approx R_F$) this gives $P_J \approx P_F$. But for a channel resistance much higher than the resistance of the leads ($R_\lambda \gg R_F$), the electrodes are invasive, and one gets a strongly reduced spin polarization in the channel

$$P_J^{\mathrm{i}} \approx \frac{R_F}{R_\lambda} P_F. \tag{2.5}$$

This is the essence of the conductivity mismatch problem described in Ref. [6].

For a system including an interface barrier and with $R_C \geq R_\lambda \gg R_F$ the contacts are non-invasive and we get

$$P_J^{\mathrm{ni}} \approx P_C. \tag{2.6}$$

The spin polarization plays an important role for spin transport measurements with electrical spin injection and detection as the spin signal ΔR is proportional to P_J^2 (see Eq. (2.9) in Section 2.3.1). It increases with growing R_C starting at $\Delta R \propto (P_J^{\mathrm{i}})^2$ and saturating for $R_C \gg R_F$ at $\Delta R \propto (P_J^{\mathrm{ni}})^2$ [11]. For local measurements this means that only a certain range of barrier resistances results in a good ratio of the measured signal and the background resistance resistance ($\Delta R/R_{bg}$) as the background resistance R_{bg} includes R_C for both the injector and the detector [10]. In non-local measurements (see Section 2.3) this is not the case and therefore all R_C larger than a certain value give the same spin signal ΔR [11]. Though, when the resistances grow large, the thermal noise of the measurements or instabilities of the contact resistances can mask spin related effects.

The lower limit for R_C will be discussed in detail in Chapter 5.

2.3 Non-local measurements

As discussed in Section 2.1 a local spin-valve measurement can be performed when combining two FM separated by a NM. Here a current is sent through the device, and the voltage drop over the whole device is measured. The measured voltage drop is therefore influenced by both J_S and J, and spin related effects are always partially masked by the charge current. Due to the current induced effects, the spin signal always has to be seen in contrast to the current induced signal and the charge current induced signal, makes it also hard to judge, if the outcome of a measurement is related to spin or charge induced effects [4].

---

[2] For a 3-dimensional channel, R_{sq}/W has to be replaced by ρ/A with ρ the resistivity and A the cross-sectional area of the channel.

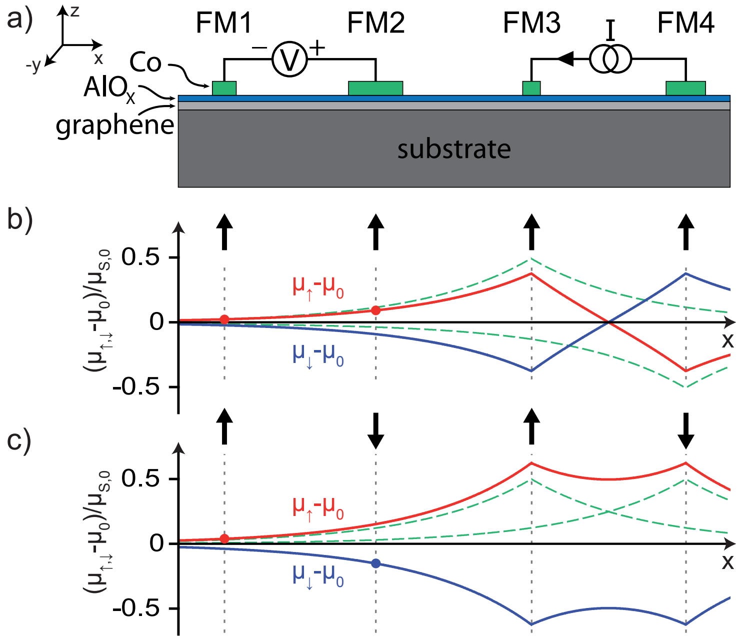

Figure 2.3: (a) Side view sketch of the lateral non-local spin-valve geometry. Here a graphene strip is contacted by four parallel ferromagnetic contacts that have different width, resulting in different coercive fields. The graphene and the contacts are separated by an AlO$_x$ insulating barrier (see Section 2.2.1). A spin accumulation is generated by sending a current from FM3 to FM4 and the spin signal is being detected using the voltage difference between contact FM2 and FM1. Sketch of the difference of the spin-dependent ($\mu_{\uparrow,\downarrow}$) versus the spin-independent chemical potentials (μ_0) as a function of the position x for the case of ferromagnetically aligned contacts (b) and for the case of partially antialigned contacts (c). The red solid curves represent the spin-up and the blue solid curves the spin-down accumulation. The green dashed curves show the respective spin-up accumulations generated by FM3 and FM4. The chemical potentials are normalized by the spin chemical potential at the injection point $\mu_{S,0}$.

An elegant way to avoid this problem is to use pure spin currents. A pure spin current is composed of spins traveling through a material without any net charge flow. Therefore the amount of spin-up electrons traveling in one direction is compensated by spin-down electrons traveling the opposite way ($J_\uparrow = -J_\downarrow$) [12].

One method to generate a pure spin current is the lateral non-local spin-valve geometry with four parallel FM contacts, see Fig. 2.3 (a). An electrical current I is sent from contact FM3 to contact FM4. If the magnetizations of all FM are aligned, this current results in a spin-up injection below FM3 and a spin-up extraction, equivalent to a negative spin-up injection below FM4 (green dashed curves in Fig. 2.3 (b)). Due to the fact that the spins diffuse in positive and negative x-direction and due to spin relaxation, the accumulations decay $\propto \exp(\pm x/\lambda)$ (see Section 2.2). The sum of the accumulations from both FM3 and FM4 is shown by the red solid curve in Fig. 2.3 (b) which is contrasted by the opposite spin-down accumulation (blue solid curve). The spin sensitive contacts FM1 and FM2 probe the spin-up potential at their respective position and the difference leads to a non-local voltage V_{nl}. The voltage can be normalized using the current I which results in the non-local resistance $R_{nl} = V_{nl}/I$. Note that though this quantity is called resistance it is just a normalized voltage and has only the unit in common with a resistor.

If the magnetizations of one of the injecting electrodes is switched and the two injectors become antialigned, FM4 extracts the opposite spin direction from FM3 so both electrodes effectively inject the same spin species and the total spin accumulation is increased as shown in Fig. 2.3 (c). When the magnetization direction of one of the detecting electrodes is switched it probes the other spin species (see Fig. 2.3 (c), contact FM2). As a result, the electrode measures a negative potential if there is a positive spin-up accumulation but it probes spin-down and vice versa.

In a spin-valve measurement, the magnetizations of the FM contacts are aligned and then switched using a magnetic field. The devices are designed in such a way that the coercive field of each contact is different, e.g., by varying the contact width, so that they switch consecutively when ramping the magnetic field up. A non-local spin-valve device with four ferromagnetic contacts can therefore show up to four switches in R_{nl}. Fig. 2.1 (d) shows a non-local spin-valve measurement performed on single layer graphene [5]. Three of the four possible switches are clearly visible and the orientation of magnetization of the ferromagnetic contacts is depicted using vertical arrows next to the curves. This measurement indicates that (i) spins are actually injected and detected,[3] (ii) the spin relaxation length is long enough to show a significant signal over a distance covering at least three of the four contacts, (iii) the contacts by themselves do not significantly disturb spin transport as spins have to travel at least underneath one of the inner contacts (FM2 or FM3 in Fig. 2.3 (a)) to show more than two switches and (iv) one of the contacts does not influence the spin-valve measurement significantly so it is either located beyond the spin relaxation length relative to the other contacts or the polarization of this contact is too small, resulting in too few injected or detected spins.

In this case they do not add another R_{nl}-level to the measurements. To study the properties of a spin transport channel, this is actually used as a desired feature, when reducing the sources for the spin signal to the inner contacts (FM2 or FM3 in Fig. 2.3 (a)). Spin signals from the outer contacts make, e.g., the interpretation of

---

[3] With a clear signal as depicted in Fig. 2.1 (d), it is certain that spin injection and detection is observed in the measurement. In case of measurement noise, this can be more questionable and then a more solid proof for the observation of spin transport can be used; a Hanle precession measurement (see Section 2.4) [13].

Hanle spin precession measurements (see Section 2.4) more difficult. If possible, the outer contacts in a measurement are therefore located at a distance of several times λ outwards from the injector and detector electrodes and/or they are fabricated as non-magnetic contacts.

When comparing the non-local measurement in Fig. 2.1 (d) with the local one in Fig. 2.1 (c), the superiority of the non-local geometry is clearly visible. The non-local signal is much more clear as it is not partly masked by current induced effects that result in a lower signal-to-noise ratio [14].

2.3.1 Spin signal

The spin signal R_{nl} of a non-local spin-valve measurement can be calculated as follows: We assume that we are in the limit of a high resistive tunnel barrier with $R_C \gg R_\lambda$ (see Section 2.2.1). Then the injected current I results in a spin chemical potential at the injection point of [3, 5, 15, 16]

$$\mu_{S,0} = eP_i I R_\lambda \tag{2.7}$$

with the polarization of the barrier of the injecting electrode P_i. As mentioned earlier, the injected spins diffuse in both positive and negative x-direction reducing the spin accumulation per direction to $\mu_{S,0}/2$. Including the spin relaxation, we get for the spin chemical potential at a distance L from the injector $\mu_S(L) = (\mu_{S,0}/2)\exp(-L/\lambda)$. The spin chemical potential converts to a non-local voltage following

$$V_{nl} = P_d/e\,(\mu_S(L) - \mu_S(\infty)) \tag{2.8}$$

with the polarization of the detector P_d [16]. Using $\mu_S(\infty) = 0$ one gets for a detector in distance L from the injection point a non-local resistance of

$$R_{nl} = \frac{V_{nl}}{I} = \pm\frac{P_i P_d R_{sq}\lambda}{2W}\exp(-L/\lambda). \tag{2.9}$$

Note: For simplicity, often $P_i = P_d$ is assumed when analyzing a spin-valve measurement.

2.4 Hanle precession

In this section we discuss non-local Hanle precession measurements that are identical to non-local spin-valve measurements but include an external magnetic field oriented perpendicular to the injected spin direction. This field causes spins to precess while traveling through the channel.

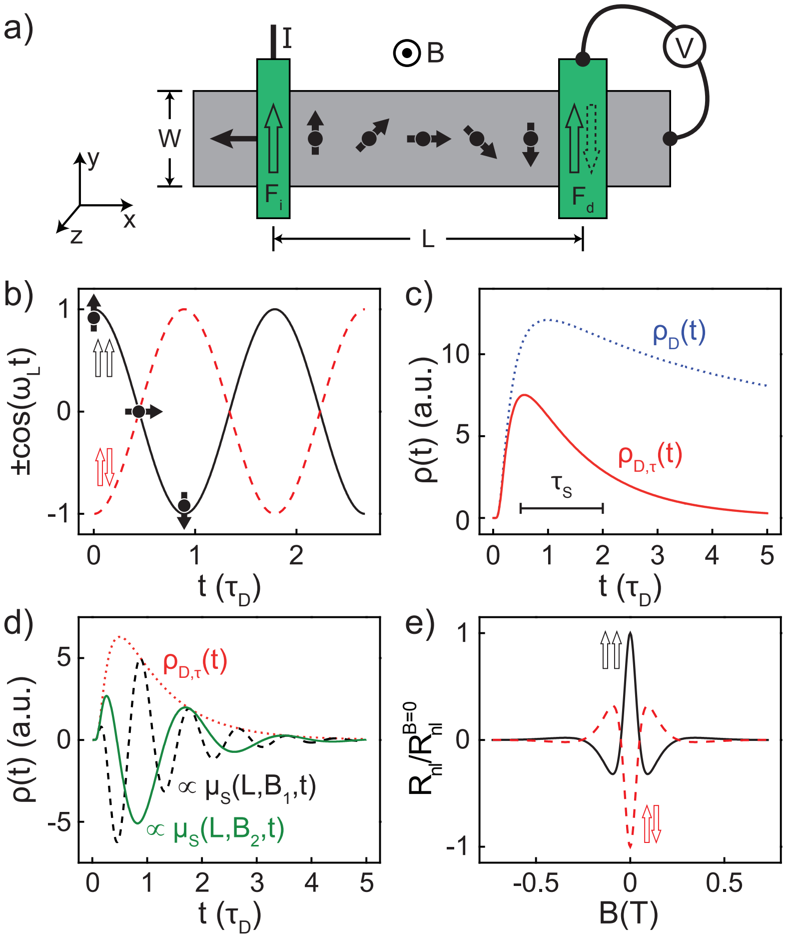

Figure 2.4: (a) Top view sketch of the central part of the lateral non-local spin-valve geometry shown in Fig. 2.3 (a). The spins are injected by contact F_i and detected by contact F_d. A magnetic field pointing in z-direction causes the spins to precess. (b) The projection of the precessed spin orientation for parallel (black solid curve) and antiparallel (red dashed curve) orientation of the magnetizations of F_i and F_d as a function of traveling time t. (c) The probability distribution of traveling times for diffusive transport ($\wp_D(t)$, blue dotted curve) and the reduced probability distribution when including spin relaxation ($\wp_{D,\tau}(t)$, red solid curve). (d) The distribution $\wp_{D,\tau}(t) \propto \mu_S(L, B = 0, t)$ (red dotted curve) and the projection of $\mu_S(L, B, t)$ at the detector for two different B-field strengths ($B_1 > B_2$, black dashed and green solid curve). All time scales are normalized with the diffusion time τ_D. (e) Hanle spin precession curves as a function of the applied B-field for parallel (black solid) and antiparallel (red dashed) orientation of the magnetizations of F_i and F_d.

As mentioned before, spin dynamics can be described by the Bloch equation (Eq. (2.3)). The magnetic field dependent term describes the precession of the spins around an external magnetic field $\vec{B}$. Let us consider one dimensional diffusive transport in a two dimensional channel along the x-axis with width W and a spin injector F_i with polarization P_i at $x = 0$ and a detector F_d with polarization P_d at $x = L$ (Figure 2.4 (a)). The injected spins point at $t = 0$ in y-direction, $\vec{\mu_S}(t = 0,\ x = 0) = \mu_{S,0}\,\hat{y}$, as the magnetization of F_i is oriented this way. At time t the spins are detected at F_d,[4] which magnetization can be oriented parallel or antiparallel to the one of F_i. As the spins precess in the magnetic field and the magnetization of F_d is oriented in y-direction, the projection of the precessed spins is detected, $\mu_S(L,t) = \vec{\mu_S}(L,t) \cdot \hat{y}$. With $\vec{B} = B\hat{z}$ we get for the projection $\mu_S(L,B,t) = \pm\,|\vec{\mu_S}(L,B=0,t)|\cos(\omega_L t)$. The prefactor is "$+$" for aligned and "$-$" for antialigned contacts. Figure 2.4 (b) shows the projection as a function of travel time t.

For diffusive transport, t depends on the individual path the electron takes to reach F_d and follows the probability distribution for the diffusion time over the distance L

$$\wp_D(t) = 1/\sqrt{4\pi D t}\ \exp(-L^2/4Dt) \tag{2.10}$$

with the most likely travel time $\tau_D = L^2/2D$ (Fig. 2.4 (c), blue dotted curve). We now include the probability that the spin relaxes during the flight $\wp_\tau = \exp(-t/\tau)$ and get the distribution of traveling times for not-relaxed spins $\wp_{D,\tau} = \wp_D \wp_\tau$ (Fig. 2.4 (c), red solid curve, the spin relaxation time is here $\tau = 1.5\ \tau_D$).

If we integrate the product of the probability distribution $\wp_{D,\tau}$ and the projection of the spin orientation $\mu_S(L,B,t)$ over all possible diffusion times we get the projection of the average spin accumulation at the detector F_d

$$\begin{aligned} \mu_S(L,B) &= \int_0^\infty dt\ \mu_S(L,B,t) \\ &= 2\sqrt{\frac{D}{\tau}}\ \mu_{S,0} \int_0^\infty dt\ \wp_D(t)\exp(-t/\tau)\cos(\omega_L t). \end{aligned} \tag{2.11}$$

The prefactor $2\sqrt{D/\tau}$ arises from the constraint $\mu_S(L=0,B=0) = \mu_{S,0}$. This spin accumulation can be measured by F_d and using Eq. (2.7) and (2.8) we get

$$R_{nl}(B) = \pm\frac{P_i P_d R_{sq} D}{W} \int_0^\infty dt\ \wp_D(t)\exp(-t/\tau)\cos(\omega_L t) \tag{2.12}$$

The integral in Eq. (2.12) can be numerically solved and used to fit Hanle precession measurements. Solving the integral for $B = 0$, we get the non-local resistance measured in a spin-valve measurement (Eq. (2.9)).

---

[4] The time t represents the individual flight time of the spins.

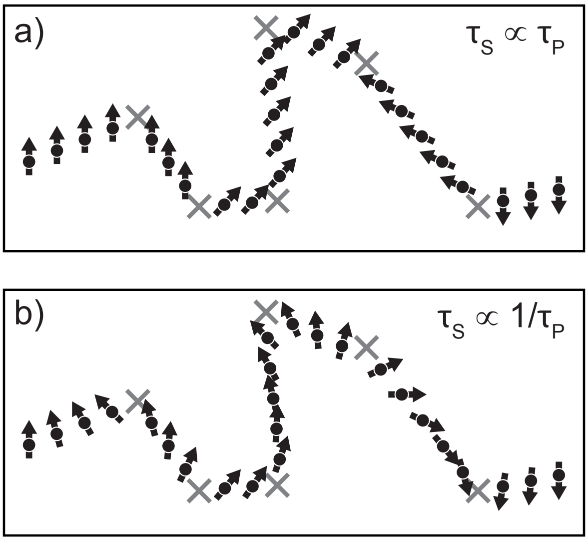

Figure 2.5: Sketch of the possible dominant spin relaxation mechanisms in graphene. In the Elliott-Yafet mechanism (a), the spin of the electron changes its direction when the electron scatters, in the D'yakonov-Perel' mechanism (b) the spin precesses due to spin-orbit fields and scattering events randomize this precession direction.

2.5 Spin relaxation mechanisms in graphene

This section focuses on the mechanisms that are most likely behind the spin relaxation in graphene: The Elliott-Yafet (EY) [17, 18] or the D'yakonov-Perel' mechanism (DP) [19] could be the main source of spin dephasing in graphene [20].

As the dominant spin relaxation mechanism in graphene is still heavily under debate, this chapter explains briefly the two mentioned mechanisms and Chapter 10 is going to present the state of affairs of this debate, based on recent results in the field. It also comments on the specific characteristics of the spin relaxation mechanisms in graphene.

For more general information on spin relaxation mechanisms we recommend the reviews from Fabian *et al.* [4] and Žutić *et al.* [21]. While Ref. [4] discusses the physics of the mechanisms including the math [4], Ref. [21] gives more descriptive explanations.

2.5.1 Elliott-Yafet mechanism

The Elliott-Yafet mechanism, which dominates, e.g., metals [21], describes spin relaxation due to electron scattering events. An electron diffusing through a material has therefore a finite chance to lose its spin information when being scattered (see Fig. 2.5 (a)). As the spin loses its phase due to spin-orbit coupling *during* the scattering event, the more the electron scatters, the higher the chance the spin flips. Therefore, the spin relaxation time is proportional to the momentum relaxation time of the electron, $\tau \propto \tau_p$. The ratio of the two is dependent on the scattering source that can be impurities, boundaries, or phonons of the channel [21]. Recently it was emphasized that the ratio in graphene also depends on the Fermi energy that can be varied using a gate electrode ($\tau/\tau_p \propto E_F^2$) [22, 23]. The consequences of this on the interpretation of the results presented in this thesis is discussed in Chapter 10.

2.5.2 D'yakonov-Perel' mechanism

The D'yakonov-Perel' mechanism plays a major role for systems without inversion symmetry. Good examples are III-V semi-conductors like GaAs or II-VI semi-conductors like ZnSe [21]. These systems exhibit intrinsic magnetic fields that are derived from spin-orbit fields and dependent on the movement direction of the electron spins. The spins precess around these fields while traveling through the material. When the electrons scatter, the direction of the spins and therefore also the intrinsic magnetic field acting on the spin is changed (see Fig. 2.5 (b)). As a result, the randomization of the direction results in less dephasing of the spin. This process is called motion narrowing as more scattering enhances the spin relaxation time. With spins losing phase due to spin-orbit coupling *in between* scattering events, we get $\tau \propto 1/\tau_p$ (with no dependence on E_F) [21].

References

[1] M. N. Baibich, J. M. Broto, A. Fert, F. N. Van Dau, F. Petroff, P. Eitenne, G. Creuzet, A. Friederich, and J. Chazelas, “Giant Magnetoresistance of (001)Fe/(001)Cr Magnetic Superlattices,” *Phys. Rev. Lett.* **61**(21), pp. 2472–2475, 1988.

[2] G. Binasch, P. Grünberg, F. Saurenbach, and W. Zinn, “Enhanced Magnetoresistance in Layered Magnetic Structures with Antiferromagnetic Interlayer Exchange,” *Phys. Rev. B* **39**(7), pp. 4828–4830, 1989.

[3] T. Valet and A. Fert, “Theory of the Perpendicular Magnetoresistance in Magnetic Multilayers,” *Phys. Rev. B* **48**, pp. 7099–7113, 1993.

[4] J. Fabian, A. Matos-Abiague, C. Ertler, P. Stano, and I. Žutić, “Semiconductor Spintronics,” *Acta Phys. Slov.* **57**, pp. 565–907, 2007.

[5] N. Tombros, C. Józsa, M. Popinciuc, H. T. Jonkman, and B. J. van Wees, “Electronic Spin Transport and Spin Precession in Single Graphene Layers at Room Temperature,” *Nature (London)* **448**, pp. 571–574, 2007.

[6] G. Schmidt, D. Ferrand, L. W. Molenkamp, A. T. Filip, and B. J. van Wees, “Fundamental Obstacle for Electrical Spin Injection from a Ferromagnetic Metal into a Diffusive Semiconductor,” *Phys. Rev. B* **62**(8), pp. R4790–R4793, 2000.

[7] R. Fiederling, M. Keim, G. Reuscher, W. Ossau, G. Schmidt, A. Waag, and L. W. Molenkamp, “Injection and Detection of a Spin-Polarized Current in a Light-Emitting Diode,” *Nature (London)* **402**(6763), pp. 787–790, 1999.

[8] Y. Ohno, D. K. Young, B. Beschoten, F. Matsukura, H. Ohno, and D. D. Awschalom, “Electrical Spin Injection in a Ferromagnetic Semiconductor Heterostructure,” *Nature (London)* **402**(6763), pp. 790–792, 1999.

[9] E. I. Rashba, “Theory of Electrical Spin Injection: Tunnel Contacts as a Solution of the Conductivity Mismatch Problem,” *Phys. Rev. B* **62**(24), pp. R16267–R16270, 2000.

[10] A. Fert and H. Jaffrès, “Conditions for efficient spin injection from a ferromagnetic metal into a semiconductor,” *Phys. Rev. B* **64**(18), p. 184420, 2001.

[11] M. Popinciuc, C. Józsa, P. J. Zomer, N. Tombros, A. Veligura, H. T. Jonkman, and B. J. van Wees, “Electronic Spin Transport in Graphene Field-Effect Transistors,” *Phys. Rev. B* **80**(21), p. 214427, 2009.

[12] M. Shiraishi, “Electrically-Generated Pure Spin Current in Graphene,” *Jpn. J. Appl. Phys.* **51**, p. 08KA01, 2012.

[13] X. Lou, C. Adelmann, S. A. Crooker, E. S. Garlid, J. Zhang, K. S. M. Reddy, S. D. Flexner, C. J. Palmstrom, and P. A. Crowell, “Electrical Detection of Spin Transport in Lateral Ferromagnet-Semiconductor Devices,” *Nat. Phys.* **3**(3), pp. 197–202, 2007.

[14] W. Han, K. McCreary, K. Pi, W. Wang, Y. Li, H. Wen, J. Chen, and R. Kawakami, “Spin Transport and Relaxation in Graphene,” *J. Magn. Magn. Mater.* **324**(4), pp. 369–381, 2012.

[15] F. J. Jedema, H. B. Heersche, A. T. Filip, J. J. A. Baselmans, and B. J. van Wees, “Electrical Detection of Spin Precession in a Metallic Mesoscopic Spin Valve,” *Nature (London)* **416**, pp. 713–716, 2002.

[16] F. J. Jedema, *Electrical Spin Injection in Metallic Mesoscopic Spin Valves*. PhD thesis, Rijksuniversiteit Groningen, 2002.

[17] R. J. Elliott, “Theory of the Effect of Spin-Orbit Coupling on Magnetic Resonance in Some Semiconductors,” *Phys. Rev.* **96**, pp. 266–279, 1954.

[18] Y. Yafet, “g Factors and Spin-Lattice Relaxation of Conduction Electrons,” *Solid State Phys.* **14**, pp. 1–98, 1963.

[19] M. I. Dyakonov and V. I. Perel, “Spin Relaxation of Conduction Electrons in Noncentrosymetric Semiconductors,” *Sov. Phys. Solid State* **13**, p. 3023, 1971.

[20] D. Huertas-Hernando, F. Guinea, and A. Brataas, “Spin-Orbit-Mediated Spin Relaxation in Graphene,” *Phys. Rev. Lett.* **103**(14), p. 146801, 2009.

[21] I. Žutić, J. Fabian, and S. Das Sarma, “Spintronics: Fundamentals and Applications,” *Rev. Mod. Phys.* **76**(2), pp. 323–410, 2004.

[22] H. Ochoa, A. H. Castro Neto, and F. Guinea, “Elliot-Yafet Mechanism in Graphene,” *Phys. Rev. Lett.* **108**, p. 206808, 2012.

[23] P. Zhang and M. W. Wu, “Electron Spin Relaxation in Graphene with Random Rashba Field: Comparison of the D’yakonov–Perel’ and Elliott–Yafet-like Mechanisms,” *New J. Phys.* **14**(3), p. 033015, 2012.

Chapter 3

Graphene

Abstract

This chapter discusses the basic electronic properties of single layer, bilayer and few-layer graphene, focusing on the band structure and density of states of these materials. It also introduces the zone-folding scheme that is used to derive the band structure of few-layer graphene from the graphite band structure.

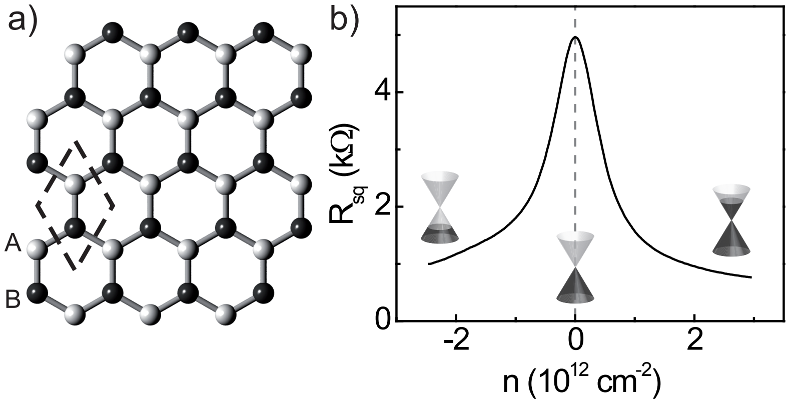

Figure 3.1: (a) Graphene lattice; white and black represent the two sublattices A and B, together forming the unit cell of graphene (dashed lozenge). (b) Dirac curve; the measured square resistance R_{sq} of a graphene sheet as a function of the induced charge carrier density n. The charge carrier type is indicated by the Fermi level in the Dirac cone sketches.

3.1 Single layer graphene

Graphene consists of carbon atoms arranged in a one atom thick honey comb lattice. This hexagonal grid can be described as a triangular lattice with a unit cell containing two atoms (A and B, see Fig. 3.1 (a)). The distance between the two atoms is $a \approx 1.42$ Å and the unit cell area is $A_{uc} = 3\sqrt{3}\,a^2/2$. The electronic properties of single layer graphene (SLG) have been discussed in great detail [1, 2] and we will give a short view on the basics to understand the charge transport measurements presented in this thesis.

3.1.1 Band structure

The band structure of graphene has already been calculated in 1947 [3] as a first step towards the band structure of graphite [1]. For this purpose a tight binding approach was used which leads to the band structure of a zero-gap semiconductor with linear energy dispersion close to the Fermi energy (see Fig. 3.2 (c)) [2]

$$E_{\pm}(\vec{k}) = \pm v_F \hbar |\vec{k}|. \tag{3.1}$$

Here E represents the difference of the energy to the Fermi energy in the neutral state, $\vec{k}$ the wave vector, $\hbar$ the reduced Planck constant and v_F the Fermi velocity. The value for v_F was calculated to be $v_F \approx 1 \times 10^6$ m/s but experiments give a slightly larger value of $v_F \approx 1.1 \times 10^6$ m/s [1, 2]. The wave vector $\vec{k}$ in Eq. (3.1) does not have its origin in the center of the Brillouin zone (BZ) Γ but in the symmetry points K and K' (see Fig. 3.2 (a)) arising from the two carbon atoms per unit cell. The graphene valence and conduction band touch but do not overlap in both points, called Dirac points, resulting in a vanishing density of states (DOS) $\nu = 0$ at $E = 0$ (see Eq. (3.2)). The linear dispersion gives rise to a cone shaped band structure around K and K', that is non-equivalent in the BZ. Both cones have identical energy dispersion that leads to the valley degree of freedom (the name arising from the cone shaped "valleys" in the band structure at these points) [2].

The linear dispersion relation shows that both electrons and holes are traveling with a velocity that is independent from their direction or energy. As they therefore cannot be accelerated or decelerated along their direction of motion, e.g., by applying an electric field, their mass is effectively infinite. On the other hand, the Hamiltonian generating the linear dispersion is equivalent to the Dirac Hamiltonian for highly relativistic particles. The effective mass of these particles if they are accelerated perpendicular to their direction of motion, e.g., by a magnetic field, is finite and at the Dirac point zero [2].

The DOS can be calculated from the band structure and has a linear dependency on the energy [1, 4]

$$\nu(E) = \frac{g_s g_v}{2\pi} \frac{|E|}{\hbar^2 v_F^2}. \tag{3.2}$$

The factors g_s and g_v represent the degeneration due to the spin and valley degree of freedom, respectively.

A demonstration of this DOS can be obtained by electrical gating of a graphene device. This can be achieved by, e.g., placing a graphene sheet on top of a silicon oxide/silicon wafer [5] (as will be discussed in Section 4.1). By using the silicon as a back gate a change in the gate voltage can shift the Fermi energy up or down the Dirac cone and change the DOS ($\nu(E_F)$) and the charge carrier density $n = \int_0^{E_F} \nu(E)\, dE$. The square resistance of the material changes following $R_{sq} = (ne\mu)^{-1}$ with the electron charge e and the mobility μ. A square resistance measurement as shown in Fig. 3.1 (b) shows therefore a maximum at $n = 0$ (the Dirac point where $\nu = 0$) and a strong decrease with increasing n. This typical measurement is called "Dirac curve". When gating to negative values of n the system is in the hole carrier regime, and for positive values of n in the electron carrier regime. Using the mentioned formulas, one would expect an infinity peak at $n = 0$. This is not the case as graphene exhibits minimum conductivity at the Dirac point [6]. While this conductivity partly arises from a broadening in the DOS due to temperature, the lifetime of the electronic states and spurious electrical potentials[1] and can be related to impurities [2], graphene also exhibits an intrinsic minimum conductivity [7].

---

[1] For a discussion of this DOS broadening, see Chapter 6.

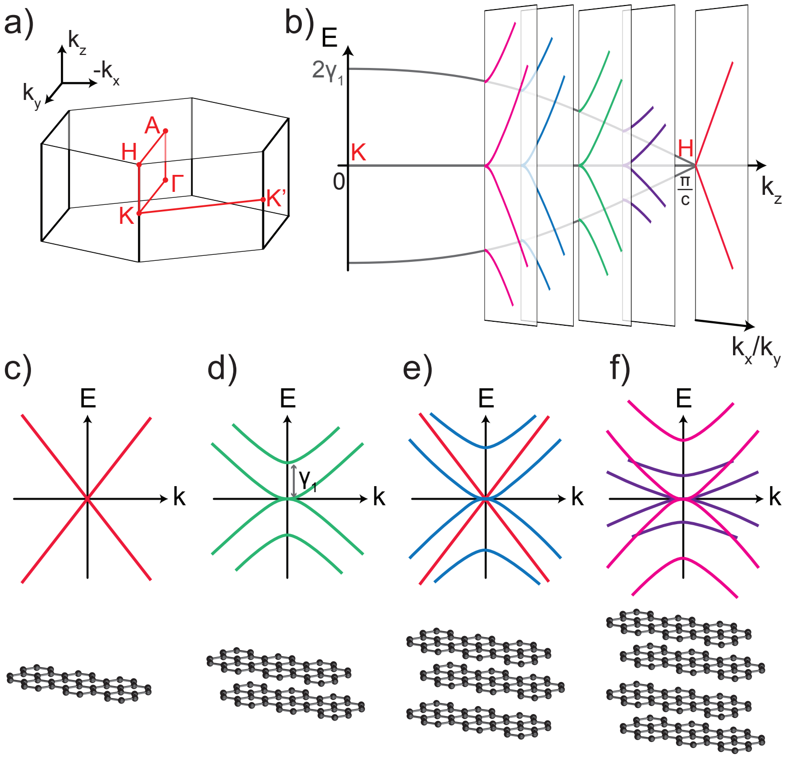

Figure 3.2: Zone-folding scheme. (a) Brillouin zone of graphite and symmetry points relevant for the discussion of the zone-folding scheme. For graphene the 3-dimensional BZ of graphite is reduced to a 2-dimensional BZ where the symmetry points A and H collapse on Γ and K. (b) 1-dimensional projection of the graphite band structure on k_z in the K-H line with planes cutting through the 3-dimensional band structure at discrete k_z resulting from Eq. (3.5). (c)–(f) Sketch of the band structures of SLG, BLG, trilayer and four layer graphene, resulting from the cutting planes from the zone-folding scheme in panel (b). The colors of the bands represent from which cutting plane they originate. This figure is adapted from Ref. [8].

3.2 Few-layer graphene

Single layer graphene (SLG) offers a lot of interesting properties, but some SLG features bring also disadvantages like the minimum conductivity and the low on-off ratio, when using it in transistors, or the strong influence of spurious potentials in the environment of the graphene sheet [6]. These are just two of the reasons why researchers look into the properties of bilayer graphene (BLG) and few-layer graphene

(FLG).[2] BLG offers the possibility to open an energy gap by applying an out-of-plane electric field [9] while FLG screens the inner layers from electrical potentials [10, 11] (see also Section 7.3).

In FLG and graphite, the graphene layers can be stacked in several ways. The most common and energetically favorable is the second layer positioned with atom A on top of atom B of the first layer (see Fig. 3.1 (a)). This stacking is referred to as AB. If this stacking is repeated, one talks about Bernal stacking (ABA).[3] If the third layer is positioned with atom A on the corner of the lozenge in Fig. 3.1 (a), the stacking is called rhombohedral (ABC). Other stackings like AA or random stacking are also possible and it is important to note that the band structure depends on this order of the layers [1].

As mentioned before, the band structure of SLG can be easily obtained using tight binding calculations. In principle this is also possible for several layer thick FLG. But while this is not difficult to achieve for bilayer, the tight binding Hamiltonian for trilayer graphene and more layers becomes increasingly complex to handle [1, 13]. The properties of FLG can also be acquired using density functional theory (DFT) calculations, but we will use an elegant approach to get the approximate band structure of these thin graphite sheets.

In a good approximation, the Hamiltonian of Bernal stacked FLG graphene can be separated into sets of BLG-like and SLG-like Hamiltonians [14]. The BLG-like and SLG-like bands in the band structure have been experimentally verified [8, 15]. We will use a "zone folding scheme" approach to reduce the 3-dimensional band structure of graphite to the 2-dimensional band structure of FLG (see Section 3.2.2). But before doing so, we briefly introduce the band structure and DOS of bilayer graphene.

3.2.1 Bilayer graphene

The band structure for AB stacked BLG, like the one for SLG, can be calculated using a tight binding approach [16]. If we only take into account the coupling to the nearest neighbors in the layers and to the nearest atom in the second layer, this results in four parabolic energy bands. Two with

$$E(\vec{k}) \approx \pm v_F^2 |\vec{k}|^2 / \gamma_1 \tag{3.3}$$

with the interlayer coupling between two atoms positioned on top of each other of $\gamma_1 = 0.37$ eV and two additional parabolic bands that start at $\pm\gamma_1$ [1] (see Fig. 3.2

---

[2] The system referred to, when talking about few-layer graphene, multilayer graphene, a graphene stack and thin graphite are in principle identical. In some cases though, the different names for this system are used to distinguish between different stacking of the graphene sheets resulting in different electronic properties

[3] This stacking is the most interesting one for this thesis as the graphite sources used for the production of exfoliated graphene (see Section 4.1) are mainly Bernal stacked [12].

(d)). The DOS close to E_F, only accounting for the two bands mentioned in Eq. (3.3), calculates to

$$\nu_{BLG} = \frac{g_s g_v}{4\pi\hbar^2 v_F^2}\left(2E + \gamma_1\right). \tag{3.4}$$

Note that the DOS of BLG is identical to the sum of the DOS of SLG and an E-independent but γ_1-dependent term.

3.2.2 Zone-folding scheme

Zone-folding schemes are a general tool to reduce the dimensionality of band structures and have been extensively used to derive the band structure of (1-dimensional) carbon nanotubes from the one of (2-dimensional) single layer graphene [17]. We are going to use the same approach to reduce the band structure of (3-dimensional) graphite [13] to the one of (2-dimensional) FLG as discussed in Ref. [8]. With the result we can calculate the DOS of FLG as this is needed for the analysis in Chapter 7.

FLG is expanded in x- and y-direction and confined in z-direction. Therefore standing waves in the electron density in z-direction are induced, like in a quantum well, resulting in the quantization of k_z with

$$k_z = \frac{2\pi l}{(N+1)c}. \tag{3.5}$$

Here N is the number of layers, the index l runs through $l = \pm 1, \pm 2, \pm\lfloor (N+1)/2 \rfloor$ and $c/2 = 3.4$ Å represents the interlayer distance of graphite [8].

At each of these k_z values, a plane cutting through the band structure is added to the respective FLG band structure (Fig. 3.2). For N odd, there is always a cutting plane through the H-point of the BZ of graphite at $k_z = \pi/c$, supplying a SLG-like linear dispersion to the band structure that does not exist for N even. The remaining layers induce BLG-like bands with different effective mass resulting in a changed effective γ_1 in Eqs. (3.3) and (3.4). The effective values for γ_1 are determined by the k_z from Eq. (3.5) so that the FLG band structure consists of one SLG-like and $(N-1)/2$ BLG-like bands for N odd and $N/2$ BLG-like bands for N even [8].

The DOS can be calculated based on this band structure by adding up the DOS for the BLG-like bands (see Eq. (3.4)) and in case of an odd number of layers the DOS for the SLG-like band (see Eq. (3.2)). The resulting DOS shows a linear increase of its minimum at the charge neutrality point with growing number of layers (see Section 7.3) [18].

References

[1] A. H. Castro Neto, F. Guinea, N. M. R. Peres, K. S. Novoselov, and A. K. Geim, "The Electronic Properties of Graphene," *Rev. Mod. Phys.* **81**(1), pp. 109–162, 2009.

[2] N. M. R. Peres, "Colloquium: The Transport Properties of Graphene: An Introduction," *Rev. Mod. Phys.* **82**(3), pp. 2673–2700, 2010.

[3] P. R. Wallace, "The Band Theory of Graphite," *Phys. Rev.* **71**(9), pp. 622–634, 1947.

[4] T. Ando, "Screening Effect and Impurity Scattering in Monolayer Graphene," *J. Phys. Soc. Jpn.* **75**(7), p. 074716, 2006.

[5] K. S. Novoselov, A. K. Geim, S. V. Morozov, D. Jiang, Y. Zhang, S. V. Dubonos, I. V. Grigorieva, and A. A. Firsov, "Electric Field Effect in Atomically Thin Carbon Films," *Science* **306**(5696), pp. 666–669, 2004.

[6] A. K. Geim and K. S. Novoselov, "The Rise of Graphene," *Nat. Mater.* **6**, pp. 183–191, 2007.

[7] M. I. Katsnelson, "Zitterbewegung, Chirality, and Minimal Conductivity in Graphene," *Eur. Phys. J. B* **51**, pp. 157–160, 2006.

[8] K. F. Mak, M. Y. Sfeir, J. A. Misewich, and T. F. Heinz, "The Evolution of Electronic Structure in Few-Layer Graphene Revealed by Optical Spectroscopy," *Proc. Natl. Acad. Sci. USA* **107**(34), pp. 14999–15004, 2010.

[9] E. McCann, "Asymmetry Gap in the Electronic Band Structure of Bilayer Graphene," *Phys. Rev. B* **74**(16), p. 161403, 2006.

[10] F. Guinea, "Charge Distribution and Screening in Layered Graphene Systems," *Phys. Rev. B* **75**(23), p. 235433, 2007.

[11] Y. Sui and J. Appenzeller, "Screening and Interlayer Coupling in Multilayer Graphene Field-Effect Transistors," *Nano Lett.* **9 (8)**, pp. 2973–2977, 2009.

[12] C. H. Lui, Z. Li, Z. Chen, P. V. Klimov, L. E. Brus, and T. F. Heinz, "Imaging Stacking Order in Few-Layer Graphene," *Nano Lett.* **11**(1), pp. 164–169, 2011.

[13] B. Partoens and F. M. Peeters, "From Graphene to Graphite: Electronic Structure around the K Point," *Phys. Rev. B* **74**(7), p. 075404, 2006.

[14] M. Koshino and T. Ando, "Orbital Diamagnetism in Multilayer Graphenes: Systematic Study with the Effective Mass Approximation," *Phys. Rev. B* **76**(8), p. 085425, 2007.

[15] M. Orlita, C. Faugeras, J. M. Schneider, G. Martinez, D. K. Maude, and M. Potemski, "Graphite from the Viewpoint of Landau Level Spectroscopy: An Effective Graphene Bilayer and Monolayer," *Phys. Rev. Lett.* **102**(16), p. 166401, 2009.

[16] E. McCann and V. I. Fal'ko, "Landau-Level Degeneracy and Quantum Hall Effect in a Graphite Bilayer," *Phys. Rev. Lett.* **96**(8), p. 086805, 2006.

[17] E. B. Barros, A. Jorio, G. G. Samsonidze, R. B. Capaz, A. G. S. Filho, J. M. Filho, G. Dresselhaus, and M. S. Dresselhaus, "Review on the Symmetry-Related Properties of Carbon Nanotubes," *Phys. Rep.* **431**(6), pp. 261–302, 2006.

[18] T. Maassen, F. K. Dejene, M. H. D. Guimarães, C. Józsa, and B. J. van Wees, "Comparison between Charge and Spin Transport in Few-layer Graphene," *Phys. Rev. B* **83**(11), p. 115410, 2011.

Chapter 4

Experimental techniques

Abstract

This chapter describes the experimental techniques applied in the research discussed in this thesis. After introducing the general concept of lithography and lift-off processes, the exfoliation technique used to obtain graphene flakes is explained and we discuss the preparation of graphene spin transport devices. Then we introduce epitaxial graphene, the types of this material used in this thesis and the differences in preparing spin transport devices with epitaxial compared to exfoliated graphene. In the end of the chapter, the setups and techniques used to measure our devices are briefly discussed.

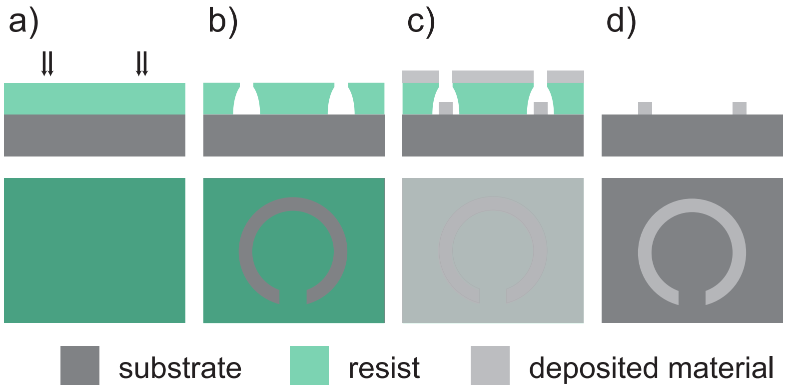

Figure 4.1: Lithography process with material deposition and lift-off. Each panel shows a side-view (upper illustration) and the top-view (lower illustration) of the device. (a) A substrate (dark gray) is covered with a photo or electron beam sensitive resist (green) and exposed. (b) The resist is developed leaving a mask in the shape defined by light or by electron beam. (c) A material, e.g., a metal is deposited and by dissolving the resist, (d) the material on top of the resist is lifted off and removed.

4.1 Sample production

In the following we are going to discuss the methods used in the sample production that was performed using the facilities of NanoLab NL and of the Physics of Nanodevices group in the Zernike Institute for Advanced Materials of the University of Groningen. The growth and preparation of the epitaxial graphene wafers was carried out in the group of Rositza Yakimova at the Linköping University, Sweden and the group of Thomas Seyller at the Universität Erlangen-Nürnberg in Germany.

4.1.1 Lithography

When (graphene) devices are contacted or patterned on a micrometer or nanometer scale, most of the time lithography techniques are applied. A typical lithography step is presented in Fig. 4.1. A light or e-beam sensitive resist is spin coated on the substrate and the polymer is exposed in the desired pattern (Fig. 4.1 (a)). For e-beam sensitive resists, the pattern is generated with a focused beam of electrons (electron beam lithography, EBL) while in case of photolithography (PL) the exposure is performed using a UV-light source that is partly covered by a mask on top of the substrate.

After exposure the resist is developed, removing the exposed and leaving the unexposed resist behind (Fig. 4.1 (b)) in case of a so-called positive resist. For a negative resist, the exposed part stays behind while the remaining part is removed by the solvent used to develop the resist. As a result, the substrate is now covered with a resist mask that can be used for further processing. For the research discussed in this thesis this kind of mask was employed to define the shape of deposited metals to contact graphene flakes or to etch the graphene into a desired shape.

To etch the graphene, the sample including the polymer mask is placed in an oxygen plasma, removing the graphene in the uncovered areas. Since not only the graphene but also the polymer of the resist is removed by the plasma, the time of the etching has to be carefully adjusted. To prepare metal structures the sample is developed and afterwards a material is deposited (Fig. 4.1 (c)). In a last step, the remaining resist is removed, lifting off the deposited material on top of the mask (Fig. 4.1 (d)). For a successful lift-off the resist thickness should be at least 2:1 compared to the thickness of the deposited material.

When depositing contacts the dose and the acceleration voltage in case of e-beam exposure is chosen to cause an “undercut” of the resist when being developed (Fig. 4.1 (b)). An undercut of the resist results from back scattering electrons or photons from the surface of the substrate that broadens the width of the exposed area close to the substrate surface. It helps to separate the layer of the material covering the resist and the actual deposited structure. An undercut can also be achieved by using a double resist layer with two different resists. Here either the upper layer is exposed and after development the sample is briefly dipped into a solvent that removes the lower layer (depending on the dip time the undercut size can be varied) or two resists can be used that need a different dose to be developed. The structures of the upper layer can then be patterned slightly larger for the lower layer, leaving an undercut when developing the resists. In case of an etching step an undercut is normally avoided as it can reduce the accuracy of the etch mask.

4.1.2 Graphene exfoliation

Most graphene research is still being performed on exfoliated graphene devices. The technique to produce these devices by the mechanical cleaving of graphite was invented by Novoselov *et al.* [1] in 2004. It uses a surprisingly easy, low-tech approach to obtain high quality graphene before using high-tech machines to prepare devices with this material.

As graphite source material we use highly ordered pyrolytic graphite (HOPG) from GE Advanced Ceramics, grade ZYA or ultra-pure Kish graphite which is separated from kish, a byproduct of the steel industry. The exfoliation and deposition of the graphene on a wafer is presented in Fig. 4.2. A piece of graphite is covered from both sides with adhesive tape (Fig. 4.2 (a) and (b)) and after pinching out air between the tapes and the graphite, the tapes are detached by carefully peeling one from the other (Fig. 4.2 (c)). This results in both tapes being partly covered with

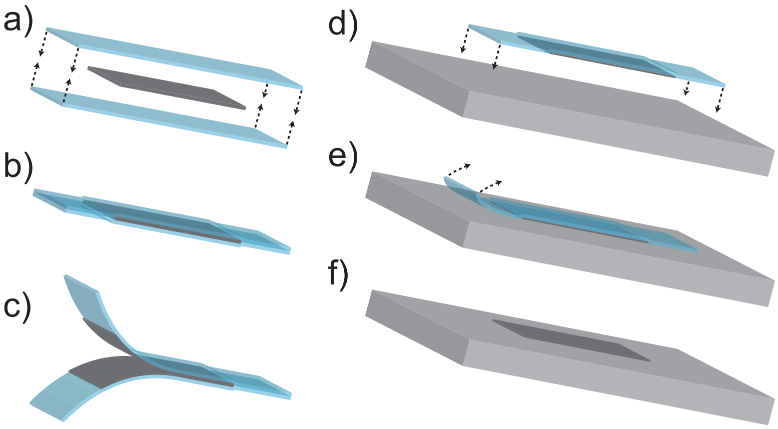

Figure 4.2: Exfoliation and deposition of graphene. (a) and (b) A piece of graphite is covered from both sides with adhesive tape. (c) The two tapes are detached from each other, cleaving the piece of graphite. Steps (a)–(c) are repeated several times. (d) One of the tapes with the cleaved graphite is pressed on a SiO_2/Si wafer and (e) detached, (f) leaving thin graphite and graphene on the substrate.

thin graphite. These steps are repeated several times, reducing the thickness of the graphite crystals.[1] One of the tapes is then pressed on a SiO_2/Si wafer and again peeled off, leaving some thin graphite flakes behind due to van-der-Waals forces between graphene and the surface of the wafer (Fig. 4.2 (d) and (e)). The wafer is now covered with small thin graphite crystals (Fig. 4.2 (f)), reaching in thickness down to single layer graphene. The amount, size and quality of the (few-layer) graphene flakes depends on different parameters like the type of tape used, the preparation of the wafer prior to the deposition of the graphene, e.g., pre-baking at $T > 100°\mathrm{C}$ to remove water from the surface, and the preparation skills of the person cleaving the graphite.

Now the challenge remains to locate the graphene flakes on the wafer. For the search and selection of graphene flakes, a normal optical stereo microscope is used. To be able to see the flakes under the microscope, the properties of the wafer play an important role. While graphene absorbs only 2.3% of the transmitted light, this contrast can be enhanced on the SiO_2/Si wafer when using certain thicknesses of SiO_2 on the wafer and certain wave length of light (color filters) when searching for the flakes [2]. The research on exfoliated graphene presented in this thesis uses Si-wafers covered with a $300\ \mathrm{nm}$ thick layer of SiO_2.

Fig. 4.3 (a) shows a picture of two few-layer graphene flakes on a $SiO_2(300\ \mathrm{nm})/Si$

---

[1] When starting with a thicker piece of graphite (as in the case of HOPG), a thin crystal for the exfoliation procedure can be obtained by cleaving one surface of the graphite using tape.

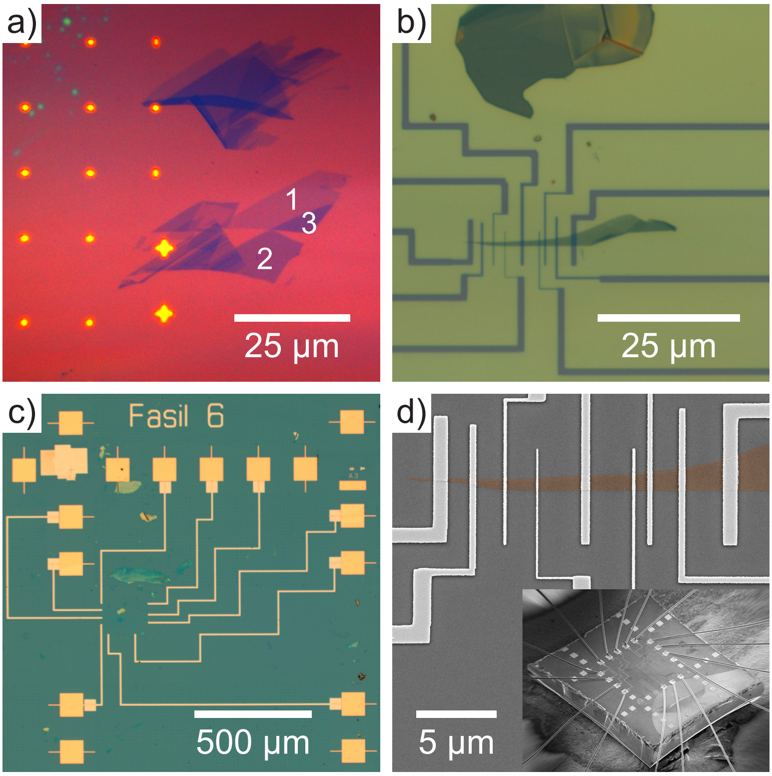

Figure 4.3: (a)–(c) Optical micrographs of exfoliated (few-layer) graphene on a SiO_2/Si wafer. (a) Using optimized color settings for the CCD microscope camera sensor, 1, 2 and 3 layer graphene can be identified on basis of the optical contrast. The pattern on the left hand side consists of Ti/Au dots and is used to map the position of the graphene flakes. (b) A 20-layer graphene strip with a PMMA contact mask for Co contacts, evading contaminations on the wafer like the thin graphite flake on top. (c) Ready-to-measure 20-layer graphene spin transport sample with Co contacts to the surrounding regular pattern of Ti/Au bonding pads enabling to contact the device on a chip carrier. (d) Scanning electron micrographs of the 20-layer graphene flake (colorized) with Co contacts (light gray) and of the wafer contacted using wire-bonding (inset).

wafer taken by an optical microscope using white light and optimized camera filter settings. Due to these software filters, the contrast of the graphene flakes is enhanced showing a clear contrast difference for thicknesses of one, two, three or more layers. The thickness can also be obtained using Raman spectroscopy [3, 4] or by scanning the flake with an atomic force microscope (AFM). The AFM can also help determining if the graphene flake has cracks, large area impurities or contaminations like residues of the adhesive tape glue as visible on the SiO_2 substrate in the upper left corner of Fig. 4.3 (a). The regular pattern on the left side of the micrograph is a grid of gold markers that is prepared using optical lithography (see below). This pattern is used to map the position of the graphene flakes and for alignment of the forthcoming lithography steps.

4.1.3 Preparing a graphene spin transport device

This section gives a general description on how to produce a spin transport device using exfoliated graphene. Appendix A gives a detailed description of the parameters used in the lithography/lift-off processes. We start with a wafer of highly n-doped silicon that is covered on both sides by a $300\ \mathrm{nm}$ thick layer of SiO_2 produced by thermally oxidizing the Si-wafer. We remove the SiO_2 layer on the back side of the wafer and deposit a double layer of Ti/Au ($5\ \mathrm{nm}/40\ \mathrm{nm}$) using electron beam (e-beam) evaporation to get a good electrical contact to the silicon that will be used as back gate. The front side of the wafer is then patterned using optical lithography. Bonding pads used to contact the sample to a chip carrier (Fig. 4.3 (c) and (d), inset) and a regular grid to map the position of the graphene flakes (left side of Fig. 4.3 (a)) are prepared with a Ti/Au e-beam deposition ($4\ \mathrm{nm}/36\ \mathrm{nm}$).

After this preparation of the wafer, the graphene is deposited by exfoliation (see Section 4.1.2). When a graphene flake is selected by optical microscopy and characterized using AFM, the wafer is covered with a layer of $0.6\ \mathrm{nm}$ of aluminum deposited by e-beam or thermal evaporation with a chamber pressure of $< 10^{-6}\ \mathrm{mbar}$. The sample is then removed from vacuum to oxidize the aluminum obtaining a $\sim 0.8\ \mathrm{nm}$ thick aluminum oxide layer.[2] By electron beam lithography a mask for the deposition of the contacts is prepared (Fig. 4.3 (b)) and Co contacts are deposited (Fig. 4.3 (c)). Due to the fact that the graphene flakes on the substrate are randomly oriented and surrounded by contaminations like other (few-layer) graphene or graphite flakes and glue residues from the tape, the contacts for each device have to be uniquely designed.

Fig. 4.3 (d) shows a ready to measure 20-layer graphene device with Co contacts. The contacts are oriented in parallel and have different width resulting in different coercive fields. Each contact has a sharp 90° bend to achieve a single-domain magnetization in the contact by inducing a domain wall in the corner which avoids coupling to magnetic domains in the leads. The inset of Fig. 4.3 (d) shows a wafer with a prepared graphene sample glued on and bonded to a chip carrier.

---

[2] The AlO_x layer is used in spin transport measurements to avoid the conductivity mismatch problem, see Section 2.2.1.

4.1.4 Epitaxial graphene

This thesis presents next to research on exfoliated (few-layer) graphene also results on epitaxial graphene samples. This type of graphene is grown on silicon carbide (SiC) and in the following we are going to discuss the details of the preparation of devices on this material.

Silicon carbide

Silicon carbide is an excellent semi-conductor with a wide band gap [5]. A SiC crystal consists of silicon and carbon atoms in two adjacent layers, forming bilayers that are stacked on top of each others in parallel (aa) or antiparallel (ab) orientation [6] (Fig. 4.4 (a), note that the relative position of the layers is not depicted by the letters "a" and "b"). Due to the bilayer structure of the crystals, one side has Si atoms on the surface and the other C atoms. These sides or faces are called Si-face and C-face (Fig. 4.4 (a)). The stacking order can be very complicated, but the SiC crystals used to grow the epitaxial graphene described in this thesis are the common types 4H-SiC (aabb, see Fig. 4.4 (a)) and 6H-SiC (aaabbb) [6].

Epitaxial growth of graphene on SiC

When heating SiC to high temperatures ($T > 1200^\circ\mathrm{C}$) the Si atoms evaporate leaving a high density of C atoms that can form graphene sheets. The graphene layers on the Si-face grow in this process much slower than on the C-face. To grow one graphene layer the C atoms of about three SiC bilayers are needed [7].

In this thesis we analyze the spin transport properties of mono-layer epitaxial graphene (MLEG) grown on the Si-face of SiC (SiC(0001)) as described in Refs. [8–10]. The energy dispersion of MLEG was confirmed to be linear by angle-resolved photoemission spectroscopy (ARPES) [7]. To grow MLEG, the SiC wafer is heated in an argon atmosphere with an ambient pressure of $1\ \mathrm{atm}$ to $T \geq 1650^\circ\mathrm{C}$ [8, 9]. Here, the argon atmosphere reduces the Si evaporation rate which makes it easier to control the graphene growth.

The resulting MLEG on SiC(0001) consists of a graphene layer on top of a so-called buffer layer (BL) that has the hexagonal C lattice of graphene [11] but is partially covalently bonded to the Si atoms on the SiC surface (Fig. 4.4 (b)). Due to the covalent bonds, the BL is electrically inactive and does not contribute to transport processes. Next to the covalent bonds between the BL and the SiC surface, some of the Si atoms have dangling bonds (DB) as shown in Fig. 4.4 (b).

The wafers are covered predominantly ($> 80\%$) by MLEG with some areas only covered by the BL or with an additional graphene layer. The results presented in this thesis are purely based on MLEG though.

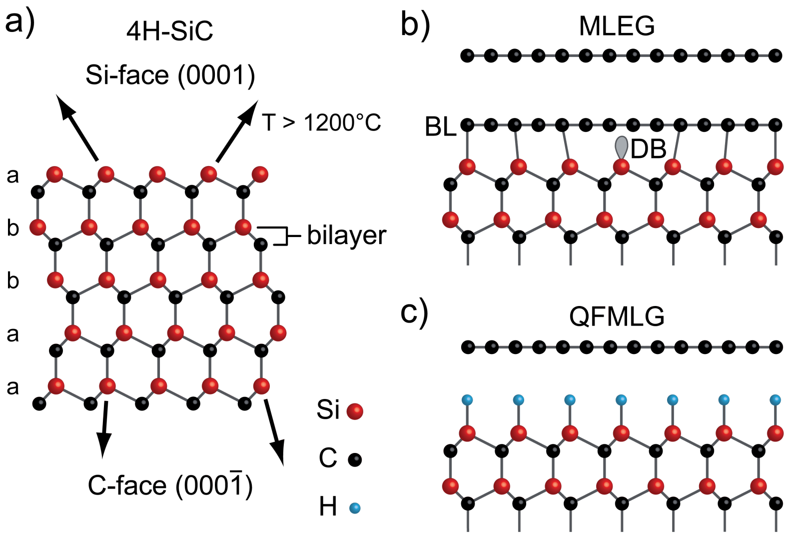

Figure 4.4: (a) 2-dimensional projection of a 4H-SiC crystal. The letters on the left side (a, b) indicate the orientation (but not the relative position) of the SiC bilayers. The orientation of a bilayer is determined by the position of the closest C atom with respect to a Si atom. If the closest C atom is located on the lower left of the Si atom, the bilayer is in orientation "a", if it is on the lower right, it is in orientation "b". (b) Mono-layer epitaxial graphene on the Si-face of SiC with one graphene layer and the buffer layer (BL). The BL is partly covalently bonded to the substrate while some Si atoms have dangling bonds (DB). (c) Quasi-free-standing mono-layer graphene on top of the hydrogen passivated Si-face of SiC. Pictures adapted from Refs. [7] and [12].

Quasi-free-standing mono-layer graphene

Riedl *et al.* [13] discuss how mono-layer graphene can be produced right on top of a passivated SiC surface without a BL in between. The so-called quasi-free-standing mono-layer graphene (QFMLG) is obtained by first growing just the BL on SiC(0001). The sample is then intercalated by hydrogen at $T \geq 600°\mathrm{C}$ [12, 13] which decouples the BL from the substrate and converts it into a graphene layer. Then there are no DB on the SiC surface since they are passivated by the hydrogen (Fig. 4.4 (c)).

Preparing MLEG or QFMLG spin transport devices

The preparation of spin transport devices on MLEG or QFMLEG is in general similar to the preparation of devices on exfoliated graphene. But while the exfoliated flakes are randomly distributed over the wafer, resulting in time-consuming unique contact designs and one or a few devices per wafer, the wafers with MLEG (and QFMLG) are nearly fully covered with graphene. Therefore a big part of the graphene has to be removed to define graphene strips for transport devices, but clear advantages are the big number of devices ($\sim$ 20) that can be fitted on a single wafer ($\sim$ 1 cm^2 size) and a standardized design for the contact (and etch) masks for both optical and e-beam lithography.

After the wafer is covered with MLEG (or QFMLG) a regular pattern of bonding pads and contacts leading to small areas (100×100 $\mu\mathrm{m}^2$) is prepared, that will in the end of the sample preparation contain the spin transport devices. These structures are defined by optical lithography and Ti/Au contacts. The graphene below the contacts is removed using O_2 plasma to enable the contacts to stick to the SiC substrate. Then graphene strips are defined using an EBL step with a negative resist and the remaining uncovered graphene is removed by a second O_2 plasma etching step. Afterwards the sample is cleaned by annealing in argon/hydrogen gas flow at $350°\mathrm{C}$ for ≥ 2 hours [14] to remove resist residues from the optical and e-beam lithography step. Then the AlO_x barrier is deposited before the Co contacts are prepared using a standard EBL step.

The sample preparation process is discussed in detail in Chapter 8, Section 8.2, and the parameters used in the lithography and lift-off processes are listed in Appendix A.

4.2 Measurement setups and techniques

4.2.1 Measurement setups

To measure the graphene devices the samples are glued on a chip carrier and the contacts, including the back gate (in case of exfoliated graphene samples), are connected to the carrier by wire bonding (Fig. 4.3 (d), inset). The chip carrier is then placed on a holder inside a vacuum tube and placed in between the poles of an electro-magnet that can be rotated around the vacuum tube. The samples are kept in vacuum as the Co contacts oxidize when they are exposed to air. Inside the tube the sample is also secure from contaminations that can influence the electronic properties of the graphene channel. As there are several different measurement setups, the specifications of the vacuum tubes and the magnets vary. The vacuum of the tubes have a pressure of $p < 10^{-5}$ mbar and the magnets can generate magnetic fields of ± 0.25 T or ± 1 T. For temperature dependent measurements we use a helium flow cryostat (MicrostatHe2 from Oxford Instruments) that can reach temperatures between 3.5 and 500 K.

The sample is connected via a switch-box and an IV-measurement box to a lock-in amplifier that is controlled by a LabView program on a computer (Fig. 4.5 (a)). The lock-in amplifier (Stanford SR 830) supplies a sine shaped voltage, V_{out}, with an RMS amplitude between 0 and 5 V and measures the voltage returned from the sample via the IV-measurement box, V_{in}. The lock-in frequencies used for our measurements

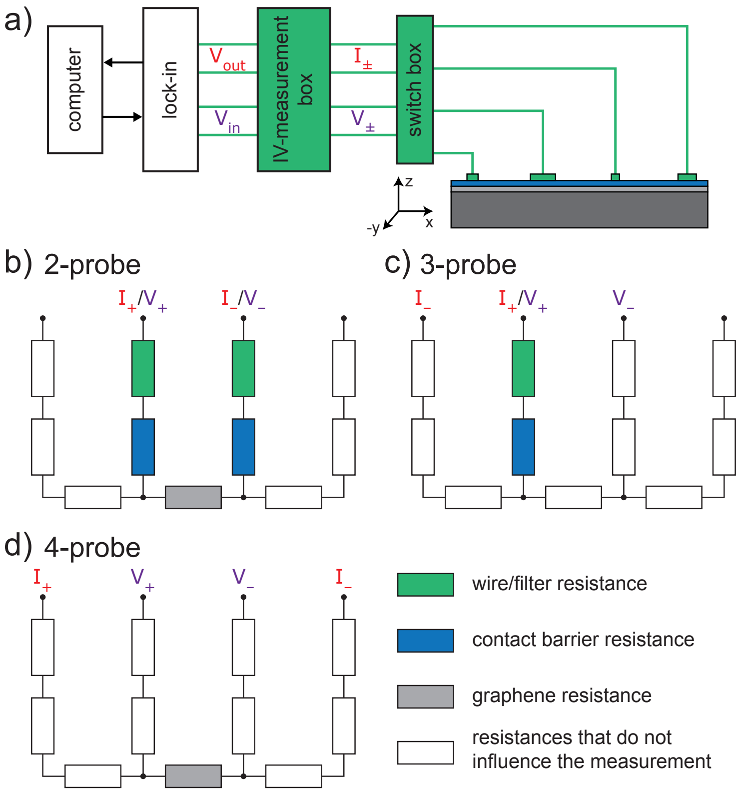

Figure 4.5: Panel (a) shows the measurement setup. The sample is placed in a vacuum tube and a magnetic field can be applied in y- or z-direction. Panels (b)–(d) show three times an electric circuit representing a graphene device with four contacts, each consisting of the contact barrier resistance of the device and the resistance of the wiring and the electrical filters in the circuit. The graphene resistance is represented by the horizontally aligned resistors. The colors in panel (a) point to the different resistors in (b)–(d). Panel (b) shows the 2-probe, (c) the 3-probe and (d) the 4-probe measurement geometry, where the measured resistances are colored. The non-local spin transport geometry is shown in Fig. 2.3.

are typically $f_{lock-in} \lesssim 20$ Hz. The IV-measurement box consists of a current source (range 1 pA/V to 100 mA/V) that is controlled by V_{out} from the lock-in and a voltage pre-amplifier for the voltage received from the sample ($V_\pm$) with amplifying factors from $10^0\times$ to $10^5\times$. The switch-box connects the contacts of the sample to the $I_\pm$ and $V_\pm$ from the IV-measurements box. Here all contacts prepared on the sample can be connected to the IV-measurements box. At the same time it includes filters that reduce noise and high frequency spikes from the electric supply network. The filters add a resistance of $1\ \mathrm{k}\Omega$ and a capacitance of 10 nF for each contact to the electronic circuit.

The lock-in amplifier significantly reduces the measurement noise by multiplying the input signal V_{in} with the output signal V_{out} and integrating the product over a specific time (in our measurements typically 0.3 to 3 s). This way it filters out all other (noise) frequencies and returns the signal amplitude and the phase shift of V_{in} compared to V_{out}.

Next to the connections of the devices to the lock-in, a gate voltage can be applied to the sample using a voltage source given by a Keithley 6517A.[3]

4.2.2 Charge transport measurements

While the goal of our research is to perform and understand spin transport measurements, charge transport measurements are needed to characterize the properties of the electrical contacts and the graphene strips of our devices. At the same time charge transport measurements can give insight into, e.g., the screening of electrical potentials (see Chapter 7) and by comparing charge transport with spin transport measurements we get insight in the nature of the electron and spin transport (Chapter 6, 7, 8 and 9).

2-probe measurements

When a new sample is put into the measurement setup we perform 2-probe measurements (Fig. 4.5 (b)) to check if the electrodes have ohmic contact to the graphene channel and if the graphene channel is undamaged and conducts. The current is sent between two electrodes and the voltage drop is measured between the same two contacts. The measured resistance consists of the graphene between the contacts, the contact barrier resistances for these R_C and the resistance of the wires and filters R_f. The value of R_f includes per contact $\sim 300\ \Omega$ due to the wires and predominantly the metal electrodes defined by optical and e-beam lithography and the filters with $1\ \mathrm{k}\Omega$. Bad working contacts or damaged parts of the graphene strip are indicated by unexpectedly high resistance values or lock-in phase shifts of $\gtrsim 10^\circ$.

3-probe measurements

After all contacts have been checked pairwise with 2-probe measurements, the contact barrier resistances are examined using 3-probe measurements. For this type of measurement, the sample is contacted as shown in Fig. 4.5 (c). As only those resistances contribute to the measured resistance, where the voltage probes enclose a part of the current path, this measurement results in the sum of R_C and R_f. This way the barrier resistance per contact can be determined when subtracting the known R_f

---

[3] More details on the measurement setup can be found in the PhD thesis of A. Veligura [15].

from the measurements. The value of R_C is an important parameter for spin transport measurements as discussed in Section 2.2.1 and Chapter 5.

4-probe measurements

4-probe measurements are performed to characterize the electrical properties of the graphene channel. In these measurements the current is sent between two electrodes and the voltage drop is probed on two electrodes in-between (see Fig. 4.5 (d)). Therefore only the resistance of the graphene sheet between the voltage probes is measured without any contributions from R_C or R_f. This resistance can be normalized to the graphene square resistance R_{sq} by dividing it by the length-width ratio (L/W) of the graphene strip between the contacts.

When applying a gate voltage V_g to the sample while measuring R_{sq}, the Fermi energy of the graphene is shifted and the charge carrier density is varied, resulting in a Dirac curve as shown in Fig. 3.1 (b). For the $300\ \mathrm{nm}$ thick layer of SiO_2 the charge carrier density is given by $n = \alpha_C(V_g - V_0)$ with $\alpha_C = C_g/e = 7.2 \times 10^{10} V^{-1} cm^{-2}$ and V_0 that is the value of the gate voltage at charge neutrality (the gate voltage at minimum conductivity).

Spin transport measurements

The spin transport measurements discussed in this thesis are performed in the non-local spin-valve geometry as discussed in Section 2.3 (see Fig. 2.3). For non-local measurements the voltage probes are located outside the charge current path. Therefore in first order no charge transport related effects are being measured. As mentioned in several recent articles [16–18] second order signals from charge transport, e.g., related to thermal effects, can still influence the non-local measurement by affecting the background resistance. Though measurements show that these signals are usually small.

References

[1] K. S. Novoselov, A. K. Geim, S. V. Morozov, D. Jiang, Y. Zhang, S. V. Dubonos, I. V. Grigorieva, and A. A. Firsov, "Electric Field Effect in Atomically Thin Carbon Films," *Science* **306**(5696), pp. 666–669, 2004.

[2] N. Tombros, *Electron Spin Transport in Graphene and Carbon Nanotubes*. PhD thesis, University of Groningen, 2008.

[3] A. C. Ferrari, J. C. Meyer, V. Scardaci, C. Casiraghi, M. Lazzeri, F. Mauri, S. Piscanec, D. Jiang, K. S. Novoselov, S. Roth, and A. K. Geim, "Raman Spectrum of Graphene and Graphene Layers," *Phys. Rev. Lett.* **97**(18), p. 187401, 2006.

[4] A. Gupta, G. Chen, P. Joshi, S. Tadigadapa, and Eklund, "Raman Scattering from High-Frequency Phonons in Supported n-Graphene Layer Films," *Nano Lett.* **6**(12), pp. 2667–2673, 2006.

[5] S. Dimitrijev, "Silicon Carbide as a Material for Mainstream Electronics," *Microelectron. Eng.* **83**(1), pp. 123–125, 2006.

[6] P. T. B. Shaffer, "A Review of the Structure of Silicon Carbide," *Acta Crystallogr. B* **25**(3), pp. 477–488, 1969.

[7] P. N. First, W. A. de Heer, T. Seyller, C. Berger, J. A. Stroscio, and J.-S. Moon, "Epitaxial Graphenes on Silicon Carbide," *MRS Bull.* **35**, pp. 296–305, 2010.

[8] C. Virojanadara, M. Syväjarvi, R. Yakimova, L. I. Johansson, A. A. Zakharov, and T. Balasubramanian, "Homogeneous Large-Area Graphene Layer Growth on 6H-SiC(0001)," *Phys. Rev. B* **78**, p. 245403, 2008.

[9] K. V. Emtsev, A. Bostwick, K. Horn, J. Jobst, G. L. Kellogg, L. Ley, J. L. McChesney, T. Ohta, S. A. Reshanov, J. Rohrl, E. Rotenberg, A. K. Schmid, D. Waldmann, H. B. Weber, and T. Seyller, "Towards Wafer-Size Graphene Layers by Atmospheric Pressure Graphitization of Silicon Carbide," *Nat. Mat.* **8**(3), pp. 203–207, 2009.

[10] A. Tzalenchuk, S. Lara-Avila, A. Kalaboukhov, S. Paolillo, M. Syvajarvi, R. Yakimova, O. Kazakova, J. T. J. B. M., V. Fal'ko, and S. Kubatkin, "Towards a Quantum Resistance Standard Based on Epitaxial Graphene," *Nat. Nanotechnol.* **5**, pp. 186–189, 2010.

[11] S. Goler, C. Coletti, V. Piazza, P. Pingue, F. Colangelo, V. Pellegrini, K. V. Emtsev, S. Forti, U. Starke, F. Beltram, and S. Heun, "Revealing the Atomic Structure of the Buffer Layer between SiC(0001) and Epitaxial Graphene," *Carbon* **51**, pp. 249–254, 2013.

[12] F. Speck, J. Jobst, F. Fromm, M. Ostler, D. Waldmann, M. Hundhausen, H. B. Weber, and T. Seyller, "The Quasi-Free-Standing Nature of Graphene on H-Saturated SiC(0001)," *Appl. Phys. Lett.* **99**(12), p. 122106, 2011.

[13] C. Riedl, C. Coletti, T. Iwasaki, A. A. Zakharov, and U. Starke, "Quasi-Free-Standing Epitaxial Graphene on SiC Obtained by Hydrogen Intercalation," *Phys. Rev. Lett.* **103**(24), p. 246804, 2009.

[14] M. Ishigami, J. H. Chen, W. G. Cullen, M. S. Fuhrer, and E. D. Williams, "Atomic Structure of Graphene on SiO2," *Nano Lett.* **7**(6), pp. 1643–1648, 2007.

[15] A. Veligura, *Quantum Transport in Two- and One-Dimensional Graphene*. PhD thesis, University of Groningen, 2012.

[16] F. L. Bakker, A. Slachter, J.-P. Adam, and B. J. van Wees, "Interplay of Peltier and Seebeck Effects in Nanoscale Nonlocal Spin Valves," *Phys. Rev. Lett.* **105**, p. 136601, 2010.

[17] I. J. Vera-Marun, V. Ranjan, and B. J. van Wees, "Nonlinear Interaction of Spin and Charge Currents in Graphene," *Phys. Rev. B* **84**, p. 241408, 2011.

[18] I. J. Vera-Marun, V. Ranjan, and B. J. van Wees, "Nonlinear Detection of Spin Currents in Graphene with Non-Magnetic Electrodes," *Nat. Phys.* **8**(4), pp. 313–316, 2012.

Chapter 5

Contact induced spin relaxation in Hanle spin precession measurements

Abstract

In the field of spintronics the "conductivity mismatch" problem remains an important issue. Here the difference between the resistance of ferromagnetic electrodes and a (high resistive) transport channel causes injected spins to be backscattered into the leads and to lose their spin information. We study the effect of the resulting contact induced spin relaxation on spin transport, in particular on non-local Hanle precession measurements. As the Hanle line shape is modified by the contact induced effects, the fits to Hanle curves can result in incorrectly determined spin transport properties of the transport channel. We quantify this effect that mimics a decrease of the spin relaxation time of the channel reaching more than 4 orders of magnitude and a minor increase of the diffusion coefficient by less than a factor of 2. Then we compare the results to spin transport measurements on graphene from the literature. We further point out guidelines for a Hanle precession fitting procedure that allows to reliably extract spin transport properties from measurements.

Published as:
T. Maassen, I. J. Vera-Marun, M. H. D. Guimarães, and B. J. van Wees,
Phys. Rev. B **86**, 235408 (2012).

5.1 Introduction

New concepts like the spin transfer torque, the transport of spin information over long distances, and the prospect of spin field effect transistors keep spintronics an inspiring field [1, 2]. But before new types of spintronic devices can be build we need both materials that efficiently generate spin currents as injector and detector electrodes and materials with long spin relaxation lengths (λ) and times (τ) to transport the spins with only little losses.

While ferromagnetic metals can spin polarize currents and are therefore used to inject and detect spins, semiconductors offer low spin relaxation which makes them good candidates to be used as transport channels. One of the main challenges when combining the two types of materials is the "conductivity mismatch" problem [3, 4]. As the electrical resistance in the ferromagnetic electrodes is in general lower than in the semiconducting transport channel, the injected spins tend to be reabsorbed by the leads and loose their spin orientation.

Graphene, being an intermediate between metal and semiconductor systems, is a prototype example for the conductivity mismatch, as graphene based devices can be well described following simple spin diffusion theory. Here, the long spin relaxation lengths of several μm measured at room temperature are already promising [5] but still stay behind the theoretical prospects based on the high mobilities combined with weak spin-orbit coupling and low hyperfine interactions [6]. While some research aims to understand the spin relaxation mechanism in graphene [7–12] and to understand the influence of the direct environment of the graphene transport channel [13–18] the conductivity mismatch can play an important role in the origin of spin relaxation in the measured devices. To prevent this mismatch, high resistive barriers between the contacts and the graphene channel are included [4, 19–23].

The most common and reliable way to probe spin transport properties is by performing measurements in the non-local spin-valve geometry [2, 5, 24] because it enables to separate spin and charge currents, avoiding spurious effects [25]. Popinciuc *et al.* [19] describe, in agreement with Takahashi and Maekawa [26], that the measured amplitude of the spin signal in the non-local geometry is strongly reduced for low contact resistances R_C.[1] To quantify the effect, Popinciuc *et al.* introduce the so-called R-parameter that is defined for a 2-dimensional channel by $R = (R_C/R_{sq})W$,

---

[1] For a negligible spin resistance of the ferromagnetic electrodes compared to the one of the barrier and to the resistance of the transport channel (R_{sq}), we call the resistance of the interface barrier between the contact electrode and the transport channel "contact resistance" (R_C). The contact resistance consists of the parallel resistance for spin up ($R_\uparrow$) and spin down ($R_\downarrow$). We assume $R_\uparrow \approx R_\downarrow$ as we are discussing polarizations of $P < 30\%$ leading to an error in determining the effect of the contact resistance on the spin relaxation of less than 10%. In the case of transparent contacts (i.e., no high resistive barrier), R_C is equal to the spin resistance of the ferromagnetic leads R^F_{spin}. In this case we also have to replace the spin polarization of the barrier P by the spin polarization of the ferromagnetic leads P^F.

where R_{sq} is the square resistance and W the width of the diffusive channel [19].[2]

We begin this article by summarizing the dependence of the non-local amplitude on the contact resistance discussed in Ref. [19]. Then we focus on how Hanle spin precession measurements are influenced by low contact resistances. These measurements are performed in the same non-local spin-valve geometry but with a perpendicular magnetic field that causes the spins to precess. The resulting Hanle curves can be fitted to determine the spin relaxation time and the diffusion coefficient. We discuss that not only the amplitude but also the shape of Hanle precession curves is changed for low values of the R-parameter (corresponding to low contact resistances) and simulate Hanle measurements including contact induced relaxation. We quantify the contacts' influence by fitting the data with the standard Hanle formula without taking contact induced effects into account, assuming $R \to \infty$. Note that fitting with the standard Hanle formula is the common method to analyze experimental spin precession data in almost all published works. The difference of the extracted spin relaxation time τ^{fit} and diffusion coefficient D^{fit} to the parameters used in the simulations is quantified and we compare these results to data obtained on graphene spin-valve devices where a reduction of τ was reported for low contact resistances [20]. Finally, we point out how to extract correctly the spin transport properties from Hanle precession measurements by excluding spurious background effects.

5.2 Contact induced spin relaxation

Fig. 5.1 (a) presents a sketch of the non-local measurement geometry with an injecting electrode at $x = L$ on the right side, sending a charge current via a resistive barrier [4] into the channel to the right side end and a detecting electrode on the left side (at $x = 0$), measuring the voltage difference V_{nl} between the contact and the left side end. As the electrodes are ferromagnetic, the injecting electrode induces a spin imbalance, described by a non-equilibrium contribution to the chemical potential μ_S, that accumulates below the electrode and diffuses away from it in both the positive and negative x-direction of the channel (red dotted curve in Fig. 5.1 (c)). The second ferromagnetic electrode detects the spins at $x = 0$, and the measured voltage is $V_{nl} = P\mu_S/e$. Here P is the polarization of the contact and e the electron charge. The non-local resistance R_{nl} is defined by normalizing V_{nl} with the injected current I. R_{nl} is given by [19, 26][1]

$$R_{nl} = \pm \frac{P^2 R_{sq}\lambda}{2W} \frac{(2R/\lambda)^2 \exp(-L/\lambda)}{(1+2R/\lambda)^2 - \exp(-2L/\lambda)} \tag{5.1}$$

The model leading to this result is based on the 1-dimensional description of a dif-

---

[2] We are discussing here a 2-dimensional channel like graphene. In the case of a 3-dimensional channel

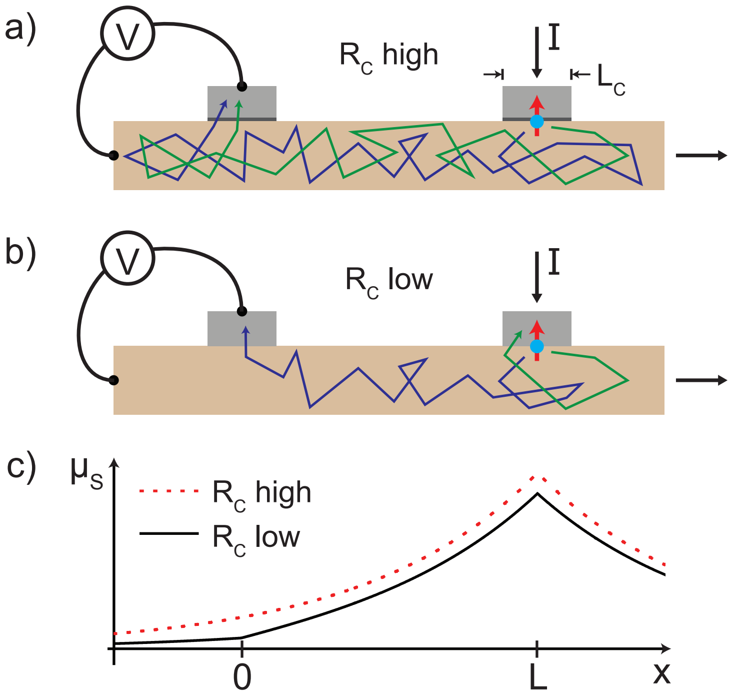

Figure 5.1: Sketches of spin diffusion through a diffusive channel with a spin injector and detector separated by a distance L in non-local geometry for (a) high and (b) low contact resistances. The width of the contacts in x-direction, L_C, is small compared to L and the spin relaxation length λ. (c) The spin chemical potential μ_S indicating the spin accumulation below the injector electrode and the exponential decay of the spin signal (red dotted curve). The spin accumulation influenced by the contact induced spin relaxation is denoted by the black solid curve.

fusive channel with an injector and detector on distance L and $\lambda = \sqrt{D\tau}$ the spin relaxation length in the channel with the diffusion coefficient D and the spin relaxation time τ. The width of the contacts (L_C) is considered to be negligible compared to L and λ [19]. Also we assume $1 - P^2 \approx 1$ (applicable to graphene devices where $P < 30\%$ [20]) and are considering an infinite homogeneous transport channel. The effect of an inhomogeneous transport channel is discussed elsewhere [16]. The R-parameter is calculated using the contact resistance of the injector and detector. In case R is not the same for the two electrodes an effective single R-parameter can be calculated using $1/R_{\mathrm{eff}} \approx (1/R_1 + 1/R_2)/2$ with the R-parameters of the injector and detector R_1 and R_2 (see Section 5.6.1, see also Tanamoto *et al.* [27]). The meaning

---

R would be $R = (R_C/\rho)A$ where A is the cross section and ρ the resistivity of the transport channel.

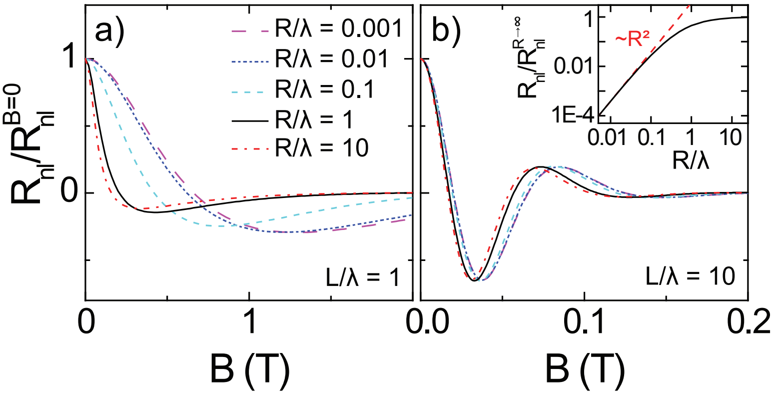

Figure 5.2: Simulated spin precession curves for different values of R/λ with (a) $L/\lambda = 1$ and (b) $L/\lambda = 10$. For the simulations we use $D = 0.01\ \mathrm{m}^2/\mathrm{s}$, $\tau = 100$ ps, $W = 1\ \mu$m and $R_{sq} = 1\ \mathrm{k}\Omega$ (representative of graphene devices) with contact resistances between 1 and $10^4\ \Omega$. The amplitude of the curves is normalized for clarity with $R_{nl}(B = 0)$. The inset in panel (b) shows R_{nl} from Eq. (5.1) as a function of R/λ for $L/\lambda = 1$, normalized by $R_{nl}^{R\to\infty}$(black solid line) and the asymptote $\propto R^2$ (red dashed line).

of the R-parameter gets clear when it is normalized with the spin relaxation length λ. The normalized value corresponds to the ratio of the contact resistance and the spin resistance of the channel $R_\lambda = R_{sq}\lambda/W$ so $R/\lambda = R_C/R_\lambda$. Hence, R/λ describes the ratio of spins diffusing through the channel and relaxing, versus those being reabsorbed by the contact, making it a good measure for the influence of the contacts.

Eq. (5.1) shows that the spin signal R_{nl} has a maximum for high contact resistances ($R \to \infty$) and is reduced for low R values. A significant change is observed for $R/\lambda \leq 1$ (Fig. 5.2 (b), inset). On the other hand the amplitude of the signal is reduced with increasing L from a maximum at $L = 0$. The characteristic length ratio of the system is L/λ. While the effect on the normalized amplitude ($R_{nl}/R_{nl}^{R\to\infty}$ with the amplitude without contact induced effects $R_{nl}^{R\to\infty}$) is smaller for short distances between injector and detector electrode, it stays approximately constant for $L/\lambda \geq 1$. Popinciuc *et al.* discuss in detail the effect of low contact resistances on the measured non-local amplitude but, while included in the model, the effect on the Hanle curve is only discussed qualitatively [19]. In the following we are going to present a quantitative analysis of the influence of low contact resistances on Hanle measurements. We show that the extracted spin transport properties of the transport channel can be limited by the contact induced relaxation and are therefore incorrectly determined when low R measurements are analyzed without considering the influence of the contacts.

Fig. 5.2 (a) shows Hanle precession data that was simulated for different values of R/λ with $L/\lambda = 1$ using the model system of Fig. 5.1 (a) described in Ref. [19]. Note that the amplitude of the Hanle curves is normalized at $B = 0$, which is necessary as the amplitude scales with $(R/\lambda)^2$ for $R/\lambda \ll 1$ and changes by 5 orders of magnitude between $R/\lambda = 0.001$ and $R/\lambda = 10$. A significant change in the Hanle shape is visible in Fig. 5.2 (a), pointing to an effective change of the spin transport properties. The strongest change in the shape is seen between $R/\lambda = 0.01$ and $R/\lambda = 1$ while the curve shape is saturating for both small and large R/λ values denoting spin transport limited by the contacts or by the properties of the channel, respectively. Fig. 5.2 (b) shows a similar dataset for $L/\lambda = 10$. We also see a change in the Hanle shape, but the effect is much weaker for this larger distance of the injector and detector. Remarkably, in both cases the curves stay in the characteristic Hanle-like shape for all R/λ. Therefore it is possible to fit the data using the solutions to the Bloch equations [28, 29] that do not take the effect of the low resistive contacts into account (see Section 5.6.2):

$$\frac{d\vec{\mu_S}}{dt} = D\nabla^2\vec{\mu_S} - \frac{\vec{\mu_S}}{\tau} + \vec{\omega_L} \times \vec{\mu_S}. \tag{5.2}$$

Here $\vec{\omega_L}$ is the Larmor frequency $\vec{\omega_L} = g\mu_B/\hbar\ \vec{B}$, with the gyromagnetic factor g (g-factor, $g \approx 2$ for free electrons), the Bohr magneton μ_B and the magnetic field $\vec{B}$. By fitting simulated data without taking the effects of the contacts into account, we can determine what happens when one fits the data obtained in samples with corresponding R and L values in the standard manner.[3]

The results from these fits are presented in Fig. 5.3. Note that while the simulations were performed with $D = 0.01\ \mathrm{m}^2/\mathrm{s}$ and $\tau = 100\ \mathrm{ps}$ they do not depend on the specific value of D and τ. Hence, we get the same results for different D and τ resulting in the same $\lambda = \sqrt{D\tau}$ as the fitting results depend only on the ratios R/λ and L/λ. The graphs show the fitted values τ^{fit} and D^{fit} normalized by the actual values for the channel τ and D as a function of R/λ for different L/λ (Figs. 5.3 (a) and (c)) and as a function of L/λ with different R/λ (Figs. 5.3 (b) and (d)). While all values converge for high R/λ to the intrinsic values, we see a strong decrease of τ^{fit} and a moderate increase of D^{fit} for small R/λ. Looking at Fig. 5.3 (a) in more detail we see that the decrease in τ^{fit} is strongest the shorter the distance L between injector and detector relative to λ. We also see that the values saturate for small values of R/λ as already perceivable in Fig. 5.2 (a). In this limit the effect of the contacts is maximized. τ^{fit} shows changes of nearly up to five orders of magnitude which

---

[3] To fit the data we first normalize the simulated R_{nl} values with $R_{nl}(B = 0)$ and keep the fitting amplitude fixed as 1. This enables a more standardized fitting procedure and reduces the fitting time considerably. The fixed amplitude can be justified as fitting with a non-fixed amplitude gives in most cases a variation of the amplitude by less than 1% and only varies more in the regime where $R/\lambda \leq 0.1$ and $L/\lambda \leq 0.1$.

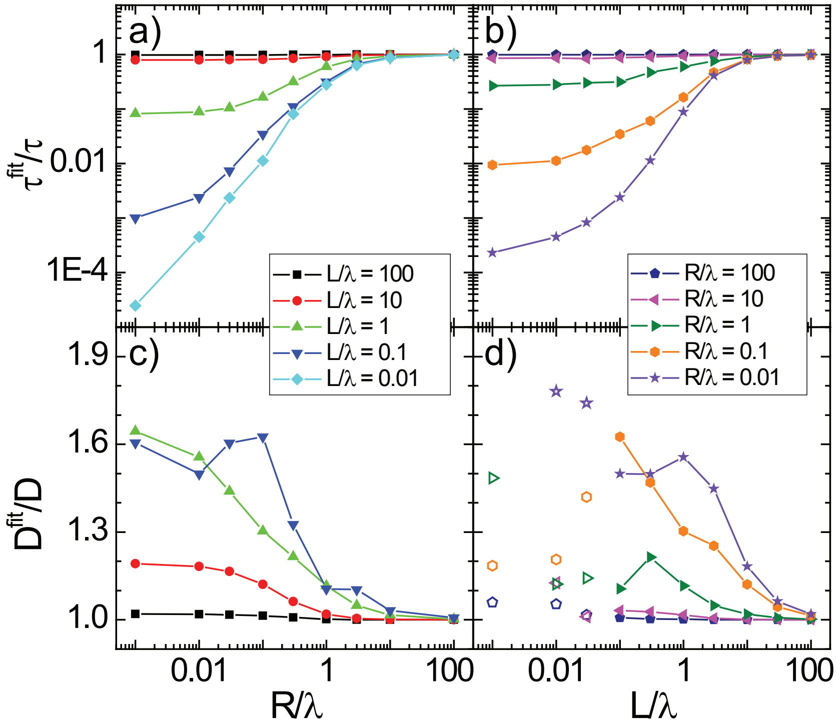

Figure 5.3: The change in τ^{fit} and D^{fit} fitted for different L/λ as a function of R/λ ((a) and (c)) and for different R/λ as a function of L/λ ((b) and (d)). For small values of L/λ the fits become insensitive to the specific value of the diffusion coefficient, resulting in the non-smooth behavior shown for $L/\lambda = 0.1$ in panel (c). Therefore the data for $L/\lambda < 0.1$ is not shown in panel (c) and is marked with open symbols in panel (d). Note that τ can still be consistently obtained (panel (a) and (b)).

means that in a measurement with parameters of $R/\lambda = 0.001$ and $L/\lambda = 0.01$ we would underestimate τ by a factor of 5×10^4.

The length dependence of the effect is more clearly presented in Fig. 5.3 (b) where the τ^{fit} data is plotted as a function of L/λ for different R/λ. Here we see that while the decrease of τ^{fit} is stronger for shorter distances the effect gets negligible for $L/\lambda \geq 10$. That means that contact induced effects can be circumvented by measuring on a longer distance. This is only limited by the reduced measured amplitude for longer distances L (see Eq. (5.1)).

Figs. 5.3 (c) and (d) show the same plots for D^{fit}. Also here we see the strongest effect for small R/λ and L/λ and no significant change for $R/\lambda = 100$ or $L/\lambda = 100$. On the other hand, the values for D^{fit} show a much weaker change than the values of τ^{fit} and the change is directed in the opposite direction than the change of τ^{fit}.

Similar to τ^{fit}, the D^{fit} values also seem to saturate for small R/λ and the changes are less than a factor of 2.

While most curves presented in Fig. 5.3 have a smooth shape and a continuous change with L/λ and R/λ, the data for D^{fit} shows for values of $L/\lambda \leq 0.1$ combined with values of $R/\lambda \leq 1$ a non-smooth behavior. This is related to the fact that the diffusion in the channel gets for small L dominated by the contact induced effects for short distances and low contact resistances and the shape of the Hanle curves gets strongly influenced. The spin accumulation has no significant decay between the injector and the detector electrode so the system becomes similar to 3-terminal Hanle precession [30]. As a result, the fits become insensitive to the specific value of D, but one can still consistently determine τ [18] (see Section 5.6.2).[4] Therefore we omitted the data for D^{fit} for $L/\lambda < 0.1$ in Fig. 5.3 (c) and marked the data with open symbols in Fig. 5.3 (d).

Note that in the limit $L/\lambda \ll 1$ and $R/\lambda < 10$ the values for τ^{fit} saturate as they are dominated by the contact induced effects and can be described by a basic formula related to the back diffusion of the spins into the contact (see Section 5.6.3).

5.3 Discussion

Fig. 5.3 shows clear trends for τ^{fit}/τ and D^{fit}/D as a function of R/λ and L/λ. We are going to discuss in the following how to understand the physics behind the presented results. The sketch in Fig. 5.1 (a) presents the spin injection and detection for high contact resistances, e.g., due to tunnel barriers between the channel and the contacts. Here the spin diffusion in the channel remains undisturbed and the injected spins diffuse freely through the channel before being detected by the spin sensitive detector. In this way, measurements detect the intrinsic spin transport properties of the channel and the simple exponential decay of the spin signal (red dotted curve in Fig. 5.1 (c)) is obtained.

In the case of low contact resistances the spin transport is influenced both at the injector and at the detector electrodes. When diffusing through the channel the low resistive detector has a high probability of detecting the spins as soon as they are near the contact as it acts as a spin sink (Fig. 5.1 (b)). Therefore the effective traveling time is reduced and the measured diffusion coefficient enhanced as $D = L^2/2\tau_D$ where τ_D is the diffusion time for the length L. At the same time the proximity to the low resistive contacts also causes spins to relax, which reduces the relaxation time. The extra relaxation is depicted by the kink at the detector in the black solid curve in Fig. 5.1 (c), describing the decay of the in general reduced spin accumulation in the system. Note that if measuring with additional electrically floating contacts

---

[4] Recently research has been posted showing that 3-terminal and 4-terminal Hanle measurements on graphene give very similar spin relaxation times [31].

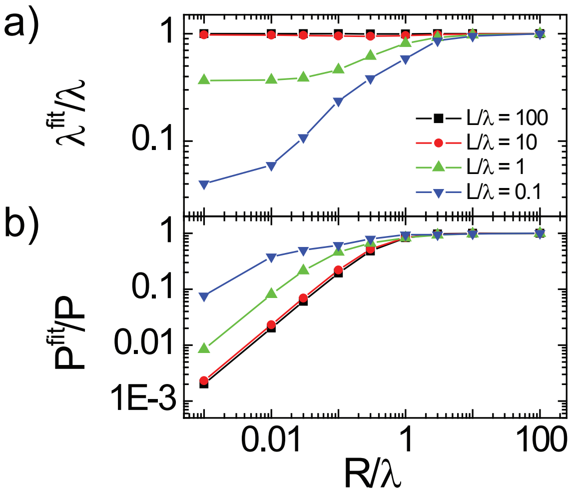

Figure 5.4: (a) The change in $\lambda^{\mathrm{fit}}/\lambda$ calculated using τ^{fit} and D^{fit} from Fig. 5.3 (b) The effective polarization P^{fit} normalized with the actual polarization P. The values are plotted as a function of R/λ for different L/λ. The values for $L/\lambda = 100$ and 10 overlap in both panels.

between the injector and detector electrode (as done, e.g., in Ref. [18]), these can also result in extra spin relaxation giving further kinks to the spin accumulation in case the contacts are invasive.

Figs. 5.3 (b) and (d) show a reduction of the contact induced effects for larger L/λ. This can be easily understood by the fact that for a longer distance between the electrodes the ratio of the time the spins stay in the channel compared to in close proximity to the contacts grows, resulting in relatively less influence of the contacts on the spin transport.

Fig. 5.4 (a) shows the spin relaxation length λ^{fit} resulting from the fitting results presented in Fig. 5.3 for $L/\lambda \geq 0.1$. The shape of the λ^{fit}-curve is comparable to the behavior of τ^{fit}. This is due to the fact that λ^{fit} is mainly influenced by the spin relaxation time τ^{fit} with a change of up to a factor 1000 (for $L/\lambda \geq 0.1$). As D^{fit} shows only a change of less than a factor 2 we get a maximum reduction of λ^{fit} by a factor 25.

This λ^{fit} value would be used in the analysis of a measurement to calculate the polarization P. If we take the amplitude simulated with Eq. (5.1) (inset, Fig. 5.2 (b)) and assume spin transport without contact induced spin relaxation (Eq. (5.1) for $R \to \infty$) we extract the effective polarization P^{fit} with $R_{nl}(\lambda^{\mathrm{fit}}, P^{\mathrm{fit}}, R \to \infty) = R_{nl}(\lambda, P, R)$. The resulting value is up to 500 times reduced for small values of R/λ compared to the real P value (Fig. 5.4 (b)). Note that the largest change in P^{fit} compared with P is observed for long distances.

After discussing the effects observed in the simulations let us have a look at measurements on real devices using graphene as the transport channel. For spin transport samples on graphene it is difficult to produce high resistive contacts and to control the quality of the contact-graphene interface. So a data set with similar quality samples with only a change of the contact resistance is difficult to produce. On the other hand in a single device the quality of the contacts is most of the time comparable. Therefore it is relatively easy to check the length dependence of the spin transport properties in this kind of system, assuming similar R-parameters for all electrodes. Two sets of data obtained on two different graphene devices with three different injector-detector distances are presented in the work by Wojtaszek *et al.* in Figs. 4 (a) and 5 (a) of the supplementary information of Ref. [32]. In both cases a minor increase of D is reported when measuring on a shorter distance, and in the first case also a minor decrease of τ, pointing to weak but apparent contact induced relaxation.[5] With $R \geq 3\ \mu\mathrm{m}$ and $\lambda \approx 5\ \mu\mathrm{m}$ the measurements were also performed in a regime where one would expect this kind of weak contact induced effects as $L/\lambda \approx R/\lambda \approx 1$ (see Fig. 5.3) [32].

Han *et al.* present a study of the dependence of the spin transport properties on the quality of the resistive barrier between the graphene channel and the contacts in Ref. [20]. They show that between tunneling injection of spins and the injection with transparent contacts the measured spin relaxation time decreases while the diffusion coefficient is increased in agreement with our simulations' results. On the other hand the results for a "pinhole" barrier with intermediate resistance present an intermediate spin relaxation time but also a reduced diffusion coefficient. While the spin relaxation time fits into the expectations for an intermediate contact resistance, the reduced diffusion coefficient cannot be explained by the contact resistance but has to be related to a lower quality sample or other effects.

Our model also points to the fact that the recent reported differences between the results for the spin relaxation length, based on the analysis of 4-terminal non-local Hanle precession measurements [20] and based on the analysis of the magnitude of spin-valve measurements in local 2-terminal geometry with very high contact resistances ($R_C > 1\ \mathrm{M}\Omega$) [22] cannot be explained by contact induced relaxation. If one would measure with the configuration of Han *et al.*[20] with $L = 5.5\ \mu\mathrm{m}$ and $R \approx 200\ \mu\mathrm{m}$ a material with a spin relaxation length of $\sim 100\ \mu\mathrm{m}$ and a spin relaxation time of $\sim 100\ \mathrm{ns}$ as reported in Ref. [22], one would only see a reduction of the fitted spin relaxation time by a factor of $\tau^{\mathrm{fit}}/\tau \approx 1/3$ (see Fig. 5.3 (a)) leading to a reduced spin relaxation length of $\lambda^{\mathrm{fit}}/\lambda \approx 1/2$ (see Fig. 5.4 (a)) as one would have $L/\lambda \approx 0.05$ and $R/\lambda \approx 2$. Therefore the standard Hanle analysis would yield

---

[5] That the data agrees only qualitatively with our simulations and that the second data set does not show a clear dependence of τ on L can be related to differences in the R-parameter between the electrodes as Wojtaszek *et al.* report R-parameters of $3\ \mu\mathrm{m} \leq R \leq 100\ \mu\mathrm{m}$. Electrically floating contacts between the injector and detector electrode could also be influencing the data.

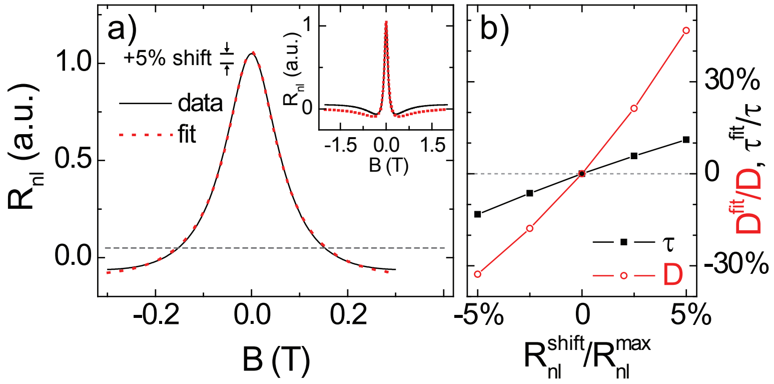

Figure 5.5: (a) The influence of a baseline shift shown by means of a Hanle spin precession curve, shifted $+5\%$ of the precession amplitude upwards (black solid curve) and a fit assuming no shift (red dotted curve). The baseline of the fit is therefore at $R_{nl} = 0$ while the baseline of the data is denoted by the black dashed line. The same Hanle curves on a larger B-field range are shown in the inset. A clear difference is visible for $|B| > 0.3$ T. (b) The change of the diffusion coefficient and the spin relaxation time resulting from data with a baseline shift and fits assuming no baseline shift. The presented data was simulated using $D = 0.01$ m^2/s, $\tau = 100$ ps and $L = 1$ μm.

$\lambda^{\text{fit}} \approx 50$ μm and $\tau^{\text{fit}} \approx 30$ ns, but Han *et al.* report $\lambda^{\text{fit}} \approx 2.5$ μm and $\tau^{\text{fit}} \approx 0.5$ ns [20]. With $\lambda^{\text{fit}} \approx 2.5$ μm Han *et al.* are in the regime of negligible contact induced relaxation with $L/\lambda \approx 2$ and $R/\lambda \approx 80$, so the difference in the measured λ is not based on contact induced relaxation but has to be related to other effects. Even for a spin relaxation length of $\lambda = 20$ μm it would be $L/\lambda \approx 0.25$ and $R/\lambda \approx 10$ for the system of Han *et al.* and they would be able to measure this λ without significant influence of the contacts (see Fig. 5.4 (a)). Such strong differences of the spin signal magnitude between non-local and local configuration as between Refs. [20] and [22] have also been observed in traditional semiconductors like silicon in the non-local [33] and 3-terminal [30, 34] configuration and recently also in metals [35].

5.4 Guidelines for a good and reliable Hanle fit

In this chapter we discuss how Hanle measurements are influenced by contact induced relaxation that can lead to incorrectly determined spin transport properties of the channel. Independently from that, the fitting procedure can also give incorrect results for the spin transport properties when performed incorrectly. In this section we are therefore commenting on typical pitfalls in analyzing Hanle precession data.

The fit to a Hanle curve is unambiguous if performed in the right way. Fig. 5.5 (a) illustrates how a fit can still give wrong results on the example of a Hanle precession fit when assuming a wrong background resistance. The background resistance is represented by the $R_{nl}(B \to \infty)$ value and is the fitting baseline. Fig. 5.5 (a) shows a fit to the central peak of a Hanle curve (without contact induced effects) with a baseline shifted by $+5\%$ of the amplitude. The fit results in an increase of τ by $> 10\%$ and of D by $> 45\%$ and therefore a misestimation of λ by more than 25% compared to the values used to simulate the data. However, when fitting the curve with these values the fit presents itself faulty when including the high field tails of the curve as shown in the inset of Fig. 5.5 (a). Fitting to high B-field values gives therefore a good indication of the quality of the fit. However, this identification of a bad fit can be partly masked by data noise in combination with anisotropic magneto resistance effects or the out-of-plane tilting of the magnetization of the ferromagnetic electrodes at high field values, adding an additional background resistance [36]. Another indication of a good fit is the fitted curve reproducing the "shoulders" of the measured curve, where R_{nl} has a minimum (for parallel alignment of the injector and detector electrode). This is obviously not accomplished in the presented case (Fig. 5.5 (a), inset). The larger the ratio L/λ the more pronounced are the shoulders, so measuring on a longer distance enhances the reliability of the fit. The significant effect of an uncertainty of the fit baseline on the determination of D has been mentioned by Salis *et al.*[37] for measurements on Fe/GaAs devices.

While measuring to high magnetic field values to determine the background resistance is in any case advisable, there is a way to avoid such spurious background effects in a fit. Measuring the spin precession both for parallel and for antiparallel orientation of the electrodes, and subtracting the signals from each other removes most spurious (not spin related) background effects as done in several recent works [14, 16, 18, 32, 38]. By taking the mean of the parallel and the antiparallel measurements, one can also extract the B-field dependent background resistance. Finally, a minor error in a fit can also occur if the magnetic field values are not properly calibrated. The effect of a correction factor for the magnetic field value is the same as the effect of a changed g-factor as $\omega_L \propto B$ and $\omega_L \propto g$. A wrong B-field calibration is therefore linearly passed on to τ and $1/D$ [39].

5.5 Conclusions

We discuss the effect of low resistance contact induced spin relaxation on Hanle precession data and quantify the misinterpretation of spin transport properties in a transport channel that can arise from this effect. As fitting Hanle curves is a common way to extract spin transport properties we use the model presented in Ref. [19] to simulate Hanle measurements and fit the data using the standard formula, neglecting the contact induced effects. The observed rescaling of the spin relaxation time and the diffusion coefficient only depend on the ratios R/λ and L/λ and the fitting results show that a strongly decreased τ^{fit} by up to nearly five orders of magnitude and a moderately increased D^{fit} by less than a factor of 2 can be observed for small R/λ and L/λ. On the other hand large values for both R/λ or L/λ show a convergence of τ^{fit} and D^{fit} on the undisturbed values τ and D, independent on L or R, respectively. This shows that the spin relaxation induced by the contacts can in principle be avoided when measuring on a longer distance. We then discuss how these values of τ^{fit} and D^{fit} lead to a wrong estimate of the contact polarization before comparing our results for τ^{fit} and D^{fit} qualitatively with measurements on graphene in the literature. The modeled effect of the contacts on spin transport only depends on the resistance of the barrier and not on the type of barrier. Hence, although most contact interfaces used in the non-local geometry to study spin transport in graphene are not truly in the tunneling regime, we can conclude that with the resistance of the commonly used barriers the effect of back diffusion into the contacts on the spin transport is only minor and the spin transport properties are mainly limited by other effects [5, 7, 10, 14, 16, 18–20, 32, 38, 40]. While explicitly discussing the effect of low resistive contacts on the non-local geometry, similar effects also play a role for local measurements [41].We also briefly discussed the guidelines for a good and reliable Hanle fit as an incorrectly performed fit can also lead to misinterpretations of the spin transport properties of a diffusive channel while a correct fit leads to unambiguous results.

5.6 Supplementary information

5.6.1 The R-parameter for dissimilar contacts

The discussion in the main text focused on the symmetric case when the injector and the detector contacts have equal R-parameters. Here we address the general case of dissimilar injector and detector contacts and demonstrate an equivalence that allows us to map this general case to the more symmetric one presented above.

Takahashi and Maekawa [26] analytically derive the general expression for the non-local resistance R_{nl} as a function of the contact resistances of the injector and detector electrode by assuming a channel in the spin diffusive transport regime. We consider that the spin resistance of the contact is dominated by either the interfacial barriers (a condition fully applicable of the case of oxide barriers and metallic ferromagnetic electrodes), or alternatively by the ferromagnetic electrodes for the case of transparent contacts.[1] Then it follows from Eq. (3) in Ref. [26] with minor changes in notation

$$R_{nl} = \pm \frac{R_{sq}\lambda}{2W} \exp\left(-\frac{L}{\lambda}\right) \prod_{i=1}^{2} \left(\frac{P\frac{2R_i}{\lambda}}{1-P^2} \right) \left[\prod_{i=1}^{2} \left(1 + \frac{\frac{2R_i}{\lambda}}{1-P^2} \right) - \exp\left(-\frac{2L}{\lambda}\right) \right]^{-1}, \quad (5.3)$$

where $R_{1,2}$ correspond to the R-parameters of the injector and detector contacts, and the rest of the parameters are the same as those presented in the discussion of Eq. (5.1).

This equation can be simplified by realizing that for highly spin polarized contacts ($P \approx 1$) there is no contact induced spin relaxation, even for low resistance contacts. Therefore if we consider $1 - P^2 \approx 1$ we obtain

$$R_{nl} = \pm \frac{P^2 R_{sq} \lambda}{2W} \frac{\left(\frac{2R_1}{\lambda}\right)\left(\frac{2R_2}{\lambda}\right) \exp\left(-\frac{L}{\lambda}\right)}{\left(1 + \frac{2R_1}{\lambda}\right)\left(1 + \frac{2R_2}{\lambda}\right) - \exp\left(-\frac{2L}{\lambda}\right)} \tag{5.4}$$

which has a similar structure as Eq. (5.1) [19]. Following simple algebra, we can equate both equations and solve for the R-parameter of Eq. (5.1), which can be understood as an effective R-parameter $R_{\text{eff}}(R_1, R_2, L, \lambda)$ given by

$$\frac{2R_{\text{eff}}}{\lambda} = \frac{\left(\frac{2R_1}{\lambda}\frac{2R_2}{\lambda}\right) + \sqrt{\left(\frac{2R_1}{\lambda}\frac{2R_2}{\lambda}\right)^2 - \left(1 + \frac{2R_1}{\lambda} + \frac{2R_2}{\lambda} - e^{-2L/\lambda}\right)\left(\frac{2R_1}{\lambda}\frac{2R_2}{\lambda}\right)\left(e^{-2L/\lambda} - 1\right)}}{1 + \frac{2R_1}{\lambda} + \frac{2R_2}{\lambda} - e^{-2L/\lambda}}, \tag{5.5}$$

allowing us to map the case of dissimilar contacts into the symmetric case of equal contacts with $R_{1,2} = R_{\text{eff}}$. One example of such a mapping is shown in Fig. 5.6 (a) for the representative case of $L/\lambda = 1$ and $R_i/\lambda = 0.1$–10. We observe that when $R_1 \neq R_2$ then $R_{\text{eff}} \approx \min(R_1, R_2)$ and also the trivial case of $R_1 = R_2 = R_{\text{eff}}$.

The exact mapping depends on L and on λ, which requires careful application to analyze experimental data. We remark that this issue is absent for the case of $2L/\lambda \approx 0$, where Eq. (5.5) reduces to the simple form,

$$\frac{1}{R_{\text{eff}}} = \frac{1}{2}\left(\frac{1}{R_1} + \frac{1}{R_2}\right) \tag{5.6}$$

equivalent to a 3-terminal measurement where both contacts are in a parallel configuration.

Although Eq. (5.6) is strictly speaking valid only when both contacts are closely spaced, we have observed that it offers a reasonable approximation even at finite separation L between the contacts. In Fig. 5.6 (b) we compare the resulting R_{eff}/λ for the extreme case of large separation ($2L/\lambda \gg 1$) from Eq. (5.5), to the value obtained from the simpler Eq. (5.6). Surprisingly, in the experimentally relevant range of intermediate conductivity mismatch $R_i/\lambda = 0.3$–10, Eq. (5.6) deviates from the exact result at infinite separation only by less than 20%. For a strong conductivity mismatch ($R_i/\lambda \leq 0.1$) one should apply the exact result of Eq. (5.5).

5.6.2 Fitting simulated Hanle curves

The research presented in this chapter is based on the following concept: Hanle precession curves are simulated following the model presented in Ref. [19] including

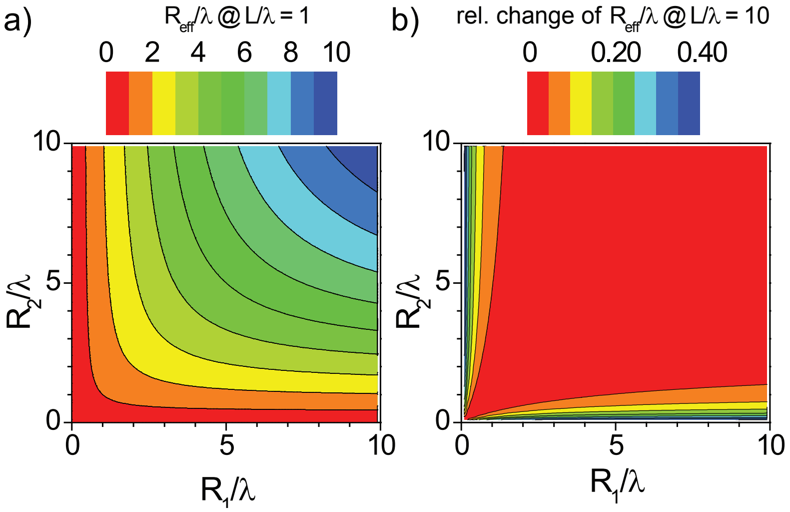

Figure 5.6: Mapping the problem of dissimilar contacts $R_1 \neq R_2$ into the simpler one of identical contacts with a common R_{eff}. (a) 2-dimensional map of equivalent R_{eff}/λ as a function of R_i/λ of the contacts for $L/\lambda = 1$ from Eq. (5.5). (b) Normalized deviation of R_{eff}/λ obtained from Eq. (5.6) relative to the exact result from Eq. (5.5) in the limit of $L/\lambda \gg 1$. The values are normalized using $(R_{\text{eff}}(L/\lambda = 10) - R_{\text{eff}}(L/\lambda = 0))/R_{\text{eff}}(L/\lambda = 10)$.

contact induced spin relaxation and are fitted neglecting the contact induced effects. Fig. 5.7 shows how well the simulated data can be fitted with a Hanle curve for different values of R/λ and L/λ. The curve for $R/\lambda = 0.1$ and $L/\lambda = 3$ shows that even for small R/λ values (corresponding to a contact resistance of $R_C = 100\ \Omega$ when $R_{sq} = 1\ \text{k}\Omega$ and $W = 1\ \mu\text{m}$) we get an excellent fit (although with a reduced τ^{fit} and increased D^{fit}). On the other hand the curve and fit for the combination $R/\lambda = 0.01$ and $L/\lambda = 0.1$ points out that the fit is not describing the curve properly for very small values of the two parameters. This is especially well visible close to $B = 0$ (Fig. 5.7 (b)) where due to the strong contact induced relaxation we observe a distinct drop of R_{nl} which the fit cannot describe. In Figs. 5.3 (c) and (d) of the main text it is visible for which sets of parameters the fits do not describe the Hanle curves well, as those are the points that do not show a smooth line shape when plotting D^{fit} as a function of R/λ or L/λ.

5.6.3 The value of τ^{fit} in the limit $L/\lambda \ll 1$

We can obtain τ^{fit} by performing a standard Hanle fit on simulated data that includes contact induced relaxation. Here we show that we can approximate the value of τ^{fit} for small L using an easy reasoning.

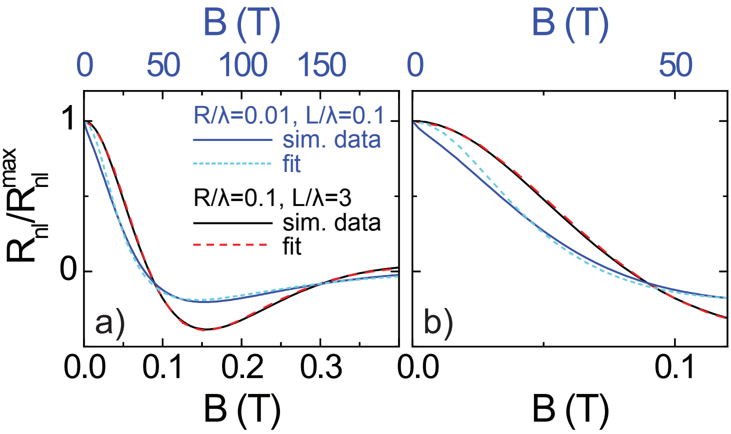

Figure 5.7: Two sets of simulated data with the corresponding fits assuming an amplitude of 1 and a baseline at 0. Both sets were simulated for $D = 0.01\ \mathrm{m}^2/\mathrm{s}$, $\tau = 100\ \mathrm{ps}$ and the values for L/λ and R/λ shown in the legend. Panel (a) shows the full Hanle curve, panel (b) zooms in on the part close to $B = 0$. The B-scale for the curve with the red dashed fit is on the bottom, the scale for the curve with the light blue dotted fit on top.

In the limit $L/\lambda \ll 1$ our system resembles the 3-terminal Hanle geometry [30] as we have two contacts connected to approximately the same point of the transport channel with one of the contacts injecting spins and the other detecting them. At the same time there is the transport channel pointing in two directions away from the injection point. Therefore we get for the spin resistance $1/R^*_{spin} = 1/R_\lambda + 1/R_C$. If we now take the ratio of the spin resistance including the contact resistance (R^*_{spin}) and $R_{spin} = R_\lambda$, which is R^*_{spin} for $R_C \to \infty$, we get

$$\frac{R^*_{spin}}{R_{spin}} = \frac{1/R_{spin}}{1/R^*_{spin}} = \frac{1/R_\lambda}{1/R_\lambda + 1/R_C} = \frac{R/\lambda}{1 + R/\lambda}. \tag{5.7}$$

The spin resistance is proportional to the non-local signal ($R_{spin} \propto R_{nl}$) and for $L = 0$ and $R \to \infty$ the non-local signal is proportional to the spin relaxation length $R_{nl} \propto \lambda$ (see Eq. (5.1)). Therefore we get:

$$\frac{R^*_{spin}}{R_{spin}} = \frac{\lambda^{\mathrm{fit}}}{\lambda} \approx \sqrt{\frac{\tau^{\mathrm{fit}}}{\tau}} \tag{5.8}$$

We can use here for both R^*_{spin} and R_{spin} the relation $R_{nl} \propto \lambda$. This is obviously valid for R_{spin}, and for $R^*_{spin} \propto \lambda^{\mathrm{fit}}$ we have to keep in mind that λ^{fit} is obtained assuming $R \to \infty$ so we have to assume this also here in this analysis.

The relation between the ratio of the spin relaxation lengths and the ratio of the spin relaxation times is valid as $D^{\mathrm{fit}}/D \approx 1$. Hence, we get the result

$$\frac{\tau^{\mathrm{fit}}}{\tau} \approx \left(\frac{R/\lambda}{1+R/\lambda}\right)^2 . \tag{5.9}$$

In the limit $L/\lambda \ll 1$ we therefore expect $\tau^{\mathrm{fit}}/\tau = (0.98, 0.83, 0.25, 8.3 \times 10^{-3}, 9.8 \times 10^{-5})$ for $R/\lambda = (100, 10, 1, 0.1, 0.01)$ in good agreement with the values in Fig. 5.3 (b) in the limit $L/\lambda \ll 1$.

References

[1] S. A. Wolf, A. Y. Chtchelkanova, and D. M. Treger, “Spintronics - A Retrospective and Perspective,” *IBM J. Res. Dev.* **50**, p. 101, 2006.

[2] J. Fabian, A. Matos-Abiague, C. Ertler, P. Stano, and I. Žutić, “Semiconductor Spintronics,” *Acta Phys. Slov.* **57**, pp. 565–907, 2007.

[3] G. Schmidt, D. Ferrand, L. W. Molenkamp, A. T. Filip, and B. J. van Wees, “Fundamental Obstacle for Electrical Spin Injection from a Ferromagnetic Metal into a Diffusive Semiconductor,” *Phys. Rev. B* **62**(8), pp. R4790–R4793, 2000.

[4] E. I. Rashba, “Theory of Electrical Spin Injection: Tunnel Contacts as a Solution of the Conductivity Mismatch Problem,” *Phys. Rev. B* **62**(24), pp. R16267–R16270, 2000.

[5] N. Tombros, C. Józsa, M. Popinciuc, H. T. Jonkman, and B. J. van Wees, “Electronic Spin Transport and Spin Precession in Single Graphene Layers at Room Temperature,” *Nature (London)* **448**, pp. 571–574, 2007.

[6] D. Huertas-Hernando, F. Guinea, and A. Brataas, “Spin Relaxation Times in Disordered Graphene,” *Eur. Phys. J. Spec. Top.* **148**(1), pp. 177–181, 2007.

[7] C. Józsa, T. Maassen, M. Popinciuc, P. J. Zomer, A. Veligura, H. T. Jonkman, and B. J. van Wees, “Linear Scaling between Momentum and Spin Scattering in Graphene,” *Phys. Rev. B* **80**(24), p. 241403(R), 2009.

[8] C. Ertler, S. Konschuh, M. Gmitra, and J. Fabian, “Electron Spin Relaxation in Graphene: The Role of the Substrate,” *Phys. Rev. B* **80**(4), p. 041405, 2009.

[9] A. H. Castro Neto and F. Guinea, “Impurity-Induced Spin-Orbit Coupling in Graphene,” *Phys. Rev. Lett.* **103**(2), p. 026804, 2009.

[10] T.-Y. Yang, J. Balakrishnan, F. Volmer, A. Avsar, M. Jaiswal, J. Samm, S. R. Ali, A. Pachoud, M. Zeng, M. Popinciuc, G. Güntherodt, B. Beschoten, and B. Özyilmaz, “Observation of Long Spin-Relaxation Times in Bilayer Graphene at Room Temperature,” *Phys. Rev. Lett.* **107**(4), p. 047206, 2011.

[11] P. Zhang and M. W. Wu, “Electron Spin Relaxation in Graphene with Random Rashba Field: Comparison of the D’yakonov-Perel’ & Elliott-Yafet-like Mechanisms,” *New J. Phys.* **14**(3), p. 033015, 2012.

[12] H. Ochoa, A. H. Castro Neto, and F. Guinea, “Elliot-Yafet Mechanism in Graphene,” *Phys. Rev. Lett.* **108**, p. 206808, 2012.

[13] K. Pi, W. Han, K. M. McCreary, A. G. Swartz, Y. Li, and R. K. Kawakami, “Manipulation of Spin Transport in Graphene by Surface Chemical Doping,” *Phys. Rev. Lett.* **104**(18), p. 187201, 2010.

[14] T. Maassen, F. K. Dejene, M. H. D. Guimarães, C. Józsa, and B. J. van Wees, “Comparison between Charge and Spin Transport in Few-layer Graphene,” *Phys. Rev. B* **83**(11), p. 115410, 2011.

[15] T. Maassen, J. J. van den Berg, N. IJbema, F. Fromm, T. Seyller, R. Yakimova, and B. J. van Wees, “Long Spin Relaxation Times in Wafer Scale Epitaxial Graphene on SiC(0001),” *Nano Lett.* **12**(3), pp. 1498–1502, 2012.

[16] M. H. D. Guimarães, A. Veligura, P. J. Zomer, T. Maassen, I. J. Vera-Marun, N. Tombros, and B. J. van Wees, “Spin Transport in High-Quality Suspended Graphene Devices,” *Nano Lett.* **12**(7), p. 3512, 2012.

[17] K. M. McCreary, A. G. Swartz, W. Han, J. Fabian, and R. K. Kawakami, “Magnetic Moment Formation in Graphene Detected by Scattering of Pure Spin Currents,” *Phys. Rev. Lett.* **109**, p. 186604, 2012.

[18] P. J. Zomer, M. H. D. Guimarães, N. Tombros, and B. J. van Wees, “Long-Distance Spin Transport in High-mobility Graphene on Hexagonal Boron Nitride,” *Phys. Rev. B* **86**, p. 161416(R), 2012.

[19] M. Popinciuc, C. Józsa, P. J. Zomer, N. Tombros, A. Veligura, H. T. Jonkman, and B. J. van Wees, “Electronic Spin Transport in Graphene Field-Effect Transistors,” *Phys. Rev. B* **80**(21), p. 214427, 2009.

[20] W. Han, K. Pi, K. M. McCreary, Y. Li, J. J. I. Wong, A. G. Swartz, and R. K. Kawakami, “Tunneling Spin Injection into Single Layer Graphene,” *Phys. Rev. Lett.* **105**(16), p. 167202, 2010.

[21] B. Dlubak, P. Seneor, A. Anane, C. Barraud, C. Deranlot, D. Deneuve, B. Servet, R. Mattana, F. Petroff, and A. Fert, "Are Al2O3 and MgO Tunnel Barriers Suitable for Spin Injection in Graphene?," *Appl. Phys. Lett.* **97**(9), p. 092502, 2010.

[22] B. Dlubak, M.-B. Martin, C. Deranlot, B. Servet, S. Xavier, R. Mattana, M. Sprinkle, C. Berger, W. A. De Heer, F. Petroff, A. Anane, P. Seneor, and A. Fert, "Highly Efficient Spin Transport in Epitaxial Graphene on SiC," *Nat. Phys.* **8**, pp. 557–561, 2012.

[23] J. Abel, A. Matsubayashi, T. Murray, C. Dimitrakopoulos, D. B. Farmer, A. Afzali, A. Grill, C. Y. Sung, and V. P. LaBella, "Fabrication of an Electrical Spin Transport Device Utilizing a Diazonium Salt/Hafnium Oxide Interface Layer on Epitaxial Graphene Grown on 6 H-SiC(0001)," *J. Vac. Sci. Technol. B* **30**(4), p. 04E109, 2012.

[24] F. J. Jedema, H. B. Heersche, A. T. Filip, J. J. A. Baselmans, and B. J. van Wees, "Electrical Detection of Spin Precession in a Metallic Mesoscopic Spin Valve," *Nature (London)* **416**, pp. 713–716, 2002.

[25] N. Tombros, S. J. van der Molen, and B. J. van Wees, "Separating Spin and Charge Transport in Single-Wall Carbon Nanotubes," *Phys. Rev. B* **73**, p. 233403, 2006.

[26] S. Takahashi and S. Maekawa, "Spin Injection and Detection in Magnetic Nanostructures," *Phys. Rev. B* **67**(5), p. 052409, 2003.

[27] T. Tanamoto, H. Sugiyama, T. Inokuchi, M. Ishikawa, and Y. Saito, "Effects of Interface Resistance Asymmetry on Local and Non-Local Magnetoresistance Structures," arXiv:1210.1377v1.

[28] M. Johnson and R. H. Silsbee, "Spin-Injection Experiment," *Phys. Rev. B* **37**(10), pp. 5326–5335, 1988.

[29] F. J. Jedema, M. V. Costache, H. B. Heersche, J. J. A. Baselmans, and B. J. van Wees, "Electrical Detection of Spin Accumulation and Spin Precession at Room Temperature in Metallic Spin Valves," *Appl. Phys. Lett.* **81**(27), pp. 5162–5164, 2002.

[30] S. P. Dash, S. Sharma, R. S. Patel, M. P. de Jong, and R. Jansen, "Electrical Creation of Spin Polarization in Silicon at Room Temperature," *Nature (London)* **462**(7272), pp. 491–494, 2009.

[31] B. Birkner, D. Pachniowski, A. Sandner, M. Ostler, T. Seyller, J. Fabian, M. Ciorga, D. Weiss, and J. Eroms, "Annealing-induced Magnetic Moments Detected by Spin Precession Measurements in Epitaxial Graphene on SiC," *Phys. Rev. B* **87**, p. 081405, 2013.

[32] M. Wojtaszek, I. J. Vera-Marun, T. Maassen, and B. J. van Wees, "Enhancement of Spin Relaxation Time in Hydrogenated Graphene Spin Valve Devices," *Phys. Rev. B* **87**, p. 081402(R), 2013.

[33] T. Suzuki, T. Sasaki, T. Oikawa, M. Shiraishi, Y. Suzuki, and K. Noguchi, "Room-Temperature Electron Spin Transport in a Highly Doped Si Channel," *Appl. Phys. Express* **4**(2), p. 023003, 2011.

[34] S. Sharma, A. Spiesser, S. P. Dash, S. Iba, S. Watanabe, B. J. van Wees, H. Saito, S. Yuasa, and R. Jansen, "Anomalous Scaling of Spin Accumulation in Ferromagnetic Tunnel Devices with Silicon and Germanium," arXiv:1211.4460v1.

[35] O. Txoperena, M. Gobbi, A. Bedoya-Pinto, F. Golmar, X. Sun, L. E. Hueso, and F. Casanova, "How Reliable are Hanle Measurements in Metals in a Three-Terminal Geometry?," arXiv:1211.7273v1.

[36] N. Tombros, S. Tanabe, A. Veligura, C. Józsa, M. Popinciuc, H. T. Jonkman, and B. J. van Wees, "Anisotropic Spin Relaxation in Graphene," *Phys. Rev. Lett.* **101**(4), p. 046601, 2008.

[37] G. Salis, A. Fuhrer, R. R. Schlittler, L. Gross, and S. F. Alvarado, "Temperature Dependence of the Nonlocal Voltage in an Fe/GaAs Electrical Spin-Injection Device," *Phys. Rev. B* **81**, p. 205323, 2010.

[38] I. J. Vera-Marun, V. Ranjan, and B. J. van Wees, "Nonlinear Detection of Spin Currents in Graphene with Non-Magnetic Electrodes," *Nat. Phys.* **8**(4), pp. 313–316, 2012.

[39] T. Maassen, J. J. van den Berg, E. H. Huisman, H. Dijkstra, F. Fromm, T. Seyller, and B. J. van Wees, "Localized States Influence Spin Transport in Epitaxial Graphene," *Phys. Rev. Lett.* **110**, p. 067209, 2013.

[40] W. Han and R. K. Kawakami, "Spin Relaxation in Single-Layer and Bilayer Graphene," *Phys. Rev. Lett.* **107**(4), p. 047207, 2011.

[41] H. Jaffrès, J.-M. George, and A. Fert, "Spin Transport in Multiterminal Devices: Large Spin Signals in Devices with Confined Geometry," *Phys. Rev. B* **82**, p. 140408, 2010.

Chapter 6

Linear scaling between momentum and spin scattering in graphene

Abstract

Spin transport in graphene carries the potential of a long spin diffusion length at room temperature. However, extrinsic relaxation processes limit the current experimental values to 1–2 μm. *We present Hanle spin precession measurements in gated lateral spin valve devices in the low to high (up to* 10^{13} cm^{-2}*) carrier density range of graphene. A linear scaling between the spin diffusion length and the diffusion coefficient is observed. We measure nearly identical spin and charge diffusion coefficients indicating that electron-electron interactions are relatively weak and transport is limited by impurity potential scattering. When extrapolated to the maximum carrier mobilities of* 2×10^5 cm^2/Vs*, our results predict that a considerable increase in the spin diffusion length should be possible.*

Published as:
C. Józsa, T. Maassen, M. Popinciuc, P. J. Zomer, A. Veligura,
H. T. Jonkman, and B. J. van Wees,
Phys. Rev. B **80**, 241403(R) (2009).

6.1 Introduction

The high charge carrier mobility [1–3] and spin diffusion length of micrometers [4, 5] measured at room temperature make graphene a possible candidate for future electronic and spintronic devices. This two-dimensional crystalline material has two electronic conduction regimes, metallic where charge carriers are of one type (holes or electrons) and the region around the Dirac neutrality point where transport of electric current happens through small regions charged locally with holes or electrons (“electron-hole puddles”). The presence of such puddles yielding a finite local density $|n| \approx 10^{11}\ \mathrm{cm}^{-2}$ was shown experimentally using scanning single electron transistor technique [6] and scanning electron spectroscopy [7, 8], the intensity of the fluctuations being strongly enhanced by substrate impurities [3].

Experiments done so far on spin transport reveal room temperature spin relaxation times of the order of 100 to $200\ \mathrm{ps}$ [4]. This is well below the theoretically predicted, intrinsic limit [9–14] but might be explained if we consider extrinsic effects [15]. Since hyperfine interactions at $300\ \mathrm{K}$ are weak in graphitic systems, there are two possible mechanisms that can be held responsible for such a strong spin relaxation [16], scaling differently on the momentum relaxation. In case of the Elliott-Yafet mechanism (spin flip occurs with a finite probability at each momentum scattering center) the spin scattering time τ is proportional to τ_p, the momentum scattering time, while the D’yakonov-Perel’ mechanism (spins precess under the influence of local spin-orbit fields in between scattering events) is characterized by $\tau \propto \tau_p^{-1}$. To identify the scattering mechanism and find the ultimate limit on spin relaxation, one can thus investigate the link between spin transport and the electronic quality of the graphene, in particular the charge carrier mobility. Since the mobility is ill-defined at or in the vicinity of the Dirac neutrality point, we will use the diffusion coefficient defined as $D = \frac{1}{2} v_F l$ and link it to the spin diffusion length $\lambda = \sqrt{D\tau}$. Here v_F is the Fermi velocity and l represents the scattering mean free path.

One way to study charge against spin diffusion would be comparing the results in a set of devices that display significantly different carrier mobilities. However, it is experimentally challenging to fabricate consistently good ferromagnetic contacts to the graphene for such a set of samples. The option we choose here is to do the experiments on individual devices tuning the carrier density from the metallic regime down to the lowest values and comparing the behavior of the spin transport to the changes in the charge diffusion coefficient.

In this chapter we present a systematic study of the spin transport and scattering at room temperature in single layer graphene samples on SiO_2 substrate. The measurements are done at a wide range of carrier densities with an accent on the Dirac neutrality point where the transport is difficult to model and Coulomb electron-electron interactions are expected to be the strongest [17, 18]. We compare this directly to the charge transport in the same samples to learn more about the diffusion phenomena and the interactions that lead to spin relaxation.

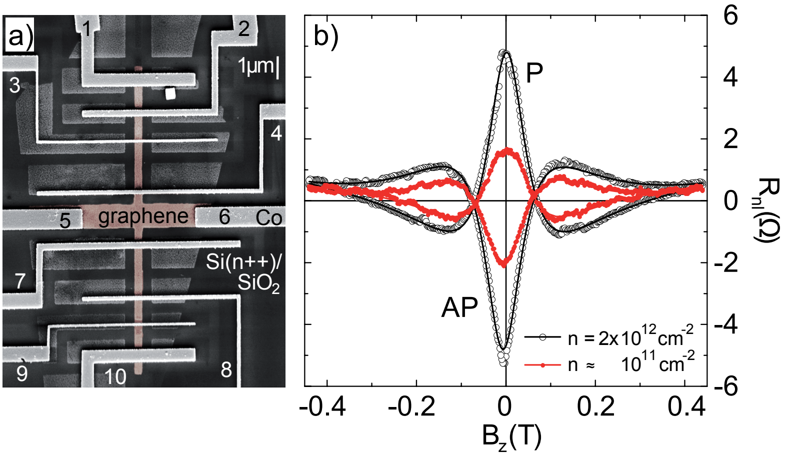

Figure 6.1: (a) SEM image of a spin valve device. A $0.3 \times 13\ \mu\mathrm{m}$ strip with a cross shape in the middle (brown/light gray) was etched with oxygen plasma out of the original graphene flake (dark gray). The Co electrodes 1–10 of widths 90 to $800\ \mathrm{nm}$ and spacings 1.1 to $2.2\ \mu\mathrm{m}$ are also visible. (b) Hanle precession measurements (dots) and fits (solid lines) at the Dirac neutrality point and in the metallic regime, with the injector/detector magnetization aligned parallel(P) and antiparallel (AP).

6.2 Energy broadening of the density of states

The charge carrier transport in graphene in the metallic regime (at an energy E sufficiently far away from the Dirac neutrality point) can be described by a diffusion process characterized by the 2-dimensional charge diffusion coefficient D. The density of states (DOS) is given by [19]

$$\nu(E) = \frac{g_s g_v}{2\pi} \frac{|E|}{\hbar^2 v_F^2} \tag{6.1}$$

with the twofold valley ($g_v = 2$) and spin ($g_s = 2$) degeneracies and the Fermi velocity $v_F \approx 10^6\ \mathrm{ms}^{-1}$. By integration we can obtain the charge carrier density $n(E_F) = g_v g_s E_F^2/(4\pi\hbar^2 v_F^2)$ with E_F the Fermi energy, and the Einstein relation $\sigma = e^2 \nu D$ allows for calculating the charge diffusion coefficient

$$D = \frac{1}{R_{sq} e^2 \nu} = \frac{\hbar v_F}{R_{sq} e^2} \sqrt{\frac{\pi}{g_v g_s}} \frac{1}{\sqrt{n}}. \tag{6.2}$$

Here e is the electron charge and R_{sq} is the square resistance of the graphene layer, inverse of the conductivity σ. Finally, using the semiclassical Drude formula one can calculate the carrier mobility $\mu = (R_{sq} n e)^{-1}$ for the metallic regime.

In order to determine the charge and spin diffusion coefficients experimentally we have fabricated field effect devices where the single layer graphene flake is contacted by several ferromagnetic cobalt electrodes. A scanning electron microscope (SEM) image of such a device is shown in Fig. 6.1 (a). The graphene flakes are obtained by mechanical exfoliation from commercially available Kish graphite and deposited on a thermally oxidized, n++ doped Si substrate ($300\ \mathrm{nm}$ thick oxide layer). The Si substrate contacted by a bottom Au electrode is used as electrostatic gate; applying a voltage V_g of typically tens of volts on it allows reaching carrier densities in the graphene $|n| \leq 10^{13}\ \mathrm{cm}^{-2}$ (electrons or holes) calculated from the capacitance [20]. A set of predefined Ti/Au markers help to accurately locate selected graphene flakes through optical- and atomic force microscope. The flakes are then etched with oxygen plasma into a cross shape, to allow for precise Hall type measurements using side contacts, e.g., the ones labeled 5 and 6 on Fig. 6.1 (a) as current injectors and contacts 4 and 7 as Hall voltage probes. The electrical contacts are patterned using electron beam lithography and evaporated thermally at a base pressure of $\sim 10^{-6}\ \mathrm{mbar}$ followed by standard lift-off technique. To achieve a high spin injection efficiency [21] a 0.8 nm thick Al_2O_3 insulating layer was introduced between the graphene and the ferromagnet, resulting in contact resistances of the order 20–$40\ \mathrm{k}\Omega$.

The graphene's square resistance R_{sq} is determined from 4-probe local measurements. Sending an electric current from, e.g., contact 1 to 4 and measuring the voltage drop between 2 and 3 we are sensitive only to the resistance of the graphene between contacts 2 and 3. Measuring the resistance against the applied gate voltage (i.e., in function of carrier density) and normalizing it to the graphene length to width ratio yields the R_{sq} curve plotted on Fig. 6.2 (a). From such measurements we calculate the charge diffusion coefficient D_C in the metallic regime using Eq. (6.2), see the solid line on Fig. 6.2 (c). The decrease of carrier density comes with a decrease in the diffusion coefficient; the singularities in the calculated D_C at the charge neutrality point will be discussed later. The asymmetry in the electron versus hole diffusion at high densities visible in panel (c) probably originates from nonuniformities in the carrier density and can be traced back to the R_{sq} measurement in panel (a). Measurements of the Hall coefficient R_H (not shown) against the gate voltage using the cross contact geometry indicate the onset of the metallic regime at a carrier density $n \simeq \pm 0.5 \times 10^{12}\ \mathrm{cm}^{-2}$ by displaying a clear $1/n$ dependence. The density value extracted from the Hall measurements in the metallic regime confirms the number calculated from the square resistance measurements and gate capacitance.

6.3 Spin transport measurements

The spin transport measurements are performed in the non-local geometry [4]: a spin-polarized current is injected, e.g., through electrode 4 and extracted through

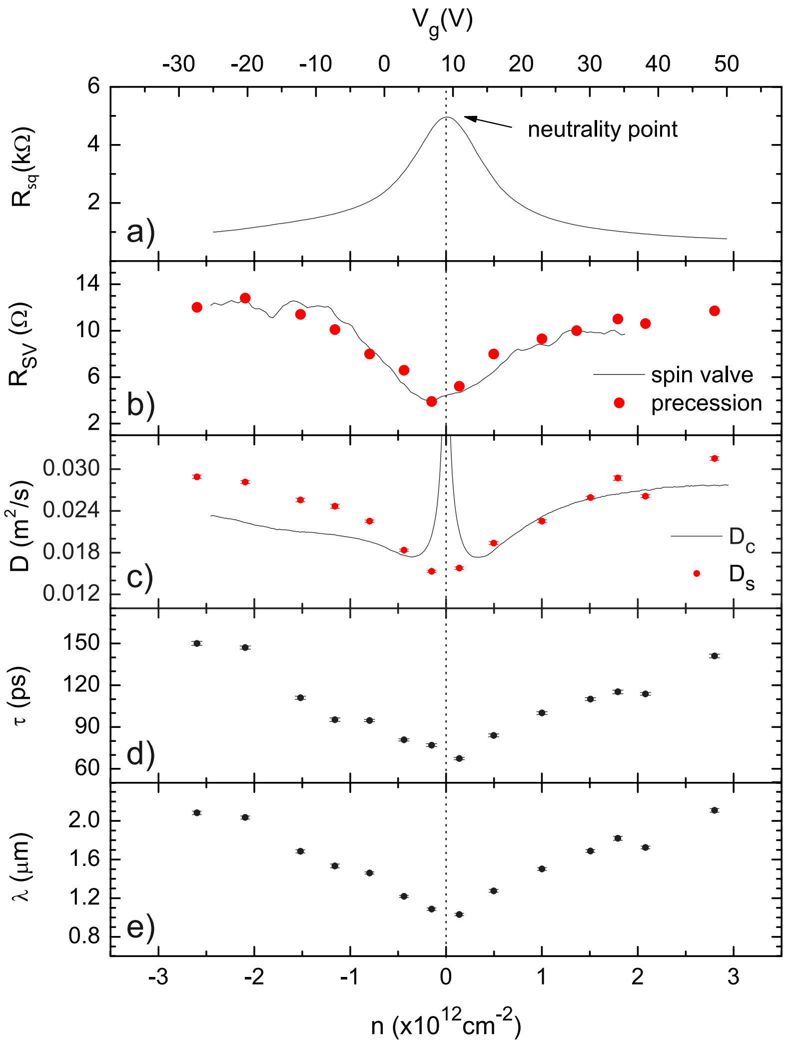

Figure 6.2: Charge- and spin transport parameters plotted against charge carrier density and gate voltage. (a) Square resistance; (b) Non-local spin valve signal determined from spin valve- and from Hanle precession measurements; (c) Charge- and spin diffusion coefficients; (d) Spin relaxation time; (e) Spin relaxation length.

electrode 10, while we measure the voltage between electrodes 2 and 1. There is no charge current flowing between 2 and 1; the detected non-local signal R_{nl} in an in-plane magnetic field is purely due to the effect of spins diffusing from the injector electrodes to the detectors. Subtracting R_{nl} at parallel and antiparallel magnetic orientation of the injector/detector electrodes while scanning the gate voltage gives the spin valve signal R_{SV} that has a significant dependence on the charge carrier density as plotted in Fig. 6.2 (b), solid line. The electrodes 1 and 10 are far enough not to contribute significantly to R_{SV}, therefore we define $L = 3.1\ \mu\mathrm{m}$ as the distance between the two inner electrodes.

Applying a magnetic field B_z orthogonal to the sample plane will result in Hanle spin precession. Measuring R_{nl} while we sweep the magnetic field (i.e., we change the precession frequency) yields the curves in fig. 6.1b). Here two measurements are plotted for the metallic regime, $V_g = +40\ \mathrm{V}$ ($n \simeq -2 \times 10^{12}\ \mathrm{cm}^{-2}$), and two for the Dirac neutrality point, $V_g = +9\ \mathrm{V}$, with the central injector/detector electrodes oriented parallel and antiparallel, respectively. The parallel-antiparallel signal difference at zero field is the same as the spin valve signal defined above and is plotted for different densities in Fig. 6.2 (b), dots. The advantage of a spin precession measurement is that it allows extracting the spin diffusion coefficient D_S and spin scattering time τ by fitting the measurements with the solutions to the Bloch equation [16] for spin accumulation $\vec{\mu_S}$:

$$D_S \nabla^2 \vec{\mu_S} - \frac{\vec{\mu_S}}{\tau} + \frac{g\mu_B}{\hbar} \vec{B} \times \vec{\mu_S} = 0 \tag{6.3}$$

where the first term on the left hand side describes the spin diffusion, the second term the spin relaxation and the last one the precession, with an effective Landé factor $g = 2$ and the Bohr magneton μ_B.

A set of precession measurements was done for different charge carrier densities; the resulting spin transport parameters D_S and τ are plotted in Fig. 6.2 (c) and (d). The spin diffusion length $\lambda = \sqrt{D_S \tau}$ is shown in panel (e).

Examining Fig. 6.2, we see that D_S, τ, and λ all decrease approximately by a factor of 2 when we approach the neutrality point. This results in a strong decrease of the detected spin valve signal as seen in Fig. 6.2 (b), consistent with the prediction of the formula for a four-terminal non-local spin injection geometry [22]:

$$R_{SV} = \frac{P^2 R_{sq} \lambda}{W} \exp(-L/\lambda), \tag{6.4}$$

where $W = 300\ \mathrm{nm}$ is the width of the graphene flake. The spin polarization of the injected current determined from this relation is $P \simeq 9\%$. Note that this value can be considered constant through the range of carrier densities we used, since the contact resistances span from 20 to 40 kΩ where impedance mismatch is suppressed.[1]

---

[1] We have considered the spin injection model for transparent contacts from Ref. [21] that corrects Eq. (6.4) addressing the impedance mismatch. The influence of the correction on the injection efficiency is below 10%.

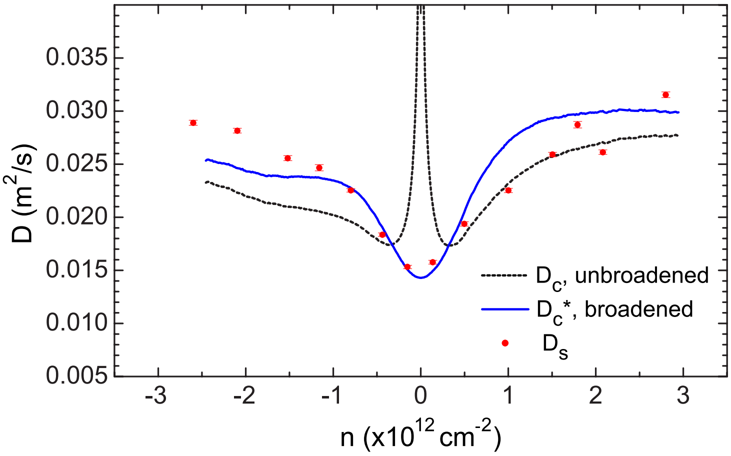

Figure 6.3: Spin vs charge diffusion coefficient with the unbroadened DOS from Eq. (6.1) and the broadened version from Eq. (6.5) using a Gaussian broadening of $\mathrm{FWHM} \simeq 176\ \mathrm{meV}$.

6.4 Discussion

Let us focus now on the diffusion of charge versus spin. As visible in Fig. 6.2 (c), in the high density case the values are practically identical for spin and charge. This is a striking observation, since the two physical entities, D_C and D_S, are determined from completely different types of experiments.

However, for $|n| < 0.5 \times 10^{12}\ \mathrm{cm}^{-2}$ equation 6.1 yields unphysical values for the diffusion coefficient and results in a singularity at the Dirac neutrality point. This comes from the unrealistic assumption of vanishing carrier density and DOS. To correct for it, one has to account for a broadened density of states $\nu^*(E)$ due to finite temperature, electron-hole puddles and possibly to the finite lifetime of electronic states. The simplest way to include all broadening effects in the DOS is to add a Gaussian broadening energy σ_b in the form of

$$\nu^*(E) = \frac{1}{\sqrt{2\pi}\sigma_b} \int_{-\infty}^{\infty} \exp\left(-\frac{(\epsilon - E)^2}{2\sigma_b^2}\right) \nu(\epsilon) d\epsilon. \tag{6.5}$$

After integration we obtain

$$\nu^*(E) = \frac{g_v g_s}{2\pi\hbar^2 v_F^2} \left[\frac{2\sigma_b}{\sqrt{2\pi}} \exp\left(-\frac{E^2}{2\sigma_b^2}\right) + E\ \mathrm{erf}\left(\frac{E}{\sigma_b\sqrt{2}}\right)\right]$$

where erf is the Gaussian error function and the only undetermined parameter is the value of σ_b. Replacing the DOS with the broadened version in Eq. (6.2) we plot

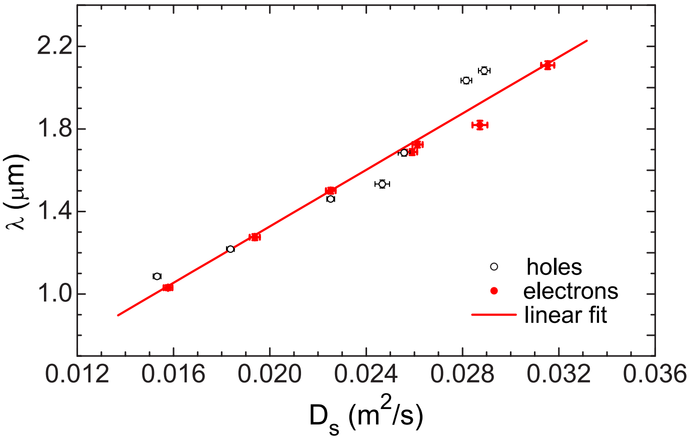

Figure 6.4: Linear relationship between the spin relaxation length and the spin diffusion coefficient, extracted from Fig. 6.2 panels (c) and (e).

the modified diffusion coefficient D_C^* in function of the density together with the unmodified charge and spin diffusion coefficients, see Fig. 6.3. We find good correspondence between D_C^* and D_S both at low and high densities if and only if we choose an energy broadening of $\sigma_b \simeq 75$ meV,[2] i.e., a Gaussian with FWHM $= 2\sqrt{2\ln 2}\sigma_b \simeq 176$ meV corresponding to a density variation of $\Delta n \simeq \pm 0.7 \times 10^{12}$ cm^{-2}. This is consistent with the literature values [7] attributed to electron-hole puddles in graphene on SiO$_2$, considering that our samples show a carrier mobility of only 3000 cm^2/Vs [23].

The observation that the spin diffusion coefficient shows no considerable difference from the charge diffusion coefficient indicates a minor role of Coulomb electron-electron interactions [24]. This is in agreement with the recent results of Li *et al.* [25] where electron-electron interactions are detected in high carrier mobility, suspended graphene flakes only. The major mechanism for limiting the (spin) diffusion seems to be the impurity potential scattering.

The most convincing argument comes, however, from the scaling between (spin or charge) diffusion coefficient and spin diffusion length. Plotting the values of λ against D_S as extracted from Fig. 6.2 shows a clear linear dependence for both the electron and the hole conduction regime, see Fig. 6.4. Since $\lambda = \sqrt{D\tau}$, the linear dependence means that the spin scattering time is directly proportional to the diffusion coefficient, i.e., to the momentum scattering time τ_p. The experiments confirm thus

---

[2] The value of σ_b is chosen to cure the singularity at $n \approx 0$ by fitting the broadened D_C^* to D_S for densities $|n| < 0.5 \times 10^{12}$ cm^{-2}. At $|n| \gtrsim 3 \times 10^{12}$ cm^{-2} the broadened curve approaches the unbroadened one determined from the measurements.

an Elliott-Yafet type spin relaxation mechanism,[3] in agreement with our earlier spin relaxation anisotropy studies presented in Ref. [26].

6.5 Conclusions

In conclusion, we expect that improving the electronic characteristics of the graphene flake by, e.g., removing the substrate (suspended graphene), annealing with high electric currents and/or using selected starting material (higher purity graphite) shall both enhance the charge transport and prolong the spin scattering time. Assuming the Elliott-Yafet mechanism is still dominating at high carrier mobilities we can extrapolate the behavior shown in Fig. 6.4 to samples displaying charge carrier mobilities in the range of 2×10^5 $\mathrm{cm}^2/\mathrm{Vs}$ reported recently, to predict a possible room temperature spin diffusion length up to 100 μm.[4]

Note added. For a discussion of the spin relaxation mechanisms in graphene see Chapter 10.

---

[3] This interpretation is as published in Phys. Rev. B **80**, 241403(R) (2009). It is not fully correct, as the relation between the spin relaxation time and the momentum scattering time for the Elliott-Yafet mechanism is $\tau_{\mathrm{EY}} = E_F^2 \tau_p / \Delta_{\mathrm{EY}}^2$, with the effective spin-orbit coupling Δ_{EY}, and the different points in Fig. 6.4 are obtained at different E_F. See Chapter 10, Section 10.2 for a discussion of this issue.

[4] In metals it is known that the ratio between spin and momentum relaxation is approximately the same for scattering induced by impurities or electron-phonon interactions. We assume that this is also the case in graphene.

References

[1] K. Bolotin, K. Sikes, Z. Jiang, M. Klima, G. Fudenberg, J. Hone, P. Kim, and H. Stormer, "Ultrahigh Electron Mobility in Suspended Graphene," *Solid State Commun.* **146**(9-10), pp. 351–355, 2008.

[2] S. V. Morozov, K. S. Novoselov, M. I. Katsnelson, F. Schedin, D. C. Elias, J. A. Jaszczak, and A. K. Geim, "Giant Intrinsic Carrier Mobilities in Graphene and Its Bilayer," *Phys. Rev. Lett.* **100**, p. 016602, 2008.

[3] X. Du, I. Skachko, A. Barker, and E. Y. Andrei, "Approaching Ballistic Transport in Suspended Graphene," *Nat. Nanotechnol.* **3**, pp. 491–495, 2008.

[4] N. Tombros, C. Józsa, M. Popinciuc, H. T. Jonkman, and B. J. van Wees, "Electronic Spin Transport and Spin Precession in Single Graphene Layers at Room Temperature," *Nature (London)* **448**, pp. 571–574, 2007.

[5] W. H. Wang, K. Pi, Y. Li, Y. F. Chiang, P. Wei, J. Shi, and R. K. Kawakami, "Magnetotransport Properties of Mesoscopic Graphite Spin Valves," *Phys. Rev. B* **77**(2), p. 020402, 2008.

[6] J. Martin, N. Akerman, G. Ulbricht, T. Lohmann, J. H. Smet, K. von Klitzing, and A. Yacoby, "Observation of Electron-Hole Puddles in Graphene Using a Scanning Single-Electron Transistor," *Nat. Phys.* **4**, pp. 144–148, 2008.

[7] A. Deshpande, W. Bao, F. Miao, C. N. Lau, and B. J. LeRoy, "Spatially resolved spectroscopy of monolayer graphene on sio_2," *Phys. Rev. B* **79**, p. 205411, 2009.

[8] Y. Zhang, V. W. Brar, C. Girit, A. Zettl, and M. F. Crommie, "Origin of Spatial Charge Inhomogeneity in Graphene," *Nat. Phys.* **5**(10), pp. 722–726, 2009.

[9] C. L. Kane and E. J. Mele, "Quantum Spin Hall Effect in Graphene," *Phys. Rev. Lett.* **95**, p. 226801, 2005.

[10] H. Min, J. E. Hill, N. A. Sinitsyn, B. R. Sahu, L. Kleinman, and A. H. MacDonald, "Intrinsic and Rashba Spin-Orbit Interactions in Graphene Sheets," *Phys. Rev. B* **74**, p. 165310, 2006.

[11] D. Huertas-Hernando, F. Guinea, and A. Brataas, "Spin-Orbit Coupling in Curved Graphene, Fullerenes, Nanotubes, and Nanotube Caps," *Phys. Rev. B* **74**(15), p. 155426, 2006.

[12] Y. Yao, F. Ye, X.-L. Qi, S.-C. Zhang, and Z. Fang, "Spin-Orbit Gap of Graphene: First-Principles Calculations," *Phys. Rev. B* **75**, p. 041401, 2007.

[13] D. Huertas-Hernando, F. Guinea, and A. Brataas, "Spin-Orbit-Mediated Spin Relaxation in Graphene," *Phys. Rev. Lett.* **103**(14), p. 146801, 2009.

[14] M. Gmitra, S. Konschuh, C. Ertler, C. Ambrosch-Draxl, and J. Fabian, "Band-Structure Topologies of Graphene: Spin-Orbit Coupling Effects from First Principles," *Phys. Rev. B* **80**(23), p. 235431, 2009.

[15] A. H. Castro Neto and F. Guinea, "Impurity-Induced Spin-Orbit Coupling in Graphene," *Phys. Rev. Lett.* **103**(2), p. 026804, 2009.

[16] J. Fabian, A. Matos-Abiague, C. Ertler, P. Stano, and I. Žutić, "Semiconductor Spintronics," *Acta Phys. Slov.* **57**, pp. 565–907, 2007.

[17] Y. Barlas, T. Pereg-Barnea, M. Polini, R. Asgari, and A. H. MacDonald, "Chirality and Correlations in Graphene," *Phys. Rev. Lett.* **98**, p. 236601, 2007.

[18] E. H. Hwang, B. Y.-K. Hu, and S. Das Sarma, "Density Dependent Exchange Contribution to $\partial\mu/\partial n$ and Compressibility in Graphene," *Phys. Rev. Lett.* **99**, p. 226801, 2007.

[19] T. Ando, "Screening Effect and Impurity Scattering in Monolayer Graphene," *J. Phys. Soc. Jpn.* **75**(7), p. 074716, 2006.

[20] A. K. Geim and K. S. Novoselov, "The Rise of Graphene," *Nat. Mater.* **6**, pp. 183–191, 2007.

[21] M. Popinciuc, C. Józsa, P. J. Zomer, N. Tombros, A. Veligura, H. T. Jonkman, and B. J. van Wees, "Electronic Spin Transport in Graphene Field-Effect Transistors," *Phys. Rev. B* **80**(21), p. 214427, 2009.

[22] F. J. Jedema, H. B. Heersche, A. T. Filip, J. J. A. Baselmans, and B. J. van Wees, "Electrical Detection of Spin Precession in a Metallic Mesoscopic Spin Valve," *Nature (London)* **416**, pp. 713–716, 2002.

[23] C. Józsa, M. Popinciuc, N. Tombros, H. T. Jonkman, and B. J. van Wees, "Electronic Spin Drift in

Graphene Field-Effect Transistors," *Phys. Rev. Lett.* **100**(23), p. 236603, 2008.

[24] C. P. Weber, N. Gedik, J. E. Moore, J. Orenstein, J. Stephens, and D. D. Awschalom, "Observation of Spin Coulomb Drag in a Two-Dimensional Electron Gas," *Nature (London)* **437**, pp. 1330–1333, 2005.

[25] G. Li, A. Luican, and E. Y. Andrei, "Scanning Tunneling Spectroscopy of Graphene on Graphite," *Phys. Rev. Lett.* **102**, p. 176804, 2009.

[26] N. Tombros, S. Tanabe, A. Veligura, C. Józsa, M. Popinciuc, H. T. Jonkman, and B. J. van Wees, "Anisotropic Spin Relaxation in Graphene," *Phys. Rev. Lett.* **101**(4), p. 046601, 2008.

Chapter 7

Comparison between charge and spin transport in few-layer graphene

Abstract

Transport measurements on few-layer graphene (FLG) are important because they interpolate between the properties of single layer graphene (SLG) as a true 2-dimensional material and the 3-dimensional bulk properties of graphite. In this article we present 4-probe local charge transport and non-local spin valve and spin precession measurements on lateral spin field-effect transistors (FET) on FLG. We study systematically the charge and spin transport properties depending on the number of layers and the electrical back gating of the device. We explain the charge transport measurements by taking the screening of scattering potentials into account and use the results to understand the spin data. The measured samples are between 3 and 20 layers thick, and we include in our analysis our earlier results of the measurements on SLG for comparison. In our room temperature spin transport measurements we manage to observe spin signals over distances up to $10\ \mu\mathrm{m}$ *and measure enhanced spin-relaxation times with an increasing number of layers, reaching* $\tau \sim 500$ ps *as a maximum, about* 4 *times higher than in SLG. The increase of* τ *can result from the screening of scattering potentials due to additional intrinsic charge carriers in FLG. We calculate the density of states (DOS) of FLG using a zone-folding scheme to determine the charge diffusion coefficient* D_C *from the square resistance* R_{sq}*. The resulting* D_C *and the spin-diffusion coefficient* D_S *show similar values and depend only weakly on the number of layers and gate induced charge carriers. We discuss the implications of this on the identification of the spin-relaxation mechanism.*

Published as:
T. Maassen, F. K. Dejene, M. H. D. Guimarães, C. Józsa, and B. J. van Wees,
Phys. Rev. B **83**, 115410 (2011).

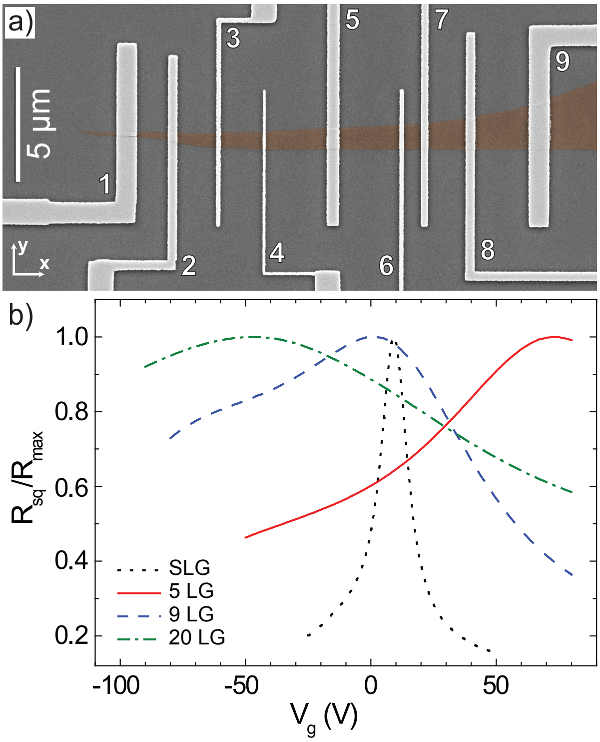

Figure 7.1: (a) SEM image of a typical spin valve device. A 20-layer graphene flake contacted with several parallel ferromagnetic cobalt electrodes (light gray). (b) Normalized square resistance vs gate voltage for 1, 5, 9, and 20 layers.

7.1 Introduction

The electronic properties of exfoliated graphene have been studied in great detail [1, 2], while the electron spin transport still brings up questions. The experimental spin-relaxation length $\lambda \sim 2\ \mu\mathrm{m}$ in single layer graphene (SLG) at room temperature is already promising [3–6] but is still at least one order of magnitude below theoretical predictions [7, 8]. As the spin-relaxation is believed to be caused mainly by extrinsic scatterers in the substrate and on the surface of the graphene flake [4, 5], reducing the effect of these scatterers should lead to an improvement of the electronic transport [9] and an increase in λ.

One way to avoid scatterers is separating the graphene flake from the substrate using suspended graphene, resulting in an increased charge carrier mobility μ [10–12]. Another way to enhance the transport properties is to screen the scattering potentials using few-layer graphene (FLG). In a stack of graphene layers, electrical potentials are screened by the outer layers with a screening length of about 1 to 5 layers [13, 14], depending on the stacking order [14]. This reduces the effect of external scatterers, resulting in only weakly influenced inner layers. The effect of screening of the gate induced charge carriers on the electrical transport in FLG has been observed in several groups' transport measurements [15, 16]. While the spin transport in FLG was examined earlier, [17–22], there are no publications on the influence of screening on the spin transport properties. The influence of gate induced charge carriers on the spin signal is presented in Ref. [19] while the effect of those charges on the spin-relaxation length still needs to be investigated. Along with studying the possible enhancement in spin transport using FLG, this investigation will also help with understanding the effect of possible multilayer inclusions in large scale graphene samples in future spintronic devices.

This chapter is organized as follows. In Section 7.2 we describe the selection and preparation of FLG samples. In Section 7.3 the charge transport properties of FLG are presented. We measure the dependence of the resistance on the number of layers and the gate induced charge carriers and explain the results considering electrical screening and a non-uniform background doping of the flake. At the end of the section we calculate the density of states (DOS) of FLG using a zone-folding scheme. In Section 7.4 we discuss the spin transport properties of FLG as a function of the gate voltage (V_g), compare the results with SLG, and show the evolution of the spin transport quantities as a function of the number of layers. Finally, we compare the spin and charge transport and discuss the dominant spin-relaxation mechanism in our devices before giving our conclusions in Section 7.5.

7.2 Sample fabrication

The presented measurements were performed at room temperature (RT) on mechanically exfoliated FLG flakes from highly oriented pyrolytic graphite (HOPG, from Advanced Ceramics, AB stacking) on a Si/SiO$_2$ substrate with an oxide thickness of 300 nm. We determine the thickness of the flakes using an atomic force microscope in tapping mode (TAFM). The measured thickness t gives the number of layers by rounding down the quotient of t and the spacing between two adjacent graphene layers $d_{SL} = 0.335$ nm (corresponding to the thickness of SLG), therefore the number of layers is $\lfloor t/d_{SL} \rfloor$. Due to the imprecise nature of the thickness measurements obtained with TAFM [23] and due to the comparison between different thickness measurements on the same sample, we estimate an error in the number of layers for the FLG samples of about 1 layer. Fig. 7.1 (a) shows a scanning electron microscope (SEM) picture of a typical sample. The illustrated 20-layer FLG flake is contacted with several parallel aligned ferromagnetic cobalt electrodes obtained with electron beam lithography, e-beam evaporation of Co, and a standard lift-off technique. To

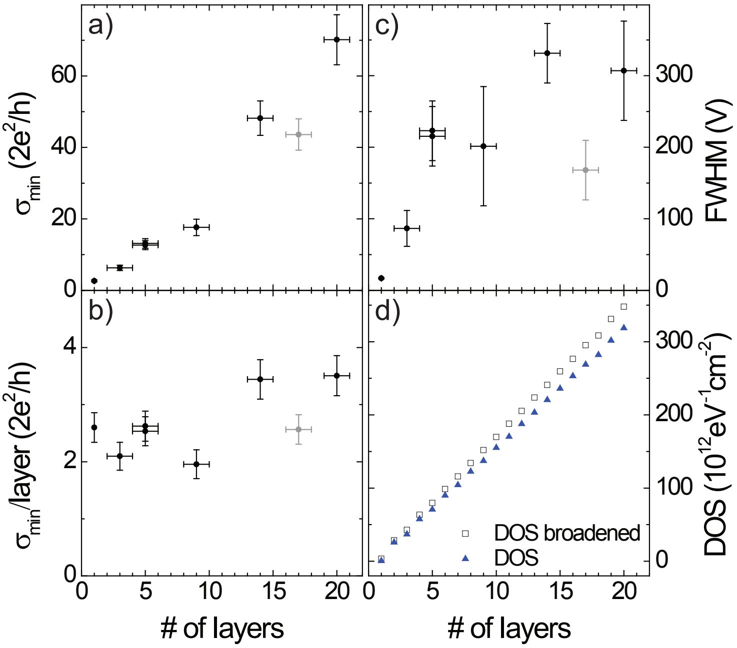

Figure 7.2: (a) The minimum conductivity, (b) the minimum conductivity per layer, and (c) the full width half maximum (FWHM) of the peak shaped resistance curves as a function of the number of layers. The gray points belong to a sample that showed overall unusual behavior.[1] (d) The DOS at $n_g = 0$ as a function of the number of layers. The blue triangles show the calculated values using a zone-folding scheme, and the open black squares show the values including an energy broadening of $\mathrm{FWHM} \approx 60\ \mathrm{meV}$.

avoid the conductivity mismatch and enhance the spin signal, we cover the graphene flake with an $0.8\ \mathrm{nm}$ thick insulating oxidized aluminum layer prior to the Co deposition, reaching contact resistances above $R_C = 2\ \mathrm{k\Omega}$. These contact resistances are larger than typical FLG resistances on a length scale of the spin-relaxation length λ, achieving in almost all cases non-invasive contacts [4, 24]. The highly doped Si-substrate is contacted by an Au electrode for the electric gating of the device and controlling the amount of induced charge carriers n_g in the system. The processing is given in detail in Ref. [4].

7.3 Charge transport

The samples are first characterized by measuring the V_g dependence of the square resistance R_{sq} of the FLG flake using local 4-probe geometry. Fig. 7.1 (b) shows three typical measurements on FLG and one measurement on SLG. All curves show a maximum resistance (minimum conductivity $\sigma_{\min}$) at the respective $V_g = V_0$, marking the state where the Fermi energy E_F coincides with the lowest DOS. $V_g = V_0$ is therefore the gate voltage with the lowest amount of induced charge carriers, corresponding to $n_g = 0$. For our samples we get $n_g = \alpha_C(V_g - V_0)$ with $\alpha_C = 7.2 \times 10^{10}\ \mathrm{cm}^{-2}\ \mathrm{V}^{-1}$, calculated using the $\mathrm{SiO_2}$ thickness.

The values of $\sigma_{\min}$ are displayed in Fig. 7.2 (a) as a function of the number of layers. The conductivity increases approximately linearly with increasing thickness. This can also be seen by the fairly constant value for $\sigma_{\min}$ per layer plotted in Fig. 7.2 (b) and can be explained by the linear increase of the DOS with the number of layers as presented in Fig. 7.2 (d). The DOS was calculated using a zone-folding scheme as described at the end of this section and the displayed points show the DOS at $n_g = 0$, corresponding to the minimum value of the DOS. The DOS is plotted with and without taking into account energy broadening, resulting in slightly different slopes. The linear increase of the DOS points to a weak influence of the graphene layer stacking on the DOS per layer. For thicker samples we see a small increase of $\sigma_{\min}/\mathrm{layer}$.[1] The conductance per layer of 20-layer graphene of $\sigma_{\min}/\mathrm{layer} \sim 3.5 \times 2e^2/h$ increases further to $\sigma/\mathrm{layer} \sim 8.5 \times 2e^2/h$ in bulk graphite [25].[2] This rise in $\sigma_{\min}/\mathrm{layer}$ for thicker samples could be explained by a stronger influence of the coupling between the layers with increasing thickness, which is consistent with the interlayer coupling tight binding parameter rising from bilayer graphene (BLG) to graphite [26].

While $\sigma_{\min}$ increases with the number of layers, the influence of the gate voltage on the resistance is reduced with increasing thickness. This can be seen by the increased full width half maximum (FWHM) of the peak shaped resistance curve (see Figs. 7.1 (b) and 7.2 (c)) and can be explained by the distribution of the induced charges over the layers. The red solid curve in Fig. 7.3 (a) shows R_{sq} vs V_g measured on a 14-layer sample. Assuming an equal division of the charges between the SLG-like layers, we get a broadened resistance curve (see Fig. 7.3 (a), green dash-dotted curve). Taking the screening of the extrinsic potentials (including the gate voltage) by a few layers [13] into account, we get even better agreement between the modeled resistance curve and the measured one (see Fig. 7.3 (a), black dotted curve). The influence of V_g on R_{sq} can be described following an easy resistor model (see Fig. 4(a) in Ref. [15]). The FLG flake is modeled as parallel resistors (the graphene sheets) contacted via an interlayer resistance $R_{int} = \rho_c\ d_{SL}/A_C$ at the source and

---

[1] We do not consider the points for 17-layer graphene here or in other analysis as this sample showed, in general, different behavior. This could be due to enhanced contact from the sides of the graphene stack because of a possible different angle in the deposition step. We still show the data for the sake of completeness.

[2] Since electrical gating is not possible in bulk graphite, no gate-related resistance dependence can be observed. Hence, we use $\sigma_{\min} = \sigma$ for graphite.

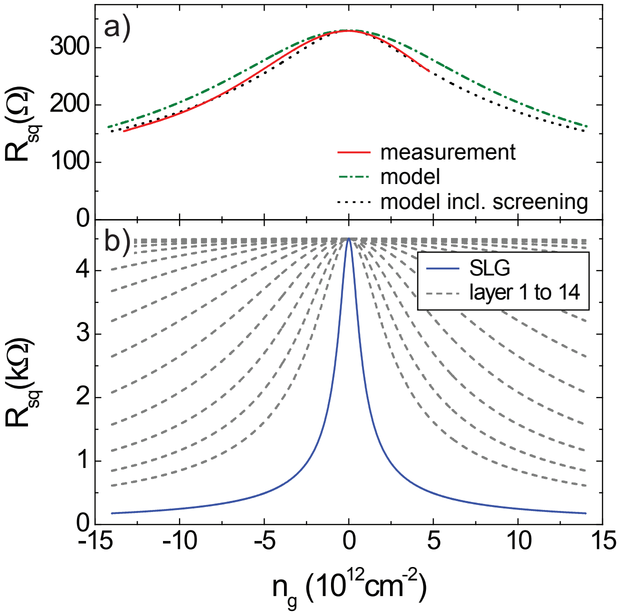

Figure 7.3: (a) R_{sq} vs V_g for a 14-layer thick sample from a 4-probe measurement (red solid curve) and from our model excluding (green dash-dotted curve) and including the screening of the gate voltage (black dotted curve). (b) Sketch of the model for a FLG stack. The blue solid curve shows the modeled SLG resistance R_{sq}^{model} considering $\mu = 2520\ \text{cm}^2\text{V}^{-1}\text{s}^{-1}$ and a minimum carrier density of $n_0 = 0.55 \times 10^{12}\ \text{cm}^{-2}$. The gray dashed curves show the square resistances for the 14-layers that, when combined, result in the black dotted curve for the modeled stack resistance in (a).

drain, where $\rho_c \approx 0.1\ \Omega\text{cm}$ is the conductance along the c-axis of HOPG [25] and A_C is the contact area. With our contact areas of $A_C \sim 0.5 \times 0.5\ \mu\text{m}^2$, we get $R_{int} \sim 1\ \Omega$, much smaller than typical SLG resistances, $R_{sq} \sim 2\ \text{k}\Omega$. No further conductance between the layers is considered.

Using Thomas-Fermi screening [14], the total induced charge is screened approximately exponentially and distributed over the layers [13, 15] shown in Fig. 7.3 (b). We assume the resistance per layer to be equal to a modeled SLG resistance $R_{sq}^{\text{model}} = (e\mu\sqrt{n_{\text{ind}}{}^2 + n_0{}^2})^{-1}$, where e is the electron charge and n_{ind} and n_0 are the induced and the minimum charge carrier densities per layer. The total induced charge carrier density n_g is distributed over the layers, with an exponential decay of the induced charge carrier density per layer n_{ind}^i (compare Ref. [15], Eq. (5)). Fig. 7.3 (b) shows R_{sq}^{model} for SLG with $\mu = 2520\ \text{cm}^2\text{V}^{-1}\text{s}^{-1}$ and $n_0 = 0.55 \times 10^{12}\ \text{cm}^{-2}$ (blue solid curve) and the calculated R_{sq} for the different layers in the stack (gray dashed curve) as a function of n_g. Considering the screening length, we follow Ref. [13] with

$\lambda_{scr} = 3$–5 layers and use the best fit to our data, $\lambda_{scr} = 3$ layers. In the case of SLG it is $n_{\mathrm{ind}} = n_g$, and for FLG $\sum n^i_{\mathrm{ind}} = n_g$. The modeled layers closest to the gate still experience a strong resistance change by changing n_g, while the resistance of layers farther away is almost unaffected. The resulting resistance of the 14-layer stack is plotted in Fig. 7.3 (a) (black dotted curve) together with the measured R_{sq} of the 14-layer graphene sample (red solid curve). We see good agreement between the two curves. In the case of modeling the resistance excluding the screening, we have to investigate $\lambda_{scr} \rightarrow \infty$ and get as a result the green dash-dotted curve in Fig. 7.3 (a), which does not fit as well to our measurements as the one that includes screening.

While the shape of the resistance curve for, e.g., the 14-layer graphene sample can be easily modeled, some samples show a further broadened or an asymmetric resistance curve as a function of V_g (see, e.g., the curve for 9-layer graphene in Fig. 7.1 (b)). This can be explained as follows: Fig. 7.4 shows the resistance of a 20-layer graphene sample, measured on different parts of the FLG flake. The black solid curve was measured on a $9\ \mu\mathrm{m}$ long strip, while the other three curves represent the resistance of sections of this strip. Between the three sections we see a shift of V_0 by ~ 50 V. Adding up the resistances, results for the full distance in the broadened curve (black solid curve) with a lower maximum resistance compared to a sample with a fixed position of V_0 for all sections. The shift of V_0 is caused by a non-uniform background doping of the flake that could be due to a locally different doped substrate, resist residues on the surface of the flake, or the metal contacts. This effect could explain the asymmetric shape of the resistance curves and the spread in the values for the minimum conductivity per layer and for the FWHM in Fig. 7.2 (b) and (c), respectively. The same effect has been observed in SLG [27].

In the following section we will discuss the spin transport properties and compare spin with charge diffusion in FLG to discuss the spin-relaxation mechanism. Therefore, we need to calculate the charge diffusion coefficient D_C based on R_{sq} using the Einstein relation

$$\sigma = e\nu D_C, \tag{7.1}$$

where $\nu(E)$ is the energy dependent DOS and $\sigma(E) = 1/R_{sq}$. In order to easily calculate the DOS for FLG we use the fact that the tight-binding Hamiltonian of a FLG graphene system can be, in a good approximation, separated into sets of BLG-like and SLG-like Hamiltonians [28]. This approach was already experimentally validated by infrared spectroscopy [29, 30].

To determine the number and shape of the BLG- and SLG-like bands, we apply a zone-folding scheme introduced by Mak *et al.* [30] that reduces the 3-dimensional (3D) band structure of graphite into a 2-dimensional (2D) band structure for FLG. This approach uses the fact that the confinement in the z-direction (perpendicular to the FLG flake) induces standing waves and therefore a quantization on the wavevector k_z. The quantization can be represented by cutting planes in the 3D Brillouin

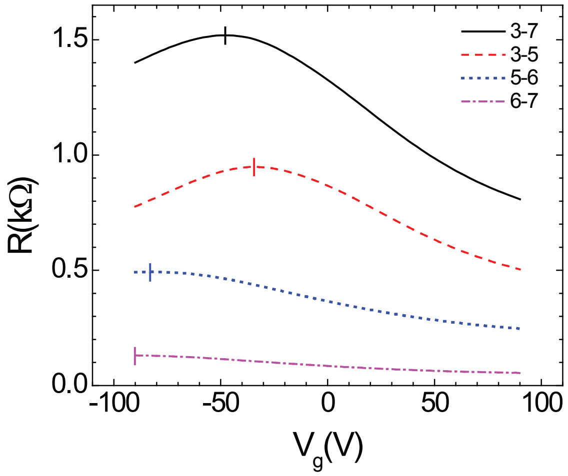

Figure 7.4: 4-probe measurements of the local resistance of the 20-layer graphene sample shown in Fig. 7.1 (a) as a function of V_g. The black solid curve shows the resistance on a 9 μm long strip (between contacts 3 and 7); the other curves represent the resistances on parts of this strip, between contacts 3 and 5 (5 μm, red dashed curve), contacts 5 and 6 (3 μm, blue dotted curve), and contacts 6 and 7 (1 μm, magenta dash-dotted curve). The vertical lines show the position of the respective maximum resistance V_0.

zone (BZ) of graphite that cut through different regions of the BZ due to the different symmetry-groups for FLG with even or odd number of layers [31]. For an odd number of layers, there is always a cutting plane through the H point, which introduces a linear dispersion band similar to SLG. For an even number of layers, such a cutting plane is not present. The other cutting planes (if any) do not pass through the borders of the graphite BZ and introduce BLG-like bands with different effective masses.

To define the energy dispersion for graphite, we use a simple tight-binding approach consisting of only the hopping parameter for next-neighbors, $\gamma_0 = 3.15\ eV$, and an interlayer coupling of $\gamma_1 = 0.37\ eV$. The inclusion of other interlayer and intralayer coupling parameters have a minor effect on our results since they are smeared out by a broadening introduced by temperature, impurities, and other disorder potentials [30]. To account for such effects, we include a Gaussian broadening in the DOS in the same way as shown in Ref. [5]. The resulting DOS at $n_g = 0$ increases linearly with the number of layers and is presented in Fig. 7.2 (d). In Fig. 7.2 (d) the calculated values using only the zone-folding scheme are presented along with the values including an energy broadening of $\mathrm{FWHM} \approx 60\ \mathrm{meV}$. This broadening also takes into account the effect of the electron and hole pockets around E_F present in graphite [32].

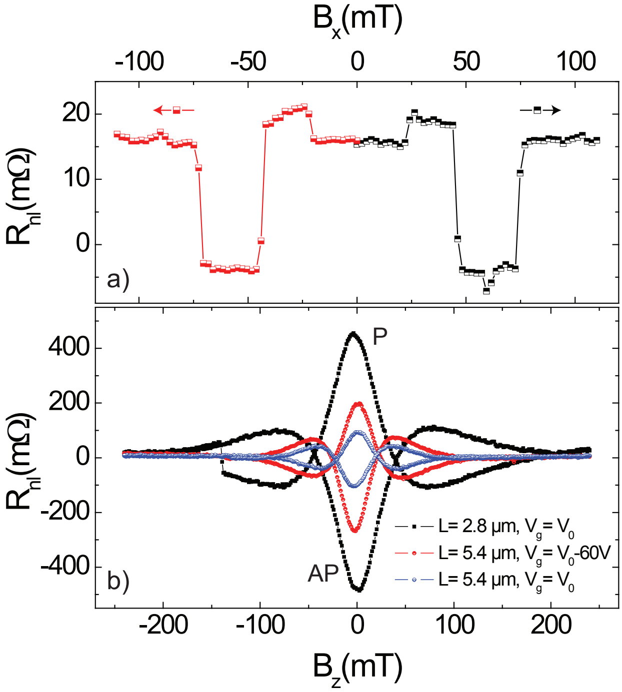

Figure 7.5: (a) Non-local spin valve signal of a 7-layer graphene sample. The sweep directions of the magnetic field are indicated (red and black arrows). The distance between the inner electrodes is $L = 8\ \mu\text{m}$. (b) Hanle precession measurements of a 5-layer graphene sample at the gate voltage resulting in the minimum conductivity $V_g = V_0$ for $L = 2.8\ \mu\text{m}$ (black, largest amplitude) and $L = 5.4\ \mu\text{m}$ (blue, smallest amplitude) and in the hole doped state at $V_g = V_0 - 60$ V for $L = 5.4\ \mu\text{m}$ (red, intermediate amplitude). The precession is measured for the parallel (P) and antiparallel (AP) configuration of the inner contacts. The curve for $L = 2.8\ \mu\text{m}$ shows a switch from the P to the AP state at -140 mT. This is due to the fact that at relatively high fields the non-avoidable in-plane component of the perpendicular field switches the magnetization of one of the inner electrodes.

7.4 Spin transport

Now we examine the spin transport properties of FLG. Fig. 7.5 (a) shows a typical non-local spin valve measurement [3] on FLG. Sending a current I from electrode 5 to electrode 1 (see Fig. 7.1 (a)) generates a spin accumulation at electrode 5. The spins diffuse on both sides of the electrode along the flake and generate a voltage drop V_{nl} between electrodes 6 and 9, defining the non-local resistance $R_{nl} = V_{nl}/I$. Switching the magnetization of one of the inner electrodes (5 or 6) using an in-plane magnetic field results in a sign change of R_{nl} (see Fig. 7.5 (a)). When the outer contacts (1 or

9) are located within the spin-relaxation length, additional switches can be observed [3]. The spin valve measurement in Fig. 7.5 (a) is taken on a 7-layer graphene sample with an inner contact distance of $L = 8\ \mu\mathrm{m}$. Including the additional switch at small field values, we see a spin signal over a distance of $L = 10\ \mu\mathrm{m}$. It is worth noting that this was the longest distance over which a spin signal had been reported for graphene based devices at the time of publication.

For further analysis of the spin transport we perform Hanle spin precession measurements [24]. They are performed in the same geometry as the spin valve measurements with the magnetic field $\vec{B}$ pointing now perpendicular to the sample plane causing the injected, in-plane oriented spins to precess. The spin dynamics are described by the Bloch equation for the spin accumulation $\vec{\mu_S}$: [24]

$$D_S \nabla^2 \vec{\mu_S} - \frac{\vec{\mu_S}}{\tau} + \vec{\omega_L} \times \vec{\mu_S} = \vec{0}. \tag{7.2}$$

The first term on the left-hand side describes the spin-diffusion represented by the spin-diffusion coefficient D_S, and the second term describes the spin-relaxation with the spin-relaxation time τ. The third term describes the precession with the Larmor frequency $\vec{\omega_L} = g\mu_B/\hbar\ \vec{B}$, where $g = 2$ is the effective Landé factor and μ_B is the Bohr magneton. In Fig. 7.5 (b) three Hanle measurements on a 5-layer graphene sample are presented. Each curve consists of the non-local signal acquired for the parallel (P) and antiparallel (AP) orientation of the inner contacts. The black and the blue dots represent the measurements for $L = 2.8\ \mu\mathrm{m}$ and $L = 5.4\ \mu\mathrm{m}$, respectively, at the gate voltage V_0. The red curve is measured on the longer distance at $V_g = V_0 - 60$ V, where electron charges are induced by the gate. The amplitude for the measurement with increased L is smaller due to additional spin-relaxation, as the spins have to travel a longer distance resulting in a longer time interval for spin-relaxation. In addition to the change in the amplitude, a shift in the B-field values for the crossing points of the parallel and the antiparallel precession curve is visible for the two curves measured at $V_g = V_0$. The crossing points represent the B-field value where the spins have, on average, precessed for $90°$, resulting in both configurations in a signal of $R_{nl} \approx 0$. An increased distance L, corresponding to an increased travel time for the spins, therefore decreases the B-field which results in $90°$-precession [4, 24].

The measurements show that the spin signal can be enhanced by inducing more charge carriers (see enhanced spin signal comparing the measurement at $V_g = V_0 - 60$ V and $V_g = V_0$). This was also observed for SLG [5].

The Hanle curves can be fitted with the solutions of the Bloch equation (7.2), yielding the spin transport quantities D_S and τ. Those solutions are calculated with the injector considered to be a spin current source and the detector considered to be a non-invasive spin voltage probe [4, 24]. To exclude (small) spurious background effects, we subtract the AP from the P curve and fit the result. For several FLG sam-

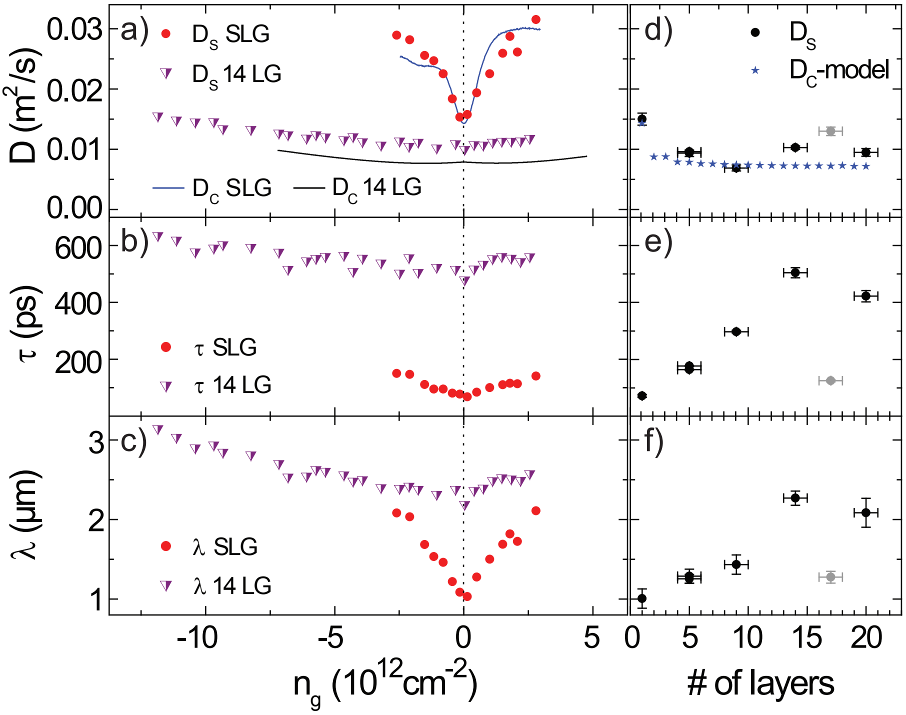

Figure 7.6: D_S, τ and λ (a)–(c) as a function of the induced charge carriers n_g for 14-layer graphene and SLG and (d)–(f) as a function of the number of layers at $V_g = V_0$. The gray points belong to a sample that showed overall unusual behavior.[1] In addition to D_S, (a) also shows D_C for 14-layer graphene and SLG and (d) shows the modeled D_C at $V_g = V_0$ assuming $R_{sq} = 5\ \mathrm{k}\Omega/\mathrm{layer}$.

ples a set of precession measurements was performed for different induced charge-carrier densities n_g. The spin transport quantities D_S and τ and the spin-relaxation length $\lambda = \sqrt{D_S\tau}$ are plotted as a function of n_g in Figs. 7.6 (a), (b), and (c), respectively. Here the results for SLG from Ref. [5] are compared with a 14-layer graphene sample representing the results for FLG. The general dependence of the quantities is the same for all samples. All curves show a minimum at $n_g = 0$ (corresponding to $V_g = V_0$). The change in the three different quantities as a function of n_g is minor compared to SLG. This can be explained by the fact that in FLG far more intrinsic charge carriers are present due to the changed band structure compared to SLG, masking the effect of the induced charge carriers n_g (see Section 7.3).

Figs. 7.6 (d), (e), and (f) show D_S, τ, and λ, respectively, at $V_g = V_0$ as a function of the number of layers. Besides a drop from SLG to BLG, D_S shows no identifiable dependence and is approximately constant, while τ increases linearly with the number of layers until this trend is reduced for the thickest samples, reaching a maximum of $\tau \sim 500$ ps. With this result, τ still stays far below the spin-relaxation times of 20 ns measured at RT with electron spin resonance (ESR) in bulk graphite [33] or $\tau = 55$ ns in graphene at $T = 150$ K [34]. There is, at this time, no explanation for that difference. The linear increase of the measured τ as a function of the number of layers can be explained by the expected screening of scattering potentials due to the linear increase of intrinsic charge carriers as a function of the number of layers (compare Fig. 7.2 (d)).

The constant value for D_S for more than one layer shows that the change in the band structure and the screening does not have a strong influence on the spin-diffusion. On the other hand the spin-relaxation length increases with the number of layers and is doubled at $V_g = V_0$ between 1 and 20 layers. The effect of the induced charge carriers on the spin transport quantities is weak for thicker samples. Therefore, we see only a small increase of λ in FLG for $n_g \neq 0$ compared to SLG (Fig. 7.6 (c)) and reach a maximum value of $\lambda \sim 3\ \mu$m. This is also because outer scattering potentials are already screened by the intrinsic charge carriers in the thicker samples.

Our results do not show values for λ as high as reported by Goto *et al.* [19] ($\lambda \gg 8\mu$m). This is probably due to the fact that the reported values were derived indirectly from spin valve measurements on short distances of $L \sim 300$ nm $\ll 8\mu$m, making it difficult to conclude the behavior over long distances. We also note that spin valve measurements are, in general, less conclusive for spin transport properties than Hanle precession measurements [24].

Han *et al.* discuss in Ref. [6] different behaviors of the spin signal depending on the induced charge carriers for different kinds of contact interfaces. We believe that in our samples the interface mainly affects the polarization of the injected current and has only weak influence on spin-relaxation and spin-diffusion. While we have seen reduced spin signals for low R_C in SLG samples before [4], the measurements presented here were performed on samples with R_C values that lead to an R parameter of $R \geq 0.1\ \mu$m. As described in Ref. [4], R/λ represents the ratio between the contact resistance and the graphene resistance over one spin-relaxation length. The values that we found for R show that the contacts in our samples are non-invasive. Hence, we can rule out effects of spins escaping into the cobalt electrodes, fringe fields, and interface spin scattering. This is also supported by the fact that we have observed spin transport under electrically floating cobalt electrodes without any measurable effects on the spin signal in SLG and FLG.

In addition to D_S, Fig. 7.6 (a) and (d) show the charge diffusion coefficient D_C, which is calculated using Eq. (7.1) requiring the DOS. For FLG we use the DOS obtained by the zone-folding scheme as discussed in Section 7.3, assuming a broadening of FWHM ≈ 60 meV[3] and, in the case of SLG, the broadened DOS discussed in Ref. [5]. In Fig. 7.6 (a) we use the measured values for the conductivity of the

---

[3] The FWHM ≈ 60 meV is here due to the fact that, for D_C in FLG, similar to D_C in SLG, we see a

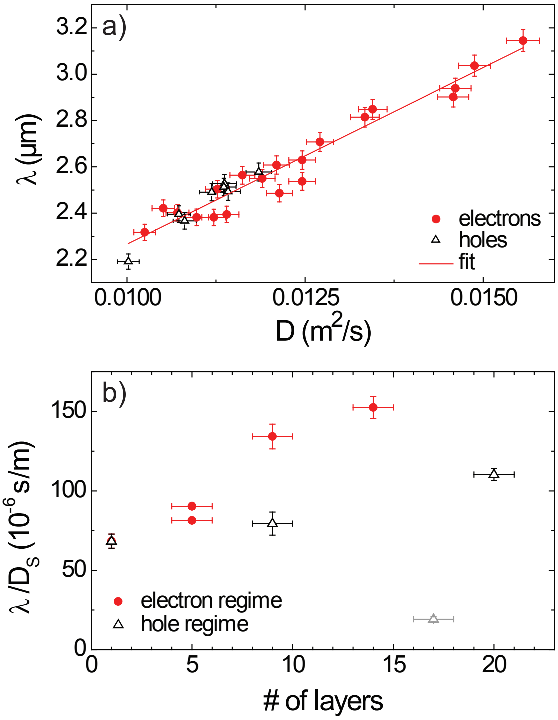

Figure 7.7: (a) Linear relationship between λ and D_S, extracted from Fig. 7.6 (a) and (c). The linear fit is performed on the red points taken in the electron conduction regime, and the black open triangles were taken in the hole regime. (b) Slopes of the linear fits of λ vs D_S for different samples as a function of the number of layers. The increase in the slopes is different for the electron and hole conduction regimes. The gray point belongs to a sample that showed overall unusual behavior.[1]

samples as a function of V_g, while in Fig. 7.6 (d) we assume a fixed resistance per layer of $R_{sq} = 5\ \text{k}\Omega/\text{layer}$ at V_0 (compare Fig. 7.2 (b)). For SLG the two diffusion coefficients have very similar values independent of n_g. In 14-layer graphene D_C is $\sim 20\%$ smaller than D_S (and $\sim 50\%$ smaller than in SLG), while both coefficients show only a slight change as a function of n_g ($D_C \propto D_S$; see Fig. 7.6 (a)). As a function of the number of layers, D_C and D_S are approximately constant after the values drop between SLG and BLG by roughly $\sim 50\%$. We still see a slight decrease from 2 to 5 layers. This shows that here D_C behaves the same way as D_S and is not affected by the changing band structure or the screening. Similar to the case for SLG, the Coulomb electron-electron interactions still play a minor role in the scattering [5].

---

non-physical peak at V_0 that is flattened by using this broadening.

The main factor limiting diffusion is still impurity potential scattering.

This can also be seen when we plot λ as a function of the corresponding D_S. We observe a linear dependence for the electron and the hole conduction regimes. Fig. 7.7 (a) shows this plot for the 14-layer graphene sample (data extracted from Fig. 7.6).[4] Combined with $D_C \propto D_S$ and $\lambda = \sqrt{D_S \tau}$, this leads to a linear dependence between the spin-relaxation time and the momentum scattering time τ_p, which points to the Elliott-Yafet-type spin-relaxation mechanism [5, 24].[5] The dominance of this mechanism and therefore the spin-relaxation due to impurity scattering in our samples can be explained by impurity-induced spin-orbit coupling as described in Ref. [35]. Fig. 7.7 (b) shows λ/D_S for different FLG samples.[6] Depending on whether the points were taken in the electron or the hole regime, we see different scalings of the slopes with an increasing number of layers. The lower values for λ/D_S in the hole conduction regime indicate that there is a higher spin-flip probability for each scattering event. Overall, λ/D_S increases with the number of layers, showing a reduced chance for spin flip with an increasing number of layers. This demonstrates the enhanced spin transport by using more than one layer graphene.

7.5 Conclusions

We have successfully produced lateral spin field-effect transistors (FET) on 3- to 20-layer graphene samples and measured the charge and spin transport properties of these devices. The reduced influence of external potentials, including the applied gate voltage, on the charge transport with an increasing number of layers has been explained by the distribution of the charges between the layers. The shape of the resistance curve can be modeled if we include screening effects. Further broadening and asymmetry of the peak shaped R_{sq} vs V_g curve have been explained by inhomogeneous background doping of the flakes. Our conductivity per layer for 20-layer graphene stays a factor of 2.4 below the value for bulk HOPG. This points to extrinsic scattering events at the bottom or the top of the flake limiting the transport in our devices. As those will be at least partly screened, impurities in the layers will also have limiting effects. A weak temperature dependence of the resistance (data not shown) also points to the fact that impurities and static scatterers are the main limiting factors.

---

[4] Note that due to the small change of D_S and λ as a function of n_g we see an increase of both values by only a factor of ~ 1.5.

[5] This interpretation is as published in Phys. Rev. B **83**, 115410 (2011). It is not fully correct, as the relation between the spin relaxation time and the momentum scattering time for the Elliott-Yafet mechanism is $\tau_{\mathrm{EY}} = E_F^2 \tau_p / \Delta_{\mathrm{EY}}^2$, with the effective spin-orbit coupling Δ_{EY}, and the different points in Fig. 7.7 are obtained at different E_F. See Chapter 10, Section 10.2 for a discussion of this issue. Note: The linear fit to the points in Fig. 7.7 does not go through the (0,0) point of the graph.

[6] As most samples are highly doped we are only able to determine trustfully the slope of λ vs D_S for just one of the two conduction regimes.

The spin transport quantities D_S and τ have been studied as a function of the induced charge carriers n_g and of the number of layers. τ increases approximately linearly with the number of layers, showing the expected enhancement of the spin lifetime due to the screening of the scattering potentials that has been modeled for the charge transport. The diffusion coefficients for spin (D_S) and charge (D_C) show a decrease from SLG to BLG and then stay approximately constant. This shows that the number of layers has only a weak influence on the diffusion, pointing to a weak coupling between the layers.

The spin-relaxation length λ is mainly enhanced for $n_g = 0$. Therefore, we see improvement primarily for the spin transport in the regime around $\sigma_{\min}$. This is due to the intrinsic charge carriers of FLG, which mask the effect of induced charge carriers. We would like to mention at this point that we see no considerable temperature effect on λ in FLG (data not shown). This points to a negligible effect of phonons on the spin-relaxation. The enhancement of λ due to screening effects in FLG therefore enables the fabrication of improved spin transport devices.

Finally, we calculate D_C, using the DOS of FLG obtained by the zone-folding scheme, and compare the result with D_S. As we observe $D_C \propto D_S$ and $\lambda \propto D_S$, it seems that the spin-relaxation in our FLG samples is mainly due to the Elliott-Yafet mechanism, which is also the case for SLG.[5] As the linear dependence in our FLG spin transport measurements is based on an increase of both values by only a factor of ~ 1.5, this result is not yet conclusive and requires further research. The theoretical expected dominance of the D'yakonov-Perel' spin scattering mechanism [7, 8] is probably only measurable in cleaner samples [36] with higher diffusion coefficients and higher mobilities μ. Therefore, measurements on high quality graphene spin valve devices have to be performed.

Note added. For a discussion of the spin relaxation mechanisms in graphene see Chapter 10.

References

[1] A. Castro Neto, F. Guinea, N. Peres, K. Novoselov, and A. Geim, “The Electronic Properties of Graphene,” *Rev. Mod. Phys.* **81**(1), pp. 109–162, 2009.

[2] N. M. R. Peres, “Colloquium: The Transport Properties of Graphene: An Introduction,” *Rev. Mod. Phys.* **82**(3), pp. 2673–2700, 2010.

[3] N. Tombros, C. Józsa, M. Popinciuc, H. T. Jonkman, and B. J. van Wees, “Electronic Spin Transport and Spin Precession in Single Graphene Layers at Room Temperature,” *Nature (London)* **448**, pp. 571–574, 2007.

[4] M. Popinciuc, C. Józsa, P. J. Zomer, N. Tombros, A. Veligura, H. T. Jonkman, and B. J. van Wees, “Electronic Spin Transport in Graphene Field-Effect Transistors,” *Phys. Rev. B* **80**(21), p. 214427, 2009.

[5] C. Józsa, T. Maassen, M. Popinciuc, P. J. Zomer, A. Veligura, H. T. Jonkman, and B. J. van Wees, “Linear Scaling between Momentum and Spin Scattering in Graphene,” *Phys. Rev. B* **80**(24), p. 241403(R), 2009.

[6] W. Han, K. Pi, K. M. McCreary, Y. Li, J. J. I. Wong, A. Swartz, and R. K. Kawakami, “Tunneling Spin Injection into Single Layer Graphene,” *Phys. Rev. Lett.* **105**(16), p. 167202, 2010.

[7] D. Huertas-Hernando, F. Guinea, and A. Brataas, “Spin Relaxation Times in Disordered Graphene,” *Eur. Phys. J.-Spec. Top.* **148**(1), pp. 177–181, 2007.

[8] D. Huertas-Hernando, F. Guinea, and A. Brataas, “Spin-Orbit-Mediated Spin Relaxation in Graphene,” *Phys. Rev. Lett.* **103**(14), p. 146801, 2009.

[9] Y. Zhang, V. W. Brar, C. Girit, A. Zettl, and M. F. Crommie, “Origin of Spatial Charge Inhomogeneity in Graphene,” *Nat. Phys.* **5**(10), pp. 722–726, 2009.

[10] K. Bolotin, K. Sikes, Z. Jiang, M. Klima, G. Fudenberg, J. Hone, P. Kim, and H. Stormer, “Ultrahigh Electron Mobility in Suspended Graphene,” *Solid State Commun.* **146**(9-10), p. 351, 2008.

[11] X. Du, I. Skachko, A. Barker, and E. Y. Andrei, “Approaching Ballistic Transport in Suspended Graphene,” *Nat. Nanotechnol.* **3**, pp. 491–495, 2008.

[12] N. Tombros, A. Veligura, J. Junesch, J. J. van den Berg, P. J. Zomer, M. Wojtaszek, I. J. V. Marun, H. T. Jonkman, and B. J. van Wees, “Large Yield Production of High Mobility Freely Suspended Graphene Electronic Devices on a Polydimethylglutarimide Based Organic Polymer,” *J. Appl. Phys.* **109**(9), p. 093702, 2011.

[13] F. Guinea, “Charge Distribution and Screening in Layered Graphene Systems,” *Phys. Rev. B* **75**(23), p. 235433, 2007.

[14] M. Koshino, “Interlayer Screening Effect in Graphene Multilayers with ABA and ABC Stacking,” *Phys. Rev. B* **81**(12), p. 125304, 2010.

[15] Y. Sui and J. Appenzeller, “Screening and Interlayer Coupling in Multilayer Graphene Field-Effect Transistors,” *Nano Lett.* **9 (8)**, pp. 2973–2977, 2009.

[16] H. Miyazaki, S. Odaka, T. Sato, S. Tanaka, H. Goto, A. Kanda, K. Tsukagoshi, Y. Ootuka, and Y. Aoyagi, “Inter-Layer Screening Length to Electric Field in Thin Graphite Film,” *Appl. Phys. Express* **1**(3), p. 034007, 2008.

[17] M. Ohishi, M. Shiraishi, R. Nouchi, T. Nozaki, T. Shinjo, and Y. Suzuki, “Spin Injection into a Graphene Thin Film at Room Temperature,” *Jpn. J. Appl. Phys.* **46**, pp. L605–L607, 2007.

[18] M. Nishioka and A. M. Goldman, “Spin Transport through Multilayer Graphene,” *Appl. Phys. Lett.* **90**(25), p. 252505, 2007.

[19] H. Goto, A. Kanda, T. Sato, S. Tanaka, Y. Ootuka, S. Odaka, H. Miyazaki, K. Tsukagoshi, and Y. Aoyagi, “Gate Control of Spin Transport in Multilayer Graphene,” *Appl. Phys. Lett.* **92**(21), p. 212110, 2008.

[20] W. Han, K. Pi, W. H. Wang, K. McCreary, Y. Li, W. Bao, P. Wei, J. Shi, C. Lau, and R. Kawakami, “Spin Transport in Graphite and Graphene Spin Valves,” *Spintronics II* **7398**(1), p. 739819, 2009.

[21] W. H. Wang, K. Pi, Y. Li, Y. F. Chiang, P. Wei, J. Shi, and R. K. Kawakami, “Magnetotransport Prop-

erties of Mesoscopic Graphite Spin Valves," *Phys. Rev. B* **77**(2), p. 020402, 2008.

[22] T.-Y. Yang, J. Balakrishnan, F. Volmer, A. Avsar, M. Jaiswal, J. Samm, S. R. Ali, A. Pachoud, M. Zeng, M. Popinciuc, G. Güntherodt, B. Beschoten, and B. Özyilmaz, "Observation of Long Spin-Relaxation Times in Bilayer Graphene at Room Temperature," *Phys. Rev. Lett.* **107**(4), p. 047206, 2011.

[23] P. Nemes-Incze, Z. Osváth, K. Kamarás, and L. Biró, "Anomalies in Thickness Measurements of Graphene and Few Layer Graphite Crystals by Tapping Mode Atomic Force Microscopy," *Carbon* **46**(11), p. 1435, 2008.

[24] J. Fabian, A. Matos-Abiague, C. Ertler, P. Stano, and I. Žutić, "Semiconductor Spintronics," *Acta Phys. Slov.* **57**, pp. 565–907, 2007.

[25] K. Matsubara, K. Sugihara, and T. Tsuzuku, "Electrical Resistance in the c Direction of Graphite," *Phys. Rev. B* **41**(2), pp. 969–974, 1990.

[26] L. M. Malard, J. Nilsson, D. C. Elias, J. C. Brant, F. Plentz, E. S. Alves, A. H. Castro Neto, and M. A. Pimenta, "Probing the Electronic Structure of Bilayer Graphene by Raman Scattering," *Phys. Rev. B* **76**(20), p. 201401, 2007.

[27] P. Blake, R. Yang, S. Morozov, F. Schedin, L. Ponomarenko, A. Zhukov, R. Nair, I. Grigorieva, K. Novoselov, and A. Geim, "Influence of Metal Contacts and Charge Inhomogeneity on Transport Properties of Graphene near the Neutrality Point," *Solid State Commun.* **149**(27-28), p. 1068, 2009.

[28] M. Koshino and T. Ando, "Orbital Diamagnetism in Multilayer Graphenes: Systematic Study with the Effective Mass Approximation," *Phys. Rev. B* **76**(8), p. 085425, 2007.

[29] M. Orlita, C. Faugeras, J. M. Schneider, G. Martinez, D. K. Maude, and M. Potemski, "Graphite from the Viewpoint of Landau Level Spectroscopy: An Effective Graphene Bilayer and Monolayer," *Phys. Rev. Lett.* **102**(16), p. 166401, 2009.

[30] K. F. Mak, M. Y. Sfeir, J. A. Misewich, and T. F. Heinz, "The Evolution of Electronic Structure in Few-Layer Graphene Revealed by Optical Spectroscopy," *Proc. Natl. Acad. Sci. USA* **107**(34), pp. 14999–15004, 2010.

[31] L. M. Malard, M. H. D. Guimarães, D. L. Mafra, M. S. C. Mazzoni, and A. Jorio, "Group-Theory Analysis of Electrons and Phonons in N -Layer Graphene Systems," *Phys. Rev. B* **79**(12), p. 125426, 2009.

[32] B. Partoens and F. M. Peeters, "From Graphene to Graphite: Electronic Structure around the K Point," *Phys. Rev. B* **74**(7), p. 075404, 2006.

[33] G. Wagoner, "Spin Resonance of Charge Carriers in Graphite," *Phys. Rev.* **118**(3), pp. 647–653, 1960.

[34] L. Ciric, A. Sienkiewicz, B. Náfrádi, M. Mionic, A. Magrez, and L. Forró, "Towards Electron Spin Resonance of Mechanically Exfoliated Graphene," *Phys. Status Solidi B* **246**(11-12), pp. 2558–2561, 2009.

[35] A. H. Castro Neto and F. Guinea, "Impurity-Induced Spin-Orbit Coupling in Graphene," *Phys. Rev. Lett.* **103**(2), p. 026804, 2009.

[36] Y. Zhou and M. W. Wu, "Electron Spin Relaxation in Graphene from a Microscopic Approach: Role of Electron-Electron Interaction," *Phys. Rev. B* **82**(8), p. 085304, 2010.

Chapter 8

Long spin relaxation times in wafer scale epitaxial graphene on SiC(0001).

Abstract

We developed an easy, upscalable process to prepare lateral spin-valve devices on epitaxially grown monolayer graphene on SiC(0001) and perform non-local spin transport measurements. We observe the longest spin relaxation times τ *in monolayer graphene, while the spin diffusion coefficient* D_S *is strongly reduced compared to typical results on exfoliated graphene. The increase of* τ *is probably related to the changed substrate, while the cause for the small value of* D_S *remains an open question.*

Published as:
T. Maassen, J. J. van den Berg, N. IJbema, F. Fromm,
T. Seyller, R. Yakimova, and B. J. van Wees,
Nano Lett. **12** (3), 1498 (2012).

8.1 Introduction

Spin transport in graphene draws great attention since the observation of spin relaxation lengths of $\lambda = 2\ \mu\mathrm{m}$ with spin relaxation times in the order of $\tau = 150\ \mathrm{ps}$ at room temperature (RT) in mechanically exfoliated single layer graphene (eSLG) [1]. Recent experiments show an increase of τ to $\tau \approx 0.5\ \mathrm{ns}$ in eSLG at RT [2, 3] and $\tau \approx 1\ \mathrm{ns}$ at $T = 4\ \mathrm{K}$ [3]. Measurements on bilayer graphene (BLG) show even higher spin relaxation times up to a few nanoseconds at low temperature [3, 4]. At the same time, a study on few-layer graphene (FLG) showed an enhancement of τ with increasing number of layers, which is attributed to the screening of external scattering potentials [5].

While most spin transport measurements were performed on exfoliated graphene, a first publication by Avsar *et al.* [6] showed measurements on graphene, grown by chemical vapor deposition (CVD) on copper foil. This publication was the first step towards large scale production of spin transport devices, which showed similar spin transport properties compared to exfoliated graphene. The disadvantage of the growth of graphene on metal substrates is however that one is forced to transfer the material to an insulating substrate to be able to perform transport measurements.

Therefore it is useful to think about an alternative, e.g., epitaxially grown graphene on semi-insulating SiC [7, 8]. This chapter presents the first report of spin transport in this material and therefore the first report of spin transport in graphene on a different substrate than $\mathrm{SiO_2}$. We present lateral non-local spin-valve and spin-precession measurements on graphene strips prepared from monolayer epitaxial graphene (MLEG) grown on the Si-face of a semi-insulating SiC substrate (SiC(0001)) by sublimation of Si in Ar atmosphere [8–10].

8.2 Sample fabrication

The 4H-SiC wafers [11] are heated to $2000^\circ\mathrm{C}$ in an ambient argon pressure of 1 atm as described in Refs. [8] and [9], leading to the growth of the so-called buffer layer that is predominately ($> 80\%$) covered with MLEG with some areas uncovered or covered with double layer graphene. The measurements were performed on MLEG[1] and with the help of Hall measurements on similar samples we estimate an electron doping with a charge carrier density of $n \approx 3 \times 10^{12}\ \mathrm{cm}^{-2}$ and a charge carrier mobility of $\mu \approx 1900\ \mathrm{cm^2/Vs}$ at RT.

Fig. 8.1 (a) shows an about $7 \times 5\ \mathrm{mm}^2$ big part of a SiC wafer covered with MLEG, prepared with a pattern of Ti/Au structures that form a periodic pattern of bondpads with leads to central $100 \times 100\ \mu\mathrm{m}^2$ areas for further device preparation. These structures are prepared in an optical lithography step, using a deep-UV mask aligner with

---

[1] The confirmation of the thickness to be MLEG is achieved by measuring R_{sq}.

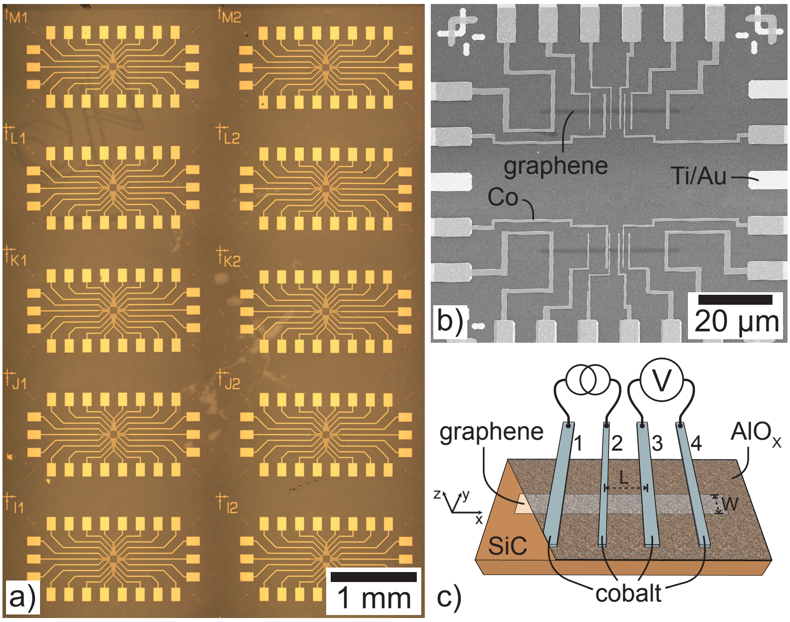

Figure 8.1: (a) Optical microscope picture of a SiC wafer prepared with Ti/Au bondpads and leads to central $100 \times 100\ \mu\text{m}^2$ areas for further device preparation. Each of these patterns has a unique label for further production steps and measurements. The changes in the background color are due to scratches and resist residues on the backside of the transparent SiC wafer. (b) SEM picture of one of the central device areas with two spin valve devices, connected with Co electrodes to the Ti/Au leads. (c) Sketch of an MLEG spin valve device with four Co contacts. The wafer including the MLEG strip is covered with AlO_x, before the Co contacts are deposited.

a double resist layer (LOR-3A / ZEP-520A, from MicroChem / ZEON Corporation). After development, the wafer is etched with oxygen plasma at 40 W for 20 seconds, before depositing a Ti/Au (5 nm/35 nm) double layer using e-beam evaporation followed by lift-off in PRS-3000 (from J.T. Baker). The etching step is necessary to enable the adhesion of the Ti/Au contacts on the substrate. To prepare the central device regions (Fig. 8.1 (b)), two MLEG strips per area are defined, using e-beam lithography (EBL) on a negative resist (ma-N 2400, from Micro Resist Technology GmbH) and the uncovered MLEG is etched in a second oxygen plasma etching step. After this, the wafer is annealed for two hours in $\text{Ar}(95\%)/\text{H}_2(5\%)$ environment at $350°\text{C}$ to remove resist residues. To avoid the conductivity mismatch [12–14], the wafer is covered with an approximately 1 nm thick AlO_x layer by evaporating 0.4 nm aluminum at a base pressure of $p < 1 \times 10^{-6}$ mbar, oxidation in situ in O_2 atmosphere at a base pressure of $p > 3 \times 10^{-5}$ mbar for 15 min and repeating the step a second time.

Finally, in a standard PMMA resist based EBL step, the 45 nm thick Co electrodes are formed (Fig. 8.1 (b)) connecting the Ti/Au leads with the two graphene strips, before the bondpads are contacted using wire bonding. By preparing the wafer with an optical step and using EBL only on the small central areas, we developed a fast and easy process to prepare a full wafer with (spin) transport devices. This process can also be used for different types of large area graphene on non-conducting substrates.

As the resolution of the ma-N resist is limited to about 50 nm, we developed a second process, replacing the ma-N resist step with a PMMA step. This enables a higher resolution but in return requires an additional step to remove the graphene outside the $100 \times 100\ \mu\mathrm{m}^2$ areas to disconnect the Ti/Au leads. This method was implemented for two devices, using an additional optical lithography step, where we cover the central device areas, while the exposed graphene is removed with oxygen plasma.

8.3 Spin transport measurements

The presented measurements are performed on a $W = 0.7\ \mu\mathrm{m}$ wide MLEG strip in vacuum at a base pressure of about 1×10^{-6} mbar using low frequency lock-in technique and AC currents between 1 and $10\ \mu\mathrm{A}$. The measurements have been confirmed with consistent results, that have been obtained on several spin-valve areas on two other devices with $W = 1\ \mu\mathrm{m}$.

The typical non-local geometry is presented in Fig. 8.1 (c). A spin polarized current I is sent from contact 2 to contact 1, generating a spin accumulation at contact 2, that diffuses in positive and negative x-direction. The $\mathrm{AlO_x}$ barrier separates the MLEG from the Co contacts and avoids reabsorption of the injected spins in the higher conducting cobalt [13]. The exponential decaying spin accumulation generates a non-local voltage V_{nl} between the spin sensitive contacts 3 and 4, which can be measured as a function of the magnetic field. In a spin-valve measurement, the magnetic field B_y, aligned with the contacts, is first used to bring the magnetization of the electrodes into a parallel (P) configuration and is then ramped in the opposite direction. When the magnetization of one of the electrodes is switched, the measured voltage shows abrupt changes. The magnetic switching fields of the contacts are different due to different coercive fields that are achieved by different width of the contacts [1, 13].

Fig. 8.2 (a) shows two spin-valve measurements, one at RT and one at 4.2 K. The non-local voltage V_{nl}, normalized to the non-local resistance $R_{nl} = V_{nl}/I$, is plotted as a function of the magnetic field. The upper measurement has been obtained at RT. After saturating the magnetization of the contacts at $B_x \approx -450$ mT no change of R_{nl} is observed, before B_y crosses $B_y = 0$ (not shown). Then at $B_y = 18$ mT a switch in R_{nl} by $250\ \mathrm{m}\Omega$ is observed, that can be attributed to the antiparallel

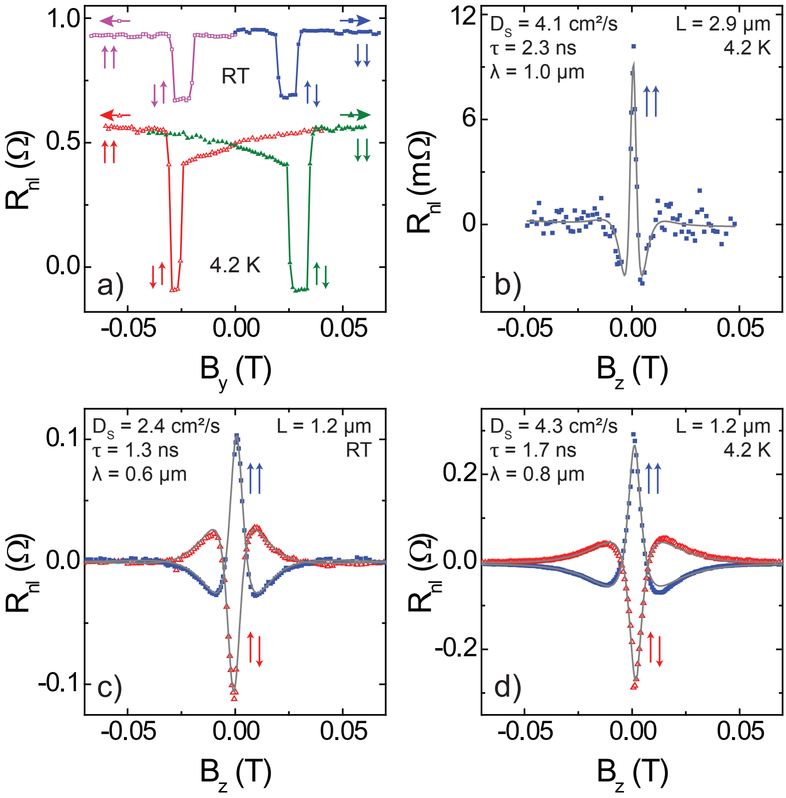

Figure 8.2: Non-local spin transport measurements. (a) Spin valve measurements on a device with $L = 1.2$ μm inner contact distance at RT (purple and blue) and 4.2 K (red and green). The sweep directions of the magnetic field are indicated by the horizontal arrows, the relative orientation of the Co contacts is illustrated by the pairs of vertical arrows. (b)–(d) Hanle precession measurement for parallel (↑↑, blue boxes) and antiparallel alignment (↑↓, red open triangles) of the inner electrodes for (b) $L = 2.9$ μm at 4.2 K, (c) $L = 1.2$ μm at RT, and (d) $L = 1.2$ μm at 4.2 K. The fits to the solutions of the Bloch equation are plotted in gray. The background resistance, which is visible in (a), is subtracted in the Hanle precession measurements (b)–(d).

alignment (AP) of injector and detector before it switches back to P and the initial R_{nl} value at $B_y = 30$ mT. On the basis of only two visible switches, it can be concluded that the outer contacts (contact 1 and 4 in Fig. 8.1 (c)) are giving no significant contribution to the signal [1]. The relatively small amplitude of the signal of $2R_{nl} \approx 0.3$ Ω is not necessarily related to spin relaxation in the graphene strip but is here related to the relatively low polarization of the contact interface. Also, the contact interface is described by the R parameter, which is in our measurements

$L(\mu\text{m})$	2.9	1.2	1.2
$T(\text{K})$	4.2	4.2	293
$D_S(\text{cm}^2/\text{s})$	4.06 ± 0.05	4.26 ± 0.06	2.38 ± 0.03
$\tau(\text{ns})$	2.34 ± 0.28	1.66 ± 0.02	1.34 ± 0.02
$\lambda(\mu\text{m})$	0.98 ± 0.06	0.84 ± 0.01	0.56 ± 0.01
$R_{nl}(\text{m}\Omega)$	9.2 ± 0.4	275.7 ± 2.2	102.9 ± 0.7

Table 8.1: Results of the fits to the measurements in Fig. 8.2 (b)–(d).

$R = W\ R_C/R_{sq}\ \geq\ 2.1\ \mu\text{m}$, with a contact resistance of $R_C \geq 3.3\ \text{k}\Omega$, a square resistance of the MLEG of $R_{sq} = 1.1\ \text{k}\Omega$ and $W = 0.7\ \mu\text{m}$ [13].[2] Therefore the contacts are almost noninvasive but can still slightly influence the spin transport measurements [13, 14].

The spin valve measurement, performed at $T = 4.2$ K, shows similar behavior. The main differences are that the amplitude is approximately doubled and the switching fields are slightly increased due to a change in the coercive fields with decreased temperature. Additional, R_{nl} shows a gradual decrease in its value before the contacts switch to AP. This is probably due to a slight misalignment of the magnetic field and the electrodes. The changed background resistance is mainly influenced by heat related effects [15, 16] and can therefore change with temperature.

To analyze the spin transport properties, we perform Hanle spin precession measurements [12]. For this purpose the magnetic field is aligned in z-direction. The resulting spin dynamics are described with the one dimensional Bloch equation for the spin accumulation $\vec{\mu_S}$ [12]

$$D_S \nabla^2 \vec{\mu_S} - \frac{\vec{\mu_S}}{\tau} + \vec{\omega_L} \times \vec{\mu_S} = \vec{0}. \tag{8.1}$$

The first term on the left-hand side describes the spin-diffusion represented by the spin-diffusion coefficient D_S, and the second term describes the spin relaxation with the spin relaxation time τ. The third term describes the precession with the Larmor frequency $\vec{\omega_L} = g\mu_B/\hbar\ \vec{B}$, where $g \approx 2$ is the effective Landé factor and μ_B is the Bohr magneton.

The Hanle precession measurements in Fig. 8.2 (b)–(d) can be fitted with the solutions of the Bloch equation (8.1), yielding the spin transport quantities D_S and τ. A summary of the fitting results are shown in Table 8.1. Fig. 8.2 (b) shows Hanle precession measurements, performed on a distance of $L = 2.9\ \mu\text{m}$ at 4.2 K. The fit gives $D_S = 4.06 \pm 0.05\ \text{cm}^2/\text{s}$ and $\tau = 2.34 \pm 0.28\ \text{ns}$, resulting in $\lambda = \sqrt{D_S\tau} = 0.98 \pm 0.06\ \mu\text{m}$.

---

[2] Both R_C and R_{sq} show only weak temperature dependence, therefore also R is not affected by T.

We would like to note that this value for τ is the longest reported spin relaxation time on monolayer graphene. And as the contacts are to some extent invasive, we can expect even higher values for τ, because a part of the injected spins relax at the contact interface. The effect of the contacts becomes apparent if one compares the fits of the measurement at $L = 2.9\ \mu\mathrm{m}$ and $L = 1.2\ \mu\mathrm{m}$ at 4.2 K (Fig. 8.2 (b) and (d)). For the measurement at $L = 1.2\ \mu\mathrm{m}$, we get $\tau = 1.66 \pm 0.02$ ns, which is around 70% of the τ obtained from the $L = 2.9\ \mu\mathrm{m}$ measurement. This is because the contact induced relaxation is more predominant, the shorter the distance the spins diffuse in the graphene strip between the contacts [14]. With invasive contacts, the shorter measurement distance also leads to a slight increase in the measured D_S [14]. Also this is observed, comparing the $L = 1.2\ \mu\mathrm{m}$ to the $L = 2.9\ \mu\mathrm{m}$ precession at 4.2 K.

When measuring at RT (Fig. 8.2 (c)) we observe a reduction of D_S by more than 40% and τ is decreased by about 20%. Therefore we get $\lambda = 0.56 \pm 0.01\ \mu\mathrm{m}$, which is one third smaller than λ at 4.2 K (see Table 8.1). We also observe slightly higher values for τ of up to ~ 1.5 ns (not shown). Fig. 8.3 shows a more detailed temperature dependence of τ, D_S, λ and the non-local signal amplitude R_{nl} between 4.2 K and RT. All four parameters show a decline between 4.2 K and RT. While D_S and λ are monotonically decreasing by 40 and 30%, respectively, the value of τ and R_{nl} drops by 20% and a factor of 3, respectively. The decrease of all four values can be related to electron-phonon scattering [12, 17]. τ and R_{nl} are approximately constant below 100 K, which could be related to the fact that the phonons are frozen out below that temperature. Given the relatively low mobility of the graphene, the temperature dependence could also be dominated by Coulomb scattering on trapped charges in the SiC substrate which shows a strong temperature dependence as described by Farmer *et al.* [18].

Our typical values for eSLG on $\mathrm{SiO_2}$ at RT are in case of D_S about a factor of 80 bigger, however the measurements on MLEG strips show an increase of τ by about a factor of 10. This still leads to a $\sim 70\%$ lower value for λ [13, 19]. The increase in τ in MLEG compared to eSLG can be attributed to the changed substrate. While $\mathrm{SiO_2}$ has an electrical inhomogeneous surface potential leading to electron-hole puddles [20] and limiting effects for spin transport in graphene [21], the SiC crystal and the buffer layer are far more homogeneous and reduce therefore scattering. We would like to note that in our measurements on exfoliated graphene the spin transport properties are only weakly influenced by the temperature [1, 5] whereas we here see an improvement at low temperatures.

8.4 Discussion of the diffusion process

Although τ is improved, we do not know the origin for the reduced values of D_S. We obtain the diffusion coefficient D_S from Hanle spin precession measurements.

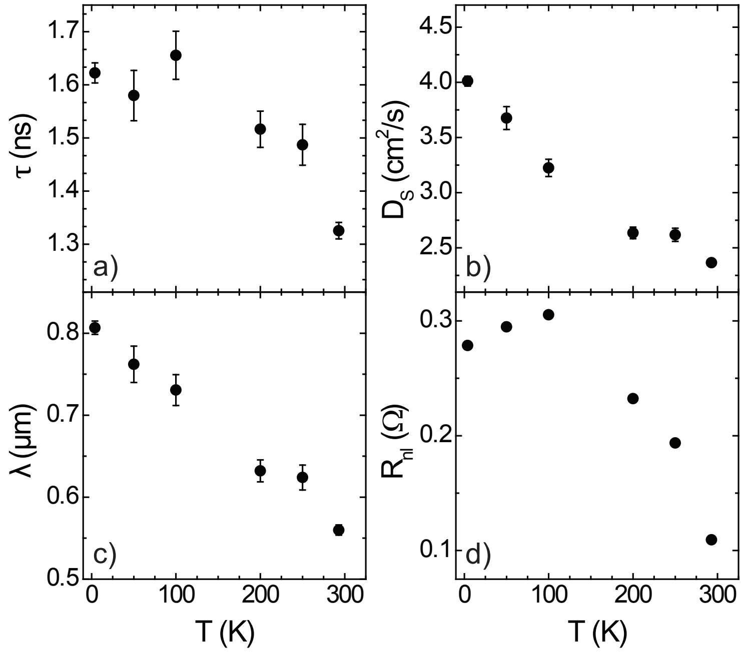

Figure 8.3: Temperature dependence of (a) the spin relaxation time, (b) the spin diffusion coefficient, (c) the spin relaxation length, and (d) the non-local signal for the sample with $L = 1.2\ \mu\mathrm{m}$. If available, several fitting results at the same temperature were averaged.

To verify if the value for D_S is correct, we compare it to the diffusion coefficient D_C acquired from charge transport measurements on the same area. D_C is calculated using the Einstein relation $D_C = (R_{sq}e^2\nu(E_F))^{-1}$, where e is the electron charge and ν is the density of states (DOS). The band structure for MLEG on SiC(0001) is the same as for eSLG [7]. Therefore, we can assume the same DOS as for eSLG, $\nu(E) = g_v g_s |E| / (2\pi\hbar^2 v_F^2)$ with the twofold valley ($g_v = 2$) and spin ($g_s = 2$) degeneracies and the Fermi velocity $v_F \approx 10^6\ \mathrm{ms}^{-1}$. With n estimated by Hall measurements on similar devices and $n(E_F) = \int_0^{E_F} \nu(E)dE$ we can calculate the Fermi energy E_F and receive $\nu(E_F)$. With $n \approx 3 \times 10^{12}\ \mathrm{cm}^{-2}$ and $R_{sq} = 1.1\ \mathrm{k}\Omega$, we get $D_C \approx 190\ \mathrm{cm}^2/\mathrm{s}$, which is similar to typical values obtained in eSLG [19]. This is not surprising, because the charge carrier mobility in our samples is with $\mu = (R_{sq}en)^{-1} \approx 1900\ \mathrm{cm}^2/\mathrm{Vs}$ reasonably close to the mobility of our eSLG devices [19].

But this value of D_C means that we observe a difference between the charge diffusion coefficient D_C and D_S of a factor 45 to 80 (compare Table 8.1) in contrast to $D_C \approx D_S$ in eSLG [19]. D_S and D_C can in principle be different as observed by Weber *et al.* [22] in a two-dimensional electron gas. Here the effect is attributed to electron-electron interactions but was significantly smaller than in our results. In FLG a slight difference of $\sim 20\%$ between the two coefficients is found [5], but that difference is not comparable to the observation here. We therefore do not expect a difference between the diffusion coefficient obtained from charge transport measurements and from Hanle precession measurements. While we cannot explain the observed difference, yet, we can exclude some possible explanations for it.[3]

We do not expect the D_C value to be incorrect as the observed charge transport is comparable to eSLG. One aspect though, that could result in a wrong D_C value, are extra current paths next to the MLEG strip which would result in a change of the observed R_{sq}. We can exclude this by carefully controlling the etched structures with a scanning electron microscope (SEM) and by confirming that contacts of different MLEG strips show no conduction between each other.

The charge carrier density n was determined by Hall measurements on similar samples but not on the spin transport samples themselves, therefore there could be an error in the value for n that would lead to an incorrect value for the DOS. The highest values for n, measured on MLEG samples on SiC(0001), under the described growth conditions, are around $n \approx 1 \times 10^{13}\ \mathrm{cm}^{-2}$ which leads to $D_C \approx 100\ \mathrm{cm}^2/\mathrm{s}$. This changes D_C by less than a factor of 2 and smaller values for n would only increase the calculated value for D_C. Hence, also this aspect does not explain the difference between D_S and D_C.

Another possibility would be a wrongly assumed DOS. Though, to result in values for D_C similar to D_S, we would need a DOS as high as ~ 50 times the DOS of BLG. But we can be sure that we do not have such a DOS in our system because similar material to that used in our studies shows the typical quantum Hall effect (QHE) of eSLG [9, 23].

Since we do not find any explanation for the difference between D_C and D_S in the way D_C is determined, let us have a look at D_S. D_S is obtained by the fit of the Hanle precession data in the same way as in earlier experiments [1, 5, 13, 19]. Therefore the fitting procedure cannot explain the difference in the values, as the result for eSLG, $D_C \approx D_S$, is based on fits to measurements on eSLG using the same procedure. Next to that, we can confirm the value for D_S in a different way. As mentioned before, the small value for D_S leads to a relatively small value for λ. The order of magnitude of this value can be confirmed by comparing the change of R_{nl} with L. By fitting an exponential decay [12] to the two R_{nl} values versus L for the data obtained at $4.2\ \mathrm{K}$ (see Table 8.1, fit not shown), we receive $\lambda \approx 0.5\ \mu\mathrm{m}$ in agreement with the order of magnitude of λ obtained from our fitted τ and D_S.[4] With $D_S = D_C \approx 200\ \mathrm{cm}^2/\mathrm{s}$ and

---

[3] The difference between the measured value for D_C and D_S can be explained by the increase of the effective g-factor due to the influence of localized states in the buffer layer as discussed in Chapter 9.

[4] This analysis is not conclusive as the polarization of the contact, and hence the induced spin accumulation, can vary between different contacts, but allows a rough estimate of the order of magnitude of λ. The same analysis has been performed for the other two devices leading to the same result.

$\tau \approx 2$ ns we would receive a λ of one order of magnitude larger.

While λ is confirmed, there is still the possibility that the prefactor of the precession term in the Bloch equation (8.1) is wrong, which would affect linearly the determination of D_S and $1/\tau$. This would be the case, if the effective Landé factor g is changed in our system. But the increase of g by a factor of ~ 50 is needed, to result in our measured D_S. This is unlikely, also since $g \approx 2$ was confirmed for epitaxial multilayer graphene on the C-face of SiC [24].[3]

A change of D_S can only be caused by the substrate as we expect the graphene to be comparable to eSLG [7] and growth related defects like grain boundaries do not show a strong effect on D_S and τ for CVD grown single layer graphene on $\mathrm{SiO_2}$ [6]. One of the substrate related effects could be inhomogeneities of the graphene thickness and doping at terrace step edges [7] and scattering potentials resulting from that. However, this is relatively unlikely since step edges are not resulting in a discontinuity of the graphene layer [7]. On the other hand, the out of plane electric field between the bulk SiC and the buffer layer [7] could have an effect on the spin transport.

Another possible reason for the change in the spin transport properties could be related to the buffer layer. Its topology is graphene-like, though a part of the C atoms is covalently bonded to the underlying Si atoms. Therefore, the layer is electrically inactive and only weakly interacts with graphene layers on top [25]. The buffer layer does not seem to affect charge transport, at least not the measured resistance or the QHE [7], although it influences the temperature dependence of the charge carrier mobility [26]. However, localized states in the buffer layer could act as hopping sites for electron spins and could influence the spin relaxation and the spin diffusion. By spins hopping into these states and back, D_S could be reduced without affecting R_{sq} and therefore the determined D_C (as we do not include these extra states in the DOS).[3] This kind of localized states could also originate from Al clusters in the $\mathrm{AlO_x}$ barrier. When depositing the barrier, some of the Al atoms could cluster and if their size exceeds some certain limit, part of the Al could stay non-oxidized. Those clusters would have a high DOS compared to the MLEG and could therefore have a relatively strong influence on the diffusion. This effect is unlikely, as we do not see it for eSLG on $\mathrm{SiO_2}$ but the less rough surface of MLEG on SiC and the resulting difference in the growth mechanism could result in this clustering. Here it would be interesting to produce samples with the $\mathrm{AlO_x}$ barrier only locally below the contacts as discussed in Ref. [13] to compare the spin transport properties with the here reported results.

One other effect that could affect the measurements is the influence that the $\mathrm{Ar(95\%)/H_2(5\%)}$ cleaning at $350°\mathrm{C}$ could have on the buffer layer. F. Speck *et al.* [26] discuss the intercalation of hydrogen in epitaxial graphene on SiC which leads to the transformation of the buffer layer into an extra graphene layer. Though the discussed experiment uses about 1 bar pure hydrogen at $550°\mathrm{C}$ for 75 minutes, our cleaning step could partly intercalate hydrogen below the graphene layer and this could lead to extra transport channels and influence the transport measurements.

Non of these considerations above led to a conclusive explanation of the observed difference between the diffusion coefficients obtained from charge and spin transport measurements. Therefore we have to wait for further measurements to determine if the difference is based on the way those values are obtained or if there is a difference between charge and spin diffusion in MLEG on SiC(0001). The effect of the buffer layer can be addressed by measuring spin transport on quasi freestanding MLEG on SiC [26] (see Chapter 9) and general substrate related effects can be examined by transferring MLEG to $\mathrm{SiO_2}$ [27].

8.5 Conclusions

In summary, we present a fast and easy process to prepare (spin) transport devices on wafer scale graphene by the example of MLEG. With this technique, we produced lateral spin-valve devices on MLEG and performed spin-valve and Hanle spin precession measurements between $T = 4.2$ K and RT. In the Hanle measurements, we observe exceptionally high values for τ of up to $\tau = 2.3\ \mathrm{ns}$ and very small values for D_S of $D_S < 5\ \mathrm{cm^2/s}$, resulting in a reduction of λ by a factor of 2 to 3 compared to eSLG. We observe a significant difference between the diffusion coefficient obtained from charge and spin transport measurements, which we discuss but cannot explain, yet. Finally we present the temperature dependence of the spin transport and show a decrease for τ, D_S, λ and R_{nl} with increasing temperature, that can be linked to electron-phonon scattering or Coulomb scattering on trapped charges in the SiC substrate.

Note added. A theoretical model that can explain the reported values for τ and D_S is discussed in the next chapter.

References

[1] N. Tombros, C. Józsa, M. Popinciuc, H. T. Jonkman, and B. J. van Wees, “Electronic Spin Transport and Spin Precession in Single Graphene Layers at Room Temperature,” *Nature (London)* **448**, pp. 571–574, 2007.

[2] W. Han, K. Pi, K. M. McCreary, Y. Li, J. J. I. Wong, A. Swartz, and R. K. Kawakami, “Tunneling Spin Injection into Single Layer Graphene,” *Phys. Rev. Lett.* **105**(16), p. 167202, 2010.

[3] W. Han and R. K. Kawakami, “Spin Relaxation in Single-Layer and Bilayer Graphene,” *Phys. Rev. Lett.* **107**(4), p. 047207, 2011.

[4] T.-Y. Yang, J. Balakrishnan, F. Volmer, A. Avsar, M. Jaiswal, J. Samm, S. R. Ali, A. Pachoud, M. Zeng, M. Popinciuc, G. Güntherodt, B. Beschoten, and B. Özyilmaz, “Observation of Long Spin-Relaxation Times in Bilayer Graphene at Room Temperature,” *Phys. Rev. Lett.* **107**(4), p. 047206, 2011.

[5] T. Maassen, F. K. Dejene, M. H. D. Guimarães, C. Józsa, and B. J. van Wees, “Comparison between Charge and Spin Transport in Few-layer Graphene,” *Phys. Rev. B* **83**(11), p. 115410, 2011.

[6] A. Avsar, T.-Y. Yang, S. Bae, J. Balakrishnan, F. Volmer, M. Jaiswal, Z. Yi, S. R. Ali, G. Güntherodt, B. H. Hong, B. Beschoten, and B. Özyilmaz, “Toward Wafer Scale Fabrication of Graphene Based Spin Valve Devices,” *Nano Lett.* **11**(6), pp. 2363–2368, 2011.

[7] P. N. First, W. A. de Heer, T. Seyller, C. Berger, J. A. Stroscio, and J.-S. Moon, “Epitaxial Graphenes on Silicon Carbide,” *MRS Bull.* **35**, pp. 296–305, 2010.

[8] C. Virojanadara, M. Syväjarvi, R. Yakimova, L. I. Johansson, A. A. Zakharov, and T. Balasubramanian, “Homogeneous Large-Area Graphene Layer Growth on 6H-SiC(0001),” *Phys. Rev. B* **78**, p. 245403, 2008.

[9] A. Tzalenchuk, S. Lara-Avila, A. Kalaboukhov, S. Paolillo, M. Syvajarvi, R. Yakimova, O. Kazakova, J. T. J. B. M., V. Fal’ko, and S. Kubatkin, “Towards a Quantum Resistance Standard Based on Epitaxial Graphene,” *Nat. Nanotechnol.* **5**, pp. 186–189, 2010.

[10] K. V. Emtsev, A. Bostwick, K. Horn, J. Jobst, G. L. Kellogg, L. Ley, J. L. McChesney, T. Ohta, S. A. Reshanov, J. Rohrl, E. Rotenberg, A. K. Schmid, D. Waldmann, H. B. Weber, and T. Seyller, “Towards Wafer-Size Graphene Layers by Atmospheric Pressure Graphitization of Silicon Carbide,” *Nat. Mat.* **8**(3), pp. 203–207, 2009.

[11] P. T. B. Shaffer, “A Review of the Structure of Silicon Carbide,” *Acta Crystallogr. B* **B25**, p. 477, 1969.

[12] J. Fabian, A. Matos-Abiague, C. Ertler, P. Stano, and I. Žutić, “Semiconductor Spintronics,” *Acta Phys. Slov.* **57**, pp. 565–907, 2007.

[13] M. Popinciuc, C. Józsa, P. J. Zomer, N. Tombros, A. Veligura, H. T. Jonkman, and B. J. van Wees, “Electronic Spin Transport in Graphene Field-Effect Transistors,” *Phys. Rev. B* **80**(21), p. 214427, 2009.

[14] T. Maassen, I. J. Vera-Marun, M. H. D. Guimarães, and B. J. van Wees, “Contact-Induced Spin Relaxation in Hanle Spin Precession Measurements,” *Phys. Rev. B* **86**, p. 235408, 2012.

[15] I. J. Vera-Marun, V. Ranjan, and B. J. van Wees, “Nonlinear Detection of Spin Currents in Graphene with Non-Magnetic Electrodes,” *Nat. Phys.* **8**(4), pp. 313–316, 2012.

[16] F. L. Bakker, A. Slachter, J.-P. Adam, and B. J. van Wees, “Interplay of Peltier and Seebeck Effects in Nanoscale Nonlocal Spin Valves,” *Phys. Rev. Lett.* **105**, p. 136601, 2010.

[17] S. Tanabe, Y. Sekine, H. Kageshima, M. Nagase, and H. Hibino, “Carrier Transport Mechanism in Graphene on SiC(0001),” *Phys. Rev. B* **84**, p. 115458, 2011.

[18] D. B. Farmer, V. Perebeinos, Y.-M. Lin, C. Dimitrakopoulos, and P. Avouris, “Charge Trapping and Scattering in Epitaxial Graphene,” *Phys. Rev. B* **84**, p. 205417, 2011.

[19] C. Józsa, T. Maassen, M. Popinciuc, P. J. Zomer, A. Veligura, H. T. Jonkman, and B. J. van Wees, “Linear Scaling between Momentum and Spin Scattering in Graphene,” *Phys. Rev. B* **80**(24), p. 241403(R), 2009.

[20] J. Martin, N. Akerman, G. Ulbricht, T. Lohmann, J. H. Smet, K. von Klitzing, and A. Yacoby, “Observation of Electron-Hole Puddles in Graphene Using a Scanning Single-Electron Transistor,” *Nat.*

Phys. **4**, pp. 144–148, 2008.

[21] C. Ertler, S. Konschuh, M. Gmitra, and J. Fabian, "Electron Spin Relaxation in Graphene: The Role of the Substrate," *Phys. Rev. B* **80**(4), p. 041405, 2009.

[22] C. P. Weber, N. Gedik, J. E. Moore, J. Orenstein, J. Stephens, and D. D. Awschalom, "Observation of Spin Coulomb Drag in a Two-Dimensional Electron Gas," *Nature (London)* **437**, pp. 1330–1333, 2005.

[23] J. Jobst, D. Waldmann, F. Speck, R. Hirner, D. K. Maude, T. Seyller, and H. B. Weber, "Quantum Oscillations and Quantum Hall Effect in Epitaxial Graphene," *Phys. Rev. B* **81**(19), p. 195434, 2010.

[24] Y. J. Song, A. F. Otte, Y. Kuk, Y. Hu, D. B. Torrance, P. N. First, W. A. de Heer, H. Min, S. Adam, M. D. Stiles, A. H. MacDonald, and J. A. Stroscio, "High-Resolution Tunnelling Spectroscopy of a Graphene Quartet," *Nature (London)* **467**(7312), pp. 185–189, 2010.

[25] K. V. Emtsev, F. Speck, T. Seyller, L. Ley, and J. D. Riley, "Interaction, Growth, and Ordering of Epitaxial Graphene on SiC0001 Surfaces: A Comparative Photoelectron Spectroscopy Study," *Phys. Rev. B* **77**, p. 155303, 2008.

[26] F. Speck, J. Jobst, F. Fromm, M. Ostler, D. Waldmann, M. Hundhausen, H. B. Weber, and T. Seyller, "The Quasi-Free-Standing Nature of Graphene on H-Saturated SiC(0001)," *Appl. Phys. Lett.* **99**(12), p. 122106, 2011.

[27] D. S. Lee, C. Riedl, B. Krauss, K. von Klitzing, U. Starke, and J. H. Smet, "Raman Spectra of Epitaxial Graphene on SiC and of Epitaxial Graphene Transferred to SiO2," *Nano Lett.* **8**(12), pp. 4320–4325, 2008.

Chapter 9

Localized states influence spin transport in epitaxial graphene

Abstract

We developed a spin transport model for a diffusive channel with coupled localized states that result in an effective increase of spin precession frequencies and a reduction of spin relaxation times in the system. We apply this model to Hanle spin precession measurements obtained on monolayer epitaxial graphene on SiC(0001) (MLEG). Combined with newly performed measurements on quasi-free-standing monolayer epitaxial graphene on SiC(0001) our analysis shows that the different values for the diffusion coefficient measured in charge and spin transport measurements on MLEG and the high values for the spin relaxation time can be explained by the influence of localized states arising from the buffer layer at the interface between the graphene and the SiC surface.

Published as:
T. Maassen, J. J. van den Berg, E. H. Huisman, H. Dijkstra, F. Fromm,
T. Seyller, and B. J. van Wees,
Phys. Rev. Lett. **110**, 067209 (2013).

9.1 Introduction

The spin dynamics in the diffusive transport regime are, in general, described by the Bloch equation for the spin chemical potential $\vec{\mu_S}$ that describes the three dimensional spin accumulation [1]:

$$\frac{d\vec{\mu_S}}{dt} = D\nabla^2\vec{\mu_S} - \frac{\vec{\mu_S}}{\tau} + \vec{\omega_L} \times \vec{\mu_S} \tag{9.1}$$

with the diffusion coefficient D, the spin relaxation time τ, and the Larmor frequency $\vec{\omega_L} = g\mu_B/\hbar\,\vec{B}$, that describes the spin precession in a perpendicular magnetic field $\vec{B}$ with the gyromagnetic factor g (g-factor, $g = 2$ for free electrons) and the Bohr magneton μ_B. Experimentally, spin transport is commonly examined by Hanle spin precession measurements (Fig. 9.1 (a)) that are fitted with the solutions of the time-independent Bloch equation (9.1) with $d\mu_S/dt = 0$. Those fits result in D, τ, and the spin relaxation length $\lambda = \sqrt{D\tau}$. However, the fits are invariant under the transformation $D \to c\tilde{D}$, $\tau \to \tilde{\tau}/c$, $g \to c\tilde{g}$ leaving the scaling factor c undefined. To unambiguously define the parameters, D can be independently determined using the diffusion coefficient from charge transport measurements D_C and the Einstein relation $D_C = (R_{sq}e^2\nu(E_F))^{-1}$.[1] Here R_{sq} is the square resistance, e the electron charge and $\nu(E_F)$ the density of states (DOS) of the diffusive channel at the Fermi energy.

Spin transport in graphene has been extensively studied in recent years [3–16]. Because of weak spin-orbit coupling, $g = 2$ is commonly assumed to fit Hanle precession data (and define c) [3–15]. This was justified for exfoliated single layer graphene (eSLG) as it was shown that $D \approx D_C$ [5]. On the contrary, recent results on monolayer epitaxial graphene on SiC(0001) (MLEG) [17, 18] show $D \ll D_C$ along with very high values for τ [11].[2]

9

In this chapter we introduce a model that can explain an apparent difference between D and D_C by the increase of the effective g-factor caused by localized states coupled to the spin transport channel. Furthermore, we discuss how this model reinterprets the results on MLEG from Ref. [11] and, finally, we compare the results on MLEG to new Hanle precession measurements on quasi-free-standing MLEG on SiC(0001) (QFMLG) [19]. In this material the graphene-like, electrical neutral buffer layer, that is in conventional MLEG located between graphene and the SiC substrate, is absent [20, 21]. The presented analysis points to the buffer layer as the origin of the localized states.

---

[1] Note that for a diffusive channel generally impurity scattering dominates and $D = D_C$ holds, while a difference can arise due to strong electron-electron interactions, e.g., in a two-dimensional electron gas as discussed by Weber *et al.* in Ref. [2].

[2] The results for MLEG from Ref. [11] using 4H-SiC have been reproduced in our lab for 6H-SiC.

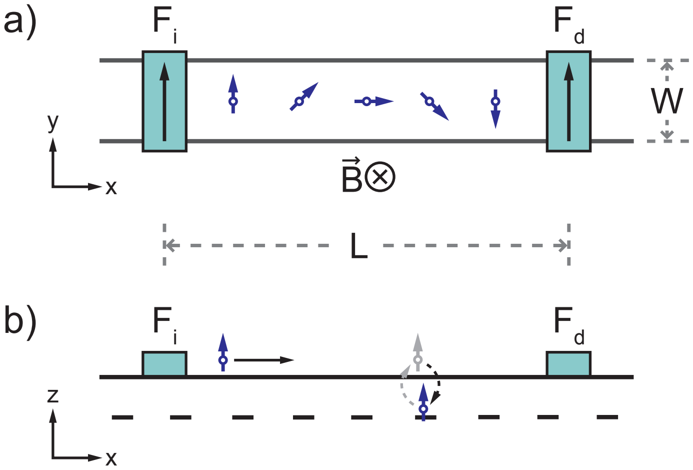

Figure 9.1: (a) Sketch of the Hanle precession geometry with a diffusive channel of width W connected to the ferromagnetic spin injector (F_i) and detector (F_d) on distance L. The out-of-plane magnetic field $\vec{B}$ causes the in-plane injected spins to precess while diffusing through the channel. (b) Extension of the Hanle precession geometry with localized states that are coupled to the channel. The spins can hop into these states and back into the channel while the states are not coupled with each other.

9.2 Spin transport model

To examine the spin transport properties of graphene, usually the non-local measurement geometry is used, consisting of a two dimensional channel with ferromagnetic electrodes that inject and detect electron spins in the graphene plane [3] (Fig. 9.1 (a)).[3] We extend this description with localized states in close proximity to the channel (Fig. 9.1 (b)). We assume the states are electrically coupled to the channel and not coupled with each other.

The spin accumulation in the localized states is represented by $\vec{\mu_S^*}$ and its dynamics can be described by a Bloch equation similar to Eq. (9.1) that does not include a diffusive term but a term for the coupling to the channel.

$$\frac{d\vec{\mu_S^*}}{dt} = -\frac{\vec{\mu_S^*}}{\tau^*} + \vec{\omega_L^*} \times \vec{\mu_S^*} - \Gamma(\vec{\mu_S^*} - \vec{\mu_S}) \qquad (9.2)$$

The Lamor frequency in the localized states $\vec{\omega_L^*} = \omega_L^* \hat{z} \equiv \alpha\omega_L \hat{z}$ can be different from $\vec{\omega_L}$ due to a possibly different g-factor $g^* \equiv \alpha g$. $\tau^* \equiv \beta\tau$ is the spin relaxation time of the localized states and the term $-\Gamma(\vec{\mu_S^*} - \vec{\mu_S})$ describes the flow of spins from the

---

[3] The spins are injected in the plane for small magnetic fields that do not tilt the magnetization of the electrodes out-of-plane.

localized states to the channel and vice versa with the coupling rate $\Gamma = \sigma/(e^2\nu_{LS})$, where σ is the conductance per unit area between the localized states and the channel and ν_{LS} the density of localized states (see Section 9.5.1).[4]

To describe the spin dynamics in the channel we also have to add on the right side of the Bloch equation (9.1) a coupling term

$$\frac{d\vec{\mu_S}}{dt} = D\nabla^2\vec{\mu_S} - \frac{\vec{\mu_S}}{\tau} + \vec{\omega_L} \times \vec{\mu_S} - \eta\Gamma(\vec{\mu_S} - \vec{\mu_S^*}). \tag{9.3}$$

Here we introduce the factor $\eta \equiv \nu_{LS}/\nu$ that accounts for the different DOS in the channel ν compared to the localized states.

The two coupled equations (9.2) and (9.3) can be reduced to *one* effective Bloch equation. For this purpose we consider the system to be in a stationary state with $\frac{d\vec{\mu_S^*}}{dt} = 0$, rewriting Eq. (9.2) to $\vec{\mu_S^*} = \underline{a} \cdot \vec{\mu_S}$ with

$$\underline{a} = \frac{\tau^*\Gamma}{(\tau^*\Gamma+1)^2 + (\tau^*\omega_L^*)^2} \begin{pmatrix} \tau^*\Gamma+1 & -\tau^*\omega_L^* & 0 \\ \tau^*\omega_L^* & \tau^*\Gamma+1 & 0 \\ 0 & 0 & \tau^*\Gamma+1+\frac{(\tau^*\omega_L^*)^2}{\tau^*\Gamma+1} \end{pmatrix}. \tag{9.4}$$

As the spin accumulation is purely perpendicular to the magnetic field in the Hanle geometry[3] ($\vec{\omega_L} \parallel \vec{\omega_L^*} \parallel \vec{B} \parallel \hat{z} \perp \vec{\mu_S}$) we get the effective Bloch equation

$$0 = D\nabla^2\vec{\mu_S} - \frac{\vec{\mu_S}}{\tau^{\text{eff}}} + \vec{\omega_L^{\text{eff}}} \times \vec{\mu_S}. \tag{9.5}$$

Here we introduce the effective spin relaxation time τ^{eff} and the effective precession frequency of the system $\vec{\omega_L^{\text{eff}}} = \omega_L^{\text{eff}}\hat{z}$ defined by

$$\frac{1}{\tau^{\text{eff}}} = \frac{1}{\tau} + \eta\Gamma\frac{1+\tau^*\Gamma+(\tau^*\omega_L^*)^2}{(1+\tau^*\Gamma)^2+(\tau^*\omega_L^*)^2} \tag{9.6}$$

$$\text{and} \quad \omega_L^{\text{eff}} = \omega_L + \eta\Gamma^2\frac{(\tau^*)^2\omega_L^*}{(1+\tau^*\Gamma)^2+(\tau^*\omega_L^*)^2}. \tag{9.7}$$

The expressions for τ^{eff} and ω_L^{eff} are plotted in Fig. 9.2 as a function of the coupling rate Γ (black solid curves). Note that independent from the value of Γ (or the value of η, τ_S^*, or α) the model shows a decrease of τ^{eff} and an increased ω_L^{eff}. Also note that a similar result for the influence of localized states on the spin relaxation time in a channel has been discussed by Tran *et al.* for the 3-terminal spin injection geometry [22] without taking the effect of spin precession on the spin relaxation time into account. An additional difference in the system discussed in Ref. [22] is the fact that the spins are injected into the material via localized states while here the influence is generated by localized states coupled to the transport channel.

---

[4] We assume that the spin orientation is conserved in the coupling process.

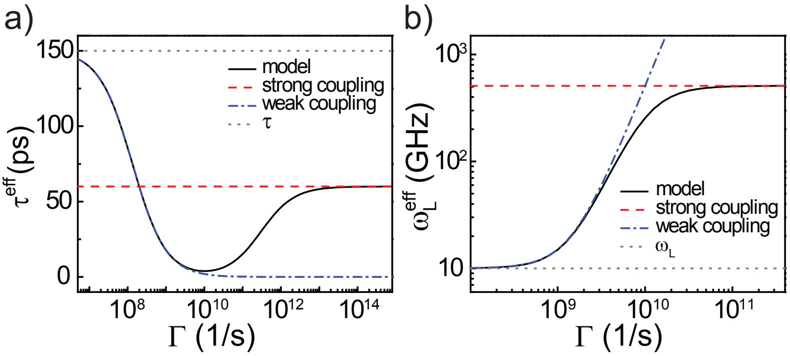

Figure 9.2: The effective spin relaxation time τ^{eff} (a) and Lamor precession frequency ω_L^{eff} (b) as a function of the coupling rate Γ (black solid curves). The asymptotic values in the limit of strong (red, dashed curves) and weak coupling (blue, dash dotted curves). In the graphs we keep $\tau = 150$ ps (gray dotted curve in panel (a)), $\tau^* = 5$ ns, $\omega_L = 10$ GHz (for a magnetic field of $B \approx 50$ mT, gray dotted curve in panel (b)) and $\eta = 50$ constant.

For weak coupling, $\Gamma \ll 1/\tau^*$ (Fig. 9.2, blue dash dotted curves), we have long dwell times for the spins in the localized states and therefore $\tau_{\mathrm{dwell}} \gg \tau^*$. As a consequence all the spins that hop into the localized states will relax before returning into the channel and are therefore "lost" for the spin transport. We get $1/\tau^{\mathrm{eff}} \approx 1/\tau + \eta\Gamma$, while $\omega_L^{\mathrm{eff}} = \omega_L + \mathcal{O}((\tau^*\Gamma)^2)$ stays approximately constant.

For strong coupling, $\Gamma \gg 1/\tau^*$ (Fig. 9.2, red dashed curves), we have to distinguish two cases. For $\omega_L^* \gg \Gamma$, we get the same result for τ^{eff} and ω_L^{eff} as for weak coupling. The strong precession in the localized states dephases all spins that hop into these states and they are lost.

The most interesting is the case of strong coupling, $\Gamma \gg 1/\tau^*$, and low precession frequencies, $\omega_L^* \ll \Gamma$, corresponding to the measurements in MLEG (see below). We get: $1/\tau^{\mathrm{eff}} = 1/\tau + \eta/\tau^*$ and $\omega_L^{\mathrm{eff}} = \omega_L + \eta\omega_L^*$. Both values are in this limit independent from the coupling rate Γ (Fig. 9.2). Note that we get an increased ω_L^{eff} also for $\omega_L = \omega_L^*$ ($g = g^*$). This is due to the fact that that spins dwelling in the localized states account for additional precession and relaxation, but they do not contribute to diffusion.

9.3 Comparison of the model with spin transport data

How does this model relate to the results on spin transport in MLEG on SiC(0001) reported in Ref. [11]? Here an increased τ and a strongly reduced diffusion coefficient ($D \ll D_C$) were observed. As mentioned before, $g = 2$ was assumed in Ref. [11] as there was no reason to assume a change of the g-factor for the graphene channel itself, e.g., a changed spin-orbit coupling. But in graphene combined with localized states, with $\omega_L^{\text{eff}} \equiv \xi\omega_L > \omega_L$ and hence $g^{\text{eff}} \equiv \xi g$, this assumption presents itself wrong. The values that are obtained by fitting assuming $g = 2$ are described by a modified Bloch equation that we receive by dividing Eq. (9.5) by the scaling factor ξ:

$$0 = D^{\text{mod}}\nabla^2\vec{\mu_S} - \frac{\vec{\mu_S}}{\tau^{\text{mod}}} + \vec{\omega_L} \times \vec{\mu_S} \tag{9.8}$$

with $D^{\text{mod}} = D/\xi$ and $\tau^{\text{mod}} = \xi\tau^{\text{eff}}$. The effective spin relaxation time of the system including the localized states can be obtained by either assuming $D = D_C$ for the fit or assuming $g = 2$ and correcting the spin relaxation time with $\tau^{\text{eff}} = \tau^{\text{mod}}/\xi$. The enhanced τ value in Ref. [11] is therefore not an intrinsic property of MLEG on SiC(0001) but is based on assuming a Bloch equation to fit the data which does not take the localized states into account.

Note that the measured spin relaxation length does not change when assuming a different g-factor as $\lambda^{\text{mod}} = (D^{\text{mod}}\tau^{\text{mod}})^{1/2} = (D\tau^{\text{eff}})^{1/2} = \lambda^{\text{eff}} < \lambda$.

The narrow room temperature (RT) Hanle precession measurements on MLEG on SiC(0001) [11] in the center of Fig. 9.3 illustrate the effect of a modified g-factor. The fit to this data (assuming $g = 2$) gives $\tau^{\text{mod}} = 1.3$ ns and $D^{\text{mod}} = 2.4\ \text{cm}^2/\text{s}$, resulting in $\lambda^{\text{eff}} = 0.56\ \mu\text{m}$. Compared to values obtained on eSLG [5] τ^{mod} is increased and D^{mod} is strongly reduced in contrast to the value of $D_C \approx 190\ \text{cm}^2/\text{s}$ obtained in charge transport measurements on the same sample and compared to $D \sim 200\ \text{cm}^2/\text{s}$ typically measured on eSLG [5].[5] At RT this discrepancy between D^{mod} and D_C is resolved using a scaling factor of $\xi = D_C/D^{\text{mod}} \approx 190/2.4 \approx 80$, which yields a spin relaxation time of $\tau^{\text{eff}} \approx 1.3\ \text{ns}/80 \approx 16\ \text{ps}$ and an effective g-factor of $g^{\text{eff}} \approx 80g$. Note that these values for τ^{eff} and g^{eff} are not describing only the graphene layer but the overall system, including the localized states.

To find out where the predicted localized states originate from, we prepared and measured spin transport samples on quasi-free-standing MLEG (QFMLG) as in Ref. [11]. QFMLG is obtained by only growing the electrical neutral buffer layer and no graphene on SiC(0001) and then intercalating the sample by hydrogen as described in Refs. [20] and [21]. Then we are left with a single graphene layer directly on the passivated SiC(0001) surface.

Fig. 9.3 shows Hanle precession curves measured on a QFMLG strip at RT next to the measurements on MLEG from Ref. [11]. The non-local resistance [3, 11] changes slower with $\vec{B}$,[6] comparable to measurements performed on eSLG [5]. The fit (assuming $g = 2$) gives $\tau = 33.6 \pm 0.9$ ps and $D = 75 \pm 2\ \text{cm}^2/\text{s}$ and, therefore, $\lambda = 0.50 \pm 0.01\ \mu\text{m}$. These values are similar to low quality eSLG samples as τ is

---

[5] With comparable D_C in both systems, the transport is still dominated by impurity scattering.

[6] In the two measurements L is slightly different ($1.2\ \mu\text{m}$ vs $1.5\ \mu\text{m}$) which has a minor influences on the width of the curve (FWHM $\sim 1/L$). The difference in the amplitude is not related to λ, which is comparable, but to a different contact polarization. There is no evidence that the minor change in W ($0.7\ \mu\text{m}$ vs $1\ \mu\text{m}$) has a significant influence on the measurements.

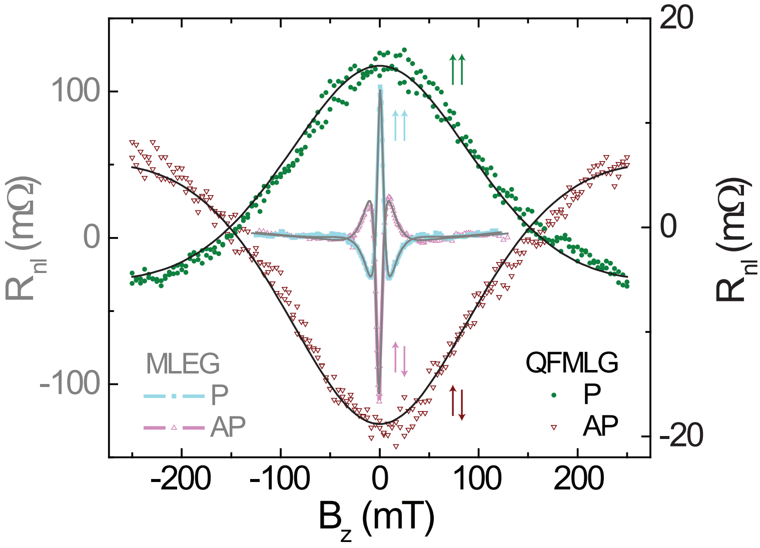

Figure 9.3: RT Hanle precession measurements with aligned (↑↑) and antialigned (↑↓) inner electrodes. The narrow curves in the middle (light colors, gray fitting curves, scale on the left axis) show a measurement on MLEG with $L = 1.2\ \mu\mathrm{m}$ and $W = 0.7\ \mu\mathrm{m}$ from Ref. [11]. The broader measurements enclosing the MLEG measurements (dark colors, black fitting curves, scale on the right axis) were performed on QFMLG with $L = 1.5\ \mu\mathrm{m}$ and $W = 1\ \mu\mathrm{m}$. For both sets of measurements a constant background resistance was subtracted.

reduced by about a factor 4 and D by a factor of approximately 3 compared to typical eSLG values [5]. Compared to MLEG we see an increase of D by a factor of ~ 30 and a decrease of τ by about 40 times. In contrast to the MLEG data we see in charge transport measurements on similar QFMLG samples a diffusion coefficient of $D_C \approx 45\ \mathrm{cm}^2/\mathrm{s} \sim D$.[7] To obtain D_C we use $R_{sq} \approx 3.5\ \mathrm{k}\Omega$ and a hole charge carrier density of $p \approx 6 \times 10^{12}\ \mathrm{cm}^{-2}$ from Hall measurements consistent with results from Ref. [21]. Comparing the results on the two graphene types on SiC(0001) it is interesting to see the striking difference of the spin relaxation times and diffusion coefficients obtained in spin transport measurements but even more important that $D_C \approx D$ in QFMLG, as expected for graphene [5]. Hence, there is no effect of the localized states. Accordingly, they have their origin in the interface between the graphene layer and the SiC substrate as this is the only structural property that is altered between conventional MLEG and QFMLG. Hence, the states could be in the dangling bonds or in the buffer layer. The strong difference of D vs D_C (and

---

[7] The difference between D and D_C (and $D_C < D$) can be explained by the low contact resistances of the measurements $R_C \geq 1.5\ \mathrm{k}\Omega$ and the influence on the spin transport measurements as described in the publication on contact induced spin relaxation by Maassen *et al.*, Ref. [23].

change in ω_L) reported in Ref. [11] points to a strong coupling of the localized states to the channel (see Eq. (9.7) and Fig. 9.2 (b)). The coupling is strongest if the localized states are located in the buffer layer as this one is closest to the channel. If we assume comparable coupling of these states to the channel and between adjacent layers in graphite and considering $\eta \sim 50$ (see below), we get $\Gamma \sim 2 \times 10^{13}\ \mathrm{s}^{-1}$ (see Section 9.5.1), justifying the strong coupling limit (see Fig. 9.2).

Now we can evaluate the model and characterize the localized states by comparing the fitting results on MLEG on SiC(0001) [11] with data obtained on other types of monolayer graphene. To compensate for different D_C values obtained in charge transport measurements on QFMLG and conventional MLEG, we use data on eSLG [5] to compare with results on conventional MLEG [11]. In the limit of strong coupling we get based on Eq. (9.8): $\xi = 1 + \alpha\eta$. Using the typical eSLG values, $\tau = 150\ \mathrm{ps}$ and $D_C = D = 200\ \mathrm{cm}^2/\mathrm{s}$, as the graphene values in the absence of localized states and the MLEG values as D^{mod} and τ^{mod} we get $\xi \approx \eta \approx 80$ at RT, assuming $g^* = g$ ($\alpha = 1$). Together with $\tau^{\mathrm{mod}}/\tau \approx 9$ we obtain $\tau^*/\tau = \beta \approx 10$. Hence, at RT spins relax in the localized states with $\tau^* \approx 1.5\ \mathrm{ns}$ about 10 times slower than in the graphene channel. This enhanced value is very reasonable for a confined state in a material with low spin-orbit coupling.

The presence of localized states can also explain the temperature dependence of spin transport in Ref. [11] in contrast to negligible change for eSLG [3]. By assuming the same values as before for D and τ in the absence of localized states, we get with the data for MLEG at $4\ \mathrm{K}$ $\eta \approx 45$ and $\beta \approx 22$ ($\tau^* \approx 3.3\ \mathrm{ns}$). These results imply less accessible localized states with longer spin relaxation times at low temperature. By assuming a Boltzmann distribution we get from the change in η an activation energy of $E_a \approx 15\ \mathrm{meV}$.

Within our analysis, η describes the ratio of the DOS in the localized states and the channel. With η up to 80 we need a high density of localized states in our system. In MLEG with an electron charge carrier density of $n \approx 3 \times 10^{12}\ \mathrm{cm}^{-2}$ [11] we have a DOS of $\nu \approx 3 \times 10^{13}\ \mathrm{eV}^{-1}\mathrm{cm}^{-2}$. With a density of carbon atoms in the graphene-like buffer layer of $3.8 \times 10^{15}\ \mathrm{cm}^{-2}$ and assuming that every carbon atom contributes one localized state, we get $\eta = 80$ if these states are, e.g., uniformly distributed over an energy range of $\sim 1\ \mathrm{eV}$. Those localized states can be the origin of the strong doping observed in MLEG on SiC(0001) [24].

The observed increase of g in MLEG could in principle also be related to magnetic moments induced by the buffer layer or dangling bonds on the surface of SiC(0001) as described for hydrogenated graphene in Ref. [14]. We argue that this does not apply here since: (i) The effect in MLEG is stronger at RT than at $4\ \mathrm{K}$ in contrast to only low temperature effects in hydrogenated graphene. (ii) We do not see any effects resulting from randomized magnetic moments at low magnetic fields like the "dip" in the spin-valve measurements in Ref. [14]. (iii) The increase of g in MLEG is much bigger than in hydrogenated graphene.

9.4 Conclusions

To summarize, we developed a spin transport model for a diffusive channel with coupled localized states that results in an increased effective g-factor and a reduced spin relaxation time for the transported spins. This model can be applied to any nanoscale systems, where spin transport occurs via extended states which are coupled to localized states. We use it to reinterpret the data from Ref. [11] where an enhanced spin relaxation time and a reduced spin diffusion coefficient were observed. By comparing the data from Ref. [11] to new measurements on QFMLG and typical values on eSLG we identified the buffer layer as possible source for the localized states and the measurements can be related to a g-factor of $g^{\text{eff}} = (45 - 80)g$. Finally we use the model to characterize the spin properties of the localized states in the buffer layer of MLEG on SiC(0001).

9.5 Supplementary Information

9.5.1 Coupling rate between the localized states and the graphene channel

To estimate the coupling rate Γ between the localized states and the graphene channel, we can set up a simplified model based on the coupling between adjacent graphene layers in graphite, as these layers have the same or similar physical distance as the buffer layer to the graphene layer.

In graphite, the conductance in z-direction perpendicular to the layers is per layer $\sigma_{IL} = \sigma_{gr}/(\zeta d)$ where σ_{gr} is the in-plane conductivity of a graphene layer, d the distance between two layers (or between the graphene layer and the localized states) and $\zeta \approx 100$ the ratio between the conductivity within the layers and perpendicular to them [25].

We can now calculate for a current I_{IL} in z-direction:

$$I_{IL} = \frac{V \sigma_{IL} A}{d} = \frac{dQ}{dt} = e\frac{dN}{dt} = e\nu_{LS}\frac{d\mu}{dt}A \tag{9.9}$$

Here $V = \mu/e$ is the voltage between the localized states and the channel, proportional to the difference in the chemical potential, A the area through which the current flows, Q is the total charge that flows, N the number of charge carriers, d is the distance to and ν_{LS} the density of states (DOS) of the localized states, and e the electron charge.

Using the Einstein relation with ν the DOS and D the diffusion coefficient of the graphene channel we get:

$$V\frac{\nu}{\nu_{LS}}\frac{D}{d^2}\frac{1}{\zeta} = \frac{dV}{dt} \tag{9.10}$$

This equation includes the ratio of the DOS of the localized states and the graphene channel, $\eta = \nu_{LS}/\nu$, that was discussed in Section 9.2.

With the coupling rate $\Gamma \sim \frac{1}{V}\frac{dV}{dt}$ we receive :

$$\Gamma = \frac{1}{\eta}\frac{D}{d^2}\frac{1}{\zeta}. \tag{9.11}$$

With this model we get for bilayer graphene with $\zeta = 100$, $\nu = \nu_{LS}$, $d = 0.3\ \mathrm{nm}$ and the typical graphene value $D \approx 0.02\ \mathrm{m^2/s}$

$$\Gamma_{BLG} \approx 10^{15}\ \mathrm{s}^{-1}. \tag{9.12}$$

For our system we have $\eta \sim 50$ while the other parameters stay the same and therefore get

$$\Gamma_{LS} \approx 2 \times 10^{13}\ \mathrm{s}^{-1}. \tag{9.13}$$

This value gives the order of magnitude of the coupling rate between the localized states and the graphene channel. With this value we are in the limit of strong coupling of the system as depicted in Fig. 2 of the main text.

References

[1] J. Fabian, A. Matos-Abiague, C. Ertler, P. Stano, and I. Žutić, "Semiconductor Spintronics," *Acta Phys. Slov.* **57**, pp. 565–907, 2007.

[2] C. P. Weber, N. Gedik, J. E. Moore, J. Orenstein, J. Stephens, and D. D. Awschalom, "Observation of Spin Coulomb Drag in a Two-Dimensional Electron Gas," *Nature (London)* **437**, pp. 1330–1333, 2005.

[3] N. Tombros, C. Józsa, M. Popinciuc, H. T. Jonkman, and B. J. van Wees, "Electronic Spin Transport and Spin Precession in Single Graphene Layers at Room Temperature," *Nature (London)* **448**, pp. 571–574, 2007.

[4] M. Popinciuc, C. Józsa, P. J. Zomer, N. Tombros, A. Veligura, H. T. Jonkman, and B. J. van Wees, "Electronic Spin Transport in Graphene Field-Effect Transistors," *Phys. Rev. B* **80**(21), p. 214427, 2009.

[5] C. Józsa, T. Maassen, M. Popinciuc, P. J. Zomer, A. Veligura, H. T. Jonkman, and B. J. van Wees, "Linear Scaling between Momentum and Spin Scattering in Graphene," *Phys. Rev. B* **80**(24), p. 241403(R), 2009.

[6] W. Han, K. Pi, K. M. McCreary, Y. Li, J. J. I. Wong, A. G. Swartz, and R. K. Kawakami, "Tunneling Spin Injection into Single Layer Graphene," *Phys. Rev. Lett.* **105**(16), p. 167202, 2010.

[7] A. Avsar, T.-Y. Yang, S. Bae, J. Balakrishnan, F. Volmer, M. Jaiswal, Z. Yi, S. R. Ali, G. Güntherodt, B. H. Hong, B. Beschoten, and B. Özyilmaz, "Toward Wafer Scale Fabrication of Graphene Based Spin Valve Devices," *Nano Lett.* **11**(6), pp. 2363–2368, 2011.

[8] W. Han and R. K. Kawakami, "Spin Relaxation in Single-Layer and Bilayer Graphene," *Phys. Rev. Lett.* **107**(4), p. 047207, 2011.

[9] T.-Y. Yang, J. Balakrishnan, F. Volmer, A. Avsar, M. Jaiswal, J. Samm, S. R. Ali, A. Pachoud, M. Zeng, M. Popinciuc, G. Güntherodt, B. Beschoten, and B. Özyilmaz, "Observation of Long Spin-Relaxation Times in Bilayer Graphene at Room Temperature," *Phys. Rev. Lett.* **107**(4), p. 047206, 2011.

[10] S. Jo, D.-K. Ki, D. Jeong, H.-J. Lee, and S. Kettemann, "Spin Relaxation Properties in Graphene Due to Its Linear Dispersion," *Phys. Rev. B* **84**(7), p. 075453, 2011.

[11] T. Maassen, J. J. van den Berg, N. IJbema, F. Fromm, T. Seyller, R. Yakimova, and B. J. van Wees, "Long Spin Relaxation Times in Wafer Scale Epitaxial Graphene on SiC(0001)," *Nano Lett.* **12**(3), pp. 1498–1502, 2012.

[12] M. H. D. Guimarães, A. Veligura, P. J. Zomer, T. Maassen, I. J. Vera-Marun, N. Tombros, and B. J. van Wees, "Spin Transport in High-Quality Suspended Graphene Devices," *Nano Lett.* **12**(7), p. 3512, 2012.

[13] J. Abel, A. Matsubayashi, T. Murray, C. Dimitrakopoulos, D. B. Farmer, A. Afzali, A. Grill, C. Y. Sung, and V. P. LaBella, "Fabrication of an Electrical Spin Transport Device Utilizing a Diazonium Salt/Hafnium Oxide Interface Layer on Epitaxial Graphene Grown on 6 H-SiC(0001)," *J. Vac. Sci. Technol. B* **30**(4), p. 04E109, 2012.

[14] K. M. McCreary, A. G. Swartz, W. Han, J. Fabian, and R. K. Kawakami, "Magnetic Moment Formation in Graphene Detected by Scattering of Pure Spin Currents," *Phys. Rev. Lett.* **109**, p. 186604, 2012.

[15] M. Wojtaszek, I. J. Vera-Marun, T. Maassen, and B. J. van Wees, "Enhancement of Spin Relaxation Time in Hydrogenated Graphene Spin Valve Devices," *Phys. Rev. B* **87**, p. 081402(R), 2013.

[16] B. Dlubak, M.-B. Martin, C. Deranlot, B. Servet, S. Xavier, R. Mattana, M. Sprinkle, C. Berger, W. A. De Heer, F. Petroff, A. Anane, P. Seneor, and A. Fert, "Highly Efficient Spin Transport in Epitaxial Graphene on SiC," *Nat. Phys.* **8**, pp. 557–561, 2012.

[17] C. Virojanadara, M. Syväjarvi, R. Yakimova, L. I. Johansson, A. A. Zakharov, and T. Balasubramanian, "Homogeneous Large-Area Graphene Layer Growth on 6H-SiC(0001)," *Phys. Rev. B* **78**, p. 245403, 2008.

[18] K. V. Emtsev, A. Bostwick, K. Horn, J. Jobst, G. L. Kellogg, L. Ley, J. L. McChesney, T. Ohta, S. A. Reshanov, J. Rohrl, E. Rotenberg, A. K. Schmid, D. Waldmann, H. B. Weber, and T. Seyller, "To-

wards Wafer-Size Graphene Layers by Atmospheric Pressure Graphitization of Silicon Carbide," *Nat. Mater.* **8**(3), pp. 203–207, 2009.

[19] J. J. van den Berg *et al.* in preparation.

[20] C. Riedl, C. Coletti, T. Iwasaki, A. A. Zakharov, and U. Starke, "Quasi-Free-Standing Epitaxial Graphene on SiC Obtained by Hydrogen Intercalation," *Phys. Rev. Lett.* **103**(24), p. 246804, 2009.

[21] F. Speck, J. Jobst, F. Fromm, M. Ostler, D. Waldmann, M. Hundhausen, H. B. Weber, and T. Seyller, "The Quasi-Free-Standing Nature of Graphene on H-Saturated SiC(0001)," *Appl. Phys. Lett.* **99**(12), p. 122106, 2011.

[22] M. Tran, H. Jaffrès, C. Deranlot, J.-M. George, A. Fert, A. Miard, and A. Lemaître, "Enhancement of the Spin Accumulation at the Interface between a Spin-Polarized Tunnel Junction and a Semiconductor," *Phys. Rev. Lett.* **102**(3), p. 036601, 2009.

[23] T. Maassen, I. J. Vera-Marun, M. H. D. Guimarães, and B. J. van Wees, "Contact-Induced Spin Relaxation in Hanle Spin Precession Measurements," *Phys. Rev. B* **86**, p. 235408, 2012.

[24] S. Kopylov, A. Tzalenchuk, S. Kubatkin, and V. I. Fal'ko, "Charge Transfer between Epitaxial Graphene and Silicon Carbide," *Appl. Phys. Lett.* **97**(11), p. 112109, 2010.

[25] K. Matsubara, K. Sugihara, and T. Tsuzuku, "Electrical Resistance in the c Direction of Graphite," *Phys. Rev. B* **41**(2), pp. 969–974, 1990.

Chapter 10

Review and outlook

Abstract

This chapter discusses the results presented in this thesis in the context of research performed by other scientists. It then focuses on the discussion of the dominant spin relaxation mechanism in graphene which is momentarily one of the most interesting questions in the field. In the end of the chapter, we give a general overview of research that should or could be performed in the coming years.

10.1 General discussion

The work presented in this thesis was performed in the period between the end of 2008 and 2012. During this time the research on spin transport in graphene developed from a very new, academic field to an established field of research with consistent results on single layer graphene (SLG) from several groups using non-local Hanle spin precession measurements to probe the spin transport properties [1–6]. At the same time there are still surprises, e.g., the relatively long spin relaxation times in bilayer graphene (BLG) [7, 8] or the results on monolayer epitaxial graphene on SiC(0001) (MLEG) (see Chapter 8) where the spin relaxation time seems enhanced and the diffusion coefficient strongly decreased which can be explained by localized states adjacent to the graphene layer influencing the measurements (see Chapter 9). This thesis presents results crucial to the understanding of the field and some that pose new questions as an outlook on the research to come.

To this day Hanle precession measurements on graphene show spin transport with spin relaxation times and lengths that stay behind theoretical predictions, and earlier works suggested that the properties are limited by the environment of the flake [1, 9]. The influence of the environment has been shown, e.g., by chemical doping of spin transport devices with gold atoms [3], by dipping the devices in water [10], by hydrogenating the graphene [11, 12] or by adding charged impurities using organic nanoparticles [13]. At the same time, the ferromagnetic contacts also influence spin transport in graphene or similar transport channels. This had already been discussed by Popinciuc *et al.* but Chapter 5 further quantifies this influence, which is useful, as to date it is still challenging to produce reproducible fully non-invasive contacts. Chapter 5 also gives general guidelines on how to analyze Hanle precession measurements.

The experiments in Chapter 6 and 7 explain the nature of charge and spin transport in SLG and few-layer graphene (FLG) and show that both spin and charge information are transported in the same manner, and that we see no significant electron-electron interactions in spin transport measurements in graphene. These experiments also give insight in the limiting factors on spin transport in graphene. The increase of the spin relaxation time and length with higher doping concentrations in SLG and FLG and with growing number of graphene layers in FLG indicate the influence of screening effects on the spin transport properties. In both cases electrical screening of spurious electrical potentials is enhanced due to additional charge carriers. These charge carriers are induced by electrical doping or by the increase of the density of states with growing numbers of graphene layers in the case of FLG. The results indicate that the screening of the spurious potentials due to impurities, contaminations or external charges increases the spin relaxation time and length. In Chapter 7 the screening effect is also shown for charge transport measurements in FLG. In the meantime Monte Carlo simulations on spin transport by others, use the change in the band structure to explain the increase of spin relaxation time and length with increasing number of layers [14, 15].

Chapter 8 of this thesis discusses the first spin transport measurements on MLEG on SiC(0001) which are also the first measurements on spin transport in graphene on a different substrate than the commonly used SiO_2. The results are surprising, as the analysis leads to enhanced spin relaxation times and, at the same time, strongly reduced spin diffusion coefficients. The values for the diffusion coefficients obtained in charge transport measurements do not agree with the results from Hanle spin precession measurements, though we expect them to agree based on the results for SLG on SiO_2 (see Chapter 6). We show in Chapter 9 that this puzzling fact can be explained if we take into account not only the graphene as the spin transport channel but if we consider the whole system consisting of the graphene layer, the SiC substrate and the electrically inactive graphene-like buffer layer in between. We introduce a theoretical model that can relate the measured results to spins hopping into localized states in the buffer of MLEG layer while traveling through the graphene channel. If not taken into account in the data analysis, these hopping events seem to result in an increased spin relaxation time and a strongly decreased diffusion coefficient in the channel. In practice, the presence of the localized states reduces the spin relaxation time in the channel while the diffusion coefficient is unchanged. This is an interesting fact observable in case of MLEG that is also supported by measurements on an epitaxial graphene system that lacks the buffer layer (quasi-free-standing monolayer graphene) and does not show any of these effects.

The results on MLEG and the explanation by the discussed model are a good example of the strong influence of the environment on measurements in graphene. The findings of the model are at the same time interesting for other experiments dealing with spin transport processes in close vicinity to localized states.

While the non-local spin transport measurements on graphene from all groups in the field comply, recent local measurements on multilayer graphene on SiC$(000\bar{1})$ [16, 17] seem to disagree with the non-local data. The local measurements are suggested to show around fifty to hundred times longer spin relaxation lengths and times than measured in graphene devices using non-local Hanle measurements. The differences in the results are being related to contact induced spin relaxation limiting non-local measurements, and screening of spurious potentials and enhanced flatness of the graphene layers in the system of the local measurements. In Chapter 5 we point out that typical non-local measurements [7, 18, 19] are not limited by the contact resistances in the order of a few ten $\mathrm{k}\Omega$. Contacts in the $\mathrm{M}\Omega$ range as in the local measurements discussed in Ref. [16] do not further improve the measured results. The screening of spurious potentials in the multilayer graphene on SiC$(000\bar{1})$ also cannot be the reason for the increase of τ and λ in the local measurements as the results of the non-local measurements on FLG in Chapter 7 show. Here the growth of the spin relaxation time is linear with the number of layers and saturates around 15–20 layers. The measurements on epitaxial graphene on SiC(0001) in Chapter 8 and 9 or on h-BN [20] also do not show strong effects enhancing the spin relaxation times due to the flat substrate. So the strong differences in the signals obtained in local vs non-local measurements, as well as a feasibility of the local measurements only at low temperatures, in contrast to non-local measurements, is currently not understood. It would be interesting to see results of non-local Hanle precession measurements on multilayer graphene on SiC($000\overline{1}$).

10.2 Spin relaxation mechanisms in graphene

One of the most interesting questions in the field stays which spin relaxation mechanism is dominant. When talking about the spin relaxation mechanism in graphene, usually the Elliott-Yafet (EY) and the D'yakonov-Perel' mechanism (DP) are considered [21]. These two mechanisms were already discussed in Chapter 2, Section 2.5. Both are based on spin-orbit coupling (SOC), while the main difference is that in case of DP, there is spin relaxation *in between* scattering events and for EY the relaxation takes place *during* scattering events. Therefore those mechanisms seem not comparable but recently a unified theory of the two has been proposed [22].

The quest for the dominant spin relaxation mechanism in graphene seemed to be settled after experimental results suggested a coupling of the spin relaxation in SLG and FLG to momentum relaxation ($\tau \propto \tau_p$ and therefore EY) [18, 23, 24] but became again under debate after results on bilayer graphene pointed to intrinsic SOC in graphene ($\tau \propto 1/\tau_p$ and therefore DP) [7, 8].

Most theoretical work points to the dominance of DP [25, 26], so the challenge is to design experiments that can clearly show the dominant mechanism. It was expected that an ideal experiment would be to perform measurements on a set of spin valve devices with varying mobility but otherwise identical properties [27]. Recent results on spin transport devices with varied mobility due to charged impurities did not show any significant influence on the spin relaxation time in SLG, though [13]. At the same time it is difficult to achieve a set of identical spin transport devices as it is challenging to fabricate graphene samples with uniform ferromagnetic contacts. Therefore researchers tried to identify the spin relaxation mechanism experimentally using the fact that both the spin relaxation time τ and the diffusion coefficient D vary with changing charge carrier density in graphene (see Chapters 6 and 7 and Refs. [8, 18, 23, 24]). When plotting the spin relaxation length λ vs D or τ vs D we see a linear dependence (Fig. 6.4 in Chapters 6 and Fig. 7.7 (a) in Chapter 7, see also Ref. [8] at low temperature). Using $\lambda = \sqrt{\tau D}$ and $D \propto \tau$ these linear dependences result in $\tau \propto \tau_p$ and therefore it was assumed that EY is the dominant spin relaxation mechanism for SLG. This was in stark contrast to results on bilayer graphene that showed in similar plots the opposite trend ($\tau \propto 1/\tau_p$) [8] which matched well with results by Yang *et al.* [7] who measure a reduction of τ with increasing mobility for different samples. DP-like behavior[1] was also observed for SLG by Pi *et al.* [3] and Wojtaszek *et al.* [12] who see an increase of τ, when reducing the graphene mobility with chemically doping of the graphene with gold adatoms or by hydrogenation, respectively. In the last two cases it cannot be ruled out though, that there are other effects responsible for this increase of τ. Results on high mobility devices using suspended graphene [28] and graphene on h-BN [20] do not show a decrease of τ, which also questions if the spin transport in lower mobility samples was limited by DP. At the same time the obtained τ is also not significantly increased [20, 28], giving no evidence for a dominance of EY.

What was not taken into account in the analysis of the studies showing $\tau \propto \tau_p$, by plotting points for different gate voltages, is that the points were obtained at different charge carrier densities and therefore different E_F. The full dependency of τ on τ_p for EY in graphene is described by

$$\tau_{\mathrm{EY}} = \frac{E_F^2}{\Delta_{\mathrm{EY}}^2}\tau_p, \tag{10.1}$$

with the effective spin-orbit coupling of EY-like[1] scattering centers Δ_{EY} [21, 25]. The points in the linear scaling plots of Chapters 6 and 7 and the other papers were obtained at different E_F. The linear scaling can therefore not be related to EY [21] but can be attributed to other extrinsic factors like locally enhanced SOC due to, e.g., impurities that cause sp3-hybridization of the carbon lattice and result in EY-like scattering [29]. The scaling shown in Eq. (10.1) can maybe also explain the increase of τ with higher charge carrier concentrations shown in Chapters 6 and 7.

Jo *et al.* present experimental results following the scaling of Eq. (10.1) [5], and also the spin transport measurements on CVD graphene on $\mathrm{SiO_2}$ [4] can be explained by EY induced by defects, probably as there are in general more impurities in CVD graphene than in exfoliated graphene [21].

Recent theoretical work suggests that the DP mechanism is dominant in graphene [30] but SOC, induced by inversion breaking related to electric fields, adatoms, the substrate or ripples results in random-Rashba-fields (RRF), is responsible for the observed effects [21, 30, 31]. RRF result in EY-like scaling of τ vs τ_p, and DP can show both a EY-like or a DP-like relation between τ and τ_p [30].

To summarize, DP seems to be the dominant spin relaxation mechanism in graphene, and depending on the strength of the RRF we see EY-like or DP-like properties when analyzing measurements [30]. Spin relaxation is only caused by SOC, while charged impurities do not show any effect as shown in Ref. [13].

To describe measured data Han and Kawakami [8] and Zomer *et al.* [20] use the

---

[1] The expressions “DP-like” and “EY-like” refer to spin relaxation mechanisms that are not the classical DP or EY mechanisms but result in the same scaling of τ vs τ_p.

combination of EY-like and DP-like spin relaxation rates

$$\frac{1}{\tau} = \frac{1}{\tau_{\mathrm{EY}}} + \frac{1}{\tau_{\mathrm{DP}}}. \tag{10.2}$$

Here the indices "EY" and "DP" describe the relation between τ and τ_p. With the formula for DP [30]

$$\tau_{\mathrm{DP}} = \frac{\hbar^2}{4\Delta_{\mathrm{DP}}^2}\frac{1}{\tau_p} \tag{10.3}$$

(Δ_{DP} is the effective DP-like spin-orbit coupling), the values of τ and τ_p can be plotted in such a way, that the contributions from EY-like and DP-like spin relaxation can be easily extracted. Therefore one has to plot the data following

$$\frac{E_F^2\tau_p}{\tau} = \Delta_{\mathrm{EY}}^2 + \frac{4\Delta_{\mathrm{DP}}^2}{\hbar^2}(E_F^2\tau_p^2) \tag{10.4}$$

as discussed in Ref. [20]. Zomer *et al.* extract from this equation the scattering rates for SLG on SiO_2 from Ref. [18] and for SLG on h-BN from their experiments [20]. The influence from EY-like and DP-like spin relaxation is in both cases comparable.

10.3 Outlook

The field of spin transport in graphene is rapidly developing, and the number of the involved scientists and research groups is growing. In this section we will comment on interesting open questions in the field and possible future research.

As mentioned before, the main quest is to find the limiting factors on spin transport in graphene, and therefore, it is important to identify the spin relaxation mechanism in graphene. To observe the intrinsic spin transport properties of graphene, it has to be measured without significant influences from the environment. That is done by measuring graphene that is either suspended, only in contact with h-BN or in a stack of graphene layers. Though suspended graphene devices examined by Guimarães *et al.* [28] approached the high mobility properties of ideal graphene the measurements did not show a significant change of τ. This was related to the fact, that the transport area is surrounded by supported areas, that strongly influence the diffusive transport and mask the spin transport properties of the suspended region [28]. Zomer *et al.* [20] measured spin transport on graphene on h-BN. While they clearly saw an enhancement of the spin transport properties, the graphene could not be cleaned from contaminations from the production process as the standard cleaning method reduced the spin injection efficiency of the Co contacts. Therefore the performance of the devices was limited [20]. Hence, by finding a cleaning method for graphene on h-BN or by encapsulating graphene in h-BN, higher quality spin transport devices closer to the intrinsic properties of graphene could be achieved.

The same would be the case if researchers find a way to fully suspend graphene devices including suspended ferromagnetic contacts.

Another important task is it to achieve reproducible, non-invasive high quality contacts on graphene. These would enable to get closer to identical spin transport devices with varying mobilities that can give new insights on the spin relaxation mechanism in graphene. One way to produce better contacts could be to use optimized deposition techniques for the tunnel barrier like atomic layer deposition. Reproducible contacts would especially be useful for large area graphene like CVD grown or epitaxial graphene samples. Here a lot of comparable devices can be produced on the same wafer, resulting in higher yield and identical samples and therefore good result statistics.

Another interesting research direction is spin transport through graphene gate controlled p-n-junctions to see the influence of the charge carrier type, and the p-n-carrier type transition on spin transport. Downscaling samples to nanoribbons or quantum dots can be used to examine the one or zero dimensional spin properties of graphene as well as the influence of the edges of the graphene layers.

Epitaxial graphene on SiC offers a great variety of possibilities for future research. Next to the upscalability that offers statistics for spin transport studies and the possible entrance to large scale spin transport device production, the combination of graphene with SiC gives interesting prospects. The localized states in the buffer layer of MLEG on SiC(0001) should be further explored to understand the strong influence on the measurements on MLEG which points to a high density of localized states. In future research these states could be used to store spin information. Furthermore, combining graphene with the semi-conductor properties of SiC can offer interesting concepts as has been shown for charge transport [32]. The combination of h-BN and SiC likewise is a promising concept [33]. To store spin information it is also interesting to think about combinations of graphene with organic semiconductors that offer very long spin relaxation times [34]. The measurements on multilayer epitaxial graphene on SiC($000\bar{1}$) by Dlubak *et al.* [16] should be compared to non-local measurements in the same system to relate the measured results to the data obtained by other groups and to rule out spurious effects.

First results on spin pumping in graphene show new possibilities to inject spins into the material. Here the precessional motion of the magnetization of a ferromagnet on top of a graphene layer is excited by a micro-wave signal. Due to the precession of the magnetization and the conservation of the total angular momentum, the ferromagnet emits spins that are injected in the graphene [35, 36].

Finally, the techniques developed to study spin transport in graphene are well suited to examine the spin transport properties of other two dimensional crystals like, e.g, molybdenum disulfide which offers strong SOC.

At the same time, there are still a lot of possibilities to explore for graphene spintronics. The existing results are already promising, and there is good hope that there are more exciting insights to come.

References

[1] N. Tombros, C. Józsa, M. Popinciuc, H. T. Jonkman, and B. J. van Wees, "Electronic Spin Transport and Spin Precession in Single Graphene Layers at Room Temperature," *Nature (London)* **448**, pp. 571–574, 2007.

[2] M. Shiraishi, M. Ohishi, R. Nouchi, N. Mitoma, T. Nozaki, T. Shinjo, and Y. Suzuki, "Robustness of Spin Polarization in Graphene-Based Spin Valves," *Adv. Funct. Mater.* **19**, pp. 3711–3716, 2009.

[3] K. Pi, W. Han, K. M. McCreary, A. G. Swartz, Y. Li, and R. K. Kawakami, "Manipulation of Spin Transport in Graphene by Surface Chemical Doping," *Phys. Rev. Lett.* **104**(18), p. 187201, 2010.

[4] A. Avsar, T.-Y. Yang, S. Bae, J. Balakrishnan, F. Volmer, M. Jaiswal, Z. Yi, S. R. Ali, G. Güntherodt, B. H. Hong, B. Beschoten, and B. Özyilmaz, "Toward Wafer Scale Fabrication of Graphene Based Spin Valve Devices," *Nano Lett.* **11**(6), pp. 2363–2368, 2011.

[5] S. Jo, D.-K. Ki, D. Jeong, H.-J. Lee, and S. Kettemann, "Spin Relaxation Properties in Graphene Due to Its Linear Dispersion," *Phys. Rev. B* **84**(7), p. 075453, 2011.

[6] B. Birkner, D. Pachniowski, A. Sandner, M. Ostler, T. Seyller, J. Fabian, M. Ciorga, D. Weiss, and J. Eroms, "Annealing-induced Magnetic Moments Detected by Spin Precession Measurements in Epitaxial Graphene on SiC," *Phys. Rev. B* **87**, p. 081405, 2013.

[7] T.-Y. Yang, J. Balakrishnan, F. Volmer, A. Avsar, M. Jaiswal, J. Samm, S. R. Ali, A. Pachoud, M. Zeng, M. Popinciuc, G. Güntherodt, B. Beschoten, and B. Özyilmaz, "Observation of Long Spin-Relaxation Times in Bilayer Graphene at Room Temperature," *Phys. Rev. Lett.* **107**(4), p. 047206, 2011.

[8] W. Han and R. K. Kawakami, "Spin Relaxation in Single-Layer and Bilayer Graphene," *Phys. Rev. Lett.* **107**(4), p. 047207, 2011.

[9] N. Tombros, S. Tanabe, A. Veligura, C. Józsa, M. Popinciuc, H. T. Jonkman, and B. J. van Wees, "Anisotropic Spin Relaxation in Graphene," *Phys. Rev. Lett.* **101**(4), p. 046601, 2008.

[10] K. M. McCreary, H. Wen, H. Yu, W. Ha, E. Johnston-Halperin, and R. K. Kawakami, "Enhancement of Spin Injection into Graphene by Water Dipping," arXiv:1108.0380v1.

[11] K. M. McCreary, A. G. Swartz, W. Han, J. Fabian, and R. K. Kawakami, "Magnetic Moment Formation in Graphene Detected by Scattering of Pure Spin Currents," *Phys. Rev. Lett.* **109**, p. 186604, 2012.

[12] M. Wojtaszek, I. J. Vera-Marun, T. Maassen, and B. J. van Wees, "Enhancement of Spin Relaxation Time in Hydrogenated Graphene Spin Valve Devices," *Phys. Rev. B* **87**, p. 081402(R), 2013.

[13] W. Han, J.-R. Chen, D. Wang, K. M. McCreary, H. Wen, A. G. Swartz, J. Shi, and R. K. Kawakami, "Spin Relaxation in Single-Layer Graphene with Tunable Mobility," *Nano Lett.* **12**(7), pp. 3443–3447, 2012.

[14] B. Ghosh and S. Misra, "Monte Carlo Simulation Study of Spin Transport in Single Layer Graphene," *J. Appl. Phys.* **110**(4), p. 043711, 2011.

[15] S. Misra, B. Ghosh, V. Nandal, and L. Dubey, "Monte Carlo Simulation Study of Spin Transport in Multilayer Graphene with Bernal Stacking," *J. Appl. Phys.* **112**(2), p. 023708, 2012.

[16] B. Dlubak, M.-B. Martin, C. Deranlot, B. Servet, S. Xavier, R. Mattana, M. Sprinkle, C. Berger, W. A. De Heer, F. Petroff, A. Anane, P. Seneor, and A. Fert, "Highly Efficient Spin Transport in Epitaxial Graphene on SiC," *Nat. Phys.* **8**, pp. 557–561, 2012.

[17] P. Seneor, B. Dlubak, M.-B. Martin, A. Anane, H. Jaffrès, and A. Fert, "Spintronics with Graphene," *MRS Bull.* **37**, pp. 1245–1254, 2012.

[18] C. Józsa, T. Maassen, M. Popinciuc, P. J. Zomer, A. Veligura, H. T. Jonkman, and B. J. van Wees, "Linear Scaling between Momentum and Spin Scattering in Graphene," *Phys. Rev. B* **80**(24), p. 241403(R), 2009.

[19] W. Han, K. Pi, K. M. McCreary, Y. Li, J. J. I. Wong, A. G. Swartz, and R. K. Kawakami, "Tunneling Spin Injection into Single Layer Graphene," *Phys. Rev. Lett.* **105**(16), p. 167202, 2010.

[20] P. J. Zomer, M. H. D. Guimarães, N. Tombros, and B. J. van Wees, "Long-Distance Spin Transport in

High-mobility Graphene on Hexagonal Boron Nitride," *Phys. Rev. B* **86**, p. 161416(R), 2012.

[21] H. Ochoa, A. H. Castro Neto, and F. Guinea, "Elliot-Yafet Mechanism in Graphene," *Phys. Rev. Lett.* **108**, p. 206808, 2012.

[22] P. Boross, B. Dora, A. Kiss, and F. Simon, "A Unified Theory of the Elliott-Yafet and the D'yakonov-Perel' Spin-Relaxation Mechanisms," arXiv:1211.0826.

[23] M. Popinciuc, C. Józsa, P. J. Zomer, N. Tombros, A. Veligura, H. T. Jonkman, and B. J. van Wees, "Electronic Spin Transport in Graphene Field-Effect Transistors," *Phys. Rev. B* **80**(21), p. 214427, 2009.

[24] T. Maassen, F. K. Dejene, M. H. D. Guimarães, C. Józsa, and B. J. van Wees, "Comparison between Charge and Spin Transport in Few-layer Graphene," *Phys. Rev. B* **83**(11), p. 115410, 2011.

[25] D. Huertas-Hernando, F. Guinea, and A. Brataas, "Spin-Orbit-Mediated Spin Relaxation in Graphene," *Phys. Rev. Lett.* **103**(14), p. 146801, 2009.

[26] C. Ertler, S. Konschuh, M. Gmitra, and J. Fabian, "Electron Spin Relaxation in Graphene: The Role of the Substrate," *Phys. Rev. B* **80**(4), p. 041405, 2009.

[27] C. Józsa and B.J. van Wees, "Graphene Spintronics," in *Handbook of Spin Transport and Magnetism*, E.Y. Tsymbal, I. Zutic, Eds. (CRC Press, Boca Raton, FL), pp. 579–598, 2011.

[28] M. H. D. Guimarães, A. Veligura, P. J. Zomer, T. Maassen, I. J. Vera-Marun, N. Tombros, and B. J. van Wees, "Spin Transport in High-Quality Suspended Graphene Devices," *Nano Lett.* **12**(7), pp. 3512–3517, 2012.

[29] A. H. Castro Neto and F. Guinea, "Impurity-Induced Spin-Orbit Coupling in Graphene," *Phys. Rev. Lett.* **103**(2), p. 026804, 2009.

[30] P. Zhang and M. W. Wu, "Electron Spin Relaxation in Graphene with Random Rashba Field: Comparison of the D'yakonov–Perel' and Elliott–Yafet-like Mechanisms," *New J. Phys.* **14**(3), p. 033015, 2012.

[31] D. Huertas-Hernando, F. Guinea, and A. Brataas, "Spin Relaxation Times in Disordered Graphene," *Eur. Phys. J-Spec. Top.* **148**(1), pp. 177–181, 2007.

[32] F. Krach, S. Hertel, D. Waldmann, J. Jobst, M. Krieger, S. Reshanov, A. Schöner, and H. B. Weber, "A Switch for Epitaxial Graphene Electronics: Utilizing the Silicon Carbide Substrate as Transistor Channel," *Appl. Phys. Lett.* **100**(12), p. 122102, 2012.

[33] M. S. Bresnehan, M. J. Hollander, M. Wetherington, M. LaBella, K. A. Trumbull, R. Cavalero, D. W. Snyder, and J. A. Robinson, "Integration of Hexagonal Boron Nitride with Quasi-freestanding Epitaxial Graphene: Toward Wafer-Scale, High-Performance Devices," *ACS Nano* **6**(6), pp. 5234–5241, 2012.

[34] G. Szulczewski, S. Sanvito, and M. Coey, "A Spin of their Own," *Nat. Mater.* **8**, pp. 693–695, 2009.

[35] A. K. Patra, S. Singh, B. Barin, Y. Lee, J.-H. Ahn, E. del Barco, E. R. Mucciolo, and B. Özyilmaz, "Dynamic Spin Injection into Chemical Vapor Deposited Graphene," *Appl. Phys. Lett.* **101**(16), p. 162407, 2012.

[36] Z. Tang, E. Shikoh, H. Ago, K. Kawahara, Y. Ando, T. Shinjo, and M. Shiraishi, "Dynamically-Generated Pure Spin Current in Single-Layer Graphene," arXiv:1211.0124v1.

Appendix A

Fabrication details

While the general sample fabrication was discussed in Chapter 4, we will present in the following some experimental parameters of some of the sample production steps.

A.1 Deep-UV Lithography

We use the EVG-620 Deep-UV Mask Aligner system and specifically designed masks to pattern Ti/Au structures on the SiO_2/Si wafers for samples using mechanically exfoliated graphene and on SiC wafers for epitaxial graphene samples. The process is described below.

Resist spinning The wafer is baked at $180°\mathrm{C}$ for $1\ \mathrm{min}$ to remove water from its surface.
Lift of resist LOR-3A (from MicroChem) is spun on the wafer for $60\ \mathrm{s}$ at 4000 rounds per minute (rpm) (layer thickness $\sim 300\ \mathrm{nm}$) and the wafer is baked for $5\ \mathrm{min}$ at $180°\mathrm{C}$ on a hotplate to remove the solvent.
The photo resist ZEP-520A (from ZEON Corporation) is spun for $60\ \mathrm{s}$ at $4000\ \mathrm{rpm}$ (layer thickness $\sim 350\ \mathrm{nm}$) and the wafer is baked at $180°\mathrm{C}$ for $90\ \mathrm{s}$.

Deep-UV Exposure The resist is exposed with the mask in hard contact mode. The exposure time depends on the age of the resist and is approximately $700\ \mathrm{mJ/cm^2}$. We use an exposure with the EVG-620 Deep-UV Mask Aligner system of $400\ \mathrm{s}$.

Development The ZEP-520A layer is developed using n-Amyl acetate for $60\ \mathrm{s}$, immediately followed by rinsing in Isopropanol (IPA) for $30\ \mathrm{s}$.
The LOR-3A layer is developed using a mixture of the developer Megaposit MF CD-26 and deionized (DI) water (1:1) for $30\ \mathrm{s}$, immediately followed by rinsing in DI water for $5\ \mathrm{min}$.

Reactive Ion Etching In case of epitaxial graphene on SiC, the sample is etched after development in a Reactive Ion Etching (RIE) system. Here a O_2 plasma is used to remove the graphene below the Ti/Au contacts as the whole surface of the wafer is covered. This enables the contacts to stick to the wafer. The etching is performed with an O_2 flow of 9.0 sccm and a gas pressure of ~ 0.02 mbar. The sample is then etched for 20 s with a plasma RF power of $P = 40$ W (the power density is $\sim 55\ \mathrm{mW/cm^2}$).

Deposition A double layer of Ti/Au ($4\ \mathrm{nm}/36\ \mathrm{nm}$) is deposited with a rate of about $1\ \mathrm{nm/s}$ using e-beam evaporation in either the Temescal TFC-2000 or the Temescal BDJ1800 evaporator.

Resist removal/Lift-off To remove the resist including the excess metal layer on top of it, the sample is placed in a bath of hot PRS3000 (from Baker) at $90°\mathrm{C}$ for 10 min before rinsing in DI water for 30 s. In case of difficulties with the lift-off process, the sample can be placed in an ultrasonic bath.
In the case of the optical lithography step for the epitaxial graphene samples, the ultrasonic bath cannot be used as it damages the graphene. (For the optical lithography step for the exfoliated graphene samples an ultrasonic bath can be used as the step is performed before the deposition of graphene.)

A.2 Electron beam lithography (EBL)

To perform electron beam lithography (EBL) steps, we use the Raith e-Line EBL system. EBL is used to define etching masks and to prepare Co contacts for graphene devices.

A.2.1 Etching graphene

Note: This recipe is still under development as the polymer etch mask still leaves too many residues on the graphene surface.

Resist spinning The negative EBL photo resist ma-N 2401 (from Micro Resist Technology) is spun for 30 s at 3000 rpm (layer thickness ~ 100 nm) and the wafer is baked at $100°\mathrm{C}$ for 60 s.

Exposure The desired structure is exposed with an e-beam acceleration voltage of $30\ \mathrm{kV}$, an aperture of $10\ \mu\mathrm{m}$ and a dose of $240\ \mu\mathrm{C/cm^2}$. The EBL system has a vacuum of $< 1 \times 10^{-5}$ mbar.

Development The non-exposed areas of the resist are developed using ma-D 525 (from Micro Resist Technology) for $4\ \mathrm{min}$, immediately followed by rinsing in DI water for $5\ \mathrm{min}$.

Reactive Ion Etching The sample is etched as described in Section A.1.

Resist removal To remove the ma-N 2401 etch mask the sample is placed in hot acetone at $40°\mathrm{C}$ for $5\ \mathrm{min}$, immediately followed by rinsing in Isopropanol (IPA) for $30\ \mathrm{s}$.

A.2.2 Preparing Co contacts

Resist spinning The positive EBL photo resist PMMA 950K (3%, from MicroChem, dissolved in ethyllactate) is spun for $60\ \mathrm{s}$ at $4000\ \mathrm{rpm}$ (layer thickness $\sim 150\ \mathrm{nm}$) and the wafer is baked at $180°\mathrm{C}$ for $90\ \mathrm{s}$.

Exposure The Co contact pattern is exposed with an e-beam acceleration voltage of $10\ \mathrm{kV}$, an aperture of $10\ \mu\mathrm{m}$ and a dose of $100\ \mu\mathrm{C/cm}^2$. For narrow contacts (down to $\sim 100\ \mathrm{nm}$ width) the dose is increased to up to $200\ \mu\mathrm{C/cm}^2$.
In case of an insulating substrate like SiC, there can be problems due to charging effects. In this case prior to the exposure an additional resist is spin coated to be used as an antistatic agent. We used Aquasave (from Mitsubishi Rayon).

Development The exposed areas of the resist are developed in a mixture of MIBK and IPA (1:3) for $75\ \mathrm{s}$, immediately followed by rinsing in IPA for $30\ \mathrm{s}$.
In case of using Aquasave, the sample is rinsed for $20\ \mathrm{s}$ in DI water prior to and after development.

Deposition A $45\ \mathrm{nm}$ thick Co layer is deposited with a rate of about $1\ \mathrm{Å/s}$ using e-beam evaporation in either the Temescal FC-2000 or the Temescal BDJ1800 evaporator.

Lift-off To remove the PMMA layer including the excess Co on top of it, the sample is placed in a bath of hot acetone at $40°\mathrm{C}$ for $10\ \mathrm{min}$ before rinsing in IPA for $60\ \mathrm{s}$.

Symbols and abbreviations

This is a list of recurring symbols and abbreviations used in this thesis and their meaning.

Symbols

$\uparrow; \downarrow$	spin-up; spin down
$\uparrow\uparrow; \uparrow\downarrow$	parallel / aligned; antiparallel / antialigned
A	cross-sectional area of the channel
α	τ^*/τ
B; $\vec{B}$	magnetic field
β	g^*/g
$c/2$	interlayer distance in graphite
d	distance between the localized states and the transport channel
D	diffusion coefficient
D_S	D, obtained by fitting Hanle spin precession measurements
D_C	D, obtained by charge transport measurements
e	electron charge
E	energy
E_F	Fermi energy
η	ν_{LS}/ν
F_i;F_d	injecting; detecting contact
g	Landé factor / gyromagnetic factor / g-factor
g_s	degeneration due to the spin degree of freedom
g_v	degeneration due to the valley degree of freedom
γ_0	nearest neighbor coupling in graphite or graphene
γ_1	graphite interlayer coupling
Γ	coupling rate between the localized states and the transport channel
$\hbar$	reduced Planck constant
I	charge current
J	charge current density
J_S	spin current density
k; $\vec{k}$	wave vector
k_x; k_y; k_z	x-; y-; z-component of the wave vector
L	distance between injector and detector in a spin transport measurement / channel length in a transport measurement
L_C	contact width
λ	spin relaxation length

λ_{scr}	electrical screening length
μ	charge carrier mobility
μ_0	electrochemical potential
μ_B	Bohr magneton
μ_S	spin electrochemical potential in the transport channel
n	charge carrier density / electron density
n_g	gate induced charge carrier density / electron density
N	number of layers in FLG
ν	density of states
ν_{LS}	density of localized states
ω_L	Larmor frequency
p	hole carrier density
P	contact spin polarization
P_i; P_d	contact spin polarization of the injector; detector
P_J	current spin polarization
$\wp_D$; $\wp_{D,\tau}$	probability distribution of traveling times for diffusive transport; including spin relaxation
R	R-parameter
R_{bg}	background resistance
R_C	contact resistance / interface barrier resistance
R_F	spin resistance of the ferromagnet
R_λ	spin resistance of the transport channel
R_{loc}	local resistance
R_{nl}	non-local resistance
R_{sq}	square resistance
R_{SV}	spin valve signal
ρ	resistivity
σ	conductivity
σ_b	Gaussian broadening of the DOS
σ_{gr}	graphene in-plane conductivity
σ_{IL}	graphite conductance in z-direction
$\sigma_{\min}$	minimum conductivity
T	temperature
τ	spin relaxation time
τ_D	diffusion time
τ_{dwell}	spin dwell time in the localized states
τ_p	momentum relaxation time
v_F	Fermi velocity
V_g	gate voltage
V_{nl}	non-local voltage
W	transport channel width
$\hat{x}$; $\hat{y}$; $\hat{z}$	unit vector in x-; y-; z-direction
ξ	g^{eff}/g
ζ	ratio between the in-plane and out-of-plane conductivity of graphite

Superscripts

*, e.g., τ^*	the value of, e.g., τ in the localized states
$^{\mathrm{eff}}$, e.g., τ^{eff}	effective value for, e.g., τ in the system of the transport channel combined with the localized states
$^{\mathrm{fit}}$, e.g., τ^{fit}	e.g., τ obtained by fitting simulated data including contact induced spin relaxation
^{mod}, e.g., τ^{mod}	data, e.g., τ obtained when assuming a g-factor of $g = 2$

Abbreviations

AP	antiparallel
BL	buffer layer between the graphene and the substrate in MLEG on SiC(0001)
BLG	bilayer graphene
CVD	chemical vapor deposition
DB	dangling bond
DP	D’yakonov-Perel’ spin relaxation mechanism
DOS	density of states
EBL	electron beam lithography
eSLG	exfoliated single layer graphene
EY	Elliott-Yafet spin relaxation mechanism
FLG	few-layer graphene
FM	ferromagnetic / ferromagnet / ferromagnetic material
HOPG	highly ordered pyrolytic graphite
MLEG	monolayer epitaxial graphene on SiC(0001)
NM	non-magnetic / non-magnetic material
P	parallel
PL	photolithography
QFMLG	quasi-free-standing MLEG on SiC(0001)
QHE	quantum Hall effect
RRF	random-Rashba-fields
SLG	single layer graphene
SOC	spin-orbit coupling

Summary

In recent years our society is becoming increasingly influenced by information technologies. While some 20 years ago computers used to be quite rare, they nowadays found their way into our everyday life via personal computers, laptops, smart phones, tablet computers and increasingly via “smart” items like smart TVs and so on. At the same time, the speed at which the processors of these devices execute instructions, also called clock rate, is being further and further enhanced. To increase the clock rate, the transistors on the computer chips, which are the switches used in logic operations, are more and more scaled down. This leads to an obvious problem: With transistor sizes of nowadays a few tens of nanometers (a nanometer is a billionth part of a meter) we are soon reaching the size of single molecules or atoms. Therefore researchers are looking for new approaches to increase the speed of our computers.

What all the mentioned devices have in common is that the transport of information in their processors is based on the charge of electrons that are sent through the chips. Next to the charge the electrons also carry a magnetic moment that can be used to transport information. This could enhance the clock rate and would actually also reduce the energy consumption of computers. The magnetic moment can be described in quantum mechanics like the rotation of the electron around its axis and is therefore called the electron “spin”. The research field that makes use of this spin is called “spintronics”.

While spintronic concepts are already used to read information stored in the magnetic bits of computer hard disks, researchers look for materials that enable to transport information carried by spins. The material should be able to transport spins over long distances without losing its orientation and therefore its information. The process of spins unintentionally changing their orientation is called spin relaxation and is described by the typical distance and time it takes for a spin to relax, the spin relaxation length and time, respectively. The long spin relaxation lengths needed for spin transport can be achieved by long spin relaxation times and moderate spin transport velocities or high velocities and moderate relaxation times. To examine the spin transport characteristics of a material, typically Hanle spin precession measurements are employed. These make use of the property of electron spins that their rotation axis precesses (rotates) around perpendicular oriented magnetic fields. Hanle precession measurements are also being used throughout the research presented in this thesis.

Graphene, the two dimensional one atom thick honeycomb lattice of carbon atoms, whose outstanding electronic properties lead Andrei Geim and Konstantin Novoselov to the Nobel prize in physics in 2010, has emerged as promising material to be used as spin transport channel. Its good prospects are based on the high speed at which electrons respond to external incentives, e.g., electric fields, and due to the weakness of internal forces that disturb spins traveling through the material. But even though theoretical works predicted long spin relaxation times and lengths, first experiments showed surprisingly small values. Therefore researchers aim to pinpoint the limiting factors in their experiments.

There are two different types of sources for spin relaxation. First the intrinsic properties of graphene, the effects that are based on the graphene crystal itself. Here the question is which mechanisms are responsible for the spin relaxation, e.g., which internal fields are the cause for the relaxation. The second type of relaxation sources are located in the environment of the crystal. These extrinsic (or external) sources can also influence which is the dominant spin relaxation mechanism. This thesis focuses on understanding the limiting factors for spin transport in graphene by examining charge and spin transport in different types of graphene.

Possible extrinsic sources for spin relaxation include the ferromagnetic contacts that are used to inject and detect spins and their interface with the graphene. It is well known in the field of spintronics that low resistive contacts can drain a part of the spins in the channel, reducing the measured signals. We discuss that low resistive contacts can not only influence the magnitude of the spin signal but also the way how spins are transported in the channel. This can have a profound influence on the interpretation of the spin transport properties of the material and the quality of the channel can be strongly underestimated. The presented simulation results give general guidelines for the minimum resistance of contact resistances in relation to the spin relaxation length in the transport channel. The low resistance of the contacts can be compensated by using high resistive barriers at the interface between the contacts and the transport channel. In case of contacts that influence the spins in the channel, this effect can also be compensated when measuring the spin transport over a longer distance. In this case the spin relaxation is dominated by the channel.

To understand which mechanisms are responsible for spin relaxation, we observe the relation between the momentum and the spin relaxation time. The momentum relaxation time is the typical time it takes for an electron to scatter. We compare spin and charge transport and show that the diffusion of spins and charges is the same in a single graphene layer and a graphene stack (few-layer graphene). Therefore we do not see evidence for strong interaction between electrons and the results from spin transport measurements can be used to determine the momentum relaxation time. While it initially seemed to be straightforward to identify the dominant relaxation mechanism in graphene, it turned out to be more complicated due to the special charge transport properties of graphene. We present the state of affairs on this issue. In short, it seems that spin relaxation in graphene is not dominated by the conventional relaxation mechanisms.

The influence of the direct surrounding of the graphene channel is governed by the substrate, deposits, e.g., from the sample preparation, and by graphene impurities. We see indications for them limiting the spin transport in single and few-layer graphene.

To examine the influence of the environment we first electrically screen its influence in few-layer graphene. We show that spurious effects can be screened by increasing the amount of charges in the system, either by electrically inducing extra charges or by increasing the density of electron states with growing thickness of the graphene stack in few-layer graphene. While this holds for charge transport we show a direct correlation of the few-layer graphene thickness to the spin transport properties.

The measurements mentioned so far were performed on exfoliated graphene. This type of high quality graphene is easy to produce by repeatedly peeling thin layers from a graphite crystal until single graphene layers remain. However, the graphene crystals produced this way demand a unique sample design and a lot of preparation time for every device. Using graphene on silicon carbide substrates is an interesting approach as the graphene is epitaxially grown. This enables us, next to examining the influence of the substrate by replacing the commonly used silicon oxide substrate, to upscale the sample production as we can standardize the sample design. Our measurements are performed on monolayer epitaxial graphene where the graphene is separated from the substrate by a graphene-like layer. This so-called buffer layer has the same structure as graphene but is not electrically conductive due to chemical bonds to the silicon carbide.

The spin transport results on epitaxial graphene are quite surprising as Hanle precession measurements show long spin relaxation times but a very slow diffusion of the spins through the system. To explain this we developed a general model that can relate the measured effect to the influence of localized electronic states on spin transport. These localized states are electrically coupled to the transport channel and result in enhanced spin dynamics and an actually reduced spin relaxation time. The relaxation time is being overestimated though when the enhanced dynamics are not taken into account in the analysis. This interpretation is valid when considering the electrons as a collective. A second equally valid interpretation considers individual electrons coupling to the localized states. This results in longer traveling times through the channel and longer relaxation times for an individual spin. Both interpretations lead to a reduction of the spin relaxation length in the system due to the localized states. We compare measurements on epitaxial graphene with and without the buffer layer and can identify this layer as origin for the localized states. These results clearly underline that it is important to the see whole system and not only the examined material when interpreting measurements.

The results presented in this thesis give a valuable insight in spin transport, mainly in graphene and are one of many steps on the path to computer operations based on spintronics. As graphene is the material with the longest spin relaxation length at room temperature, spin-based computers could in the future be accomplished using graphene channels to transport spins from one logic operation to the next one.

Samenvatting

De impact van informatietechnologie op de samenleving is in de afgelopen jaren in toenemende mate gegroeid. Terwijl zo'n 20 jaar geleden computers in woningen zeldzaam waren, hebben ze tegenwoordig hun plaats in ons dagelijks leven gevonden via desktop computers, laptops, smartphones, tablets, en meer en meer via "smart" apparaten, zoals smart-tv's en ga zo maar door. Tegelijkertijd neemt de snelheid waarmee de processoren van deze apparaten instructies uitvoeren, ook wel kloksnelheid, verder toe. Om de kloksnelheid te verhogen worden de transistoren op chips, de schakelaars in logische operaties, steeds verder verkleind. Dit leidt tot een duidelijk probleem: met de huidige transistorafmetingen van enkele tientallen nanometers (een nanometer is een miljardste deel van een meter), bereiken we al snel de grootte van enkele moleculen of atomen. Daarom zijn onderzoekers op zoek naar nieuwe benaderingen om de snelheid van computers te verhogen.

Wat al deze genoemde apparaten met elkaar gemeen hebben is dat de informatieoverdracht in hun processoren gebaseerd is op het verzenden van de lading van elektronen door de chip. Naast lading hebben elektronen ook een magnetisch moment, dat kan worden gebruikt als informatiedrager. Het gebruik van dit moment zou de kloksnelheid kunnen verhogen en zou daarnaast het energieverbruik van computers kunnen reduceren. In de kwantummechanica kan het magnetisch moment van het elektron als een rotatie (een "spin") rond zijn as worden beschreven, en wordt daarom "elektron spin" genoemd. Het onderzoeksveld dat gebruik maakt van deze spin heet "spintronica".

Terwijl spintronische concepten al worden gebruikt om informatie te lezen die in de magnetische bits op harde schijven in computers is opgeslagen, zijn onderzoekers op zoek naar materialen die het mogelijk maken om informatie te vervoeren met spins. Het materiaal moet spins over lange afstanden kunnen transporteren zonder de spinoriëntatie, dus de informatie, te verliezen. Een ongewenste verandering van de spinoriëntatie wordt spinrelaxatie genoemd en kan worden beschreven door de typische lengte en tijd die voor de spinrelaxatie nodig is, respectievelijk de spinrelaxatielengte en spinrelaxatietijd. De lange spinrelaxatielengte die nodig is voor spintransport kan worden bereikt door een combinatie van lange spinrelaxatietijden en gemiddelde spintransportsnelheden of door een hoge snelheid en een gemiddelde relaxatietijd. Om de spintransporteigenschappen van een materiaal te bestuderen, worden meestal Hanle-spinprecessiemetingen gebruikt. Dit type metingen maakt gebruik van het feit dat de draaiingsas van elektronspins door de invloed van een loodrecht gericht magnetisch veld precessie uitvoert (roteert). Hanleprecessiemetingen worden in het onderzoek gebruikt dat in dit proefschrift wordt beschreven.

Grafeen is het tweedimensionaal honingraatrooster van koolstofatomen met een dikte van één atoom. Het heeft uitstekende elektronische eigenschappen, wat leidde tot de Nobelprijs voor de Natuurkunde 2010 voor Andrei Geim en Konstantin Novoselov. Ook de spintransporteigenschappen van grafeen zijn veelbelovend. De vooruitzichten zijn goed omdat de hoge snelheid waarmee elektronen reageren op externe prikkels zoals elektrische velden en vanwege de geringe sterkte van interne krachten die spins op hun weg door het materiaal verstoren. Maar hoewel theoretische onderzoeksresultaten lange spinrelaxatielengten en -tijden voorspelden, lieten eerste experimenten verrassend lage waarden zien. Daarom proberen onderzoekers in hun experimenten de beperkende factoren voor spintransport te vinden.

Er zijn twee verschillende soorten oorzaken van spinrelaxatie. Enerzijds, de intrinsieke eigenschappen van grafeen, effecten die van het grafeenkristal zelf afkomstig zijn. Hier is de vraag welke mechanismen, bijvoorbeeld welke interne velden, verantwoordelijk zijn voor de spinrelaxatie. Anderzijds zijn er invloeden uit de directe omgeving van het grafeen die leiden tot spinrelaxatie. Deze extrinsieke (of externe) factoren kunnen ook bepalen welk spinrelaxatiemechanisme dominant is. Dit proefschrift richt zich op het begrijpen van de beperkende factoren voor spintransport in grafeen door het bestuderen van ladings- en spintransport in verschillende soorten grafeen.

Een van de mogelijke extrinsieke oorzaken van spinrelaxatie zijn de ferromagnetische contacten die worden gebruikt om spins te injecteren en te detecteren en hun grensvlak met het grafeen. In het onderzoeksveld van spintronica is het algemeen bekend dat het contact met lage, ohmse weerstanden relaxatie van een deel van de spins in het spintransportkanaal kan veroorzaken, waardoor de gemeten spinsignalen worden verlaagd. We laten zien dat contacten met lage weerstanden niet alleen de grootte van het gemeten signaal verlagen, maar ook van invloed zijn op de wijze waarop de spins in het kanaal worden getransporteerd. Dit kan een sterke invloed hebben op de interpretatie van de spintransporteigenschappen van het materiaal en de kwaliteit van het kanaal kan daardoor aanzienlijk worden onderschat. De resultaten van de simulaties die in deze thesis worden gepresenteerd tonen algemene richtlijnen aan voor een minimum contactweerstand in vergelijking met de spinrelaxatielengte in het transportkanaal. Een lage contactweerstand kan worden gecompenseerd door de invoering van isolatie tussen het kanaal en de contacten. Als de contacten nog steeds het spintransport blijven beïnvloeden, kan ook de afstand tussen de spininjectie en -detectie worden verhoogd, zodat de eigenschappen van het spintransportkanaal de overhand krijg in de spinrelaxatie.

Om te begrijpen welke mechanismen verantwoordelijk zijn voor de spinrelaxatie doen we onderzoek naar de relatie tussen de impulsrelaxatietijd en de spinrelaxatietijd. De impulsrelaxatietijd is de typische tijd die een elektron kan reizen zonder te worden verstrooid. We vergelijken spin- en ladingstransport en laten zien dat de diffusie van spins en ladingen in zowel individuele grafeenlaagjes als in grafeen stapels (grafiet van een paar lagen dik of een grafeenmultilaag) identiek is. We zien daarom geen bewijs van sterke interacties tussen elektronen en kunnen de impulsrelaxatietijd uit de spintransportmetingen afleiden. Hoewel aanvankelijk werd gedacht dat de dominante spinrelaxatiemechanisme van grafeen makkelijk te identificeren zouden zijn, werd vastgesteld dat de bepaling wordt bemoeilijkt door de bijzondere elektronische eigenschappen van grafeen. We presenteren in dit proefschrift de huidige stand van zaken op dit punt. Kort samengevat lijkt het erop dat geen van de conventionele relaxatiemechanismen de belangrijkste oorzaak is van spinrelaxatie in grafeen.

De voornaamste omgevingsinvloeden op het grafeenkanaal zijn het substraat (de ondergrond van het grafeenkristal), ongewenste residuen van bijvoorbeeld de samplefabricage en onzuiverheden in het grafeenkristal. We zien indicaties dat deze drie factoren spintransport beperken in zowel individuele grafeenlaagjes als in grafeenmultilagen.

Om de invloed van de omgeving te onderzoeken, schermen we die invloed af door het gebruik van grafeenmultilagen. We tonen aan dat verstoringen kunnen worden afgeschermd door de hoeveelheid lading in het systeem te vergroten, hetzij door het elektrisch induceren van extra ladingen, hetzij door de dichtheid van de elektronische toestanden groter te maken door het aantal grafeenlagen te verhogen. Hoewel dit voor het ladingstransport geldt, tonen wij een directe correlatie aan tussen de dikte van het meerlagige systeem en de spintransporteigenschappen.

De tot nu toe beschreven metingen zijn uitgevoerd op geëxfolieerd (gepeld) grafeen. Dit grafeentype heeft een zeer goede kwaliteit en is gemakkelijk te produceren door dunne lagen van een grafietkristal af te pellen, net zo lang tot een individuele laag grafeen overblijft. De resulterende grafeenkristallen vereisen echter een individueel ontwerp voor elk sample en veel arbeidstijd in de sampleproductie. Het gebruik van grafeen op siliciumcarbide is een aantrekkelijk alternatief, omdat het grafeen epitaxiaal wordt gegroeid. Met dit materiaal kunnen we niet alleen het effect van het nieuwe substraat onderzoeken in vergelijking met het doorgaans gebruikte siliciumoxide, maar het maakt het ook mogelijk om het sampleontwerp te standaardiseren een daarmee de sampleproductie op grote schaal toe te passen. De metingen zijn uitgevoerd op epitaxiaal grafeen die door een grafeenachtige laag van het substraat gescheiden wordt. Deze zogenaamde bufferlaag heeft dezelfde structuur als grafeen, maar is niet elektrisch geleidend, aangezien zij gedeeltelijk chemisch aan het siliciumcarbidesubstraat is gebonden.

De experimentele resultaten van spintransport in epitaxiaal grafeen zijn heel verrassend, omdat Hanle-spinprecessiemetingen lange spinrelaxatietijden en zeer trage diffusie van de spins door het systeem laten zien. Om dit verschijnsel te verklaren, hebben we een algemeen model opgesteld dat het gemeten effect relateert aan de invloed van gelokaliseerde elektronische toestanden op spintransport. Deze gelokaliseerde toestanden zijn elektrisch gekoppeld aan het transportkanaal en resulteren in versterkte spindynamica en verminderde spinrelaxatietijden. De relaxatietijd wordt overschat als er geen rekenening wordt gehouden met de versterkte spindynamica tijdens de data-analyse. Deze interpretatie is van toepassing als men de elektronen als een collectief beschouwd. Een tweede, gelijkwaardige interpretatie beschrijft een enkel elektron dat koppelt met de gelokaliseerde toestanden. Dit leidt tot langere verblijftijden in het kanaal en langere relaxatietijden voor individuele spins. Beide interpretaties resulteren in een vermindering van de spinrelaxatielengte als gevolg van de gelokaliseerde toestanden. Door vergelijking van de meetresultaten aan epitaxiaal grafeen met en zonder de bufferlaag, kunnen we de bufferlaag identificeren als de oorsprong van de gelokaliseerde toestanden. Deze resultaten tonen duidelijk aan, dat het belangrijk is om bij de interpretatie van metingen het gehele systeem te beschouwen en niet alleen het onderzochte materiaal.

De resultaten in dit proefschrift geven een waardevol inzicht in spintransport, in het bijzonder in grafeen, en zijn een van de vele stappen op de weg naar spintronische computerberekeningen. Omdat grafeen het materiaal is met de langste spinrelaxatielengte bij kamertemperatuur, zouden deze computers gebruik kunnen maken van grafeenkanalen om spins te vervoeren van de ene logische bewerking naar de volgende.

Zusammenfassung

Der Einfluss der Informationstechnik auf unsere Gesellschaft ist in den letzten Jahren zunehmend gewachsen. Während Computer in Haushalten vor etwa 20 Jahren eher selten waren, haben sie heute ihren Weg in unser tägliches Leben gefunden über Desktop Computer, Laptops, Smartphones, Tablet-Computer und immer mehr über „smart" Geräte wie Smart TVs und so weiter. Gleichzeitig wird die Geschwindigkeit, mit der die Prozessoren dieser Geräte Anweisungen (Programmabläufe) ausführen, auch Taktfrequenz genannt, ständig erhöht. Um die Taktfrequenz zu erhöhen, werden die Transistoren auf den Computer-Chips, also die Schalter in logischen Operationen, immer weiter verkleinert. Das führt zu einem offensichtlichen Problem: Mit heutigen Transistoren in der Größe von ein paar Dutzend Nanometern (ein Nanometer ist der Milliardste Teil eines Meters), werden die Bausteine der Computer bald die Größe von einzelnen Molekülen oder Atomen erreichen. Daher suchen Forscher nach neuen Ansätzen, um die Geschwindigkeit von Computern zu erhöhen.

Was all die genannten Geräte gemeinsam haben, ist dass der Transport von Informationen in ihren Prozessoren über das Senden der Ladung von Elektronen durch die Chips bewerkstelligt wird. Neben der Ladung tragen die Elektronen aber auch ein magnetisches Moment, das als Informationsträger verwendet werden kann. Die Nutzung dieses Momentes könnte die Taktfrequenz erhöhen und würde dabei sogar noch den Energieverbrauch von Computern senken. Das magnetische Moment kann in der Quantenmechanik wie eine Rotation (einen „Spin") von Elektronen um ihre eigene Achse beschrieben werden und wird daher „Elektronenspin" genannt. Das Forschungsgebiet, das sich diesen Spin zu Nutze macht, wird „Spintronik" genannt.

Während Spintronikkonzepte bereits verwendet werden um Informationen auszulesen, die in magnetischen Bits auf Computerfestplatten gespeichert sind, suchen Forscher nach Materialien, die es ermöglichen Informationen mit Spins zu transportieren. Ein solches Material sollte in der Lage sein, Spins über lange Distanzen zu transportieren, ohne die Ausrichtung des Spins und damit die zu übertragende Information zu verlieren. Die ungewollte Änderung der Spinrichtung wird Spinrelaxation genannt und über die typische Länge und Zeit definiert, die es dauert bis der Spin relaxiert, die Spinrelaxationslänge bzw. -zeit. Die langen Relaxationslängen, die für Spintransport benötigt werden, können entweder über das Zusammenspiel von langen Spinrelaxationszeiten und durchschnittlichen Spintransportgeschwindigkeiten oder über hohe Geschwindigkeiten und durchschnittliche Relaxationszeiten erreicht werden. Um die Spintransporteigenschaften eines Materials zu untersuchen, werden typischerweise Hanle-Spinpräzessionsmessungen durchgeführt. Hierbei wird ausgenutzt, dass die Rotationsachse der Elektronenspins um senkrecht ausgerichtete magnetische Felder präzediert (rotiert). Diese Hanle-Präzessionsmessungen werden auch durchweg in der Forschung genutzt, die in dieser Dissertation vorgestellt wird.

Graphen, das zweidimensionale, ein Atom dicke Bienenwabengitter aus Kohlenstoffatomen, dessen hervorragenden elektronischen Eigenschaften Andrei Geim und Konstantin Novoselov zum Nobelpreis in Physik 2010 führten, hat vielversprechende Spintransporteigenschaften. Die guten Aussichten sind auf die hohe Geschwindigkeit, mit der Elektronen auf externe Anreize wie z.B. elektrische Felder reagieren, sowie die Schwäche der internen Kräfte, die die Spins auf dem Weg durch das Material stören zurück zu führen. Aber obwohl theoretische Forschungsergebnisse auf lange Spinrelaxationslängen und -zeiten hin deuteten, zeigten erste Experimente überraschend kleine Werte der beiden Größen. Daher versuchen Forscher die begrenzenden Faktoren für den Spintransport in ihren Experimenten zu finden.

Es gibt grundsätzlich zwei verschiedene Arten von Ursachen für Spinrelaxation. Da sind zum einen die intrinsischen Eigenschaften des Graphens, dies sind Effekte, die vom Graphenkristall selbst herrühren. Hier ist die Frage welcher Mechanismus für die Spinrelaxation verantwortlich ist, z.B. welche internen Felder sind die Ursache der Relaxation. Zum anderen gibt es Einflüsse aus der direkten Umgebung des Graphens, die zur Spinrelaxation führen. Diese extrinsischen (oder externen) Einflüsse können auch bestimmen, welcher Spinrelaxationsmechanismus dominant ist. Diese Dissertation zielt darauf, die begrenzenden Faktoren für Spintransport in Graphen zu finden, indem Ladungs- und Spintransport in verschiedenen Graphentypen untersucht werden.

Mögliche extrinsische Spinrelaxationsursachen sind die ferromagnetischen Kontakte, die zum Injizieren und Detektieren der Spins genutzt werden und ihre Schnittstelle mit dem Graphen. Es ist im Spintronikforschungsgebiet allgemein bekannt, dass Kontakte mit niedrigen ohmschen Widerständen einen Teil der Spins im Spintransportkanal relaxieren können und damit die gemessen Spinsignale reduzieren. Wir zeigen, dass Kontakte mit niedrigen Widerständen nicht nur die Größe des gemessenen Signals beeinflussen, sondern auch die Art und Weise wie Spins im Kanal transportiert werden. Dies kann einen großen Einfluss auf die Interpretation der Spintransporteigenschaften des Materials haben und dazu führen, dass die Qualität des Kanals erheblich unterschätzt wird. Die dargestellten Simulationsergebnisse zeigen allgemeine Richtlinien für minimale Kontaktwiderstände in Bezug auf die Spinrelaxationslänge des Spintransportkanals. Der geringe Kontaktwiderstand kann durch die Einbringung von isolierenden Schichten zwischen dem Kanal und den Kontakten kompensiert werden. Wenn die Kontakte den Spintransport weiterhin beeinflussen, kann auch der Abstand zwischen Spininjektion und -detektion erhöht werden um den Einfluss zu reduzieren. Dann wird die Spinrelaxation durch die Eigenschaften des Spintransportkanals dominiert.

Um zu verstehen, welche Mechanismen für die Spinrelaxation verantwortlich sind, beobachten wir das Verhältnis zwischen der Impuls- und der Spinrelaxationszeit. Die Impulsrelaxationszeit ist die typische Zeit, die ein Elektron frei von Stößen fliegen kann. Wir vergleichen Spin- und Ladungstransport und zeigen, dass die Diffusion von Spins und Ladungen in sowohl einzelnen Graphenlagen als auch in Graphenstapeln, also einige Lagen dickem Graphit oder Graphenmehrfachschichten, identisch ist. Wir sehen damit keine Hinweise auf eine starke Wechselwirkung zwischen Elektronen und können die Impulsrelaxationszeit aus den Spintransportmessungen ableiten. Während es zunächst einfach erschien, den dominierenden Spinrelaxationsmechanismus in Graphen zu identifizieren, zeigte es sich, dass die Bestimmung des Mechanismus durch die ungewöhnlichen elektronischen Eigenschaften des Graphens erschwert wird. Wir stellen in dieser Arbeit den aktuellen Stand der Dinge zu diesem Thema dar. Kurz gesagt scheint es, als wäre keiner der herkömmlichen Relaxationsmechanismen die Hauptursache für Spinrelaxation in Graphen.

Die wichtigsten Einflüsse in der Umgebung des Graphenkanals sind das Material, auf dem der Kristall aufliegt, ungewollte Ablagerungen z.B. von der Probenherstellung und Verunreinigungen im Graphenkristall. Wir sehen Anzeichen dafür, dass diese drei Faktoren den Spintransport sowohl in einzelnen Graphenlagen als auch in Graphenmehrfachschichten begrenzen.

Um den Einfluss der Umgebung auf den Spin- und Ladunsgtransport abzuschätzen, schirmen wir sie mit Hilfe von Graphenmehrfachschichten ab. Wir zeigen, dass Störeffekte durch das Erhöhen der Ladungsmenge im System abgeschirmt werden, entweder indem zusätzliche Ladungen elektrisch angeregt werden oder indem wir die Dichte der elektrischen Zustände durch das Vergrößern der Materialdicke von Graphenmehrfachschichten erhöhen. Dies gilt für den Ladungstransport und wir zeigen einen direkten Zusammenhang zwischen der Materialdicke des Mehrfachschichtsystems und den Spintransporteigenschaften.

Die bisher beschriebenen Messungen wurden auf exfoliiertem (abgeschältem) Graphen durchgeführt. Dieser Graphentyp hat eine sehr gute Qualität und ist einfach zu produzieren. Von Graphit werden so lange dünne Lagen abgeschält, bis einzelne Lagen Graphen übrig bleiben. Die so gewonnenen Graphenkristalle benötigen jedoch ein individuelles Probendesign für jeden gewonnenen Kristall, und viel Arbeitszeit in der Probenherstellung. Die Verwendung von Graphen auf Siliziumkarbid ist daher eine interessante Alternative, da das Graphen epitaktisch gewachsen wird. Das erlaubt uns nicht nur den Einfluss des neuen Substrats zu untersuchen, welches das gewöhnlich genutzte Siliziumoxid ersetzt, sondern es ermöglicht auch das Probendesign zu standardisieren und damit die Probenproduktion hoch zu skalieren. Unsere Messungen werden auf epitaktischem Graphen durchgeführt, das durch eine graphenähnliche Schicht vom Substrat separiert wird. Diese sogenannte „Pufferschicht" hat die gleiche Struktur wie Graphen, ist jedoch nicht elektrisch leitfähig, da sie teilweise chemisch an das Siliziumkarbidsubstrat gebunden ist.

Die Ergebnisse von Spintransportmessungen an epitaktischem Graphen sind überraschend, da die Hanle-Präzessionsmessungen lange Spinrelaxationszeiten aber eine sehr langsame Diffusion der Spins durch das System zeigen. Um dieses Phänomen zu erklären, haben wir ein allgemeines Modell entwickelt, welches den gemessenen Effekt auf den Einfluss von lokalisierten elektronischen Zuständen auf den Spintransport zurückführt. Diese lokalisierten Zustände sind elektrisch an den Transportkanal gekoppelt und führen zu verstärkter Spindynamik und reduzierten Spinrelaxationszeiten. Die Relaxationszeiten werden jedoch überschätzt, wenn die verstärkte Spindynamik in der Datenanalyse nicht berücksichtigt wird. Diese Interpretation gilt, wenn man die Elektronen als Kollektiv betrachtet. Eine zweite, gleichwertige Interpretation betrachtet einzelne Elektronen, die mit den lokalisierten Zuständen gekoppelt sind. Dies führt zu längeren Flugzeiten durch den Kanal und längeren Relaxationszeiten für einen individuellen Spins. Beide Interpretationen resultieren in einer Verringerung der Spinrelaxationslänge aufgrund der lokalisierten Zustände. Indem wir Ergebnisse von Messungen an epitaktischem Graphen mit und ohne die genannte Pufferschicht vergleichen, können wir die Pufferschicht als den Ursprung der lokalisierten Zustände identifizieren. Diese Ergebnisse zeigen deutlich, dass es wichtig ist, bei der Analyse von Messungen das Gesamtsystem zu betrachten und nicht nur das untersuchte Material zu berücksichtigen.

Die in dieser Dissertation vorgestellten Ergebnisse geben einen wertvollen Einblick in Spintransport vor allem in Graphen. Sie sind einer von vielen Schritten auf dem Weg zu Rechenoperationen mit Spintronik-Computern. Da Graphen das Material mit der längsten Spinrelaxationslänge bei Raumtemperatur ist, könnten diese Computer Graphenkanäle verwenden, um Spins von einer logischen Operation zur nächsten zu transportieren.

Acknowledgements

In December 2008 a number of lucky coincidences made me leave Germany and start my PhD research in Groningen. While working on metallic spintronics during my Diplom thesis in Aachen I got fascinated by spintronic phenomena, and with graphene coming up as a "wonder material" it seemed a good idea to do my PhD on spintronics in graphene. And it turned out to be just that. On the one hand the topic led to many interesting results, and on the other hand the timing was perfect, as the basis of the field was just established, and the research on spintronics in graphene grew dramatically during my time in Groningen. While the initial planning was to downscale spin transport devices, during my research I got interested in the upscaling of sample production and started working on epitaxially grown graphene. A good decision considering the papers we managed to publish on this topic and the interest from others working in the field. While the research gave me joy and allowed me to widen my horizon, both on the scientific as on the personal level, I cannot omit that there were difficult and frustrating times, and I learned that besides the friendly atmosphere in scientific research, there can be quite fierce competition. A lot of people helped me on my way through my PhD, and I would like to name some of them.

I would like to start by thanking my promoter Bart van Wees. Bart, I am very happy I found you and your research group, and I never regretted the choice to join you for my PhD. You are a brilliant physicist with a great understanding of the nature of transport phenomena on the nanoscale. When I was stuck with the interpretation of my results you gave invaluable input, though it sometimes took some time until we really were communicating on the same wavelength. Your criticism, while sometimes hard to take, made me think carefully about any flaws in my interpretations and prepared me to meet difficult questions on the many scientific conferences you allowed me to attend. I also would like to congratulate you with your group, the FND. We were sometimes musing how you manage, but somehow you keep up a great atmosphere in the group, where research and friendship thrives. One of the reasons for this atmosphere surely is the coffee room and the social events of the FND.

Dear Jaroslav Fabian, Albert Fert and Roland Kawakami, thank you for accepting to be member of my reading committee and for your comments on my thesis. I feel lucky to have three outstanding scientists with very different backgrounds read my thesis and enjoyed meeting you in the past years.

Dear Gernot Güntherodt and Bernd Beschoten, thank you for teaching me the basics of spintronics during the time I wrote my Diplom thesis in your group at the RWTH Aachen and for preparing me to start my PhD. I am happy that we stayed in contact during this time. Bernd, I enjoyed our exchange of ideas on spin transport in graphene, and Gernot, I thank you for your invitation to speak at the DPG spring meeting in Berlin in 2012. In context of my bonds to Aachen, I would like to thank Coen Smits for the advice to apply in Bart's group.

That brings me to the first person from our group I would like to thank: Csaba. You were the connection to the Aachen group via Coen who did his PhD simultaneously with you in Eindhoven. After I joined the FND, we worked closely together, and you showed me the tricks of the trade. I learned a lot about physics and experimentation but you were also a good friend. Pity, you left our group after a bit more than a year of my PhD, but I guess that made me to work more independent. I am happy we stayed in touch.

Marcos, I noticed we get along well the day you applied, but you were also a great help from the day you started working in our group. Your support in getting my few-layer graphene data published came at the right time, and I value your theoretical and technical understanding of physics and experimental setups when working with you. Thank you for all your feedback on this thesis. Just when talking about work: Relax! About our free time: I enjoyed all the things we did together. You are a great friend, and I am very happy you came to Groningen. Right from the beginning we spent most of the weekends together, and it is great that you became good friends with Marta, too. I hope we will meet often in the years to come, in the Netherlands, Canada, Brazil, the US, Germany or wherever we have a chance.

Alok, even though we never worked together on a project, I have to mention you here. You helped me cope with all the frustration physics research and politics in science can bring, and I enjoyed our special connection and sense of humor. Keep up your good mood at work! I enjoyed the time we spent after work, the great food you make and all the conversations we had. I am looking forward to a double date with you, Mayuri and Marta. Hopefully after you and your girl find a job in Canada. I am happy that you and Marcos accepted to be my paranymphs.

Jasper, when I felt like I was working on my own in our group, you started your PhD, and we started our own small SiC-team. I would say we did well. Good luck with continuing the exciting work on the upscaled approach. I shouldn't forget to mention our travels. There is nobody at FND that I attended so many conferences and meetings with, and you know that from all FND, you were my favorite travel mate. I hope that we can travel together again sometime. Thank you also for the good times we had together when having dinners or playing games. And thanks for your Dutch support and feedback on this thesis.

Frank, I am happy that you were my office mate for nearly all the four years I was at the FND. I clearly see the advantage of the policy to put people from different projects in one office. When there were some issues in the graphene team I could come to you and complain :-). I remember all the fun we had in our small breaks when we watched Tyson Eberly, Knick Knack or some of your favorite videos that showed me clearly the differences between German and Dutch humor. I also welcomed our mutual feedback on graphics and physics. All the best for you and Kim.

Arramel, it took some time for you to warm up, and I guess you also needed to get used to Frank and me in the office. But especially in your last year I enjoyed your company and your special kind of humor. I also value our discussions on the differences in our cultural background. And thank you for asking me to be your paranymph. Good luck for your future!

Fasil, you were my first and only master student and we started out on a difficult project. After a short while I realized that this project needed a lot of attention so I joined you full time, and we explored few-layer graphene. You always worked hard, but I noticed the difficulties you had in the beginning to adjust to the Dutch type of hierarchy. I think we worked well together, and I enjoyed your very friendly and respectful way of communicating. Your PhD research shows how talented you are.

Johan and Natasja, as my two bachelor students we spent a lot of time together. Johan, you are a smart guy with a lot of ideas. A bit more focus would have helped, though, and I am sure that you manage this now. Natasja, I enjoyed working with you. You were independent and full of energy to do tests and more tests to figure out how to deal with graphene on SiC. I would have loved to supervise you during your masters.

Alina, FND without you wouldn't have been the FND I experienced. You were always full of energy, and when you were in a good mood, you were the sunshine of the group. I know we didn't always agree on everything but I enjoyed your company also on our work related travels and especially in Kirchberg and Brazil, and I wish you and Csaba all the best for the future.

Ivan, the group is lucky to have you. You come from an electronics background, and while some people might think that gives you a disadvantage, it certainly does not. Your knowledge on physics contexts is impressive, and your expertise on electronics is a great ingredient for the knowledge pool of the group. However, sometimes your explanations can be rather complicated :-). I am sure that you would be a good professor.

Paul, you always impressed me as it seems like you can get along with anybody. You have a calming influence on groups working together, and that's probably one of the reasons why so many people ask you to join their project. Another one surely is your skill in experimentation, especially with the EBL. But next to your calm appearance, I know still waters run deep. I guess you now stay unbeaten in UT.

Eek, I am glad you came back from the US and joined me on my quest to figure out the nature of spin transport in graphene on SiC. Your positive feedback is very uncommon in physics but a great trait of yours.

Magda, you are a very warm hearted person. We got along well, and I am happy to see your research is going smoothly. I gladly joined you on your project on hydrogenated graphene, and I am happy it got finally published.

Niko, I applied to the FND on your defense day and the good atmosphere around it was one of the reasons that I started working at the FND. Your experimental talent and your persistence in the clean-room is impressive. Unfortunately we never worked closely together.

Joost, I enjoyed your good mood and am happy to see that together with Fasil you keep up the good work of Frank and Bram. From all the things we did together outside work I especially remember the nice dinners with you, Roos and Marta.

Bram, though you left the group a while ago, I still would like to mention how impressed I was by your brilliant mind. I sometimes envied you and Frank for being part of such an effective duo.

Vincent, I connected with few people in the group as fast as with you. Marta and me are happy to have met you and Chantal and hope to visit you one day in the beautiful Brittany.

Javaid, you were a lonesome member of the FND, working on your own. I enjoyed our open discussions about Pakistan and was happy to be able to help you with some PC questions. I wish you all the best for your future and for combining the different point of views you got in your past and during your time in Groningen.

Hilbert, even though you were Jaspers student, I felt responsible for you and your research. Nice that our work together ended up in PRL.

When acknowledging people I surely shouldn't forget the FND-staff.

Bernard, you were my favorite technician. Your humor and experience made you a great guy to have around. But I will also remember going swimming with you and sharing thoughts on all kind of things. I wish you all the best for your retirement.

Siemon, you were a great guy. It came as a shock for all of us when we heard about your condition and when you died in 2011. I am happy to have met you, and FND misses you and your unforgettable sense of humor.

Johan and Martijn, you were there when needed, and while Johan got more and more filled up with all kind of tasks, Martijn grew into his role as technician and also represented the staff on all the borrels we had.

Anna and Sonja, a group needs a secretary, and everybody is happy when she is doing a good job. Anna, thank you for all the support, and Sonja, thank you for your warm welcome when I came from Germany and had to deal with more new things than I expected.

Caspar, I enjoyed working with you on the quantum mechanics tutorials and liked to see your passion for teaching.

Tamalika, I admire your endurance in your tenure track and am glad it is crowned with success. I enjoyed our conversations on the dynamics in research below the surface and on possible future jobs for me.

I also do not want to forget to mention Harry Jonkman and the rest of FND, Maksym, Sergii, Mihai, Jean-Paul, Nynke, both Sanders, Jakko, Olger, our Indian community: Subir, Gaurav, Saurabh, Saroj and Vishal, my office mates for the last few weeks of my contract: Danny and Parta, and all the master and bachelor students.

I also would like to mention some people from outside the group for their support and influence. From the ConceptGraphene collaboration I would like to thank especially Rosistza Yakimova, Thomas Seyller, Felix Fromm, Florian Speck, Sergey Kubatkin, Mikael Syväjärvi and Samuel Lara-Avila.

I would like to thank Walt de Heer for his suggestion to look into epitaxial graphene research and am happy to see that the two fields of epitaxial and exfoliated graphene, that seemed to develop parallel to each other, now seem to grow closer.

A special thanks goes to Antonio Castro Neto. He fulfilled for me the dream of every PhD student: A conference with all the people you want to talk to. Thank you for allowing me to be part of the advisory committee of the amazing workshop in Singapore with nearly all the high level scientist I could have asked for. Thank you also for inviting me to speak there as this opened the door for me to be invited at other meetings.

Now I would like to mention a group of people outside physics who made these four years a great time.

This part of my acknowledgements I would like to start with Lara. You were, together with Marcos and Alok, Marta's and my family in Groningen. There are only a few weekends we didn't do anything together. I can talk with you about anything, and I am grateful for all the trust and friendship that connects us. I also enjoyed the trips we did together. The festivals also shouldn't be forgotten here. Good luck with finishing up your thesis.

Bruno, I am happy to be your friend. I like to thank you for all the conversations we had and also for all the special "Bruno-discussions". I appreciate your beliefs, though, as you know, at times I do not agree with them :-). I hope I manage another time to visit you in your beautiful oasis in France. And please visit me in Vancouver. Maybe, we go for another festival, this time in America?

Elena, together with Bruno you enabled me to become part of the international community in Groningen. I enjoyed the dinners, parties and trips we did in the first years of my PhD.

Stijn, even though you also work on the physics of graphene I feel more connected to you as a friend than as a colleague. I felt good in your company from the moment on we met, and I am glad we stayed in contact since. I also enjoyed the time with your family when our camping trip was rained off.

Ildiko, Ilse, Gisi and Ryan, it was nice to be friends with you. Ildiko, I am happy you found a great job in Budapest. Hopefully I will manage to visit you there soon. Ilse, with your happiness and lightheartedness it was a pleasure to have you around all the slightly depressed PhD students. Gisi, thank you for your backup at the Grasp borrels, and thanks for supporting my photography. Ryan, thanks for your help with framing my pictures, and all the best for you and Velia in Mexico.

Romke, I enjoyed our video evenings, and thanks for letting me stay at your place during the last weeks of my PhD contract. Good luck for you and Anne.

Tali, we only met very late during my PhD but I still feel like we became good friends. Keep up your music!

I would like to thank all the people who worked with me in the PhD association, Grasp, and helped setting up the new foundation, Gopher. Especially I would like to thank Genia, Daniël, Jesse, Barbara, Gimon and Olga. Also thanks to Prof Lou de Leij and Ineke Ganzeveld for their collaboration in the work for the PhDs of Groningen.

While there are still so many people I met during my PhD, I can’t name them all. Thanks to Fany, Jihane, Henrik and all the others.

I also would like to thank my friends at home and from my studies in Aachen, who stayed in contact while I am living abroad.

Finally, I would like to say thank you to my family. Thanks for all your help and support. Without you, I wouldn’t be where I am today. It is good that I can count on you. Marta, meeting you was the best thing that happened to me during my PhD. I am proud of you for fighting your way through the difficulties of your PhD, I value you for your love and support, and I am looking forward to our new life in Vancouver with you at my side.

Thomas Maassen
Vancouver, Canada
April 2, 2013

List of publications

1. "Localized States Influence Spin Transport in Epitaxial Graphene,"
   T. Maassen, J. J. van den Berg, E. H. Huisman, H. Dijkstra, F. Fromm, T. Seyller, and B. J. van Wees,
   Phys. Rev. Lett. **110**, 067209 (2013).
2. "Enhancement of Spin Relaxation Time in Hydrogenated Graphene Spin Valve Devices,"
   M. Wojtaszek, I. J. Vera-Marun, T. Maassen, and B. J. van Wees,
   Phys. Rev. B **87**, 081402(R) (2013).
3. "Contact Induced Spin Relaxation in Hanle Spin Precession Measurements,"
   T. Maassen, I. J. Vera-Marun, M. H. D. Guimarães, and B. J. van Wees,
   Phys. Rev. B **86**, 235408 (2012).
4. "Spins in Epitaxiaal Grafeen Leven Langer,"
   J. J. van den Berg, T. Maassen, and B. J. van Wees,
   Nederlands Tijdschrift van Natuurkunde **78-08**, 304 (2012).
5. "Spin Transport in High-Quality Suspended Graphene Devices,"
   M. H. D. Guimarães, A. Veligura, P. J. Zomer, T. Maassen, I. J. Vera-Marun, N. Tombros, and B. J. van Wees,
   Nano Lett. **12** (7), 3512 (2012).
6. "Long Spin Relaxation Times in Wafer Scale Epitaxial Graphene on SiC(0001),"
   T. Maassen, J. J. van den Berg, N. IJbema, F. Fromm, T. Seyller, R. Yakimova, and B. J. van Wees,
   Nano Lett. **12** (3), 1498 (2012).
7. "Comparison between Charge and Spin Transport in Few-Layer Graphene,"
   T. Maassen, F. K. Dejene, M. H. D. Guimarães, C. Józsa, and B. J. van Wees,
   Phys. Rev. B **83**, 115410 (2011).
8. "Linear Scaling between Momentum and Spin Scattering in Graphene,"
   C. Józsa, T. Maassen, M. Popinciuc, P. J. Zomer, A. Veligura, H. T. Jonkman, and B. J. van Wees,
   Phys. Rev. B **80**, 241403(R) (2009).

Curriculum Vitae

Thomas Maassen

12 February 1984	Born in Viersen, Germany.

Education

12/2008–1/2013	Foundation for Fundamental Research on Matter (FOM) PhD research in the group “Physics of Nanodevices” (prof.dr.ir. B. J. van Wees) Performed at the Zernike Institute for Advanced Materials, University of Groningen, The Netherlands
10/2003–9/2008	RWTH Aachen, Germany Master (Diplom) Physics Graduation with distinction Diplom project on current-induced magnetization dynamics in ferromagnetic nanostructures (prof.dr.sc.nat. G. Güntherodt)
6/2003	Gymnasium am Geroweiher, Mönchengladbach, Germany Abitur, best graduate of the high-school in 2003